



MONASH University

Fractures and their ancestors

Exploring structural inheritance through multi-scale fracture analysis

Anindita Suryandari Samsu

Dipl.-Ing., BSc

A thesis submitted for the degree of

Doctor of Philosophy

at Monash University in 2019

School of Earth, Atmosphere and Environment

Faculty of Science

Copyright notice

© Anindita S. Samsu 2019.

I certify that I have made all reasonable efforts to secure copyright permissions for third-party content included in this thesis and have not knowingly added copyright content to my work without the owner's permission.

Publications during enrolment

- **Rapid, semi-automatic fracture and contact mapping for point clouds, images and geophysical data**

Dec 2017 *Solid Earth*

Samuel T. Thiele, Lachlan Grose, Anindita Samsu, Steven Micklethwaite, Stefan A. Vollgger, and Alexander R. Cruden

- **The influence of basement faults on local extension directions: Insights from potential field geophysics and field observations**

Feb 2019 *Basin Research*

Anindita Samsu, Alexander R. Cruden, Mike Hall, Steven Micklethwaite, and Steven W. Denyszyn

Thesis including published works declaration

I hereby declare that this thesis contains no material which has been accepted for the award of any other degree or diploma at any university or equivalent institution and that, to the best of my knowledge and belief, this thesis contains no material previously published or written by another person, except where due reference is made in the text of the thesis.

This thesis includes one original paper accepted for publication in a peer reviewed journal. The core theme of the thesis is structural inheritance. The ideas, development and writing up of all the papers in the thesis were the principal responsibility of myself, the student, working within the School of Earth, Atmosphere and Environment under the supervision of Alexander R. Cruden.

The inclusion of co-authors reflects the fact that the work came from active collaboration between researchers and acknowledges input into team-based research.

In the case of Chapters 3, 4, and 5, my contribution to the work involved the following:

Thesis chapter	Publication title	Status	Nature and % of student contribution	Co-authors	Monash student
3	The influence of basement faults on local extension directions: Insights from potential field geophysics and field observations	Accepted	87.5% Design, data acquisition and analysis, manuscript writing	ARC 5%	No
				MH 2.5%	No
				SM 2.5%	No
				SWD 2.5%	No
4	Who's your daddy? The scale-dependent influence of structural inheritance on fracture patterns	Submitted	85% Design, data acquisition and analysis, manuscript writing	ARC 5%	No
				SM 4%	No
				LG 4%	No
				SAV 2%	No
5	Inheritance without reactivation: Insights from analogue experiments	Not submitted	90% Design, experiments, manuscript writing	ARC 5%	No
				NM 3%	No
				RFW 2%	No

I have renumbered sections of the accepted paper in order to generate a consistent presentation within the thesis.

Student name: Anindita Samsu

Student signature:

Date:

The undersigned hereby certify that the above declaration correctly reflects the nature and extent of the student's and co-authors' contributions to this work. In instances where I am not the responsible author I have consulted with the responsible author to agree on the respective contributions of the authors.

Main supervisor name: Alexander Cruden

Main supervisor signature:

Date:

Abstract

Rifts generally occur in pre-deformed continental crust. The strength anisotropies that have resulted from previous deformation events can impact the formation of new fractures, exerting multiple orders of control on the architecture of the rift system, individual basins, and basin-internal structures. This influence of pre-existing structures on syn-rift and post-rift deformation is described in literature as *structural inheritance*. Reactivation of pre-existing basement faults, shear zones, and fabric during rifting produces new faults in cover rocks that strike parallel to the reactivated structures. However, reactivation is only one form of inheritance, and here I investigate an alternative, more subtle mechanism based on a rotation of the strain and stress fields due to inherited basement structures.

The aim of this thesis is to contribute to further understanding of how structural inheritance affects later brittle deformation (i.e., fracturing) in rift basins, with a focus on its influence on fracture orientations and distribution in cover rocks and the scale at which inheritance operates. The onshore Gippsland Basin of southeast Australia is an ideal natural laboratory, where the exposure of the folded and fractured basement and the overlying cover rocks provides a unique opportunity to map structures in these units at comparable scales. Mapping of fractures at meter to kilometre scale was conducted using a combination of geophysical potential field data, high-resolution digital aerial imagery derived from unmanned aerial vehicle (UAV) photogrammetry, and traditional field mapping techniques. From this multi-scale dataset, an interpretation of the scale-dependent influence of structural inheritance on syn-rift and post-rift deformation in the onshore Gippsland Basin was formulated. Based on the field evidence, I inferred that structural inheritance can lead to the formation of rift-oblique and extension-oblique faults during rifting without direct reactivation of a basement structure, which was demonstrated by means of analogue experiments.

Structural inheritance has a significant impact on natural fractures at the scale of hydrocarbon, geothermal, and groundwater reservoirs. Moreover, it has broad implications for global plate modelling and interpreting regional tectonics. The findings of this thesis are applicable to rift basins globally, which are likely to have been influenced, to some degree, by structural inheritance.

Plain language summary

When tectonic plates move, parts of the Earth's crust are stretched, causing its uppermost layers to break in a brittle fashion and creating fractures. Certain relationships between the direction of regional basin-forming stretching and fracture orientations in rocks that fill the basin (here referred to as "cover" rocks) have been established. However, new fractures can inherit the properties of the underlying, stretched "basement" rocks, so that they are oblique to their expected orientation. The aim of this research is to better understand the impact of this basement-cover interaction, known as structural inheritance, on fractures at different scales. The findings presented here have broad implications for reconstructing earlier movements and configurations of tectonic plates and predicting the accumulation of natural resources in the Earth's crust.

Acknowledgements

First and foremost, I want to thank my main supervisor, Sandy Cruden, for his guidance and support throughout my candidature. Sandy, for some wild reason you trusted in my ability to carry out this project, and for some reason I got on a plane to Melbourne because of it. Thank you for giving me the freedom to shape the project and make it my own. You're a man of few words, but I never doubted that you have my back.

I would also like to thank my co-supervisors, Steven Micklethwaite and Mike Hall, for their support. Mike, thanks for your sharing your extensive knowledge of the Gippsland Basin and your generosity in the field. Steve, thanks for the exciting discussions, for improving my writing, and – most of all – for encouraging me to aim high and be bold.

Thank you to my milestone panel members, Roberto Weinberg, Fabio Capitanio, Chris Wilson, and Peter Cawood, for your constructive input and for leaving your doors open for a chat. Thank you to the Structural Geophysics group for the interesting discussions. All of your support reflects the positive and collaborative attitude of the academics at the School of Earth, Atmosphere, and Environment. I am thankful to have been part of such a stimulating and supportive community.

To all the professional staff at EAE: We all know that you're really in charge around here. Caroline, Silvana, Ada, Tien Chin, Emily, Christine, Katie, Junnel, Leigh, Massimo, and Rachelle, thank you for your help, day in day out. To Pete Betts and the Faculty of Science, thank you for your commitment to supporting us postgraduate students and for looking after our well-being. Also, thank you to my fellow postgraduate committee members for the immense effort and time you have put into strengthening our community.

To my friends and fellow postgrads: Thank you for making it easy to come into uni and plonk myself down at my desk every day. Marianne and Martin, thanks for a memorable time in our house in the Gully. Thank you to my officemates, Emily, Lauren, Sophia, and Julia, for keeping our space warm. I would like to thank Ivan, Nathan, Jonathan, Andrew, and Megan for taking time out of your own research to help me with fieldwork. Nic, thank you for showing me the ways of the analogue modeller – you are an exceptional teacher. Uchi and Hany, thanks for your help in the lab. Thanks David, Mathias, and many of others before me, who have helped me feel like part of the group from Day 1. I've also benefited so much from feedback from Cass, Lynn, Bethan, and others who have helped me improve my presentations. Jonas, thanks for the countless cups of coffee and running in circles with me. Sam and Lachie, thank you for believing in me.

Stefan and Tephy, your faces were a welcome sight when Joel and I first arrived in Melbourne. Thank you for welcoming us into your home and helping us settle in, both at uni and in this new city.

Thanks to Trevor Vincent and friends at RunMonash and Glenhuntly Athletics for inviting me into your running tribe. The time I've spent with you at the ovals, on the cross country circuit, and on the trails have helped me find balance throughout my PhD and taught me to “find my fierce”. Thanks for encouraging me to push my limits.

I wouldn't be where or who I am without my parents, Reny and Dhar Samsu. Thank you for believing in me, for trusting that we can be close despite the distance, and for always encouraging me to be my best self. Gudrun, André, Flavia, and Jenny, thank you for supporting Joel's and my decision to explore life in Australia. To my family in Indonesia and Austria, this is for you.

Joel, thank you for being here, always.

Table of contents

Abstract	vii
Plain language summary.....	ix
Acknowledgements	xi
Table of contents	xiii
List of figures	xvii
List of tables	xxv
Chapter 1	1
1.1. Scope of the thesis.....	3
1.2. Thesis structure.....	4
1.3. Structural inheritance.....	5
1.3.1. Tectonic inheritance	5
1.3.2. Basin and sub-basin-scale basement inheritance.....	8
1.3.3. Stress rotation near pre-existing structures.....	10
1.3.4. Scale dependency of inheritance	12
1.4. Natural fractures	12
1.5. Methods	13
1.5.1. Fracture mapping using a multi-scale dataset.....	13
1.5.2. Analogue modelling	15
Chapter 2	19
2.1. The Australian Southern Margin	19
2.2. The Gippsland Basin	21
2.3. The basement beneath the onshore Gippsland Basin	24
2.4. Structural inheritance in the Gippsland Basin	25
Chapter 3	29
Abstract	31

3.1.	Introduction	32
3.2.	Geological setting.....	34
3.2.1.	Stratigraphy and evolution of the Gippsland Basin.....	35
3.2.2.	Onshore study area	37
3.3.	Methods	37
3.3.1.	Potential field geophysics.....	39
3.3.2.	Field data acquisition.....	39
3.3.3.	Fracture interpretation from integrated datasets	42
3.3.4.	U-Pb ID-TIMS dating of a mafic dike.....	43
3.4.	Results	46
3.4.1.	Fault orientations in basement and basin sediments.....	47
3.4.2.	Kinematics.....	48
3.4.3.	Geochronology	53
3.4.4.	Overprinting relationships and timing.....	53
3.5.	Discussion	57
3.5.1.	Sequence of deformation from outcrop data	57
3.5.2.	Early Cretaceous magmatism in the Gippsland Basin.....	58
3.5.3.	The role of basement faults in syn-rift faulting	60
3.6.	Conclusions	62
	Acknowledgements	63
	Chapter 4	65
4.1.	Introduction	67
4.2.	Geological setting.....	70
4.2.1.	Cretaceous cover rocks.....	71
4.2.2.	The Paleozoic basement	71
4.2.3.	The Neoproterozoic–Cambrian basement	72
4.3.	Methods	74
4.3.1.	Semi-automated fracture tracing	74
4.3.2.	Fracture orientation analysis using length-coloured rose diagrams	75

4.3.3.	Fracture orientation analysis using gridded rose diagrams.....	77
4.4.	Results	78
4.4.1.	Structural characteristics of basement rocks (Cape Liptrap).....	78
4.4.2.	The orientation of fractures in cover rocks (Cape Paterson area).....	84
4.4.3.	Basin-scale fracture trends.....	87
4.5.	Discussion	87
4.5.1.	The influence of multiple levels of basement on rift-related faults.....	87
4.5.2.	Comparing outcrop-scale basement and cover structures	90
4.5.3	Comparing regional-scale faults with outcrop-scale fractures	90
4.6	Conclusions	92
	Acknowledgements	93
	Data availability	94
Chapter 5	95
	Abstract	97
5.1.	Introduction	97
5.2.	Crustal-scale inheritance in Australia.....	98
5.3.	Experimental methods.....	100
5.3.1.	Boundary and initial conditions.....	100
5.3.2.	Scaling and materials.....	101
5.3.3.	Construction of the model layers.....	104
5.3.4.	Deformation monitoring and analysis	106
5.4.	Results	107
5.4.1.	Reference experiment: quasi-homogeneous lower crust (Exp LE-01).....	107
5.4.2.	Strong vs. normal lower crust (Exp LE-05)	108
5.4.3.	Long-wavelength anisotropy in the strong lower crust (Exp LE-07)	112
5.4.4.	Short-wavelength anisotropy in the strong lower crust (Exp LE-08).....	112
5.5.	Discussion	113
5.5.1.	The influence of crustal strength on fault distribution.....	113
5.5.2.	Rotation of strain axes above a strong, anisotropic lower crustal block.....	113

5.5.3.	The scale-dependent role of lower crustal anisotropies on fault patterns.....	115
5.5.4.	Implications for natural rift basins and model limitations.....	117
5.6.	Conclusions	118
	Acknowledgements	118
Chapter 6	119
6.1.	Thesis summary.....	121
6.2.	Research implications and future research recommendations.....	122
6.2.1.	Terminology: reactivation vs. basement inheritance.....	122
6.2.2.	The mechanisms of basement inheritance.....	123
6.2.3.	From 2D to 3D fracture datasets.....	123
6.2.4.	Recommendations for future studies in the Gippsland Basin.....	124
6.2.5.	Differentiating between oblique rift kinematics and inheritance.....	124
6.3.	Concluding remarks.....	125
References	127
Appendix 1	153
Appendix 2	155
Appendix 3	157

List of figures

Figure 1.1 Simplified maps of (a) the North Atlantic Caledonian–Hercynian belts and (b) the South Atlantic Pan-African belts, represented by the dashed lines (modified from Tommasi and Vauchez, 2001). Grey circles indicate the inferred locations of mantle plumes associated with the Atlantic rifting. Light grey lines in (a) mark the Central Atlantic giant radiating dike swarm (Ernst et al., 1995). The black dot in (b) marks the location of a slow seismic anomaly (Schimmel et al., 2003; VanDecar et al., 1995) that represents a remnant conduit of the Parana plume. The role of the mantle plume in rift initiation is still unclear, as rifting initiated somewhat simultaneously along segments more than 2,000 km long, parallel to the trend of the orogenic belts (Klitgord and Schouten, 1986; Tommasi and Vauchez, 2001).	6
Figure 1.2 Conceptual diagram of lithospheric-scale and crustal-scale inheritance of pre-existing orogenic structures (Salazar-Mora et al., 2018). The weak suture in the lithospheric mantle (green) may be reactivated, competing with mantle lithosphere necking to accommodate lithospheric extension. At the crustal level (orange), thrust faults may be reactivated in a normal sense during extension.....	7
Figure 1.3 Schematic illustrations of crustal-scale inheritance by means of basement reactivation (Daly et al., 1989). In (a), shallowly dipping thrust faults are reactivated in a normal sense. In (b), a steeply dipping basement shear zone experiences strike-slip reactivation, forming a pull-apart basin.	8
Figure 1.4 Aerial photo of an outcrop (a) at Nash Point, UK, and interpreted fracture traces (b) (Maerten et al., 2016). Paleostress inversion resulted in a modelled NNW-SSE (163°) oriented maximum horizontal stress. Joints deviate from this orientation near fault tips or fault intersections.....	11
Figure 1.5 Datasets used for fracture interpretation in this study, data types typically used in studies of fracture systems (grey), and the scale of observation.	14
Figure 2.1 Map of free-air satellite gravity (Andersen et al., 2010) highlighting the major tectonic features of the Australian Southern Ocean between Australia and Antarctica (Williams et al., 2011). Br = Bremer Basin; GAB = Great Australian Bight Basin; Ot = Otway Basin; So = Sorell Basin; Ba = Bass Basin; Gi = Gippsland Basin.	20

Figure 2.2 Map of the Bass Strait basins (modified from Samsu et al., 2019), which include the Otway, Bass, and Gippsland basins.....	20
Figure 2.3 Map of the structural elements of the Gippsland Basin (a), with the red dashed line indicating the location of the basin cross section (b) and chronostratigraphic section (c) (modified from Norvick et al., 2001).	22
Figure 2.4 Map of the structural zones of the Lachlan Orogen in Victoria (modified after VandenBerg et al., 2000). The grey dashed box indicates the location of the onshore Gippsland Basin study area.....	24
Figure 2.5 Schematic illustration of the evolution of VanDieland and the Selwyn Block (Cayley, 2011) in the Late Cambrian (505–500 Ma): The arrival of VanDieland between western Victoria (Australia) and Northern Victoria Land (Antarctica) during the Tyennan Orogeny, stalling paleo-Pacific subduction west of VanDieland.....	26
Figure 2.6 Schematic illustration of the evolution of VanDieland and the Selwyn Block (Cayley, 2011) in the Early Ordovician (470 Ma): A re-established paleo-Pacific subduction south of VanDieland triggered sinistral lateral escape, transporting VanDieland northeast and trapping a segment of the paleo-Pacific oceanic crust that would later become the Stawell and Bendigo Zones.....	27
Figure 2.7 Schematic illustration of the evolution of VanDieland and the Selwyn Block (Cayley, 2011) in the Late Ordovician–Early Silurian (450–430 Ma): A continuous subduction zone has been re-established along the eastern Gondwana margin. In the Benambran Orogeny, the Stawell and Bendigo Zones undergo shortening, forming the western Lachlan Orogen. An E-W trending transform causes differential shortening between the Lachlan Orogen and the Antarctic craton, moving them to within 30 km of their present-day locations.	28
Figure 3.1 (a) Location and major faults (in red) of the eastern Australian Southern Margin basins (Constantine, 2001; Geoscience Australia, 2018a, 2018b; K. C. Hill et al., 1995; Power et al., 2001). The Gippsland Basin is separated by the blue dashed line into a western onshore area (the subject of this study; b) and an eastern onshore and offshore area. SA = South Australia; VIC = Victoria; NSW = New South Wales; TAS = Tasmania. (b) Faults in the western onshore Gippsland Basin study area. Onshore geology is modified after the Victoria s – Seamless Geology 2014 dataset (Victorian Department of State Development Business and Innovation, 2014). Structures of the onshore Gippsland Basin study area are modified after Constantine (2001) and Power et al. (2001).	33
Figure 3.2 Summary of the stratigraphy and tectonic history of the Gippsland Basin (after Bernecker & Partridge, 2001) and deformation events derived from seismic reflection studies in the offshore Gippsland Basin (after Power et al., 2003). The stratigraphic column is from the Central Deep, offshore Gippsland Basin.	36

- Figure 3.3** Map of onshore first-order faults overlain on grayscale image of the first vertical derivative of the RTP high-pass filtered (33,000 m), upward continued (200 m) aeromagnetic data. Faults in red were interpreted from onshore gravity and aeromagnetic data (see **Figure 3.4** for examples) and integrated with surface geology. Structures in blue were mapped by Willcox et al. (1992) and Smith et al. (2000). Lower Cretaceous Strzelecki Group outcrops are shown in green (Early Cretaceous sediments). Domains with a high frequency or “stippled” magnetic response correlate with Cenozoic volcanic rocks (orange). The rose diagram of the mapped faults (this study) was created using the Line Direction Histogram plugin (Tveite, 2015) in QGIS and is weighted by fault trace length. 38
- Figure 3.4** Examples of geophysical potential field grids used for interpreting faults and fracture zones at >10 km-scale down to the scale of several kilometres. (a) Colour image of the onshore isostatic residual gravity map of the onshore Gippsland Basin overlain on a Bouguer Gravity anomaly map of Victoria; (b) Colour image of the reduced to the pole (RTP) aeromagnetic data of the onshore Gippsland Basin; (c) Grayscale image of the first vertical derivative (1VD) of the RTP aeromagnetic data; (d) Composite colour image of the tilt derivative of the RTP aeromagnetic data superimposed on the RTP high-pass filtered (33,000 m), upward continued (200 m) aeromagnetic data. WP = Wilsons Promontory..... 40
- Figure 3.5** Map of UAV survey locations and faults interpreted from geophysical potential field data and near-shore bathymetry, overlain with shaded grayscale image of near-shore bathymetry. The azimuth and inclination of the illumination source for the hillshade algorithm are 55° and 66°, respectively. The location of this map is shown in **Figure 3.3**. 42
- Figure 3.6** Map of faults and a mafic dike at the Caves and Kilcunda (see **Figure 3.3** and **Figure 3.5** for location). (a) Satellite image of the Caves locality overlain with UAV-based orthophoto of a wavecut platform and (b) interpreted faults and dike. The dashed line indicates the extent of the orthophoto. A NNW-SSE trending dike (D004) exploits fault TC-05, indicating that dike intrusion postdates initial fault activity. The sampling site for D004 is indicated by the yellow star. The rose diagram of the fracture traces was created using the Line Direction Histogram plugin (Tveite, 2015) in QGIS and is weighted by fault trace length. (c) Digital aerial image of a wavecut platform at Kilcunda (7.5 cm/pixel resolution; Nearmap, 2018) and interpreted faults. The inset (d) shows a NE-SW trending normal fault that is filled with a breccia injectite, signalling soft-sediment deformation. The breccia contains a massive, coarse-grained matrix that may have originated from an unconsolidated unit below the outcropping sandstone. Clasts of fine-grained sandstone in the breccia suggest that parts of the host rock were incorporated into the injectite as it was forced upwards. At both localities, NE-SW to ENE-WSW striking normal faults are overprinted by NNW-SSE and N-S to NNE-SSW trending conjugate faults. 44

- Figure 3.7** (a-c) Various dike geometries and forms of dike-fracture interaction at Harmers Haven South and Harmers Haven North (see **Figure 3.5** for location). Red lines are fault traces, purple polygons are dikes, and yellow dashed lines are joint traces. The joint set in (b) has an azimuth of 344° . The yellow star in (d) represents the D006 sampling site..... 46
- Figure 3.8** Field photos of outcrop-scale Cretaceous Strzelecki Group structures at the Caves (see **Figure 3.5** and **Figure 3.6** for location). (a) Fault TC-01, a normal fault that protrudes out of the wavecut platform and exhibits up to 5 m dip-slip displacement. A fault orientation measurement from TC-01 is plotted on an equal area lower hemisphere stereonet. (b, c) Clay smear and deformation bands (photo courtesy of R. Weinberg) associated with fault TC-01, located within the footwall. (d) Fault TC-02, a normal fault showing dip-slip displacement, north of TC-01. (e, f) Subvertical mafic dike (D004) overprinting Fault TC-05. 50
- Figure 3.9** Field photos of evidence of outcrop-scale reactivation (see **Figure 3.5** and **Figure 3.6** for location). (a, b; FR-01) Mineralized faults at Flat Rocks. (c, d; TC-V) Veins at the Caves. Shallowly-plunging striations on vein surfaces indicate slip with a major strike-slip component that is either coeval with or postdates mineralization. Fault FR-01 is a NNW-SSE striking fault that is partly filled with a breccia injectite. A lower hemisphere, equal area stereonet shows the orientations of structures summarized in **Table 3.4**. Dots represent striation orientations. The green great circles and dot correspond to normal faults (TC-01 and TC-02). The black great circles and dots correspond to strike-slip faults. The dashed line represents Vein TC-V. (e, f; TC-06) Centimetre-scale shear fractures in the steeply-dipping, N-S striking fault. Normal dip-slip displacement is overprinted by reverse dip-slip displacement. The photograph was taken facing NW. SD = sand-dominated layer; CD = coal-dominated layer. 52
- Figure 3.10** Results of U-Pb ID-TIMS analysis of four zircon crystals from Dike D006 (Harmers Haven; see **Figure 3.5** and **Figure 3.7d** for location). The weighted mean $^{206}\text{Pb}/^{238}\text{U}$ age calculated from a coherent, concordant population of single-crystal analyses is 116.04 ± 0.15 Ma (2σ , MSWD = 0.23, N = 4). This is interpreted to be the age of emplacement for Dike D006. 55
- Figure 3.11** Schematic illustration of the sequence of Early Cretaceous outcrop-scale deformation in the onshore Gippsland Basin study area, based on field observations (refer to text for details on overprinting relationships). Red arrows indicate the inferred paleo-extension direction if Early Cretaceous magmatism were linked with ENE-WSW extension along the East Gondwana margin and the opening of the Tasman Sea, as opposed to NNW-SSE directed shortening. Events 2 and 3 could have been coeval. 58
- Figure 3.12** Schematic illustration of the influence of a pre-existing basement fault on faulting in the cover during subsequent extension. In (a) the strike-slip component of basement fault reactivation influences the kinematics of the new cover faults, resulting in oblique slip. In (b) locally misoriented faults form due to the topographic expression of the basement fault at the

basement-cover interface or because the basement fault creeps slightly, rotating the stress field locally. (a) and (b) are possible scenarios for the onshore Gippsland Basin, where the cover is underlain by basement rocks with a NNE-SSW structural trend. These structures may be less influential or absent offshore, so that new cover faults are orthogonal to the inferred far-field extension direction (c). BF = basement fault; CF = cover fault. 62

Figure 4.1 Location and major structures of the Cretaceous Gippsland Basin and the nearby Otway Basin and Bass Basin (shaded in blue). (a) Grey lines indicate major structures and boundaries of the underlying Neoproterozoic–Cambrian Selwyn Block (continuous lines are zone boundaries; dashed lines are faults), modified after Moore et al. (2016). Areas that are underlain by the Selwyn Block are shaded in grey. Brown lines represent the boundaries of tectonic zones of the Lachlan Orogen. HMFZ = Heathcote-Mt. William Fault Zone. (b) Faults and folds in the Gippsland Basin, modified after Constantine (2001) and Power et al. (2001). From west to east, structural trends change from NE-SW and ENE-WSW (western onshore Gippsland Basin), to E-W and NW-SE (eastern onshore and offshore Gippsland Basin); this transition coincides spatially with the eastern margin of the Selwyn Block. The coordinate reference system is GDA94 / MGA zone 55..... 69

Figure 4.2 Summary of the deformation history in the Gippsland Basin and associated tectonic events. Deformation events in the offshore Gippsland Basin are derived from seismic reflection studies (Power et al., 2003). Cretaceous deformation in the onshore Gippsland Basin is derived from field studies and regional potential field geophysics (Samsu et al., 2019). 70

Figure 4.3 Map of basin-scale (>1 km-scale) faults interpreted from magnetic and gravity data (modified after Samsu et al., 2019). The rose diagram of fault traces was created using the GeoTrace plugin (Thiele et al., 2017) in QGIS and is coloured by fault length. Colours on the rose diagram correlate with fault length bins shown on the length histogram. 73

Figure 4.4 Map of the UAV photogrammetry survey areas, where outcrop-scale fractures in the Lower Cretaceous Strzelecki Group were traced, overlain on a greyscale image of near-shore bathymetry (modified after Samsu et al., 2019). The frequency of the orientations of fracture traces from each area is visualized as length-coloured rose diagrams. Colours correspond to fracture length, subdivided into 10 m bins (see **Figure 4.5** for colour ramp of length bins). See **Figure 4.3** for location of map. 75

Figure 4.5 Fracture trace maps and rose diagrams, representing fractures <50 m in length, for the five studied outcrops (see **Figure 4.4** for locations). Fracture traces (interpreted at a scale of 1:500) are overlain on UAV orthophotos. Colours on the rose diagram correspond to fracture length, subdivided into 10 m bins..... 76

Figure 4.6 Fracture traces (green) interpreted from UAV orthophotos at 1:500 and 1:100 zoom levels. Fractures that can be seen at the 1:500 scale (thick, continuous lines) were included in

the analyses of fracture orientations, so that we only compare fractures between outcrops that are observable at the same scale. Purple traces represent mafic dikes. 77

Figure 4.7 (a) Fracture trace map of the Harmers Haven North locality. The basemap is a high-resolution (3 cm/pixel) UAV orthophoto. A grid made up of 100 m x 100 m tiles is overlain on the orthophoto. (b) Length-weighted rose diagrams of fracture trace orientations calculated for each tile using the Line Direction Histogram plugin (Tveite, 2015) in QGIS. The background is a satellite image (source: Google Earth, 38.657362° and 145.572051°, May 14, 2016, accessed July 30, 2017). 78

Figure 4.8 (a) Location of Shark Stack study area at the southwestern end of Cape Liptrap (see **Figure 4.3** for location), where a UAV orthophoto (b; 2 cm/pixel) was used as a basemap for structural mapping in the field. Structures at the Fold Stack locality have been described in detail in Vollgger and Cruden (2016). (c) Map of fractures, axial traces of folds, and structural measurements at Shark Stack. All of the fractures that are visible at a 1:500 scale are shown. 79

Figure 4.9 Structures at Shark Stack, Cape Liptrap: (a) Photograph of steeply dipping, alternating beds of sandstone and mudstone cropping out on a horizontal wavecut platform and along vertical cliff faces. These rocks form the Devonian basement underlying the onshore Gippsland Basin. (b) Photograph of disharmonic second-order F2 folds exposed in a cliff face. The inset shows a fold accommodation fault offsetting a sandstone bed in a reverse sense near the fold hinge. The arrow indicates the measured orientation of the hinge line. (c) Photograph of axial planar cleavage and parasitic folds on the limb of an F1 fold. All photographs were taken facing NNE. (d) Plot of poles to bedding measurements and the axis of a first-order F1 fold calculated from bedding measurements. The calculated fold axis is consistent with the orientation of the measured axial planar cleavage, which is orthogonal to the fold axis. (e) Plot of measured fold hinges; shallowly plunging fold hinges are F2 fold hinges associated with a D2 contractional event. All measurements are plotted on equal area lower hemisphere stereonet. 80

Figure 4.10 N-S trending zones of kinking in the wavecut platform (a) and cliff (b). Axial traces of folds are marked by the dashed lines. Kink bands at Shark Stack are analogous to kink bands in nanolamellar pearlitic steel (c) (Kapp et al., 2016). 82

Figure 4.11 (a) Length-coloured rose diagram of outcrop-scale fractures at Shark Stack. (b) The NW-SE trending peak represents a large population of kinks that make up the NW-SE trending F3 kink bands. The length-coloured rose diagram allows us to assign fractures of different length ranges to certain orientation trends. NW-SE kinks are <10 m in length, most of them being shorter than 5 m. Fractures that are longer than 10 m trend NNW-SSE and ENE-WSW. 83

Figure 4.12 (a) Fracture traces at the northern part of the Eagles Nest locality, overlain on a high-resolution (3.2 cm/pixel) UAV orthophoto (See **Figure 4.4** for location). Veering of NNW-SSE trending joints in the vicinity of the large N-S trending fault is observed, which may be caused by perturbed stress trajectories around the larger fault. A similar phenomenon has been observed in photoelastic experiments of biaxial loading on analogue materials (b; modified from de Joussineau et al., 2003)..... 88

Figure 4.13 (a) Schematic cross section demonstrating the influence of different basement units on overlying units. Devonian faulting in the Melbourne Zone could have been controlled by the reactivation of pre-existing Cambrian faults in the Selwyn Block (A). The complex array of Early Cretaceous normal faults could have resulted from local stress re-orientation above Devonian faults and penetrative fabrics in the Melbourne Zone (B). It remains unclear how the relatively high strength of the Selwyn Block, juxtaposed against the weaker surrounding lower crust, could have affected Early Cretaceous rifting (C). GB = Gippsland Basin; MZ = Melbourne Zone; SB = Selwyn Block. (b) Schematic map-view illustration of normal fault orientations: They are oblique to the regional extension direction above an anisotropic basement, but they are orthogonal to regional extension where the basement is less influential. 89

Figure 4.14 Plan-view schematic illustration of fracture traces in the cover – associated with Early Cretaceous extension (a) followed by shortening (b) – and their trends. The purple lines represent structures in the underlying Melbourne Zone basement. Extension-related fractures show the same ENE-WSW trend at basin scale (>1 km) and outcrop scale (meters-scale). During subsequent shortening, pre-existing basement structures and rift-related ENE-WW trending fractures are reactivated, so that new fractures are localized above or near reactivated structures at the basin scale. At outcrop scale, new sub-vertical joints formed parallel to the direction of shortening, though some joints veer towards larger, pre-existing faults..... 91

Figure 5.1 Map of the eastern basins of the Australian Southern Margin rift system, including the Otway, Sorrell, Gippsland, and Bass basins (modified from Samsu et al., 2019). The eastern part of the Otway Basin and the western part of the Gippsland Basin is underlain by the Paleozoic Melbourne Zone (Lachlan Fold Belt) basement and the Neoproterozoic – Cambrian Selwyn Block basement (Cayley et al., 2002; McLean et al., 2010)..... 99

Figure 5.2 Experimental setup for orthogonal extension. In (a) and (b), the red arrow indicates the direction of extension. (c) Top view photograph of the model surface (Exp LE-05) at the end of the experiment. The dashed line indicates the final geometry of the lower crustal SLC-NLC boundary. 103

Figure 5.3 Structure (a) and strength profiles (b-c) of the multi-layer model lithosphere.... 103

Figure 5.4 Preparation of the ductile lower crust and lithospheric mantle layers. (a) The SLC and NLC material were placed in separate rigid frames on top of a flat workbench; the two parts

were united to form the lower crust once the mixtures have settled. (b) The lithospheric mantle material was placed into a rectangular rigid frame and attached to horizontal grips. Flattening of this layer was facilitated with a rolling pin. (c–e) Assembly of the lower crust layer for Exp LE-08. A pasta maker was used to uniformly flatten SLC and weak zone materials to a thickness < 2 mm (c). For the assembly of the “strong” domain, they were cut into strips and placed vertically in an alternating manner within the rigid frame (d), after which this domain was attached to the “normal” domain (e). Photos (c–e) courtesy of J. Samsu. 105

Figure 5.5 Initial lower crustal geometry (a) and results of reference experiment LE-01. (b) is a top-down photograph with oblique illumination, and (c) is the cumulative maximum normal strain on the surface at the end of the experiment. There is no difference in the fault pattern across the SLC-NLC boundary because of the negligible viscosity contrast between the SLC and NLC materials..... 108

Figure 5.6 Results of orthogonal extension experiments at 4.5 h (47% strain) in map view, with no anisotropy (a.i), 5.4 cm-wide weak zones (a.ii), and ~2 mm-wide weak zones (a.iii) in the strong lower crustal block. The inset shows where the NW and SE domains are located when describing fault patterns. (b) Topographic DEM (in mm) from photogrammetric PIV data; (c) photograph of surface of upper crust; (d) photograph of surface of lower crust. SLC = strong lower crust; NLC = normal lower crust..... 109

Figure 5.7 Results from Exp LE-07: (a) cumulative maximum normal strain on surface at the end of the experiment, overlain by 2D strain ellipses; (b) top-down photo of upper crust surface, (c) fault traces, and (d) rose diagram of fault traces. 110

Figure 5.8 Results from Exp LE-08: (a) cumulative maximum normal strain on surface at the end of the experiment, overlain by 2D strain ellipses; (b) top-down photo of upper crust surface, (c) fault traces, and (d) rose diagram of fault traces. 111

Figure 5.9 Schematic plan view illustration of the ways that the net N-S extension is accommodated in Exp LE-08: (a) an orthorhombic fault set, where the acute bisector trends WNW-ESE (100°); and (b) E-W trending faults which are orthogonal to the net extension direction..... 114

Figure 5.10 Schematic illustration of the components of strain in the highly anisotropic NW domain of Exp LE-08. Strike-slip kinematics at the interfaces between the strong and weak materials in the anisotropic lower crust result in internal sinistral shearing within the narrow SLC zones. These representative 2D strain ellipses are not to scale; the relative contributions of the strike-slip and coaxial component may be different in the experiment..... 115

Figure 5.11 Schematic illustration of deformation and associated kinematics in the NW domain of Exp LE-08. (a) Representative finite strain ellipse (calculated from PIV data), with predicted normal fault and strike-slip fault orientations when the maximum horizontal stretching direction ϵ_{Hmax} is NNW-SSE. (b) The orientations of faults at the upper crust surface at the end of the

experiment. ENE-WSW trending faults are wider than NW-SE faults, suggesting that they have accommodated a significant amount of dip-slip displacement (greater than strike-slip displacement).....	115
Figure 5.12 (a) Strain partitioning in the NW domain of Exp LE-07. The 2D strain ellipses are rotated anticlockwise in the SLC zones, but they remain consistent with the NLC in the weak zones. (b) Strike-slip movement along all strong-weak interfaces in the NW domain of Exp LE-08 results in an “averaging effect” of the anisotropic properties of the lower crust. Hence the strain ellipse is rotated anticlockwise across the entire NW domain. WZ = weak zone.	116

List of tables

Table 3.1 Summary of inferred Early Cretaceous paleo-extension directions in the Bass Strait basins.	34
Table 3.2 Summary of UAV survey parameters for Harmers Haven North (HHN), Harmers Haven South (HHS), and The Caves – Flat Rocks (TC-FR) and properties of the resulting orthophotos. The locations for outcrop access points are given in GDA94 / MGA zone 55 (EPSG:28355) coordinates. See Figure 3.5 for outcrop locations. AGL = above ground level; GSD = ground sampling distance; GCP = ground control point.	41
Table 3.3 Azimuth of basin-scale (>1 km) and outcrop-scale fracture traces from geophysical potential field data and UAV orthophotos of outcrops, respectively. The maximum shortening direction inferred from strike-slip faults at the Caves and Kilcunda, assuming that Fault Set 1 and 2 are a conjugate pair, is consistent with the maximum shortening direction that can be inferred from the trend of the regional joint set. From this we infer that the regional joint set and the NNW-SSE and NNE-SSW faults formed coevally.	46
Table 3.4 Summary of structure data collected in the field. All structures are faults with the exception of Vein TC-V. Latitude and longitude are given as WGS	49
Table 3.5 U-Pb isotopic data for zircons from Sample D006. Sample weights are calculated from crystal dimensions and are associated with as much as 50% uncertainty (estimated). Pb_c = Total common Pb including analytical blank (0.8 ± 0.3 pg per analysis). Blank composition is: $^{206}Pb/^{204}Pb = 18.55 \pm 0.63$, $^{207}Pb/^{204}Pb = 15.50 \pm 0.55$, $^{208}Pb/^{204}Pb = 38.07 \pm 1.56$ (all 2σ), and a $^{206}Pb/^{204}Pb - ^{207}Pb/^{204}Pb$ correlation of 0.9. Th/U is calculated from radiogenic $^{208}Pb/^{206}Pb$ and age. Measured isotopic ratios are corrected for tracer contribution and mass fractionation (0.02 ± 0.06 %/amu). ρ = error correlation coefficient of radiogenic $^{207}Pb/^{235}U$ vs. $^{206}Pb/^{238}U$. All	

uncertainties are given at 2σ . Ratios involving ^{206}Pb are corrected for initial disequilibrium in $^{230}\text{Th}/^{238}\text{U}$ using $\text{Th}/\text{U} = 4$ in the crystallization environment. 54

Table 4.1 Summary of the sequence of ductile and brittle deformation at Shark Stack. The orientation of the trace of the structure on aerial imagery, the sense of movement along the horizontal, and the inferred orientation of the maximum horizontal principle stress (σ_H) are included. 81

Table 4.2 Fracture trends in Lower Cretaceous Strzelecki Group outcrops based on length-coloured rose diagrams (**Figure 4.5**). $N_{L \leq 50\text{m}}$ = total number of fracture traces at each locality with a length ≤ 50 m; N_{Trend} = number of fracture traces belonging to the corresponding trend. 85

Table 5.1 Model scaling parameters and material properties. ESPH = Envirospheres; PDMS = polydimethylsiloxane; WPL = white Plasticine; BPL = black Plasticine; K1 = hollow ceramic microspheres; NS = Natrosol..... 104

Chapter 1

Introduction

1.1. Scope of the thesis

Rifts generally occur in pre-conditioned continental crust. The strength anisotropies that have resulted from previous deformation events can impact the formation of new fractures, exerting multiple orders of control on the architecture of the rift system, individual basins, and basin-internal structures. This influence of pre-existing structures on syn-rift and post-rift deformation is described in literature as *structural inheritance*.

Structural inheritance is invoked when one of the following is observed: (i) parallelism or “geometric similarity” (sensu Holdsworth et al., 1997) between reactivated pre-rift basement structures and new rift-related faults or (ii) fractures that are inconsistent with their expected orientation given their structural position and the inferred regional strain or stress regime in which they formed (e.g., Abul Khair et al., 2015; Beacom et al., 2001; Bergbauer and Pollard, 2004; Lavenu et al., 2013). The basement influence is attributed to a local perturbation of the far-field stress near zones that are mechanically weaker or stronger than the surrounding rock. One form of inheritance – *reactivation* of pre-existing faults, shear zones, magmatic fabric, and magmatic intrusions – has been studied extensively, hence its mechanisms and impact on new fractures is well-understood (Holdsworth et al., 2001, 1997; Sibson, 2012, 1985). Much of the existing literature uses the terms *structural inheritance* and *reactivation* interchangeably, which means that mechanisms of more subtle forms inheritance that do not involve reactivation have remained underexplored. Our limited knowledge on the physical processes that occur in non-reactivation-related inheritance was the initial motivation to explore the lesser-known forms of basement-cover interaction in this project.

The ultimate aim of this thesis is to contribute to understanding of the role of structural inheritance in shaping the architecture of a rift basin, with a focus on its influence on the distribution and orientation of natural fractures and the scale at which inheritance operates. Understanding the scale-dependent influence of structural inheritance on fractures in outcrop analogues is useful for predicting whether the regional fault system or a localized area is impacted, which affects the compartmentalization of fluid migration pathways in the crust. Such knowledge is helpful for modelling fracture networks in hydrocarbon, geothermal, and groundwater reservoirs (Bergbauer and Pollard, 2004; Gillespie et al., 1993; Pérez-Flores et al., 2017; Philipp et al., 2007; Zeeb et al., 2013). For predicting the preferential orientation of fluid pathways in reservoirs, it is important to understand the geometry, topology (and therefore connectivity), relative timing, and kinematics of fractures, as well as the tectonics, stresses, and mechanics involved in their formation (Aydin, A., 2000; Nelson, 1985; Peacock and Sanderson, 2018).

Structural inheritance also has implications for reconstructing the tectonic history of a rift basin. The local state of stress in which fractures form is affected by the interaction between the far-field (tectonic) stress and pre-existing structures that perturb the far-field stress. The orientation and distribution of fracture sets (i.e., whether they are pervasive or clustered) aid in inferring whether fractures have recorded the far-field or local paleostress state. For this reason, one of the objectives of this thesis is to characterize fracture patterns in a rift basin that is likely to have been affected by structural inheritance. Here we unravel the sequence of syn-rift and post-rift brittle deformation structures and link their formation to the basin's tectonic evolution and the geology of the underlying basement rocks.

The onshore Gippsland Basin of southeast Australia is an ideal natural laboratory for investigating the impact of structural inheritance on deformation in a rift basin. Exposure of the folded and fractured basement and the overlying “cover” rocks provides a unique opportunity to map structures in these units at the same scale. Using a combination of high-resolution digital aerial imagery, collected with the aid of an unmanned aerial vehicle (UAV), and traditional field mapping techniques, I mapped fractures (including joints, faults, veins, and dikes) and other meso-scale structures in outcropping basement and cover rocks along the coast. Geophysical potential field data, near-shore bathymetric data, aerial (airplane) imagery, and existing maps of surface geology were used to interpret fault traces that exceeded 1 km in length, which are referred to here as “basin-scale” structures. Combining these multi-scale datasets allowed me to build a georeferenced database of onshore fractures, enabling the interpretation of the scale-dependent influence of structural inheritance on syn-rift and post-rift deformation in the onshore Gippsland Basin. Based on the field evidence, a hypothesis was posed that structural inheritance can lead to the formation of rift-oblique and extension-oblique faults during rifting without direct reactivation of a basement structure, and this was tested by means of analogue experiments. The findings of this thesis are applicable to rift basins globally, which exclusively form in pre-deformed crust and are therefore likely to have been influenced, to some degree, by structural inheritance.

1.2. Thesis structure

The remainder of this chapter consists of brief literature reviews on structural inheritance, natural fractures and the data acquisition methods employed in this project to better understand the influence of structural inheritance on the formation of fractures at different scales. Chapter 2 introduces the geological background of the onshore Gippsland Basin study area. Chapters 3, 4, and 5 present findings arising from this research project. Together, Chapters 3 and 4 are the culmination of the first part of this research project, which focused on synthesizing already existing and newly acquired multi-scale fracture data from the onshore Gippsland Basin in order

to understand the sequence of brittle deformation in the study area, link outcrop-scale deformation to what is currently known about the regional tectonics from the Devonian onwards, and identify the impact of different forms of structural inheritance on observed fracture patterns. Chapter 5 focuses on the second part of this project, namely a series of analogue experiments, which were designed to determine the mechanism required to simulate the fracture patterns documented in Chapters 3 and 4.

1.3. Structural inheritance

1.3.1. Tectonic inheritance

Wilson (1966) proposed that the Atlantic Ocean opened, closed, and re-opened along old suture zones. His theory on the cyclic breakup and re-assembly of supercontinents has inspired others to investigate the mechanisms of *tectonic inheritance*, which involves the exploitation of zones of reduced strength during successive deformation events and explains the long-lived nature of plate boundaries (e.g., Tommasi and Vauchez, 2001). Based on the geometry of the Iapetan and Atlantic rifted margins in North America, Thomas (2006) proposed that tectonic inheritance occurs at lithospheric and crustal scales, in both collisional and extensional settings. Lithospheric-scale inheritance may play a role in plate-scale deformation, such as the influence of pre-existing upper mantle structures on the formation of continental margins and rift systems. Crustal-scale inheritance involves crustal-level mechanical discontinuities that may exert significant control on strain localisation and the orientation of shallow, brittle structures.

1.3.1.1. Lithospheric-scale inheritance

The location of rift initiation is controlled by lithospheric-scale anisotropies that act as rheologically weak zones (Will and Frimmel, 2018). Rifts tend to propagate along ancient lithospheric structures (e.g., orogenic belts; **Figure 1.1**) while at the same time avoiding cratons (Daly et al., 1989; Tommasi and Vauchez, 2001; Wilson, 1966). Some examples include the North Atlantic rift (Wilson, 1966), Rio Grande rift (Olsen et al., 1987), Northeast China rift (Ma and Wu, 1987), Baikal rift (Delvaux et al., 1997), East African and West African rifts (Daly et al., 1989; Fairhead and Binks, 1991; Ring, 1994), and Eastern Brazilian rift (Chang et al., 1992). When rifting occurs shortly after orogenesis, crustal thickening and therefore reduction of the total strength of the continental lithosphere may contribute to rift localisation (Dunbar and Sawyer, 1989). Alternatively, Daly et al. (1989) postulated that orogenic suture zones between cratons contain crustal-scale shear zones that are mechanically weaker and therefore more prone to reactivation. However, the source of inheritance may lie at greater depths, in the lithospheric mantle (**Figure 1.2**). Rheological models of the multi-layer lithosphere show that the lithospheric mantle is the strongest layer, so that weaknesses therein

would play a substantial role in localizing lithospheric failure, therefore controlling rift nucleation and propagation (Daly et al., 1989; Tommasi and Vauchez, 2001). Ancient shear zones can also act as conduits for the percolation of fluids through the lithosphere, which facilitates delamination of the lithospheric mantle and therefore weakening (Sarafian et al., 2018).

Observations of shear wave splitting – a manifestation of seismic anisotropy – in the Appalachians and the Pyrenees of North America (Vauchez et al., 1997 and references therein) show that the source of inheritance during rifting can also be a mechanical anisotropy (i.e., fabric) in the lithosphere that formed during previous orogenic episodes, which has been preserved since then. The anisotropy occurs in the form of a lattice preferred orientation (LPO) of olivine crystals that formed during orogenesis, and it can be reactivated when the orientation of the far-field maximum extensional stress is oblique or orthogonal to the fabric trend, resulting in transtensional or coaxial deformation, respectively (Tommasi and Vauchez, 2001; Vauchez et al., 1997).

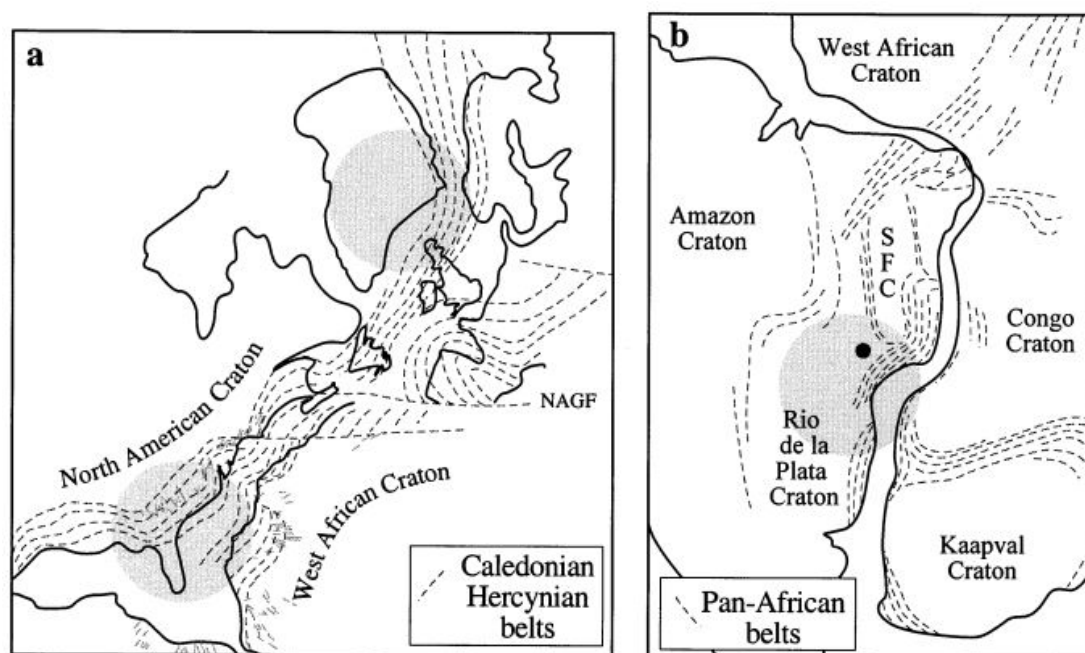


Figure 1.1 Simplified maps of (a) the North Atlantic Caledonian–Hercynian belts and (b) the South Atlantic Pan-African belts, represented by the dashed lines (modified from Tommasi and Vauchez, 2001). Grey circles indicate the inferred locations of mantle plumes associated with the Atlantic rifting. Light grey lines in (a) mark the Central Atlantic giant radiating dike swarm (Ernst et al., 1995). The black dot in (b) marks the location of a slow seismic anomaly (Schimmel et al., 2003; VanDecar et al., 1995) that represents a remnant conduit of the Parana plume. The role of the mantle plume in rift initiation is still unclear, as rifting initiated somewhat simultaneously along segments more than 2,000 km long, parallel to the trend of the orogenic belts (Klitgord and Schouten, 1986; Tommasi and Vauchez, 2001).

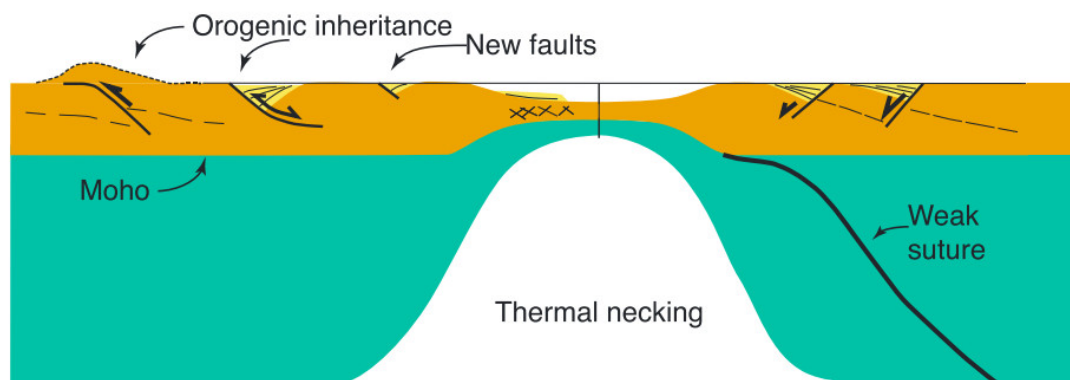


Figure 1.2 Conceptual diagram of lithospheric-scale and crustal-scale inheritance of pre-existing orogenic structures (Salazar-Mora et al., 2018). The weak suture in the lithospheric mantle (green) may be reactivated, competing with mantle lithosphere necking to accommodate lithospheric extension. At the crustal level (orange), thrust faults may be reactivated in a normal sense during extension.

Tommasi and Vauchez (2001) suggested that the “directional strain softening” caused by LPO may explain the long-lived nature of plate boundaries, which experience multiple episodes of reactivation, giving rise to the Wilson Cycle. They also proposed that structures of certain orientations with respect to the maximum extensional stress are prone to reactivation, with the LPO being particularly effective at strike-slip (e.g., transform) boundaries. The location of transform faults at rift offsets in successive rifting events suggests vertical partitioning of the lithosphere by a steeply dipping, pervasive fabric or shear zone that contributes to a reduction of elastic strength (Thomas, 2006). The presence of these weak zones determine the location and propagation of rifts and rift basins (Daly et al., 1989; Theunissen et al., 1996).

1.3.1.2. Crustal-scale inheritance

Crustal-scale inheritance controls brittle structures in the shallow crust, e.g., through reactivation of individual faults or shear zones (Thomas, 2006). While the role of lithospheric-scale inheritance is significant in the initiation and localisation of rifts, crustal-scale inheritance may contribute to along-strike variations in their style of deformation and the geometry of associated basins. Earlier work by Daly et al. (1989) suggested that transfer zones form when steeply dipping basement shear zones and faults undergo strike-slip reactivation during rifting. A spatial relationship between the pre-existing basement structures and the geometry of the newly formed basins was also proposed: pull-apart basins formed along the reactivated structures, while those away from the site of reactivation experienced oblique extension (**Figure 1.3**).

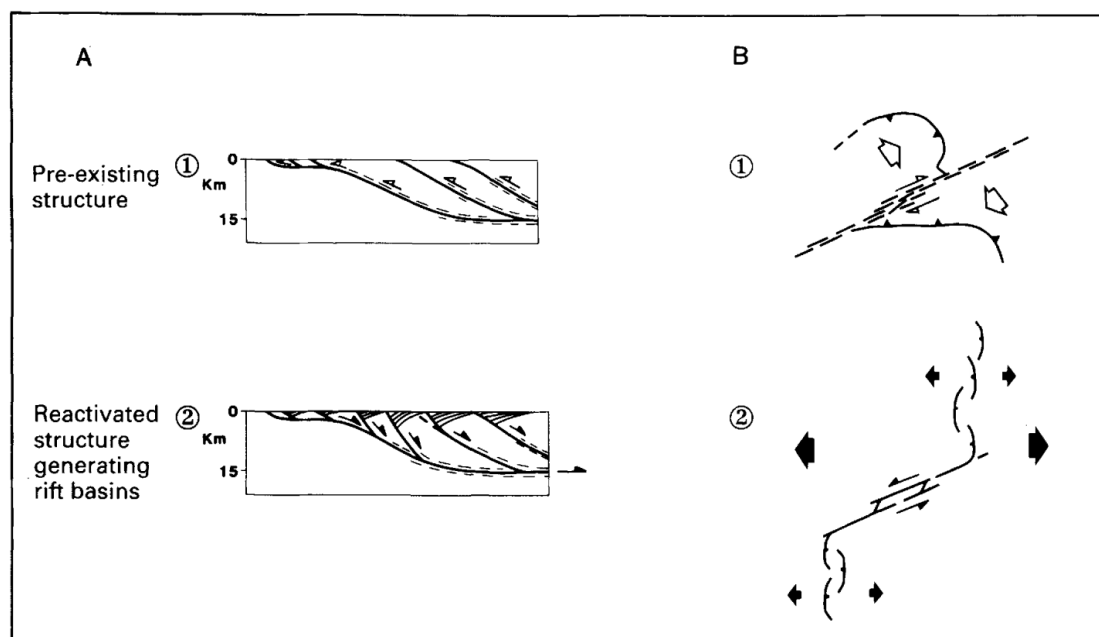


Figure 1.3 Schematic illustrations of crustal-scale inheritance by means of basement reactivation (Daly et al., 1989). In (a), shallowly dipping thrust faults are reactivated in a normal sense. In (b), a steeply dipping basement shear zone experiences strike-slip reactivation, forming a pull-apart basin.

Other studies focused on the East African Rift system have found that rift-oblique, pre-existing basement fabrics influence the architecture of transfer zones, controlling strain partitioning and the orientations of adjacent rift and basin-bounding faults (e.g., Agostini et al., 2009; Corti, 2004; Heilman et al., 2019; Philippon et al., 2015; Rosendahl, 1987; van Wijk, 2005). Apart from rift basin formation, crustal-scale inheritance also contributes to the localisation of active intra-plate deformation and seismicity, as illustrated by Sandiford et al. (2004) in an example from southeast Australia, where they observed a zone of seismicity parallel to an inherited Paleozoic structural grain.

1.3.2. Basin and sub-basin-scale basement inheritance

The forms of inheritance outlined in this section can be considered to operate at crustal scale, as they may impart significant control on the location of rift basins, as discussed in the previous section. However, their impact is also evident at the sub-basin scale, often through the study of fracture networks using seismic reflection data, fracture data derived directly from drill core or from borehole geophysics, or outcrop analogues.

1.3.2.1. Reactivation

Reactivation refers to re-occurring slip along weakened zones in the crust, which occurs because it is easier to initiate failure along a pre-existing structure, i.e., a zone with a lower shear strength than previously undeformed rock, than to nucleate new faults (Byerlee, 1978;

Sibson, 1985). This rationale is supported by a study by Beacom et al. (2001), who observed a correlation between the orientation and intensity of a pre-existing foliation and the clustering of subsequent fractures. A range of pre-existing basement weaknesses can reactivate and control the formation of new rift-related structures, including faults and fault zones (Holdsworth et al., 2001; McCaffrey, 1997), pre-existing magma pathways (Ashby, 2013), metamorphic fabric (Bird et al., 2014; Peace et al., 2018a), pervasive fabric within shear zones (e.g., mylonitic foliations) (Fazlikhani et al., 2017; Heilman et al., 2019; Kirkpatrick et al., 2013; Phillips et al., 2016), and pre-existing rift basins or rift fabrics (Bellahsen et al., 2006; Whipp et al., 2014).

The reactivation of a pre-existing structure in basement rocks, whether discrete (e.g., a fault) or pervasive (e.g., a fabric), results in the formation of new fractures in the overlying cover that is parallel to the reactivated basement structure (e.g., Holdsworth et al., 1997; Kirkpatrick et al., 2013; Phillips et al., 2016). Therefore reactivation is suspected when “geometric similarity” – or apparent parallelism between structures in basement rocks and the overlying cover rocks (sensu Holdsworth et al., 1997) – is observed (e.g., Bertrand et al., 2018). However, this criteria alone is unreliable for inferring whether reactivation has occurred (Holdsworth et al., 1997). Determining the role of basement reactivation requires knowledge on the kinematics associated with deformation and the spatial and temporal relationship between fracture sets, which can be gained from studying three-dimensional (3D) seismic reflection data (e.g., Collanega et al., 2019; Fazlikhani et al., 2017; Phillips et al., 2016; Reeve et al., 2015; Whipp et al., 2014).

1.3.2.2. Basement-induced stress rotation

The idea that rift basins can inherit basement structures without invoking reactivation can be considered from the perspective of stress coupling between the basin’s sedimentary units and the underlying basement rocks. Bell (1996) proposed that in “attached stress regimes”, where sedimentary units directly overlie another tectonostratigraphic unit or basement rocks without any low strength rocks in between to create a mechanical detachment, the stress orientations of the sedimentary units “exhibit the signature” of the underlying rocks. He used the Labrador Shelf (offshore eastern Canada) as an example, where the in-situ maximum horizontal stress measured from borehole breakouts are similarly oriented to the focal mechanism P-axis of a 1971 earthquake with a basement-hosted epicentre.

Lateral variations in the elastic properties of rocks contribute to anomalous local stress orientations, as demonstrated by borehole breakout data from western Canada, eastern Canada, the North Sea, and around the San Andreas fault (Bell, 1996 and references therein). Deviation from the far-field or regional stress trajectories occurs because principal stresses are deflected when they cross an interface between two materials with contrasting elastic properties, with the

amount and direction of deflection being dependent on the amount of contrast (Zhang et al., 1994) and the anisotropy of the medium (Zang and Stephansson, 2010), respectively.

Assuming that stresses in the cover are coupled with the stress regime within the underlying basement, we can infer that deformation in the cover will be influenced by mechanical anisotropies in the basement. This relationship was demonstrated by regional mapping of fractures in NW Scotland, which showed that the complexity of onshore fault patterns can be correlated with changes in the underlying basement structures which are oblique to the regional rifting vectors (Wilson et al., 2010). This subtle basement influence may reflect localized changes in 3D strain, despite limited direct reactivation of pre-existing structures. Similarly, Collanega et al. (2019) demonstrated using 3D seismic reflection data that the nucleation of new rift-related faults above pre-existing basement structures which was not initiated by direct reactivation of the basement structures, emphasizing that perturbation of the local stress field may play a key role in the influence of basement structures on rift-related deformation.

1.3.2.3. Passive inheritance

Basement-controlled fractures do not always form during contractional or extensional tectonic events. Passive inheritance refers to the transfer of basement-hosted geometries to the overlying cover during non-tectonic deformation. This occurs when sediments are deposited on top of an irregular basement topography. In a lineament analysis of aerial imagery, Mollard (1962) recognized that some geomorphological features follow the trace of bedrock fractures that are buried under thick, unconsolidated sediments. He proposed that minor depressions at the ground surface formed above pre-existing bedrock fractures as a result of differential compaction.

The genesis and scale of polygonal faults are also controlled by passive inheritance. Polygonal fault networks on Earth and Mars occur in fine-grained sediments (e.g., mudrocks and chalk). They form as a result of volume reduction through fluid loss during burial, which is accommodated by extensional faulting (Cartwright and Lonergan, 1996; Lonergan et al., 1998). Using numerical modelling, Tuckwell et al. (2003) have shown that polygonal fractures nucleate at fracture seeds that propagate into polygonal fracture networks. These initial flaws are likely to occur at zones of localized stresses at the tops of large basement slopes (Cooke et al., 2011).

1.3.3. Stress rotation near pre-existing structures

In addition to basement inheritance, the formation of new fractures in sedimentary cover units can be significantly influenced by pre-existing structures (within the same units) by means of local stress re-orientation (**Figure 1.4**; also see Section 1.3.2.2) (Maerten et al., 2016). Brittle

discontinuities in rocks perturb the surrounding stress field during slip events (Pollard and Segall, 1987), as demonstrated by photoelastic studies using analogue materials (de Jussineau et al., 2003), numerical models (Maerten et al., 2002), and analyses of borehole breakout data (Barton and Zoback, 1994). The consequences of this effect for the mode, orientation, and distribution of smaller “secondary” structures have been investigated using different numerical approaches, such as the boundary element method (Becker, 1992; Crouch and Starfield, 1983; e.g., Bourne and Willemse, 2001; Kattenhorn et al., 2000) and elastic dislocation modelling (Okada, 1992; e.g., Dee et al., 2007; Healy et al., 2004; Maerten et al., 2002). During basin evolution, older primary faults affect the growth of younger faults to varying degrees during later stages of rifting (e.g., Whipp et al., 2014).

Local stress re-orientation is also demonstrated in outcrop by curved joints adjacent to larger faults (Cruikshank and Aydin, 1995; Rawnsley et al., 1992). Joints act as paleostress indicators, as they are assumed to be mode I (opening) fractures that form perpendicular to the minimum compressive stress. While this relationship is useful for paleostress inversion, accurate estimates of the regional paleostress field can only be obtained if fractures that reflect the far-field stress are separated from those that formed within locally perturbed stress fields (Maerten et al., 2016), and if the fracture data is representative of the study area (Homburg et al., 1997).

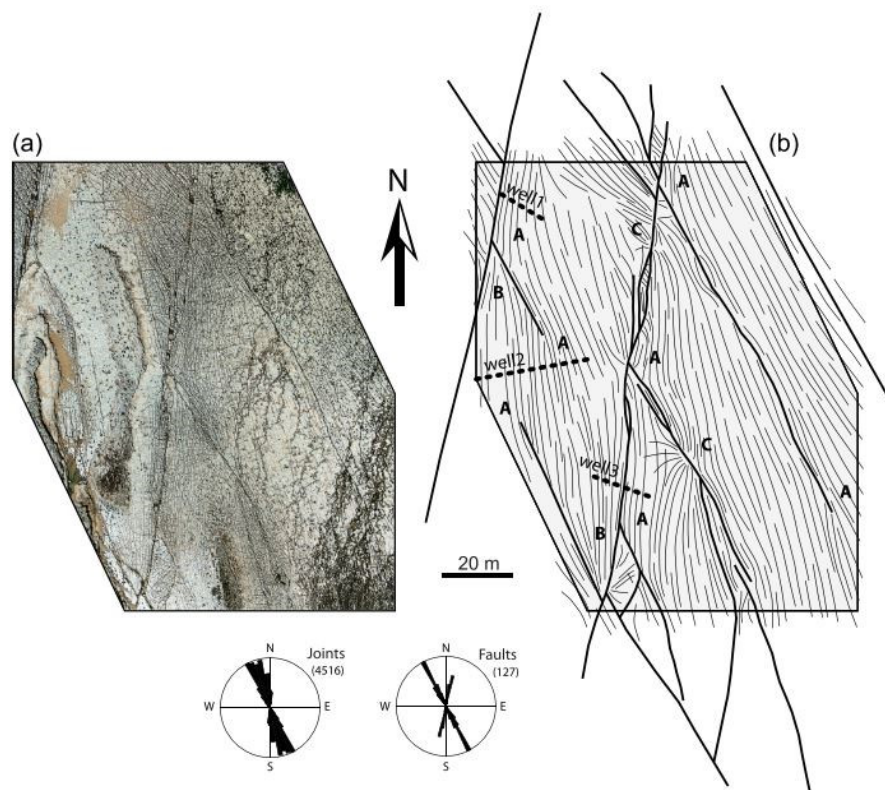


Figure 1.4 Aerial photo of an outcrop (a) at Nash Point, UK, and interpreted fracture traces (b) (Maerten et al., 2016). Paleostress inversion resulted in a modelled NNW-SSE (163°) oriented maximum horizontal stress. Joints deviate from this orientation near fault tips or fault intersections.

1.3.4. Scale dependency of inheritance

Basin-scale inheritance has been invoked in rift basins where there is an apparent geometric relationship between reactivated basement structures and fabrics and basin-bounding faults (Corti et al., 2007; Kirkpatrick et al., 2013; Lezzar et al., 2002). Bertrand et al. (2018) inferred from regional fault orientations in the Upper Rhine Graben that there is a geometric relationship between petrographic variations in the basement rocks (i.e., magmatic fabric) and ~10 km-scale, horst and graben-bounding faults. Similarly, rift fault orientations in the Northeast Highlands of Scotland were affected by the metamorphic fabric of the underlying basement terranes (Ashby, 2013). However, the influence of these relatively large-scale basement structures less apparent at sub-basin scale (e.g., at scales below hundreds of meters), where fractures locally crosscut foliations (Kirkpatrick et al., 2013).

1.4. Natural fractures

Fractures are discrete discontinuities within rocks that form by brittle failure when differential stresses exceed the brittle strength of the rock. They include faults and shear fractures, which have fracture plane-parallel shear displacement, joints, which have an aperture but show no macroscopic fracture plane-parallel displacement, and filled opening mode fractures such as veins and dikes (Gillespie et al., 1993). Fracture networks exert significant controls on rock permeability and therefore the storage and flow of fluids in the crust.

Based on their type of displacement, fractures can be classified into: a) mode I (opening mode; i.e., extensional and tensile fractures); b) mode II (sliding mode); and c) mode III (tearing mode). According to the Coulomb-Mohr failure criterion (Jaeger and Cook, 1979), shear fractures (i.e., faults) form along a plane on which the ratio between shear stress and normal stress is at a maximum. This applies for classic Andersonian faults (Anderson, 1905), which accommodate two-dimensional (2D) plane strain (De Paola et al., 2005; Healy et al., 2006) and form conjugate fault sets. The acute angle between the two fault sets is bisected by the direction of the maximum principal compressive stress, and one of the principal stresses is parallel to the Earth's surface (Anderson, 1905). According to Anderson (1905), the orientation of fractures is a product of the three-dimensional stress imposed upon the host rock. He outlined end member models of faulting in three tectonic regimes, in which two of the principal stress axes are parallel to the horizontal, and one principal stress axis is normal to the horizontal. Multiple fault sets, polymodal or orthorhombic faults (Healy et al., 2014; Krantz, 1988), and reactivated faults cannot be explained by Anderson's theory of faulting or the Coulomb-Mohr failure criterion (Blenkinsop, 2008), therefore requiring analysis of stress and strain in 3D.

Fracture orientation and clustering is dependent on the regional and local stress regime, and hence their structural position relative to faults and also folds (e.g., Stearns and Friedman, 1969; Watkins et al., 2015). Other factors that control fracture distribution (i.e., spacing, clustering) are lithology, mechanical layering, and bed thickness (e.g., Cilona et al., 2016; De Paola et al., 2005; Gross et al., 1995; McGinnis et al., 2017; Narr and Suppe, 1991; Strijker et al., 2012; Watkins et al., 2019). Although deformation is controlled by the far-field tectonic stress, local heterogeneities in the crust can deviate or rotate the stress field (e.g., Maerten et al., 2002; Riller et al., 2017), resulting in the formation of structures that are not consistent with the far-field tectonic stress. As certain relationships between the orientation of the principal stress axes and the orientation and kinematics of brittle structures have been established, fracture data can be used to estimate the orientation of the paleostress field through inversion analysis (e.g., Angelier, 1990; Maerten et al., 2016; Michael, 1984). Likewise, being able to estimate the paleostress field enables prediction of the likelihood and orientation of brittle failure (Bourne and Willemse, 2001; Healy et al., 2004; Maerten et al., 2002). In either of these situations, it is important to be able to differentiate between the far-field stress or a locally re-oriented stress regime (Riller et al., 2017).

1.5. Methods

This section is focused on the background of the methods, which were used to: (i) acquire fracture data (UAV photogrammetry and potential field geophysics) and (ii) test the hypotheses which were formed from their interpretation (analogue modelling). The specific application of the methods to this project is discussed in detail within the individual research chapters (Chapters 3, 4, and 5).

1.5.1. Fracture mapping using a multi-scale dataset

Digital mapping of fractures enables the compilation of spatially located fracture data in a GIS data structure. In this project, raster data which aided in fracture interpretation, such as geophysical potential field grids, satellite imagery, aerial photography, and UAV orthophotos, were treated as basemaps and imported into a GIS environment (QGIS; QGIS Development Team, 2019) for subsequent digital fracture tracing. The resolution of the datasets varied, so that fractures could be interpreted at a range of scales (**Figure 1.5**). In this section, a brief summary on the background and the use of geophysical potential field data and UAV photogrammetry for fracture mapping is provided.

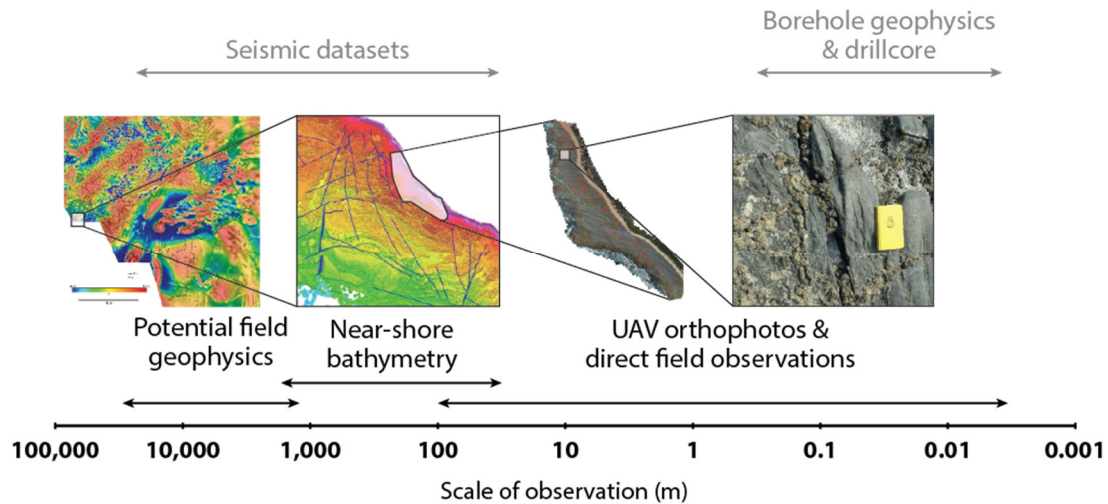


Figure 1.5 Datasets used for fracture interpretation in this study, data types typically used in studies of fracture systems (grey), and the scale of observation.

1.5.1.1. Geophysical potential field data

Potential field geophysics survey data enables the extraction of subsurface geological information from the geophysical properties of rocks. Anomalies in gravity data arise due to density contrasts between rocks. Anomalies in magnetic data indicate the occurrence and distribution of magnetic minerals in the upper crust. These datasets provide an ideal basis for regional structural mapping, especially of terrains with limited outcrop exposure, and for delineating deep basement features that are buried under cover rocks (Blaikie et al., 2017; McLean et al., 2010; Moore et al., 2016, 2015). Geophysical anomalies can provide insights at multiple scales, from the large-scale crustal architecture of the study area to localized zones of alteration due to fluid flow, magma emplacement, or metamorphism (Aitken et al., 2009; Dentith and Mudge, 2014). For examples, in Australia, potential field geophysics is used extensively in mineral exploration, as ore deposits tend to have a strong structural control (Wilson et al., 2017). In the context of petroleum exploration, regional geophysics have also been used to map large crustal trends that may have controlled the architecture of hydrocarbon-bearing basins (Holdgate et al., 2015; Moore and Wong, 2001).

Regional geophysical potential field data allows us to recognize the structural trends and fabric of basement rocks, which makes it a powerful tool for determining the influence of basement inheritance on rift and basin architecture, when combined with other datasets. This is demonstrated in the East African rift system, where it is apparent that basement fabrics controlled the orientation of parallel rift-bounding faults, and pre-rift basement shear zones affected the rift interaction at transfer zones (Heilman et al., 2019).

1.5.1.2. UAV photogrammetry

Digital photogrammetry combines computer vision algorithms known as structure from motion (SfM) and multi view stereo (MVS) to extract the 3D geometry of a scene from a series of digital 2D images (Bemis et al., 2014; Dering et al., 2019; Vollgger and Cruden, 2016). In geology, digital photogrammetry enables the construction of the 3D structure of an outcrop from overlapping photographs, which can be captured using a handheld camera (ground-based photogrammetry) or a camera mounted on an unmanned aerial vehicle (“UAV photogrammetry”; Eisenbeiß, 2009). Following image acquisition, the SfM-MVS processing workflow is used to generate a dense point cloud, which is a detailed 3D representation of the geometry, colour, and texture of the outcrop. From the dense point cloud, datasets such as digital elevation models (DEM), triangulated textured meshes, and orthomosaics (stitched orthorectified images projected onto the DEM; also known as “orthophotos”) can be generated for analysis. Detailed descriptions of this workflow can be found in Bemis et al. (2014), Dering et al. (2019), and Vollgger and Cruden (2016), among others.

UAV-aided fracture mapping is a useful complementary method to traditional fieldwork, enabling increased efficiency in mapping fractures over a relatively large area at scales as small as several centimetres (Thiele et al., 2017; Vollgger and Cruden, 2016). Images from an aerial perspective can also highlight large-scale trends or structures which may not be obvious from an observation point directly on or next to the outcrop. Additionally, UAV photogrammetry enables us to make geological observations and obtain structural measurements in areas that are difficult or dangerous to access (Salvini et al., 2017). Digital fracture traces and best-fit fracture plane orientation measurements can be used to characterize the fracture networks in 2D and 3D (e.g., Bisdom et al., 2017; Hardebol and Bertotti, 2013; Healy et al., 2016). Important parameters for generating discrete fracture networks and fluid flow models, such as fracture orientation, density, and connectivity, can be quantified from these datasets.

Wave cut platforms in the onshore Gippsland Basin study area, which extend over hundreds of meters along the coast, are ideal for UAV-aided fracture mapping (McCaffrey et al., 2005). The rapid collection of images for later processing and analysis makes this technique especially useful considering the brief low-tide time window during which outcrops are exposed. In this project, fracture interpretation was performed on 2D orthophotos because of the sub-horizontal nature and simple topography of the outcrops. Structural measurements in 3D space were collected where possible using a compass clinometer.

1.5.2. Analogue modelling

Analogue modelling or more generally “experimental tectonics” refers to the study of tectonic processes by means of scale models (Ranalli, 2001). This approach enables us to test – in a

controlled environment – hypotheses on the mechanisms of tectonic processes that lead to what we can observe in nature (the prototype), using simplified, practically-sized models in the laboratory (Hubbert, 1937; Ramberg, 1967). Numerous tectonic processes, from global to outcrop scale, have been studied using analogue models (Duarte et al., 2014 and references therein). Materials used for analogue modelling are chosen so that geometric, kinematic, and dynamic similarity is approximately met between the model and nature (Hubbert, 1937; Ramberg, 1967). Such analogue materials include granular materials (e.g., sand, clays) and viscous or viscoplastic materials (e.g., hydrocarbon mixtures, modelling clay, syrups, gelatines), the properties of which must be characterized as functions of stress, strain, strain rate, and temperature to ensure correct scaling (Poirier, 1988).

Previous experiments on lithospheric extension confirm that rift obliquity and inherited, elongate lithospheric weaknesses that are transverse to the main rift trend play a role in rift segmentation and fault localisation (e.g., Corti, 2008; Zwaan et al., 2016). In such experiments, lithospheric weaknesses were implemented in brittle-ductile, lithospheric-scale models either by incorporating a rheological weakness within the lithospheric mantle layer (Agostini et al., 2009; Autin et al., 2013; Corti, 2012; Molnar et al., 2017) or introducing a viscous “seed” between the brittle and ductile layer (Molnar et al., 2018; Zwaan et al., 2016; Zwaan and Schreurs, 2017). The relative angles of the imposed extension direction and the inherited structures – in addition to the spatial arrangement of inherited structures – determine fault localisation and the orientations of transfer zones, rift boundary faults, and rift-internal faults (Corti, 2008; Molnar et al., 2017; Zwaan et al., 2016; Zwaan and Schreurs, 2017). Other crustal-scale studies have focused on the role of discrete crustal weaknesses in crustal-scale and basin-scale inheritance (Bellahsen and Daniel, 2005; Brune et al., 2017; Corti, 2008, 2004; Corti et al., 2007). These weaknesses represent zones of thermally weakened crust or pre-existing faults that are prone to reactivation during extension. However, the role of pervasive crustal fabrics (e.g., Chattopadhyay and Chakra, 2013), such as shear zone and metamorphic foliation, have not been explored to same extent using analogue models.

In this project, a series of analogue experiments were run to determine whether: (a) the presence of a homogeneous, strong crustal block alone is sufficient to create extension-oblique faults during a single phase of extension or (b) if a pervasive anisotropy (i.e., fabric) within the strong crustal block is required to form such “misoriented” faults. These hypotheses arose from observations of the fault patterns in the onshore Gippsland Basin, which are discussed in Chapters 3 and 4 of this thesis. A secondary aim was to determine if it is possible to form extension-oblique normal faults without direct reactivation of the underlying basement weaknesses (e.g., Collanega et al., 2019; Wilson et al., 2010). The aims, setup, and results of these experiments are discussed in detail in Chapter 5.

Chapter 2

Geological background

2.1. The Australian Southern Margin

The Australian Southern Margin (ASM) rift system comprises a series of basins which formed during Jurassic–Cretaceous, west-to-east propagating rifting between Australia and Antarctica. The present-day southern boundary of the Australian plate is characterized by an ENE–WSW trending segment to the west of longitude 130°E and a more complex geometry to the east (**Figure 2.1**). The non-linearity of the rift axis – hence the along-axis change in the strike of major rift faults (Totterdell and Bradshaw, 2004) – can potentially be attributed to the presence of rift-oblique to rift-orthogonal lithospheric weaknesses (e.g., Gibson et al., 2013) or temporal variations in rifting kinematics (e.g., Brune et al., 2018; Williams et al., 2011). Evidence of intra-plate deformation in Australia (e.g., Sandiford et al., 2004) suggests that pre-existing basement structures can locally change the orientation and magnitude of stresses, despite relatively uniform regional stresses from plate boundary interactions (Dyksterhuis and Müller, 2008). As there is no evidence of relative motion between the western and eastern halves of the Australian continent, it is likely that such pre-existing structures contributed to the spatial variation of basin-defining structures (Gibson et al., 2013; Totterdell et al., 2000; Totterdell and Bradshaw, 2004; Willcox and Stagg, 1990).

This ASM has been the subject of several paleo-reconstruction studies that resolved to model the direction and rate of extension between the two continental plates, guided by crustal-scale structural trends, correlations between structures at the Australia–Antarctica conjugate margins, plate boundary geometries, and constraints from features related to the initiation of seafloor spreading. Palinspastic rift reconstructions by Williams et al. (2011) resulted in a model with NNW–SSE directed extension between the onset of continental rifting at ~160 Ma and break-up at ~83.5 Ma, orthogonal to the western ASM segment. However, others have shown that relative plate motions did not remain constant, with an increase in the rift obliquity and divergence rate occurring at ca. 100 Ma, coincident with a global plate reorganization event (Matthews et al., 2012; Müller et al., 2016).

The model of Williams et al. (2011) mostly took into account structural trends (e.g., conjugate “fracture zones”, basin-scale rift faults) in the western half of the ASM, acknowledging that the structural variation to the east of the 130°E boundary line may be attributed to structural inheritance. Indeed, the eastern half of the ASM is enigmatic; Early Cretaceous rifting in the Bass Strait, which formed the Otway, Gippsland, and Bass basins (**Figure 2.2**) eventually halted, and the rift system propagated southwards, west of Tasmania. Analytical and numerical modelling showed that oblique extension requires less tectonic force than orthogonal extension (Brune et al., 2012), which may explain why Bass Strait rifting was eventually abandoned as it unsuccessfully competed with a more oblique rift (Brune et al., 2018).

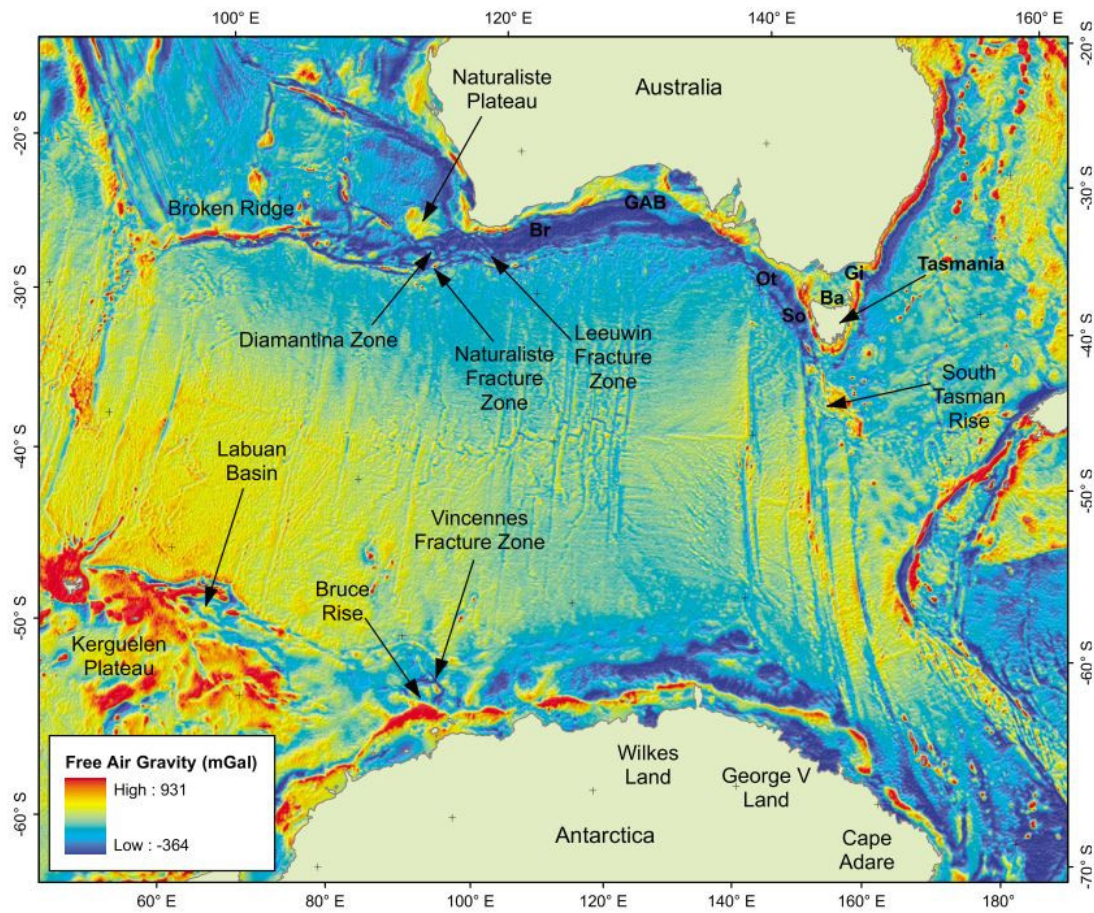


Figure 2.1 Map of free-air satellite gravity (Andersen et al., 2010) highlighting the major tectonic features of the Australian Southern Ocean between Australia and Antarctica (Williams et al., 2011). Br = Bremer Basin; GAB = Great Australian Bight Basin; Ot = Otway Basin; So = Sorell Basin; Ba = Bass Basin; Gi = Gippsland Basin.

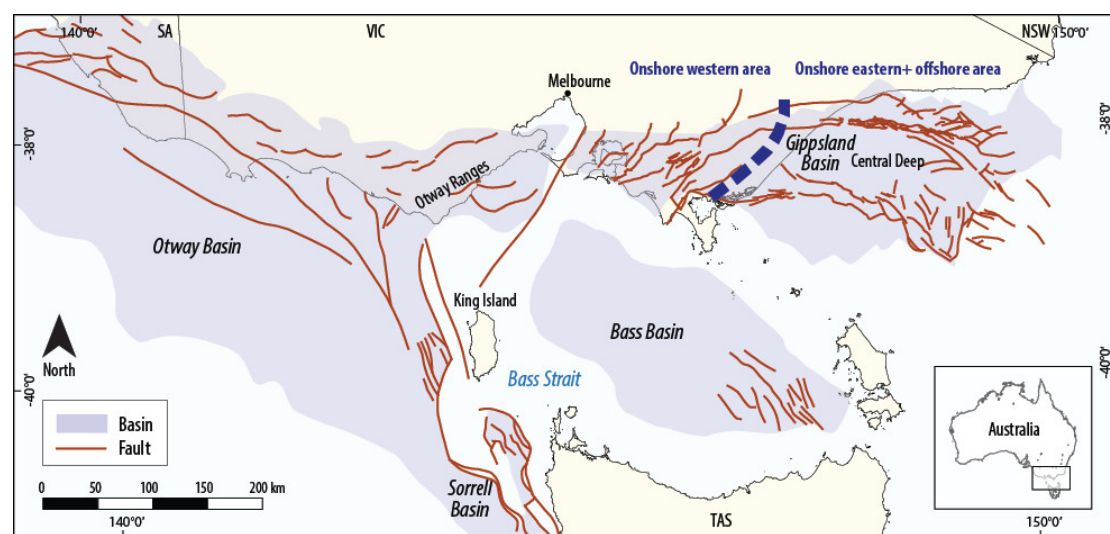


Figure 2.2 Map of the Bass Strait basins (modified from Samsu et al., 2019), which include the Otway, Bass, and Gippsland basins.

Kinematic reconstructions for the Bass Strait region are complicated by the wide array of rift fault orientations, based on which a variety of regional extension directions have been proposed. As an example, the direction of Late Jurassic–Early Cretaceous extension in the Otway Basin has been interpreted as NW-SE (O’Brien et al., 1994; Willcox and Stagg, 1990), N-S (Finlayson et al., 1996; Hill et al., 1994), NNE-SSW (Chantraprasert et al., 2001; K. C. Hill et al., 1995; Krassay et al., 2004), and NE-SW (Perincek et al., 1994). While K. A. Hill et al. (1995) attributed this discrepancy to structural overprinting, limited control from seismic reflection data, and interpretive bias, others have acknowledged the potential role of pre-existing basement structures at various scales on the basin’s geometry and evolution (Finlayson et al., 1996; Hill et al., 1994).

2.2. The Gippsland Basin

The E-W-trending Gippsland Basin is located approximately 200 km southeast of Melbourne, Australia (**Figure 2.2**). The offshore part of the Gippsland Basin hosts major oil and gas fields (**Figure 2.3a**), while large brown coal deposits occur onshore (O’Brien et al., 2013). The potential for CO₂ storage in existing hydrocarbon fields has also been explored (e.g., O’Brien et al., 2013).

Rifting of the Gippsland Basin, associated with the formation of the ASM, commenced in the Late Jurassic–Early Cretaceous (Tithonian–Berriasian), coeval with the onset of rifting in the Otway Basin (Norvick et al., 2001). In the onshore part of the Gippsland Basin (**Figure 2.3a**), the basin fill consists of Lower Cretaceous and relatively thin Paleocene–Recent units (**Figure 2.3a** **Figure 2.3b**). The lowermost sedimentary unit (Lower Strzelecki Group) unconformably overlies the Paleozoic basement. The offshore part of the basin that lies on the continental shelf is characterized by thick and relatively continuous Cretaceous and Cenozoic sequences, forming a total of 10 km of fill (Colwell and Willcox, 1993; Rahmanian et al., 1990; Willcox et al., 1992)

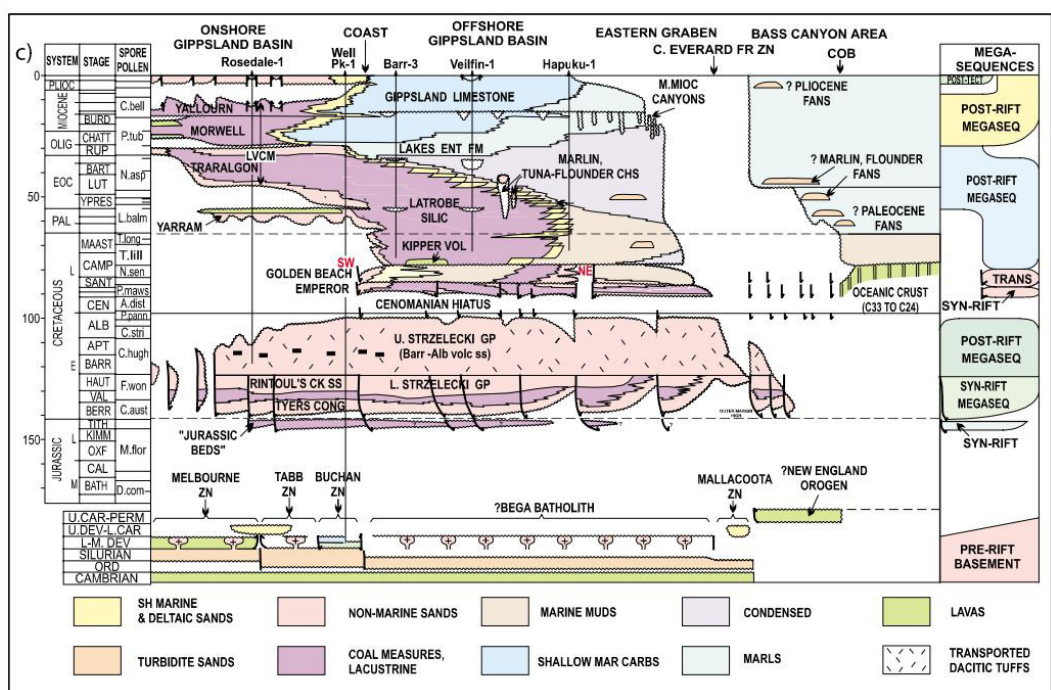
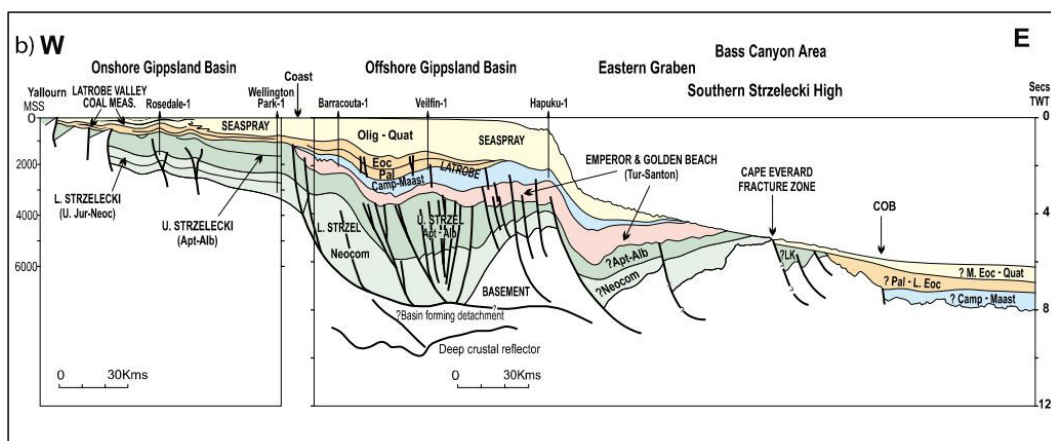
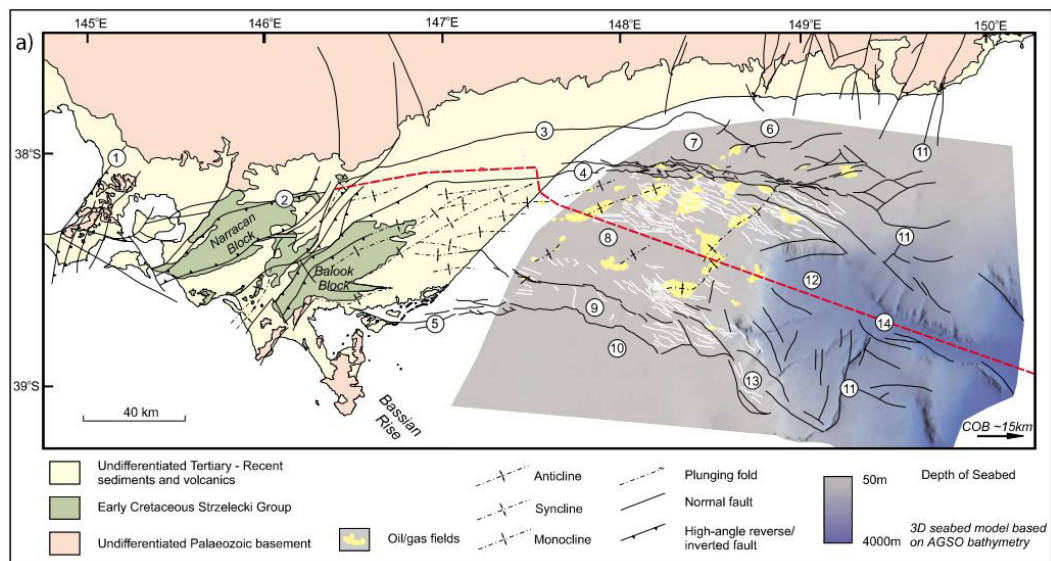
The first rift phase was followed by a post-rift volcanoclastic phase in the Barremian and then a Cenomanian hiatus associated with basin reorganization, block faulting, and uplift (Norvick et al., 2001; O’Brien et al., 2013). The hiatus coincided temporally with a global plate reorganization event that affected rifting in the ASM (Matthews et al., 2012; Müller et al., 2016) (see Chapter 3). A second rift phase occurred in the Turonian–Campanian, which led to the opening of the Bass Canyon in the easternmost part of the basin (Norvick et al., 2001) (**Figure 2.3**). Fault-controlled Turonian–Santonian depocenters formed in the Bass Canyon, which were filled with distal Campanian–Recent sediments (Bernecker et al., 2001; Norvick et al., 2001; Smith et al., 2000). Following the Cenomanian hiatus, the syn-rift and transitional, lacustrine to shallow marine Emperor and Golden Beach subgroups were deposited in the offshore

Gippsland Basin (Bernecker et al., 2001; Smith et al., 2000). These were overlain by Latrobe siliciclastics and Lakes Entrance and Gippsland carbonates during the basin's post-rift sag phase, which was punctuated by an Eocene contractional event (Power et al., 2001). Siliciclastic deposition continued until the end of the Miocene (Norvick et al., 2001). From the Miocene until recent times, the basin has experienced NW-SE directed contraction, as evidenced by present-day in-situ stress measurements (Hillis and Reynolds, 2000).

The distinct tectonostratigraphic characteristics between the onshore, offshore, and Eastern Graben–Bass Canyon area reflect an along-axis variation in the structural history of the basin. These changes are also evident in different orientations of basin-scale, rift-related faults, which have contributed to competing models for Gippsland Basin rifting. NW-SE to NE-SW extension directions have been proposed based on normal faults interpreted from seismic reflection data (e.g., Etheridge et al., 1987; Power et al., 2001; Willcox and Stagg, 1990), often with the assumption that the regional extension direction is perpendicular to the strike of normal faults. These models are discussed in detail in Chapter 3.

Previous studies on the evolution of the Gippsland Basin, which have helped to inform hydrocarbon exploration efforts, have focused largely on the offshore Gippsland Basin (e.g., Bernecker et al., 2001; Bernecker and Partridge, 2001; Colwell and Willcox, 1993; Holdgate et al., 2003; O'Halloran and Johnstone, 2001; Power et al., 2003, 2001). Drilling has also been conducted in the eastern onshore (Latrobe Valley) portion of the basin, where basement rocks were encountered (**Figure 2.3b**) (Holdgate et al., 2015). As basement structures and fabrics are inferred to have played a significant role in defining the basin architecture and therefore the development of petroleum systems, efforts have been made to characterize the basement rocks using deep seismic surveys and potential field geophysics (Bernecker et al., 2001; Holdgate et al., 2015; Moore and Wong, 2001). The western onshore part of the Gippsland Basin, which exhibits NE-SW structural trends (**Figure 2.3a**) that are different to the eastern onshore area, has received less attention. Previous studies here have focused on reconstructing the paleogeography (Constantine, 2001) and thermal history (Aghaei et al., 2017), while the relationship between the major structures, and the overall structural history and tectonic evolution of the onshore Gippsland Basin, and the control potentially exerted by basement structures remains unclear.

Figure 2.3 Map of the structural elements of the Gippsland Basin (a), with the red dashed line indicating the location of the basin cross section (b) and chronostratigraphic section (c) (modified from Norvick et al., 2001).



2.3. The basement beneath the onshore Gippsland Basin

The Gippsland Basin is underlain by the Melbourne, Tabberabbera, Kuark, and Mallacoota tectonostratigraphic zones of the Paleozoic Lachlan Orogen (VandenBerg et al., 2000; Willman et al., 2002) (**Figure 2.4**). The Lachlan Orogen constitutes the south central part of the Tasmanides of eastern Australia, which formed in an accretionary setting along the southern or eastern margin of Gondwana from the Neoproterozoic through to the Mesozoic (Cawood, 2005; Coney et al., 1990). It is bound by the Delamerian Orogen to the west.

This thesis focuses on the onshore Gippsland Basin, which is underlain by the Melbourne Zone (**Figure 2.4**). The Melbourne Zone comprises Lower Silurian to Middle Devonian sediments of the Murrindindi Supergroup, which conformably overlies Ordovician sediments (VandenBerg et al., 2000). These sedimentary sequences underwent roughly E-W shortening associated with the Middle Devonian Tabberabberan Orogeny and were later intruded by Middle to Upper Devonian granites (VandenBerg et al., 2000).

Cayley et al. (2002) postulated that the Paleozoic turbidites of the Melbourne Zone and the eastern Bendigo Zone are underlain by a rigid piece of Proterozoic to Cambrian continental crust which extends southwards underneath the Bass Strait into Tasmania, and which protected overlying sediments from extensive deformation during the Tabberabberan Orogeny. The rigidity and relatively high strength of the Selwyn Block is attributed to the Proterozoic (or older) age of the underlying lithospheric mantle (Cayley et al., 2011; Seymour et al., 2007).

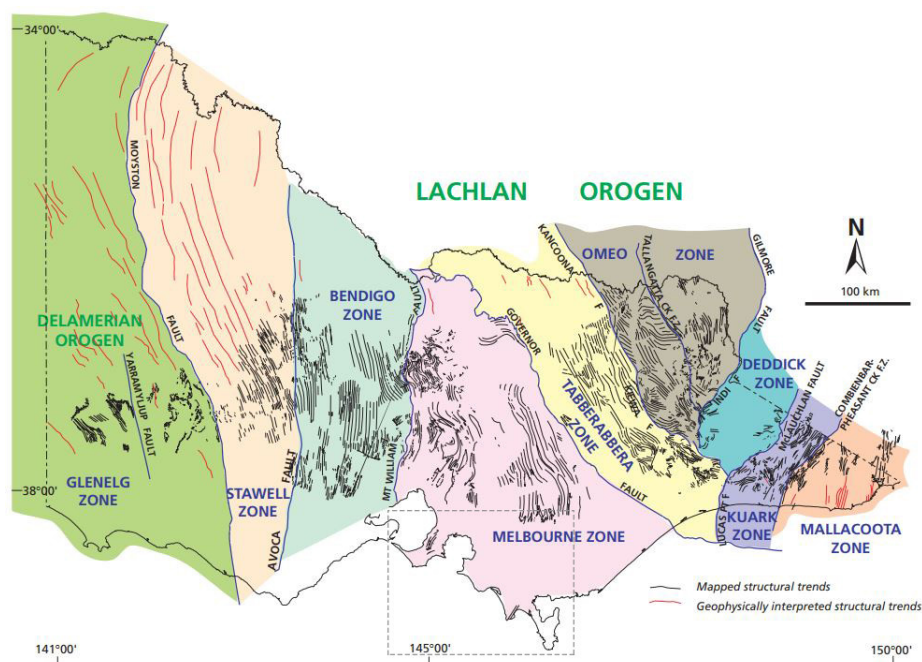


Figure 2.4 Map of the structural zones of the Lachlan Orogen in Victoria (modified after VandenBerg et al., 2000). The grey dashed box indicates the location of the onshore Gippsland Basin study area.

The Selwyn Block, also known as the microcontinent “VanDieland”, collided onto the eastern Gondwana margin – south of western Victoria (Australia) and the Northern Victoria Land (Antarctica) – in the Late Cambrian during the Delamerian Orogeny (Cayley, 2011) (**Figure 2.5**). This event coincided temporally with the stalling of west-dipping subduction underneath the eastern Gondwana margin (Cayley et al., 2011). In the Early–Middle Ordovician, after collision with the Gondwana margin, VanDieland experienced northward oblique lateral escape to its present position at the eastern edge of the western Lachlan Orogen, in the process trapping an oceanic plate segment of the paleo-Pacific that would eventually form the proto-Stawell and Bendigo zones of the western Lachlan Orogen (Cayley, 2011) (**Figure 2.6**).

Subduction migrated to the east of VanDieland, evolving into a convergent plate margin along the entire length of eastern Gondwana. The establishment of this continuous subduction system marks the beginning of the Benambran Orogeny. The Stawell and Bendigo zones experienced Ordovician–Silurian shortening, which did not impact VanDieland and its overlying Melbourne Zone units (Cayley, 2011; Cayley et al., 2011) (**Figure 2.7**). Right lateral, E-W transform movement along the future Australia–Antarctica breakup boundary is inferred to have caused differential shortening between the western Lachlan Orogen and the along-strike Antarctic craton to the south (Cayley, 2011). This right-lateral movement, followed by the Late Silurian Bindian Orogeny and the Middle Devonian Tabberabberan Orogeny, allowed the Selwyn Block to move closer to its present-day location.

2.4. Structural inheritance in the Gippsland Basin

The Paleozoic history of the Selwyn Block and the Melbourne Zone plays an important role in the Australia–Antarctica breakup in the Mesozoic. During west-to-east propagation of the ASM rift system, rifting was likely to have reactivated the E-W trending transform weaknesses (**Figure 2.7**) associated with the Benambran Orogeny. This transform weakness terminated at the western edge of VanDieland, so that rifting in the Bass Strait (between Victoria and Tasmania) failed, and the rift deviated southwards by reactivating the N-S trending suture zone between the east Gondwana margin and VanDieland. At the basin scale, a distinct change in major basin-bounding fault orientations from the western onshore area of the Gippsland Basin to the eastern offshore portion coincides with the postulated eastern boundary of the Selwyn Block underneath the Melbourne Zone (Cayley et al., 2002; Moore et al., 2016). This thesis aims to distinguish between the “sources” of basement inheritance (i.e., the Selwyn Block and Melbourne Zone basement rocks), and their influence on brittle deformation in the sedimentary cover at basin to outcrop scale.

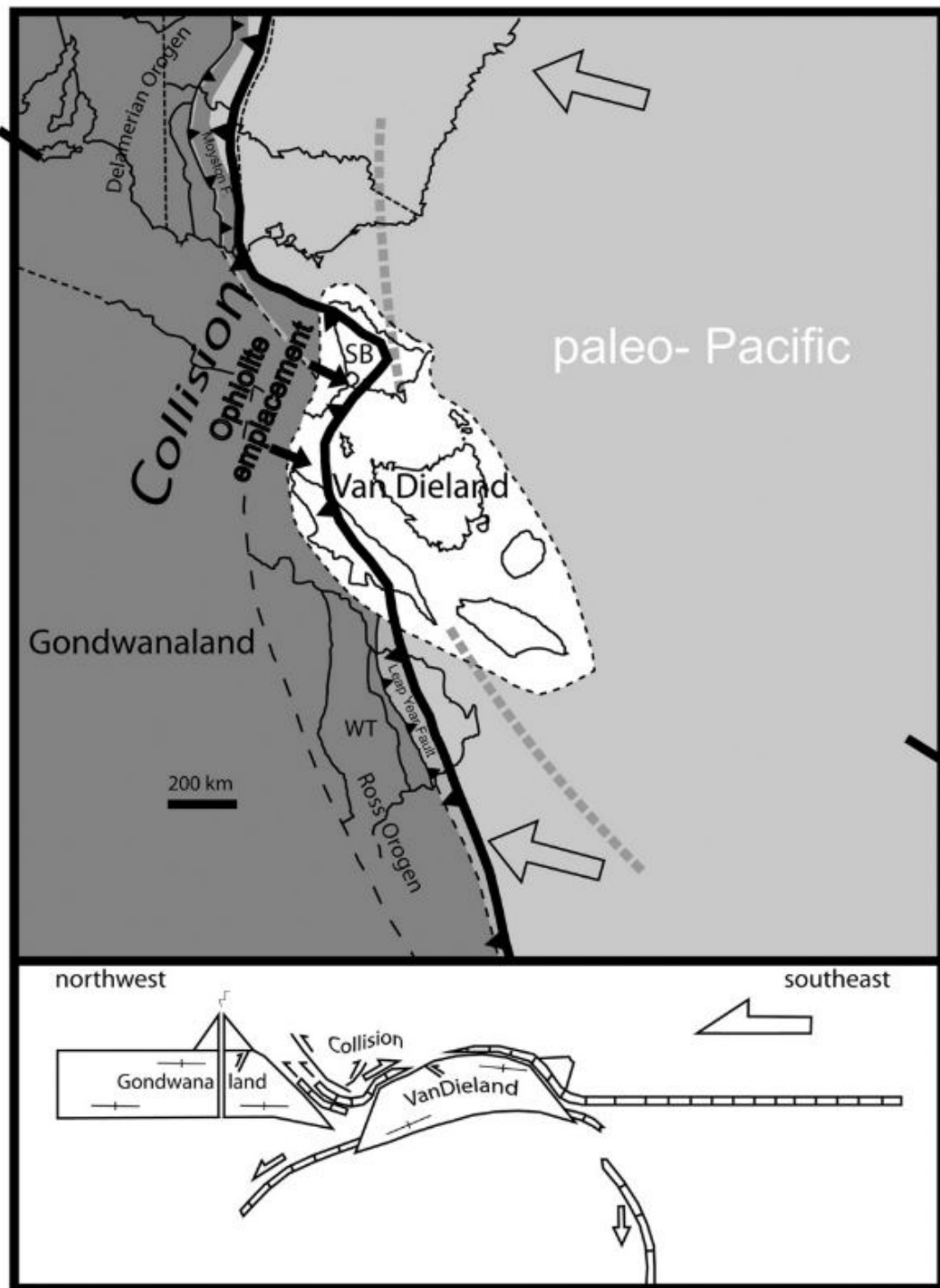


Figure 2.5 Schematic illustration of the evolution of VanDieland and the Selwyn Block (Cayley, 2011) in the Late Cambrian (505–500 Ma): The arrival of VanDieland between western Victoria (Australia) and Northern Victoria Land (Antarctica) during the Tyennan Orogeny, stalling paleo-Pacific subduction west of VanDieland.

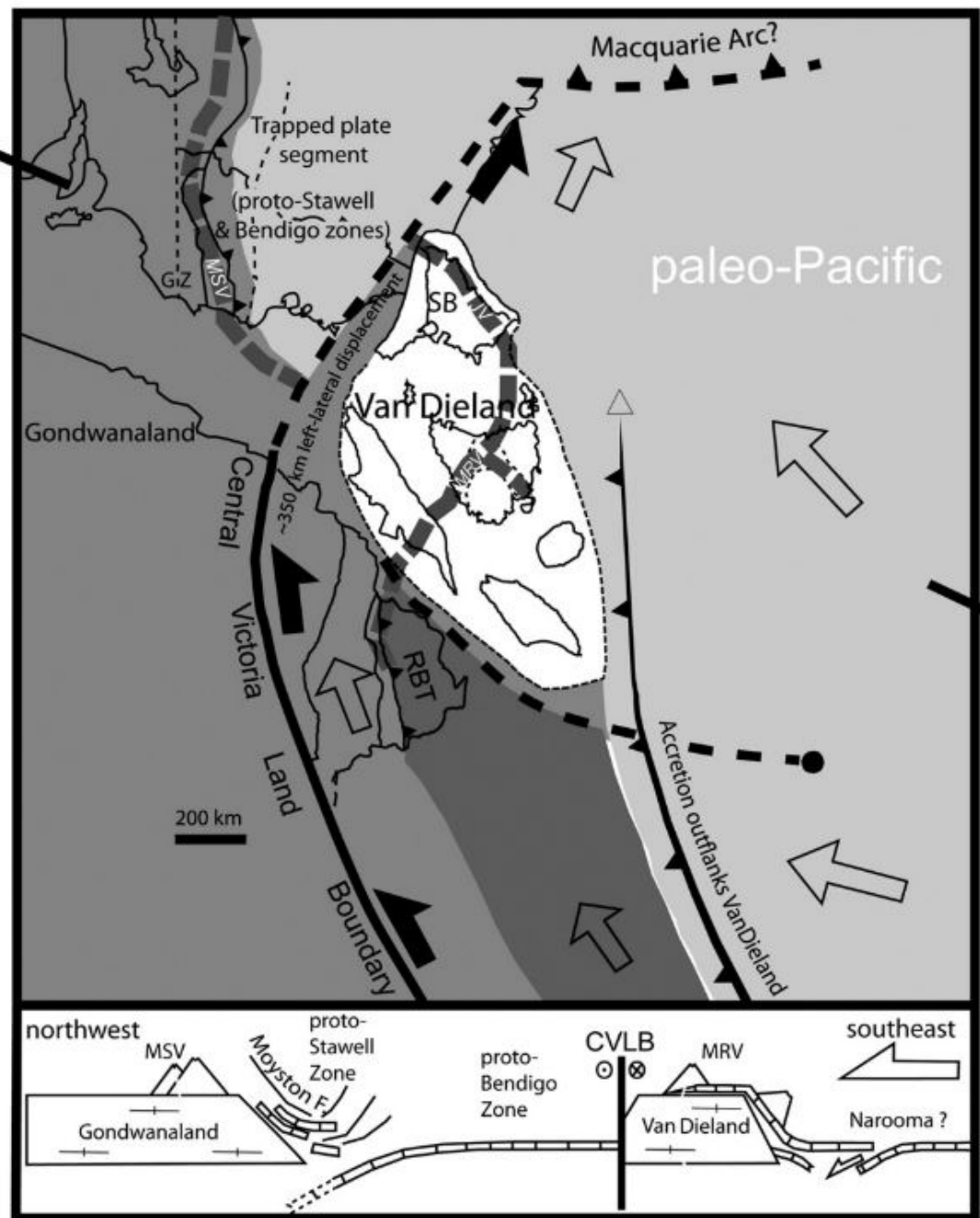


Figure 2.6 Schematic illustration of the evolution of VanDieland and the Selwyn Block (Cayley, 2011) in the Early Ordovician (470 Ma): A re-established paleo-Pacific subduction south of VanDieland triggered sinistral lateral escape, transporting VanDieland northeast and trapping a segment of the paleo-Pacific oceanic crust that would later become the Stawell and Bendigo Zones.

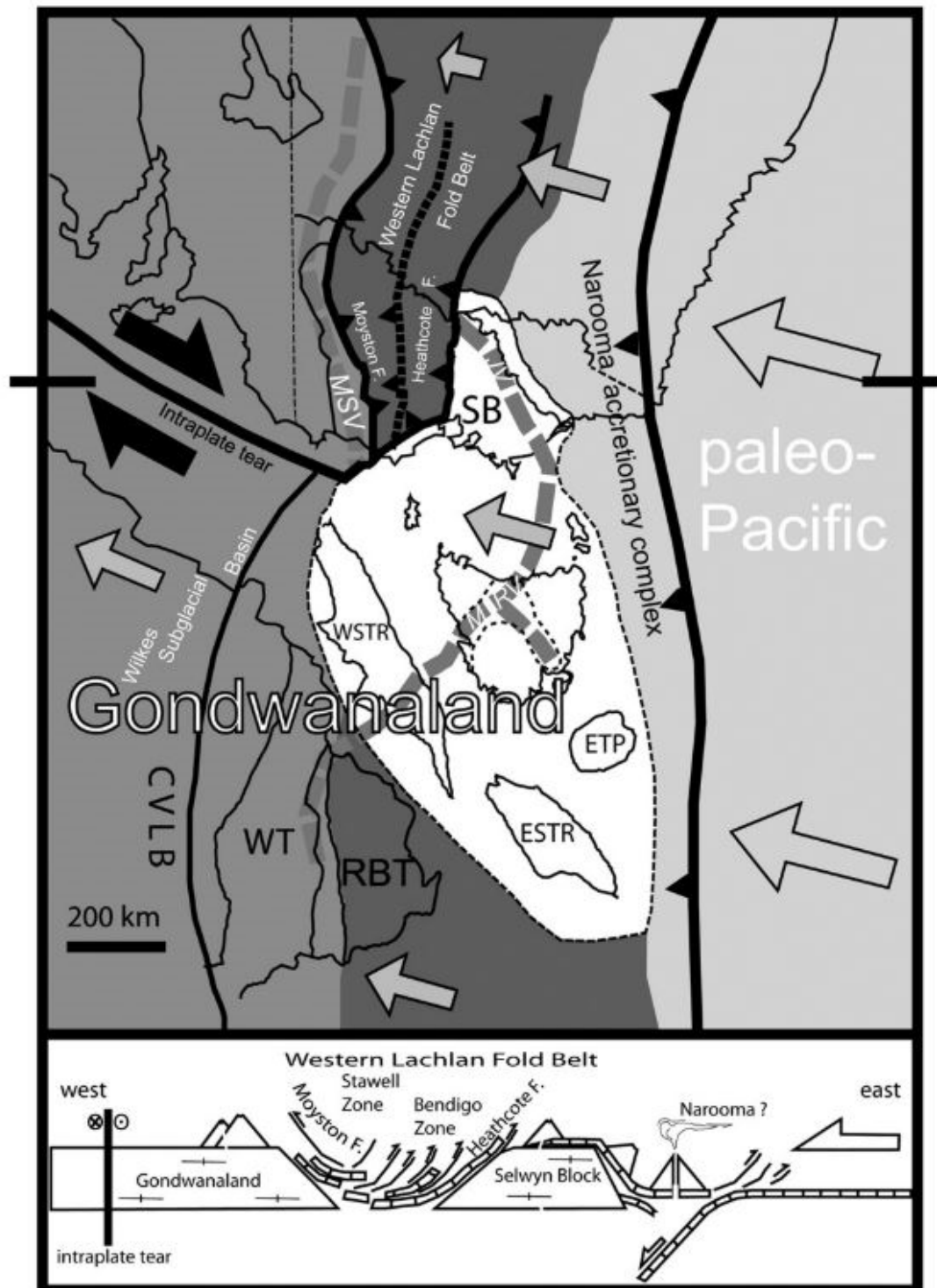


Figure 2.7 Schematic illustration of the evolution of VanDieland and the Selwyn Block (Cayley, 2011) in the Late Ordovician–Early Silurian (450–430 Ma): A continuous subduction zone has been re-established along the eastern Gondwana margin. In the Benambran Orogeny, the Stawell and Bendigo Zones undergo shortening, forming the western Lachlan Orogen. An E-W trending transform causes differential shortening between the Lachlan Orogen and the Antarctic craton, moving them to within 30 km of their present-day locations.

Chapter 3

The influence of basement faults on local extension directions: Insights from potential field geophysics and field observations

A. Samsu¹, A. R. Cruden¹, M. Hall¹, S. Micklethwaite¹, S. W. Denyszyn²

¹School of Earth, Atmosphere and Environment, Monash University
Clayton, VIC 3800, Australia

²School of Earth Sciences, University of Western Australia
Crawley, WA 6009, Australia

Basin Research, accepted manuscript (2019), doi:10.1111/bre.12344

Abstract

Complex arrays of faults in extensional basins are potentially influenced by pre-existing zones of weakness in the underlying basement, such as faults, shear zones, foliation, and terrane boundaries. Separating the influence of such basement heterogeneities from far-field tectonics proves to be challenging, especially when the timing and character of deformation cannot be interpreted from seismic reflection data. Here we aim to determine the influence of basement heterogeneities on fault patterns in overlying cover rocks using interpretations of potential field geophysical data and outcrop-scale observations.

We mapped >1 km to meter scale fractures in the western onshore Gippsland Basin of southeast Australia and its underlying basement. Overprinting relationships between fractures and mafic intrusions are used to determine the sequence of faulting and reactivation, beginning with initial Early Cretaceous rifting. Our interpretations are constrained by a new Early Cretaceous U-Pb zircon ID-TIMS age (116.04 ± 0.15 Ma) for an outcropping subvertical, NNW-SSE striking dolerite dike hosted in Lower Cretaceous Strzelecki Group sandstone. NW-SE to NNW-SSE striking dikes may have signalled the onset of Early Cretaceous rifting along the East Gondwana margin at ca. 105–100 Ma.

Our results show that rift faults can be oblique to their expected orientation when pre-existing basement heterogeneities are present, and they are orthogonal to the extension direction where basement structures are less influential or absent. NE-SW to ENE-WSW trending Early Cretaceous rift-related normal faults traced on unmanned aerial vehicle (UAV) orthophotos and digital aerial images of outcrops are strongly oblique to the inferred Early Cretaceous N-S to NNE-SSW regional extension direction. However, previously mapped rift-related faults in the offshore Gippsland Basin (to the east of the study area) trend E-W to WNW-ESE, consistent with the inferred regional extension direction. This discrepancy is attributed to the influence of NNE-SSW trending basement faults underneath the onshore part of the basin, which caused local re-orientation of the Early Cretaceous far-field stress above the basement during rifting. Two possible mechanisms for inheritance are discussed – reactivation of pre-existing basement faults or local re-orientation of extension vectors. Multiple stages of extension with rotated extension vectors are not required to achieve non-parallel fault sets observed at the rift basin scale. Our findings demonstrate the importance of (1) using integrated, multi-scale datasets to map faults and (2) mapping basement geology when investigating the structural evolution of an overlying sedimentary basin.

3.1. Introduction

The orientation of faults in rift basins can be useful for inferring strain during basin formation. However, pre-existing mechanical heterogeneities (e.g., faults and fabrics) in the pre-rift “basement” rocks can influence subsequent rifting, resulting in one or more of the following: (i) syn-rift faults that are not orthogonal to far-field extension vectors (e.g., Maerten *et al.* 2002; Morley 2010; Henza *et al.* 2011; Reeve *et al.* 2015); (ii) complex fault arrays comprising non-parallel fault sets that may or may not have formed coevally (cf. orthorhombic fault arrays; Krantz 1988; Healy *et al.* 2014); and (iii) rift segmentation and variation in rift orientations along major rift systems (e.g. East African rift system; Corti *et al.* 2007; Corti 2012; Muirhead & Kattenhorn 2018). The mechanisms responsible for structural inheritance can be reactivation of pre-existing basement faults (e.g., Holdsworth *et al.* 1997; Corti *et al.* 2007; Agostini *et al.* 2009; Wilson *et al.* 2010; Kirkpatrick *et al.* 2013; Phillips *et al.* 2016; Muirhead & Kattenhorn 2018) or local deflection or re-orientation of the far-field stress (e.g., Morley 2010; Philippon *et al.* 2015; Reeve *et al.* 2015). The studies above show that the orientation of syn-rift faults is controlled – to varying degrees – by pre-existing basement structures, so that the relationship between extension direction and fault orientations is not straightforward and will vary between localities. Attributing fault and fracture populations to specific tectonic events is challenging, especially when the relative timing of structures is unclear and the contact between the basement and the cover is not observed.

While many findings on the impact of structural inheritance on rift basins are based on seismic reflection data interpretation (e.g., Reeve *et al.* 2015; Phillips *et al.* 2016; Peace *et al.* 2018), establishing the timing of deformation events, understanding the structure of the underlying basement, and inferring genetic relationships between basement and cover structures become more challenging when seismic reflection data is unavailable. Here we explore the influence of structural inheritance on brittle deformation in a rift basin during and after rifting in an area where seismic coverage and fault slip data is limited. We focus on the Gippsland Basin of southeastern Australia (**Figure 3.1**), where the obliquity between NE-SW to ENE-WSW trending extensional faults in the onshore western domain and E-W and NW-SE trending faults in the (mostly) offshore eastern domain have led to basin evolution models that invoke multiple stages of rifting with different extension vectors (Power *et al.* 2003; cf. Otway Basin, Williamson *et al.* 1990).

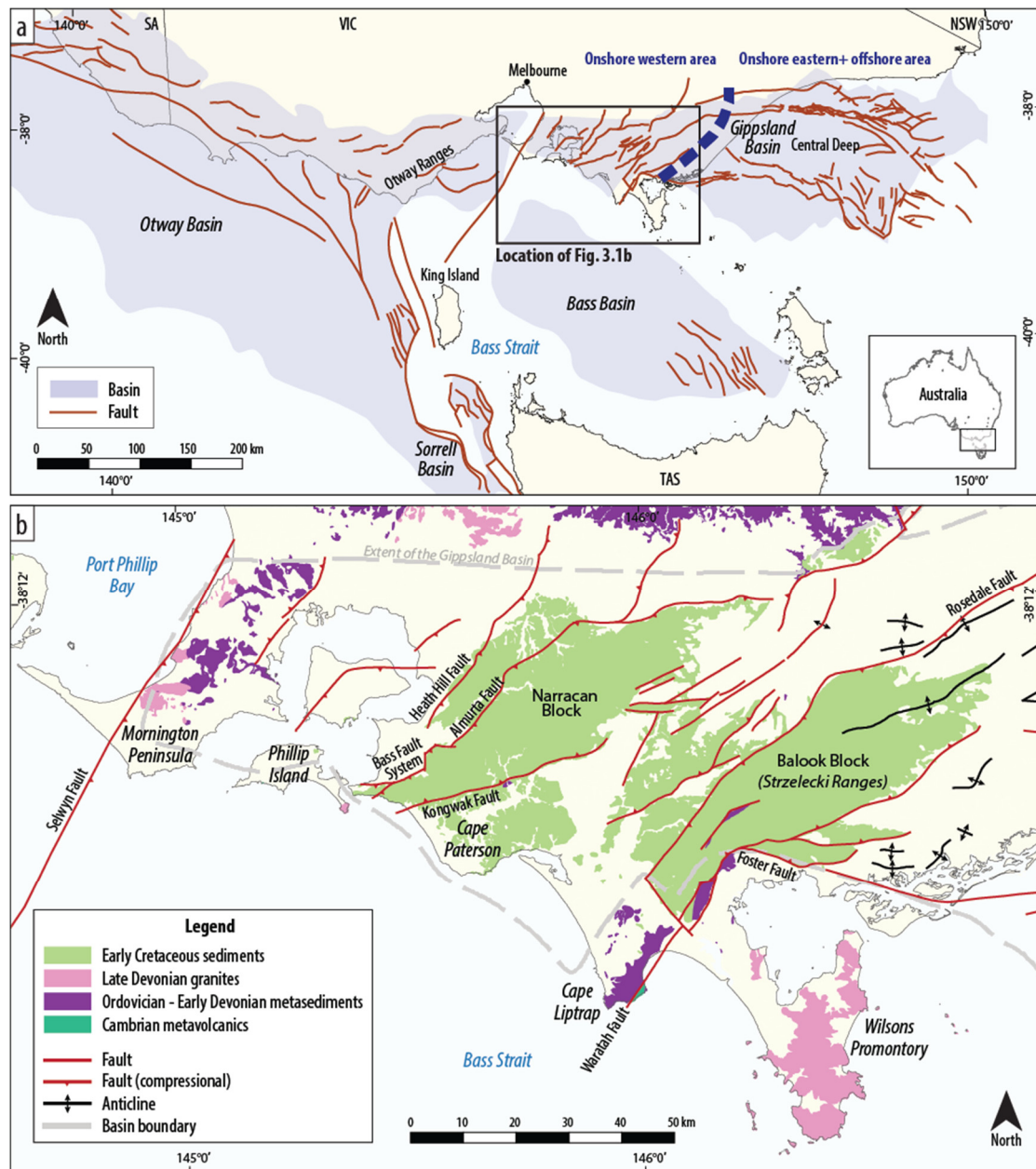


Figure 3.1 (a) Location and major faults (in red) of the eastern Australian Southern Margin basins (Constantine, 2001; Geoscience Australia, 2018a, 2018b; K. C. Hill et al., 1995; Power et al., 2001). The Gippsland Basin is separated by the blue dashed line into a western onshore area (the subject of this study; b) and an eastern onshore and offshore area. SA = South Australia; VIC = Victoria; NSW = New South Wales; TAS = Tasmania. (b) Faults in the western onshore Gippsland Basin study area. Onshore geology is modified after the Victoria s – Seamless Geology 2014 dataset (Victorian Department of State Development Business and Innovation, 2014). Structures of the onshore Gippsland Basin study area are modified after Constantine (2001) and Power et al. (2001).

We aim to determine whether the geometries and orientations of onshore faults in the Gippsland Basin support existing multi-stage extension models or if they allow for the possibility that basement structures played an important role in the structural evolution of the basin. We employ

an innovative workflow that utilizes data from basin (>1 km) to outcrop scales to map and characterize crosscutting and overprinting relationships between fractures (i.e., faults, joints, veins, and dikes) in the basement and cover rocks. The timing of selected fracturing events is constrained by high-precision U-Pb geochronology, which we use to reconstruct the history of brittle deformation and link fracturing events to the broader tectonic evolution of the basin.

This study contributes to understanding the influence of inherited basement structures on the Gippsland Basin at basin to outcrop scale. We propose that NE-SW to ENE-WSW trending rift-related faults in the onshore Gippsland Basin, which is underlain by a basement with a NNE-SSW trending structural grain, were influenced by basement structures that locally re-oriented the extension vector.

3.2. Geological setting

The Gippsland Basin is part of the Australian Southern Margin (ASM) rift system, which developed during broadly N-S extension between present-day Australia and Antarctica (Miller et al., 2002). Previous studies of the Bass Strait basins at the eastern end of the ASM (i.e., the Otway, Bass, and Gippsland basins) report varying directions of regional paleo-extension based on the orientation of rift-related faults. These interpretations (summarized in **Table 3.1** Summary of inferred Early Cretaceous paleo-extension directions in the Bass Strait basins.) support either NW-SE directed Early Cretaceous extension or N-S to NNE-SSW extension in the Bass Strait (Chantraprasert et al., 2001; Etheridge et al., 1985; Hill et al., 1994; K. C. Hill et al., 1995; Krassay et al., 2004; Norvick et al., 2001; Willcox et al., 1992).

Table 3.1 Summary of inferred Early Cretaceous paleo-extension directions in the Bass Strait basins.

Extension direction	Area	Reference
NW-SE	Bight Basin	Willcox & Stagg (1990) Totterdell et al. (2000)
NW-SE	Otway Basin	O'Brien et al. (1994)
N-S		Hill et al. (1994) Finlayson et al. (1996)
NNE-SSW		Cooper et al. (1995) Chantraprasert et al. (2001) Krassay et al. (2004)
NW-SE	Gippsland Basin	Willcox & Stagg (1990) Willcox et al. (1992) Sandwell & Smith (1997) Power et al. (2001)
NNE-SSW	Bass Strait	Etheridge et al. (1985)
N-S	ASM	Miller et al. (2002)

NW-SE, E-W, and NE-SW trending rift-related faults in the Gippsland Basin have been mapped in detail using seismic datasets (Power *et al.*, 2003; Willcox *et al.*, 1992). Power *et al.* (2001, 2003) attribute the different fault orientations to changes in extension vectors and propose that NE-SW trending offshore depocenters formed under NW-SE oblique extension during an Early Cretaceous (Stage 1) rift phase, and E-W to WNW-ESE normal faults were first active during a Late Cretaceous (Stage 2) rift phase. Power *et al.* (2003) suggest that this requires a rotation of the extension vectors from NNW-SSE to NE-SW. However, several studies of the Bass Strait basins have suggested that basement structures could be just as important as regional extension vectors in controlling rift fault orientations. For example, Finlayson *et al.* (1996) and Hill *et al.* (1994) acknowledge that the variability of fault orientations in the Otway Basin was probably controlled by basement faults.

3.2.1. Stratigraphy and evolution of the Gippsland Basin

The Gippsland Basin is characterized by syn-rift, volcanoclastic, non-marine and marine sedimentary Mesozoic rocks overlain by post-rift Cenozoic non-marine and marine sedimentary and volcanic rocks (Norvick *et al.*, 2001) (**Figure 3.2**). It overlies Ordovician–Devonian folded turbidites of the Lachlan Fold Belt (Gray *et al.*, 2003; VandenBerg *et al.*, 2000), which were folded during E-W shortening associated with the mid-Devonian Tabberabberan Orogeny (Gray, 1997; VandenBerg *et al.*, 2000).

The stratigraphic record suggests that rifting in the Gippsland Basin occurred in two stages (Rahmanian *et al.*, 1990; Power *et al.*, 2001). Early Cretaceous Stage 1 rifting commenced in the Tithonian (ca. 142–146 Ma) (Norvick and Smith, 2001), providing accommodation space for the syn-rift Early Cretaceous Lower Strzelecki Group, comprising quartzose to arkosic fluvio-lacustrine clastic sedimentary rocks (Holdgate and McNicol, 1992; Tosolini *et al.*, 1999) (**Figure 3.2**). Rifting ceased in the Barremian (ca. 115–123 Ma) and was followed by a period of thermal subsidence and then rapid cooling, kilometre-scale uplift, inversion, and denudation in the mid-Cretaceous (ca. 90–95 Ma) (Duddy and Green, 1992; Dumitru *et al.*, 1991; Foster and Gleadow, 1992; Willcox *et al.*, 1992). The latter are associated with folding, reverse faulting along reactivated normal faults (Norvick and Smith, 2001; Power *et al.*, 2003), and basin-wide erosional unconformities constrained in age by vitrinite reflectance and apatite fission track analysis (AFTA) data (Duddy and Green, 1992; Rahmanian *et al.*, 1990). The mid-Cretaceous is also associated with a reorganization of plate movements at ca. 100 Ma (Matthews *et al.*, 2012), after which divergence between Australia and Antarctica continued at an increased rate (from ~3 mm/yr to ~20 mm/yr) and switched from NNE-SSW to NW-SE according to global plate motion models (Müller *et al.*, 2016).

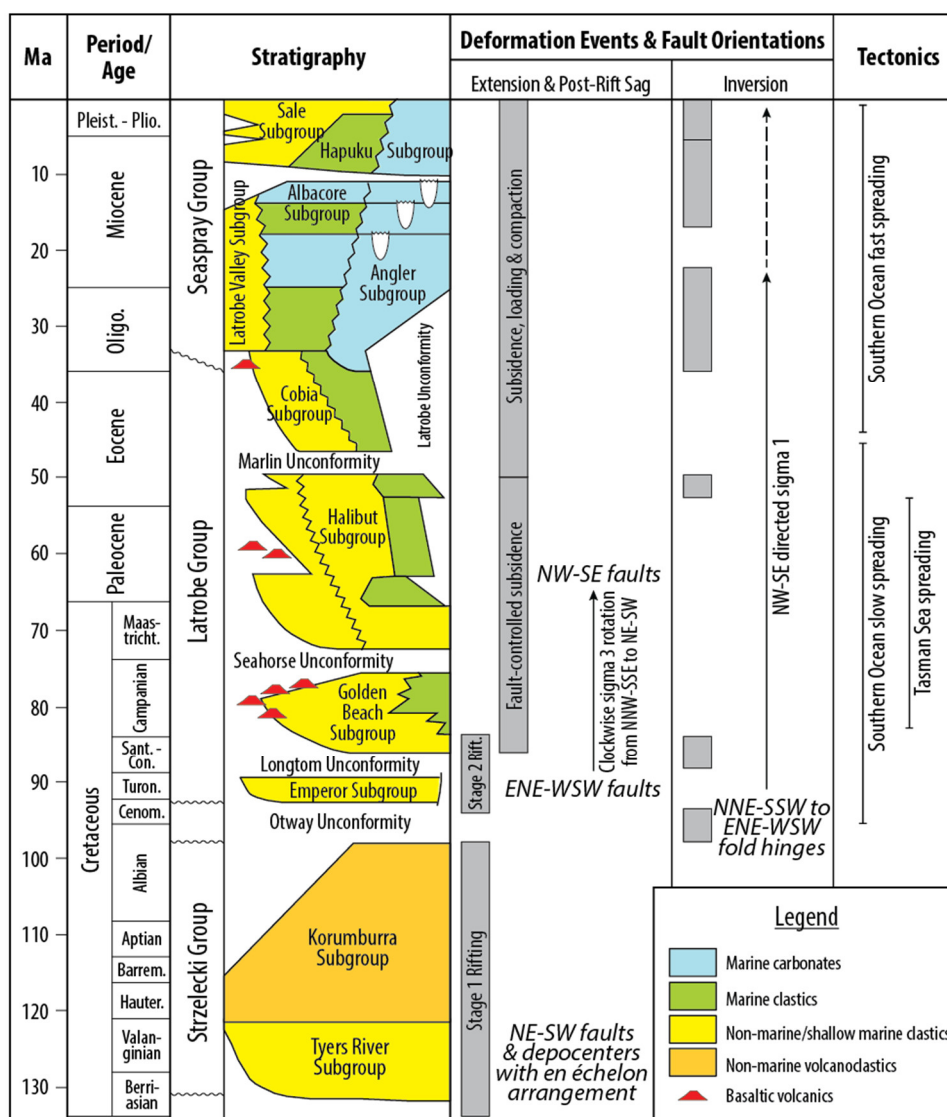


Figure 3.2 Summary of the stratigraphy and tectonic history of the Gippsland Basin (after Bernecker & Partridge, 2001) and deformation events derived from seismic reflection studies in the offshore Gippsland Basin (after Power et al., 2003). The stratigraphic column is from the Central Deep, offshore Gippsland Basin.

Late Cretaceous Stage 2 rifting began in the Cenomanian (ca. 92-97.5 Ma), coinciding temporally with the opening of the Tasman Sea between Australia, the Lord Howe Rise and New Zealand (Norvick and Smith, 2001; Veevers et al., 1991). This extensional period formed a system of “new” rift basins along the eastern Southern Margin of Australia, including the offshore portions of the Otway and Gippsland basins (K. C. Hill et al., 1995). O’Halloran and Johnstone (2001) proposed that spreading of the Tasman Sea at 80 – 90 Ma is also responsible for Late Cretaceous magmatic activity in the Gippsland Basin based on interpretation of offshore seismic reflection data. Ages for intrusive and extrusive rocks between 100 and 49 Ma have been inferred from stratigraphic relationships and geochronology (Birch, 1987; Duddy

and Green, 1992; McPhail, 2000; Meeuws et al., 2016), indicating that magmatic activity occurred from the Late Cretaceous to the Eocene.

Cenozoic post-rift sagging was punctuated by periods of shortening, fault reactivation, inversion, and uplift (Etheridge et al., 1985; K. C. Hill et al., 1995; Müller et al., 2012). From Miocene to recent times, the region has experienced contraction, which led to the uplift of the Otway and Strzelecki Ranges, north of the Otway and Gippsland basins, respectively (Krassay et al., 2004; Perincek et al., 1994; Perincek and Cockshell, 1995; Sandiford, 2003). This is supported by present-day in-situ stress measurements derived from borehole breakouts (Hillis and Reynolds, 2000), signifying a NW-SE directed ($130 \pm 20^\circ$) maximum horizontal principal stress.

3.2.2. Onshore study area

Our study of the western onshore Gippsland Basin (**Figure 3.1b**) focuses on the syn-rift Early Cretaceous Lower Strzelecki Group and on establishing its sequence of deformation since Cretaceous rifting. Previous structural studies of the Gippsland Basin have focused on the Latrobe and Seaspray groups, which overlie the Strzelecki Group (Bernecker & Partridge 2001; **Figure 3.2**), in the context of hydrocarbon exploration (e.g., Bernecker *et al.* 2003; Holdgate & Gallagher 2003).

Our study area is located approximately 200 km southeast of Melbourne, southeast Australia (**Figure 3.1b**). Outcrops of the Lower Strzelecki Group are exposed along the coast between San Remo and Inverloch (**Figure 3.3**). Here they consist of alternating sand-dominated and mud-dominated layers with conglomerate and organic matter-rich interbeds, deposited in a fluvial setting (Constantine, 2001). NW-SE to NNW-SSE trending mafic dikes that crosscut the Lower Strzelecki Group (Constantine, 2001) have an inferred minimum intrusion age of ca. 96-100 Ma, based on the AFTA-derived thermal history of the host rock of one mafic dike (Duddy & Green, 1992). The underlying Devonian basement rocks are exposed at Cape Liptrap (**Figure 3.3**), where they exhibit NNE-SSW trending fold axes and faults (e.g., the Waratah and Bell Point faults), consistent with mid-Devonian E-W shortening (Vollgger and Cruden, 2016). The NNE-SSW trending Selwyn Fault (**Figure 3.1b**) may extend into an even deeper Neoproterozoic-Cambrian basement (Cayley et al., 2002).

3.3. Methods

Here we introduce the datasets and processing techniques we used to map fractures in the study area. We define fractures as discontinuities in rocks that resulted from brittle failure, which include shear fractures, joints, veins, and dikes. While the term “fault” is often used synonymously with shear fracture, here we use the term for describing a zone consisting of

linked segments of shear fractures as opposed to a single surface. A shear fracture, by this definition, has no upper length limit, but we use the term “fault” where we can no longer distinguish between individual shear fractures at the scale of observation.

Onshore gravity and aeromagnetic data were integrated with bathymetry data and existing surface geology maps to interpret onshore regional-scale (>1 km-long) fractures, including faults. Local-scale faults, dikes, and joints (centimetre to <1 km scale) were interpreted from UAV-based orthophotos and bathymetry data. These datasets were used to determine first-order fault kinematics, as fault-slip data collected in the field was too sparse for fault-slip analysis. The overprinting relationships between mafic dikes, faults, and joints provided additional constraints for determining the relative timing between deformation events, while absolute age dating of one mafic dike further strengthened our interpretation.

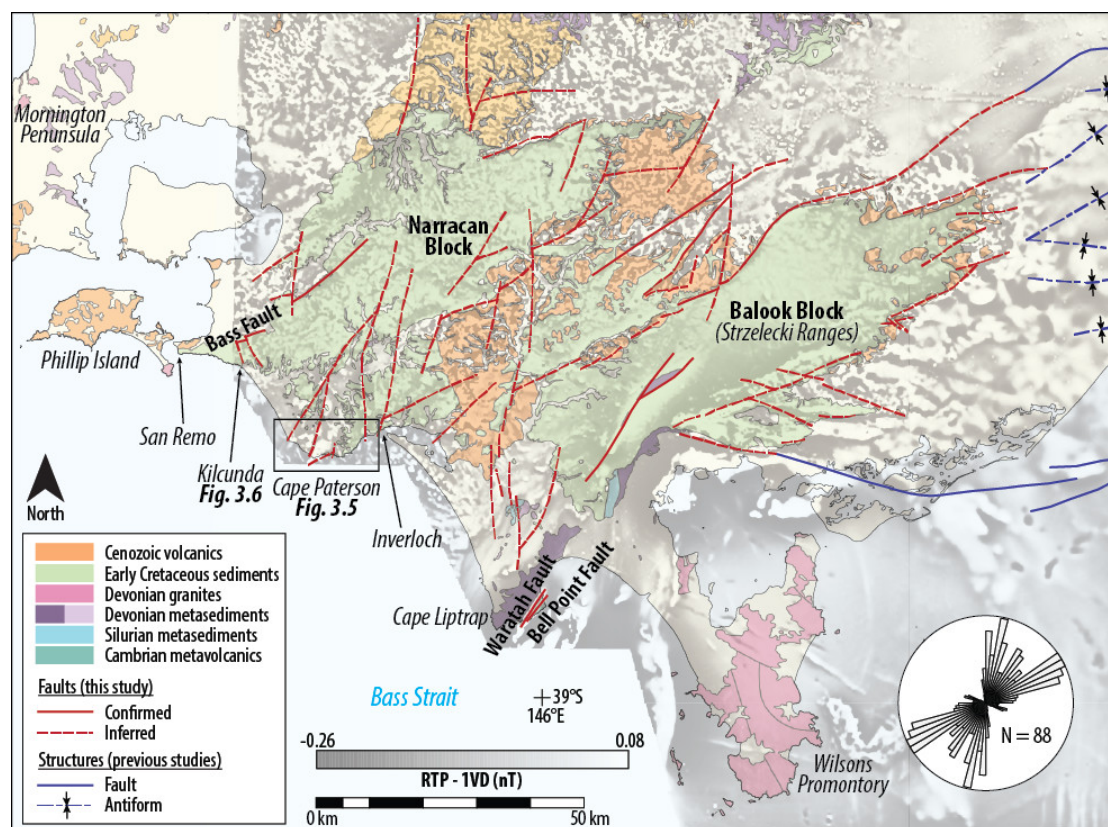


Figure 3.3 Map of onshore first-order faults overlain on grayscale image of the first vertical derivative of the RTP high-pass filtered (33,000 m), upward continued (200 m) aeromagnetic data. Faults in red were interpreted from onshore gravity and aeromagnetic data (see **Figure 3.4** for examples) and integrated with surface geology. Structures in blue were mapped by Willcox et al. (1992) and Smith et al. (2000). Lower Cretaceous Strzelecki Group outcrops are shown in green (Early Cretaceous sediments). Domains with a high frequency or “stippled” magnetic response correlate with Cenozoic volcanic rocks (orange). The rose diagram of the mapped faults (this study) was created using the Line Direction Histogram plugin (Tveite, 2015) in QGIS and is weighted by fault trace length.

3.3.1. Potential field geophysics

Gravity and magnetic anomaly grids, which are particularly useful for identifying subsurface features, were used to map faults and fracture zones at the kilometre scale. All geophysical potential field grids were obtained from the Geophysical Archive Data Delivery System (Geoscience Australia, 2018c). Image enhancement was performed using Geosoft Oasis Montaj™ version 9.3 (**Figure 3.4**). Filters were applied to enhance contrasts between relatively long and short-wavelength anomalies that are related to deep and shallow sources respectively (Heath, 2007 and references therein). We applied colour transforms (histogram equalization colour stretches) and hillshading to the processed images to better define the boundaries and extent of anomalies.

Basin-bounding structures were interpreted from the Isostatic Residual Gravity Anomaly Grid of Onshore Australia (~800 m grid spacing; Nakamura 2016). Low-pass filters (2000 m and 10,000 m) were applied to remove short-wavelength features, which aided in interpreting >10 km-scale major basement structures within the onshore Gippsland Basin. Faults and fracture zones from >10 km - several km scale were interpreted from a total magnetic intensity (TMI) grid (~50 m grid spacing; Geoscience Australia 2001). The TMI grid was reduced to the pole (RTP) assuming a magnetic declination of 11.996° and inclination of -69.511°. The analytical signal grid was used to identify possible mineralized faults. High-pass (33,000 m) and first vertical derivative filters were applied to enhance shallow short-wavelength features. Automatic gain correction and a tilt derivative filter were applied to add continuity to magnetic anomalies. Upward continuation (200 m) enhanced the deeper long-wavelength features. Examples of the geophysical potential field grids used for structural interpretation are shown in **Figure 3.4**.

Lava flows of the 95-18 Ma Older Volcanics province (Price *et al.* 1988) overlie the Cretaceous Strzelecki Group in parts of the study area (**Figure 3.3**). They are characterized by short-wavelength “noise” with a stippled texture in the TMI grids, which could not be removed by applying bandpass filters. As a result, the spatial interpretation of faults based on TMI grids is associated with some uncertainty, which was reduced with the use of constraints from surface geology, digital elevation models (DEMs), near-shore bathymetry, and outcrops.

3.3.2. Field data acquisition

UAV photogrammetry data was acquired at the Harmers Haven North, Harmers Haven South and the Caves – Flat Rocks localities following the workflow of Vollgger & Cruden (2016). The three survey areas are horizontal wave-cut platforms made up of the Cretaceous Strzelecki Group, providing a two-dimensional (2D) dataset that sufficed for accurate fracture mapping. Surveys parameters are summarized in **Table 3.2**.

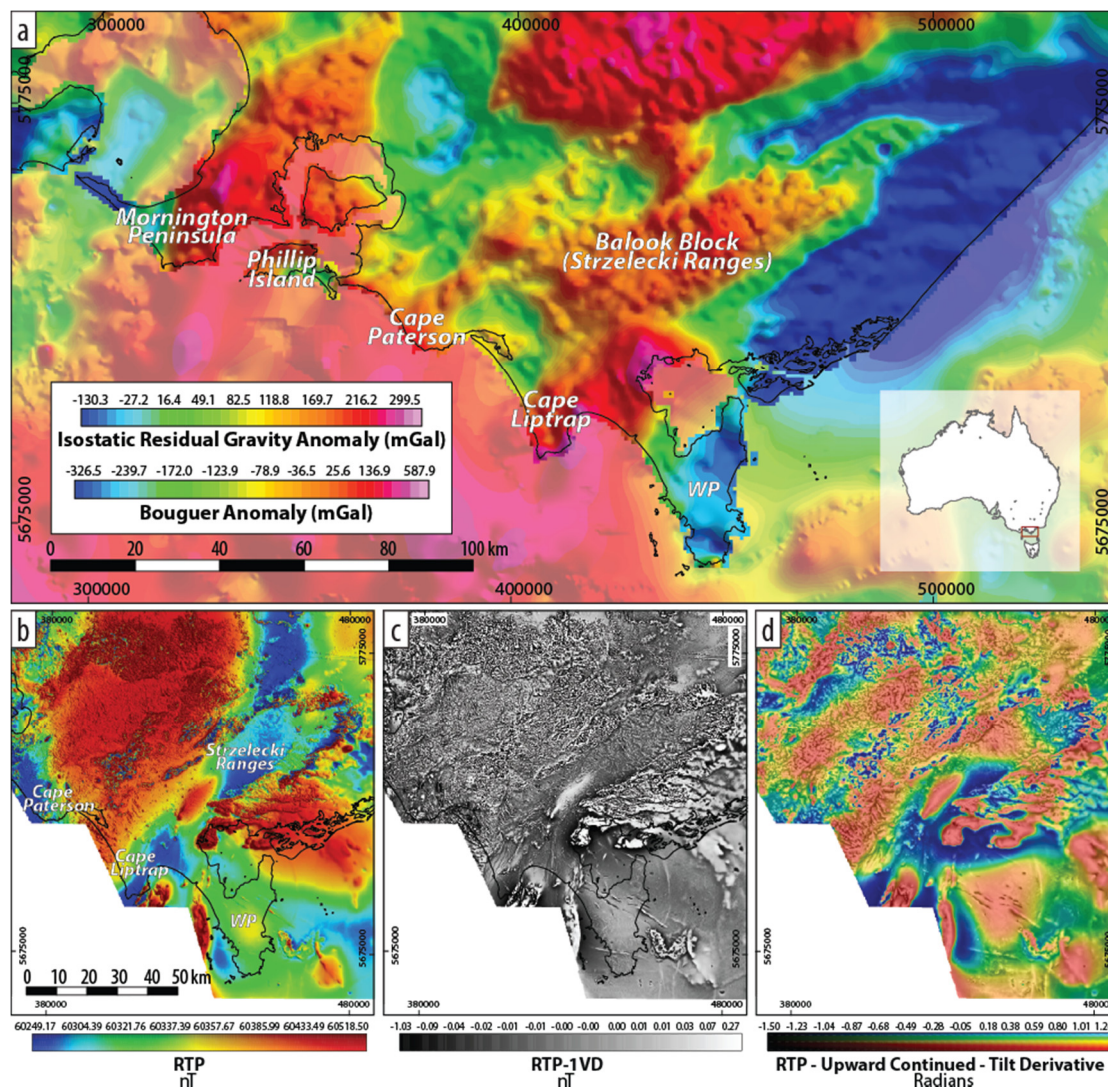


Figure 3.4 Examples of geophysical potential field grids used for interpreting faults and fracture zones at >10 km-scale down to the scale of several kilometres. (a) Colour image of the onshore isostatic residual gravity map of the onshore Gippsland Basin overlain on a Bouguer Gravity anomaly map of Victoria; (b) Colour image of the reduced to the pole (RTP) aeromagnetic data of the onshore Gippsland Basin; (c) Grayscale image of the first vertical derivative (1VD) of the RTP aeromagnetic data; (d) Composite colour image of the tilt derivative of the RTP aeromagnetic data superimposed on the RTP high-pass filtered (33,000 m), upward continued (200 m) aeromagnetic data. WP = Wilsons Promontory.

Prior to capturing aerial photographs, we randomly distributed ground control points (GCP) across each survey area. The GCP were surveyed using either a Garmin eTrex handheld GPS with an accuracy of ~3 m or a dual-frequency ProMark 500 RTK GPS with an accuracy of 1 – 5 cm and were later used for model georeferencing. For the Harmers Haven North survey area, instead of using GCP for georeferencing, we employed coordinates from the UAV's onboard GPS.

Table 3.2 Summary of UAV survey parameters for Harmers Haven North (HHN), Harmers Haven South (HHS), and The Caves – Flat Rocks (TC-FR) and properties of the resulting orthophotos. The locations for outcrop access points are given in GDA94 / MGA zone 55 (EPSG:28355) coordinates. See **Figure 3.5** for outcrop locations. AGL = above ground level; GSD = ground sampling distance; GCP = ground control point.

Locality		HHN	HHS	TC-FR
Access point	Easting	375636	376471	385183
	Northing	5720519	5720025	5719940
Image capture	Date	20-10-2016	24-11-2015	07-09-2016
	Time	9:15 - 10:25	12:00 - 14:00	9:50 - 12:05
	Cloud cover	sunny	cloudy	partly cloudy
	Interval	2 - 4 s	4 - 6 s	2 - 4 s
	Altitude (AGL)	80 m	50 m	90 m
	Velocity	< 4 m/s	< 4 m/s	< 4 m/s
	Aperture	f/2.8	f/2.8	f/2.8
	Forward overlap	85%	85%	85%
	Side overlap	75%	75%	75%
	Ground resolution	2.94 cm/pixel	1.94 cm/pixel	3.50 cm/pixel
Processing	No. of images	427	704	605
	No. of GCPs	11	15	0
	GPS	Handheld GPS	DGPS RTK	Onboard GPS
Orthophoto	Coverage area	0.148 km ²	0.330 km ²	0.234 km ²
	Resolution	2.94 cm/pixel	2.0 cm/pixel	3.50 cm/pixel

A Zenmuse X3 (FC350) camera with a 20 mm fixed focal length lens, mounted on a DJI Inspire 1 multi-rotor UAV was used to capture downward-looking (nadir) aerial photographs at 2-6 s intervals. The UAV was flown at constant altitude above ground level with a maximum speed of 4 m/s. The camera was set to aperture priority (f/2.8). Missions were flown along transects that were oriented roughly parallel to the length of the outcrop. Flights were configured with an 85% forward overlap and a 75% side overlap. Selected images were imported into Agisoft Photoscan and processed into 2D orthophotos using structure-from-motion algorithms. The resulting point clouds and orthophotos cover areas up to ~300,000 m² for each locality at approximately 2.0–3.5 cm/pixel resolution.

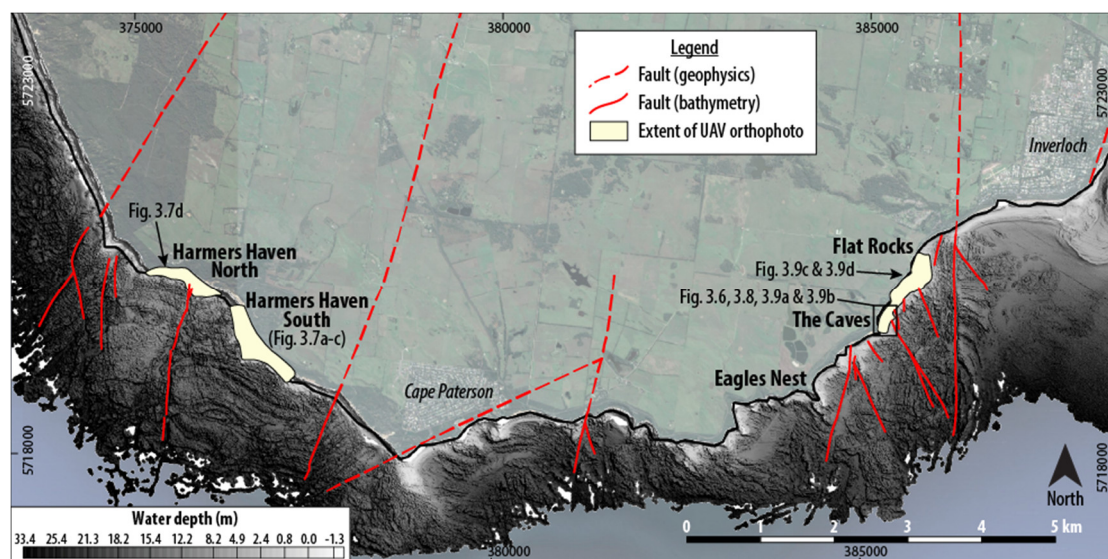


Figure 3.5 Map of UAV survey locations and faults interpreted from geophysical potential field data and near-shore bathymetry, overlain with shaded grayscale image of near-shore bathymetry. The azimuth and inclination of the illumination source for the hillshade algorithm are 55° and 66° , respectively. The location of this map is shown in **Figure 3.3**.

3.3.3. Fracture interpretation from integrated datasets

All of the datasets used for fracture mapping were imported into an open source geographic information system (GIS) environment (QGIS Development Team 2018). This allowed manual digitization of fractures on individual datasets, while enabling correlation of features across different datasets and scales.

Faults at each scale were interpreted based on several diagnostic characteristics. In the geophysical data, some appear as well-defined gravity anomalies or lineaments separating two areas of highly contrasting magnetic intensities. A number of these lineaments coincide with outcropping faults. Basin-bounding faults coincide with steep gradients in the gravity anomaly grid.

Mapping of outcrop-scale fractures in the Cretaceous Strzelecki Group was based on UAV orthophotos (**Table 3.2**; **Figure 3.5**), near-shore bathymetry, and field observations. Areal mapping (as defined in Watkins *et al.*, 2015) of fractures was conducted for the Caves locality at a scale of 1:500. Here, fractures were classified as faults when clear offsets could be identified in the orthophotos (**Figure 3.6**). Dikes hosted in the Strzelecki Group were mapped from UAV orthophotos of the Harmers Haven North and Harmers Haven South localities (**Figure 3.7**). Their absolute age, obtained from U-Pb geochronology, and overprinting relationships with fractures enabled us to infer the relative age of fracture sets. Fractures at Kilcunda (**Figure 3.6**; see **Figure 3.3** for location) were traced on digital aerial imagery with a

resolution of 7.5 cm/pixel (Nearmap, 2018). A certain amount of censoring bias may have occurred while tracing fractures on aerial orthophotos, because parts of the outcrop are covered by sand or water. The actual length of fractures could be longer than what is interpreted from the orthophotos.

3.3.4. U-Pb ID-TIMS dating of a mafic dike

The occurrence of mafic dikes in the study area (Constantine, 2001; Duddy and Green, 1992) provided a maximum age for several fracture sets (see Results section). Sample D006, obtained from a NNW-SSE trending dike at Harmers Haven North (**Figure 3.7d**), was collected for isotope dilution thermal ionization mass spectrometry (ID-TIMS). Zircon crystals from Sample D006 were separated using standard mineral-separation techniques, using magnetic and density separation methods. Several small grains and fragments were isolated and pre-treated according to the chemical-abrasion method of Mattinson (2005), with 60 hours of annealing at 850°C followed by 12 hours of leaching in HF and HNO₃. Six single grains were selected and cleaned with concentrated distilled HNO₃ and HCl. Due to their small size, no chemical separation methods were required. For ID-TIMS analysis, the samples were spiked with an in-house ²⁰⁵Pb-²³⁵U tracer solution, which had been calibrated against SRM981, SRM 982 (for Pb), and CRM 115 (for U), as well as an externally-calibrated U-Pb solution (the JMM solution from the EarthTime consortium).

Dissolution and equilibration of spiked single crystals was by vapour transfer of HF using Teflon microcapsules in a Parr pressure vessel placed in a 200°C oven for six days. The resulting residue was re-dissolved in HCl and H₃PO₄ and placed on an outgassed, zone-refined rhenium single filament with 5 µL of silicic acid gel. U-Pb isotope analyses were carried out using a Thermo Triton Plus mass spectrometer at Curtin University, in peak-jumping mode using a secondary electron multiplier. Uranium was measured as an oxide (UO₂). Fractionation and deadtime were monitored using SRM981 and SRM982. Mass fractionation was 0.02 ± 0.06 ‰/amu. U decay constants are from Jaffey *et al.* (1971). Data were reduced and plotted using the software packages Tripoli (from CIRDLES.org) and Isoplot 4.15 (Ludwig, 2012). All uncertainties are reported at 2σ.

The weights of the zircon crystals were calculated from measurements of photomicrographs and estimates of the third dimension. The weights are used to determine U concentration and do not contribute to the age calculation, and an uncertainty of 50 % may be attributed to the concentration estimate.

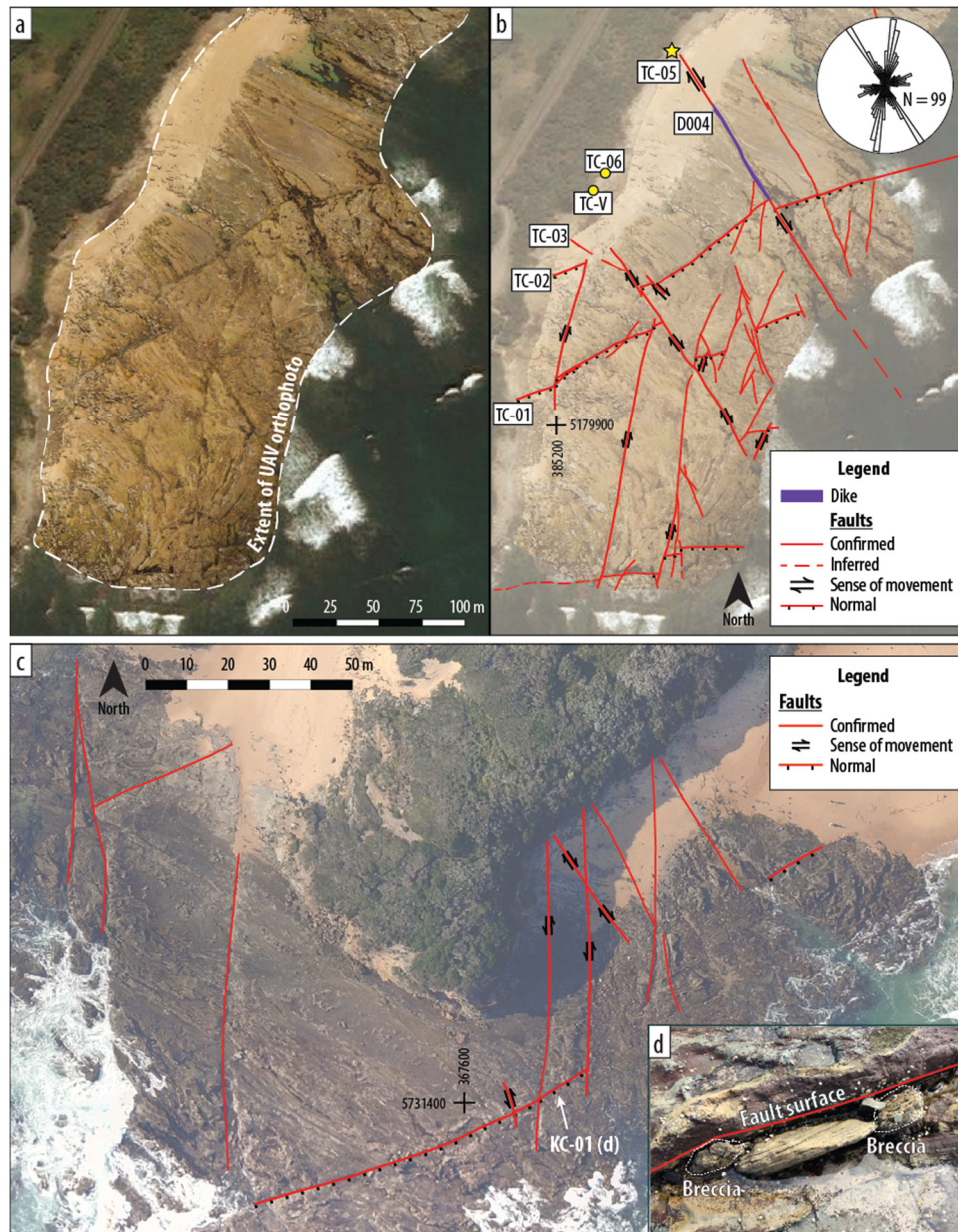


Figure 3.6 Map of faults and a mafic dike at the Caves and Kilcunda (see **Figure 3.3** and **Figure 3.5** for location). (a) Satellite image of the Caves locality overlain with UAV-based orthophoto of a wavecut platform and (b) interpreted faults and dike. The dashed line indicates the extent of the orthophoto. A NNW-SSE trending dike (D004) exploits fault TC-05, indicating that dike intrusion postdates initial fault activity. The sampling site for D004 is indicated by the yellow star. The rose diagram of the fracture traces was created using the Line Direction Histogram plugin (Tveite, 2015) in QGIS and is weighted by fault trace length. (c) Digital aerial image of a wavecut platform at Kilcunda (7.5 cm/pixel resolution; Nearmap, 2018) and interpreted faults. The inset (d) shows a NE-SW trending normal fault that is filled with a breccia injectite, signalling soft-sediment deformation. The breccia contains a massive, coarse-grained matrix that may have originated from an unconsolidated unit below the outcropping sandstone. Clasts of fine-grained sandstone in the breccia suggest that parts of the host rock were incorporated into the injectite as it was forced upwards. At both localities, NE-SW to ENE-WSW striking normal faults are overprinted by NNW-SSE and N-S to NNE-SSW trending conjugate faults.

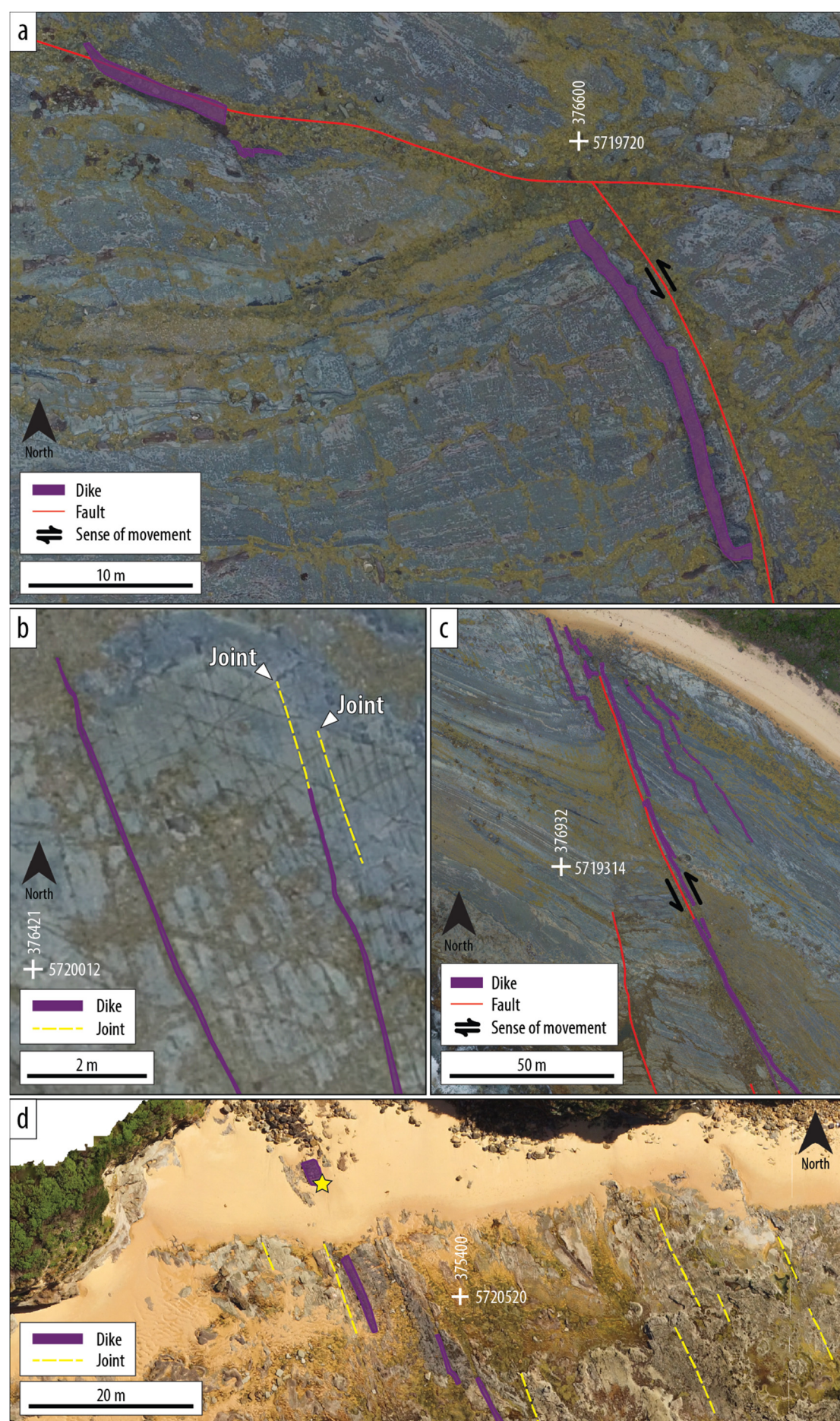


Figure 3.7 (a-c) Various dike geometries and forms of dike-fracture interaction at Harmers Haven South and Harmers Haven North (see **Figure 3.5** for location). Red lines are fault traces, purple polygons are dikes, and yellow dashed lines are joint traces. The joint set in (b) has an azimuth of 344°. The yellow star in (d) represents the D006 sampling site.

3.4. Results

Here we discuss the orientations of fracture sets (summarized in **Table 3.3**), their kinematics, and their timing based on overprinting relationships and newly obtained geochronology data. The location of Cretaceous Strzelecki Group outcrops (i.e., Kilcunda, Harmers Haven, Eagles Nest, the Caves, and Flat Rocks) are shown in **Figure 3.3** and **Figure 3.5**.

Table 3.3 Azimuth of basin-scale (>1 km) and outcrop-scale fracture traces from geophysical potential field data and UAV orthophotos of outcrops, respectively. The maximum shortening direction inferred from strike-slip faults at the Caves and Kilcunda, assuming that Fault Set 1 and 2 are a conjugate pair, is consistent with the maximum shortening direction that can be inferred from the trend of the regional joint set. From this we infer that the regional joint set and the NNW-SSE and NNE-SSW faults formed coevally.

Potential field geophysics

Selwyn Fault	30°	NNE-SSW
Waratah Fault	33°	NNE-SSW
Bell Point Fault	38°	NNE-SSW
Bass Fault	73 - 76°	ENE-WSW

UAV orthophotos

Normal faults - the Caves	52 - 88°	ENE-WSW to NE-SW
Fault set 1 - the Caves	325 - 330°	NNW-SSE
Fault set 2 - the Caves	5 - 10°	NNE-SSW
Inferred max. shortening - the Caves	345 - 350°	NNW-SSE
Normal faults - Kilcunda	58 - 71°	ENE-WSW to NE-SW
Fault set 1 - Kilcunda	324 - 333°	NNW-SSE
Fault set 2 - Kilcunda	179 - 186°	N-S
Inferred max. shortening - Kilcunda	345 - 350°	NNW-SSE
Regional joint set	334 - 344°	NNW-SSE

Borehole breakout (Hillis & Reynolds, 2000)

Present-day σ_1	310° ($\pm 20^\circ$)	NW-SE
------------------------	-------------------------	-------

3.4.1. Fault orientations in basement and basin sediments

Geophysical potential field data provided insight into the major internal structures of the basin. First-order fault traces interpreted from filtered TMI and onshore isostatic residual gravity grids are mostly ~10 to 40 km long. Their orientations vary from N-S to ENE-WSW (**Figure 3.3**).

Some of the first-order faults correspond to well-known structures that were active during the Paleozoic formation of the Lachlan Fold Belt. For example, the NNE-SSW trending Waratah Fault and adjacent Bell Point Fault at Cape Liptrap (**Figure 3.3**), characterized by a high-intensity magnetic signature in the TMI data, were active during the Devonian Tabberabberan Orogeny (Cayley *et al.*, 2002). The Waratah Fault has a long post-Devonian history of reactivation (Gardner *et al.* 2009).

The NNE-SSW trending Selwyn Fault (**Figure 3.1**; Willcox *et al.* 1992) juxtaposes an area with a high-intensity magnetic signature against an area with a low-intensity magnetic signature. This fault is characterized by a steep gravity gradient extending along the western flank of the Mornington Peninsula (**Figure 3.1b** and **Figure 3.4a**). Based on the different magnetic characteristics of the juxtaposed rocks, Cayley *et al.* (2002) speculate that movement along the fault began in the Cambrian Tyennan Orogeny. Willcox *et al.* (1992) inferred from field mapping and seismic interpretation that the fault was reactivated throughout the Cenozoic – recent times. It is therefore likely that first-order NNE-SSW trending faults are reactivated basement faults that influenced the internal architecture of the basin and the current onshore distribution of Strzelecki Group rocks.

Two orders of N-S to NNE-SSW trending faults within the Strzelecki Group rocks were mapped in outcrop. Kilometre-scale NNE-SSW trending faults crop out between Harmers Haven and Inverloch (**Figure 3.5**). They appear as up to ~20 m-wide fracture zones in near-shore bathymetry data, marked by sharp transitions in the strike of bedding. Meter-scale N-S to NNE-SSW trending faults were mapped at the Caves and Kilcunda localities (**Figure 3.6**). While these meter-scale faults may not link directly into the basement, similarities in their orientation and kinematics (see below) suggest that their formation could be associated with reactivation of NNE-SSW basement faults.

NE-SW to ENE-WSW trending geophysical lineaments characterized by steep gravity gradients can be traced over tens of km across the onshore Gippsland Basin (**Figure 3.3** and **Figure 3.4**). Some of these lineaments correspond with known faults such as the Bass and Kongwak faults, which bound the Narracan Block to the north and south, respectively (**Figure 3.3**). These faults have been mapped as reverse faults that dip steeply toward each other (**Figure 3.1b**). A similar relationship was observed for the NE-SW to ENE-WSW lineaments that bound

the Balook Block and the Mornington Peninsula, which correspond to previously mapped reverse faults or monoclines (Willcox et al., 1992).

Thirty NE-SW to ENE-WSW striking faults with horizontal traces up to ~90 m long were identified in the Strzelecki Group on wave-cut platforms and steep cliff faces at the Caves and Kilcunda (**Figure 3.6**; see **Figure 3.3** and **Figure 3.5** for location). These faults dip steeply ($60\text{--}65^\circ$) to the southeast and record meter-scale, normal dip-slip displacement (**Table 3.4**; **Figure 3.8**).

NNW-SSE trending meter to decimetre-scale faults were mapped in Strzelecki Group outcrops at the Caves, Harmers Haven and Kilcunda (**Figure 3.6** and **Figure 3.7**). Similarly oriented structures are not expressed in the magnetic and gravity grids, suggesting that they either do not extend to depth below the sedimentary cover, or they have insufficient lateral or vertical offset to be detected in ~800 m-spaced gravity and ~50 m-spaced TMI grids.

NNW-SSE trending subvertical joints are pervasive in Strzelecki Group outcrops at Harmers Haven North and Harmers Haven South (**Figure 3.7**). The azimuth of the fracture traces varies only slightly, ranging between 334 and 344° . This is the only systematic joint set that we have mapped across the study area.

3.4.2. Kinematics

Coastal outcrops of meter to decimetre-scale faults between Kilcunda and Inverloch (**Figure 3.3**) allow direct observation of offset and sense of movement. The location, measured orientation, and kinematics of these faults are summarized in Table 4. NE-SW to ENE-WSW striking normal faults at the Caves exhibit up to 5 m dip-slip displacement (**Figure 3.8**). Fault TC-01 (**Figure 3.8a**) is exposed within a subvertical cliff face. Here, the sandstone-dominated hanging wall is juxtaposed against a sandstone-dominated footwall. At fault TC-02 (~80 m north of TC-01; **Figure 3.8d**), a sandstone-dominated hanging wall is juxtaposed against a mudstone-dominated footwall. The hanging walls of both faults contain dense networks of subvertical deformation bands, representing fault-related damage. These are recognizable from millimetre to centimetre-scale dip-slip offsets of thin, alternating coarse-grained sandstone units and fine-grained organic matter-rich siltstone and mudstone units (**Figure 3.8b**). These structures are equivalent to the deformation bands observed in more massive units, where sedimentary layers are not macroscopically recognizable, and thin, organic matter-rich units are absent. The footwall of TC-01 exhibits conjugate pairs of deformation bands with subvertical acute bisectors, suggesting a local subvertical maximum principal stress (σ_1) axis (**Figure 3.8c**).

Table 3.4 Summary of structure data collected in the field. All structures are faults with the exception of Vein TC-V. Latitude and longitude are given as WGS 84 (EPSG:4326) coordinates.

Name	Locality	Latitude	Longitude	Plane		Lineation on Plane			Displacement	Kinematics
				Strike	Dip	Rake	Trend	Plunge		
TC-01	The Caves	-38.661916	145.680202	050	65	64 SW			Dip-slip (normal), SE down	Oblique-slip
TC-02	The Caves	-38.661170	145.680448	054	60				Dip-slip (normal), SE down, 5 m	
TC-03	The Caves	-38.660992	145.680591	116	70	15 NW			Dip-slip (normal), 1.5 m	Strike-slip
TC-04	The Caves			150	81	10 NW			Strike-slip (dextral)	Strike-slip
TC-05	The Caves	-38.660096	145.681334							
TC-06	The Caves	-38.660761	145.680882	006	80				Dip-slip (normal, reverse reactivation)	
TC-V	The Caves	-38.660841	145.680841	126	84	20 NW				Strike-slip
FR-01	Flat Rocks	-38.656548	145.683816	166	85	20 NW				Strike-slip
FR-01	Flat Rocks	-38.656548	145.683816	169	73		341	17		Strike-slip
FR-01	Flat Rocks	-38.656548	145.683816	169	73		348	30		Strike-slip

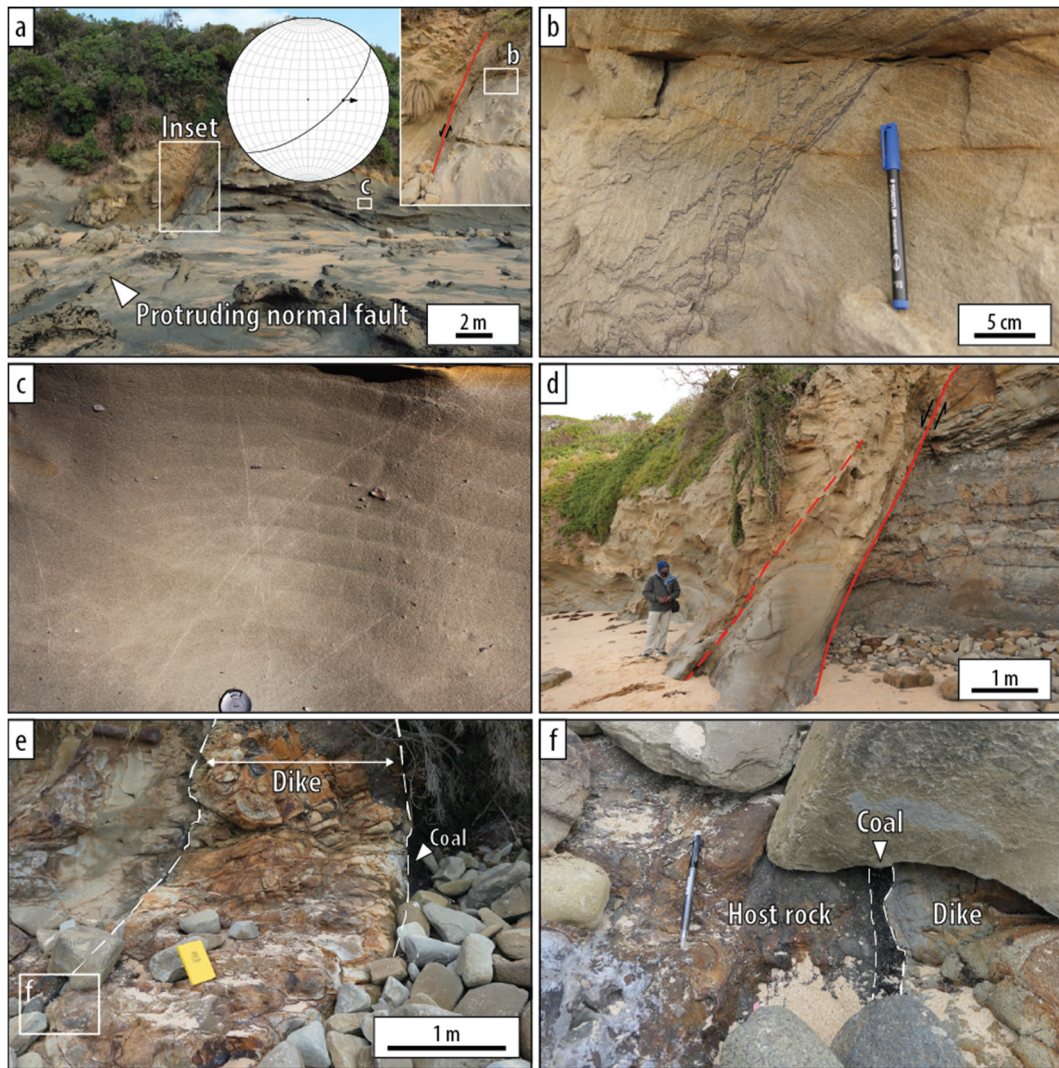


Figure 3.8 Field photos of outcrop-scale Cretaceous Strzelecki Group structures at the Caves (see **Figure 3.5** and **Figure 3.6** for location). (a) Fault TC-01, a normal fault that protrudes out of the wavecut platform and exhibits up to 5 m dip-slip displacement. A fault orientation measurement from TC-01 is plotted on an equal area lower hemisphere stereonet. (b, c) Clay smear and deformation bands (photo courtesy of R. Weinberg) associated with fault TC-01, located within the footwall. (d) Fault TC-02, a normal fault showing dip-slip displacement, north of TC-01. (e, f) Subvertical mafic dike (D004) overprinting Fault TC-05.

While normal faults at the Caves (**Figure 3.5**, **Figure 3.6**, and **Figure 3.8**) exhibit clear dip-slip offset, plunging slickenlines provide evidence for a strike-slip component of movement along the faults. One set of slickenlines along fault TC-01 exhibits a steep rake (64° SW; **Figure 3.8a**). These plunging lineations, along with the visible dip-slip offset along the primary fault surface, suggests that TC-01 is either: a) an oblique-slip normal fault, or b) a dip-slip normal fault that has undergone oblique-slip reactivation.

The morphology of normal faults that are exposed on wave-cut platforms at the Caves, Eagles Nest, and Kilcunda (**Figure 3.3** and **Figure 3.5**) vary from being heavily eroded to protruding. Normal faults that have been eroded to the extent that only a gap remains do not exhibit a discrete fault plane with slip lineations. Several diagnostic characteristics of sense of shear include fault drag of fine-grained layers downwards along a steeply-dipping fault, resulting in the fine-grained layers being approximately parallel to the inferred slip surface. Protruding normal faults (**Figure 3.8a**) can be up to 3 m wide and are associated with clusters of steeply dipping deformation bands that are parallel to the main slip surface. Compaction during cataclasis and cementation with orange-brown Fe-rich minerals (similar to **Figure 3.6** in Philit *et al.* 2015) make the fault rocks more resistant to weathering than those outside of the damage zone, causing them to form linear topographic highs above the mean elevation of the wave cut platforms.

Meter- to decimetre-scale NW-SE and N-S to NNE-SSW trending faults show predominantly lateral offsets. The kinematics of these fault sets are consistent between the Caves and Kilcunda localities (**Figure 3.6**), where NW-SE faults exhibit dextral strike-slip displacement, and N-S to NNE-SSW faults show sinistral strike-slip displacement. Some of the faults contain calcite mineralization and exhibit shallowly plunging slickenlines, recording predominantly strike-slip movement (**Figure 3.9**). A cluster of NW-SE striking fault-fill veins exposed at the Caves (TC-V, **Figure 3.9**; see **Figure 3.6** for location) exhibit feather-like features at their ends. One of the vein surfaces exposes partially preserved, shallowly plunging slickenlines (**Figure 3.9c**), which is an indicator of re-shearing along the primary fracture and vein. These slickenlines may have been coeval with mineralization or formed during shearing along an already existing vein, signalling reactivation. Some N-S striking centimetre-scale shear fractures at the Caves (including TC-06) exhibit normal dip-slip displacement that has been overprinted by reverse dip-slip displacement (**Table 3.4**), showing that centimetre-scale reactivation has occurred at this locality. At Flat Rocks (see **Figure 3.5** for location), NNW-SSE striking fault-fill veins exhibit two distinct sets of shallowly plunging slickenlines, recording at least two episodes of movement (**Figure 3.9b**).

The orientation and strike-slip kinematics of NNE-SSW trending faults in the Strzelecki Group outcrops are consistent with those of the NNE-SSW trending Waratah Fault (**Figure 3.1b** and **Figure 3.3**), which is a reactivated basement fault (Gardner *et al.*, 2009). Our own outcrop observations of rotated fold axes near the Waratah Fault and those of Gray *et al.* (1999) allow for both dextral and sinistral strike-slip motion along the fault. We therefore infer that the formation of NNE-SSW trending strike-slip faults in the Strzelecki Group could have been influenced by the reactivation of pre-existing basement faults. In our study area, there is no outcrop evidence that the NNE-SSW trending strike-slip faults in the Strzelecki Group cover

are physically linked with NNE-SSW trending basement faults. However, studies on the North Sea rift show that basement weaknesses, or zones of relatively low shear strength (e.g., shear zones), can locally perturb the regional stress field so that the orientation of new faults are aligned with the strike of the basement weaknesses (Phillips et al., 2016; Rotevatn et al., 2018).

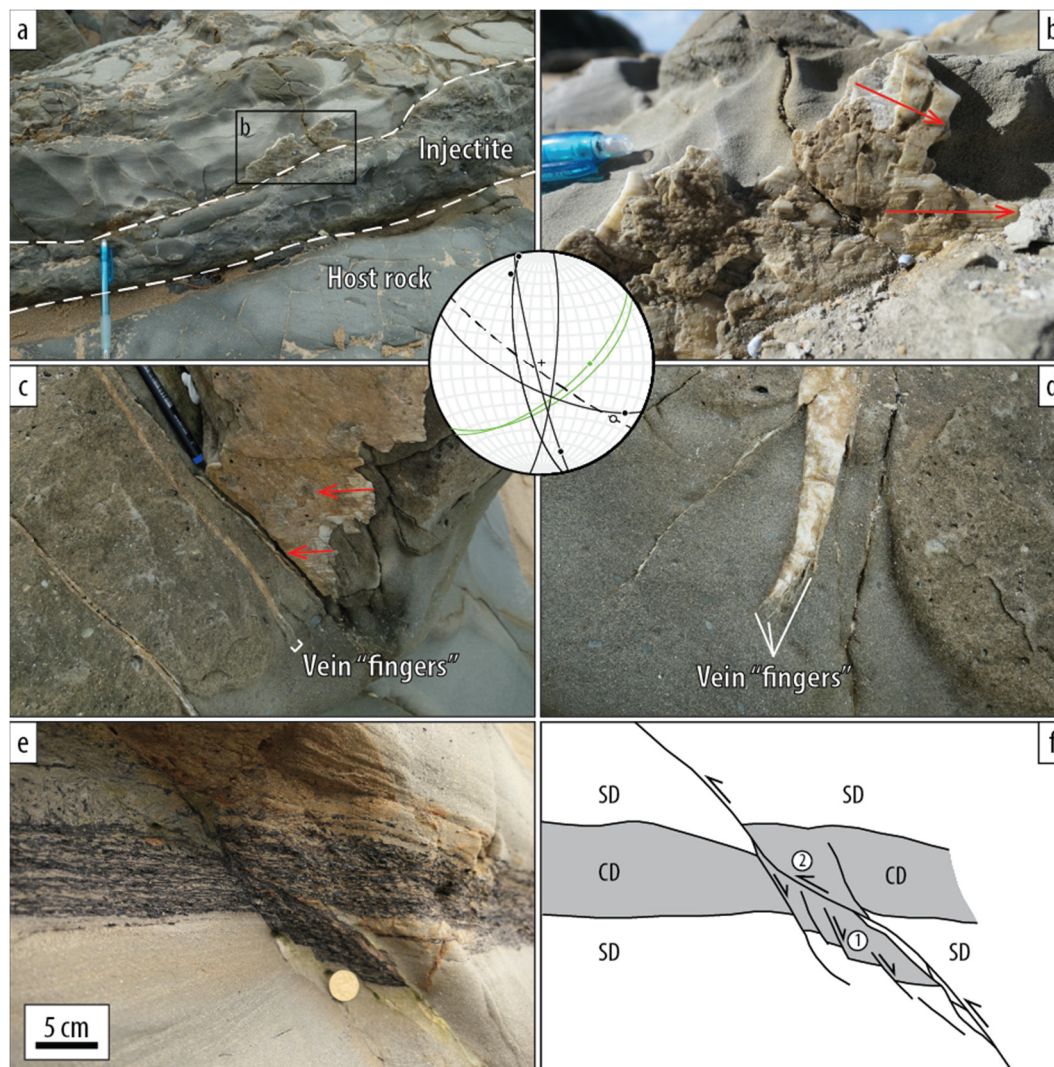


Figure 3.9 Field photos of evidence of outcrop-scale reactivation (see **Figure 3.5** and **Figure 3.6** for location). (a, b; FR-01) Mineralized faults at Flat Rocks. (c, d; TC-V) Veins at the Caves. Shallowly-plunging striations on vein surfaces indicate slip with a major strike-slip component that is either coeval with or postdates mineralization. Fault FR-01 is a NNW-SSE striking fault that is partly filled with a breccia injectite. A lower hemisphere, equal area stereonet shows the orientations of structures summarized in **Table 3.4**. Dots represent striation orientations. The green great circles and dot correspond to normal faults (TC-01 and TC-02). The black great circles and dots correspond to strike-slip faults. The dashed line represents Vein TC-V. (e, f; TC-06) Centimetre-scale shear fractures in the steeply-dipping, N-S striking fault. Normal dip-slip displacement is overprinted by reverse dip-slip displacement. The photograph was taken facing NW. SD = sand-dominated layer; CD = coal-dominated layer.

3.4.3. Geochronology

Six zircon crystals were analysed from Sample D006 (Table 5; see **Figure 3.7d** for sampling location). Calculated weights are between 0.3 and 1.1 μg , with variable calculated U concentrations. Th/U ratios are typical for magmatic zircon, around 0.5. All data are concordant and support our interpretation of the analyses representing a magmatic crystallization age. Two zircons yielded dates of ca. 366 Ma and are interpreted to be xenocrysts from the basement rocks (Foster and Gray, 2000). The weighted-mean $^{206}\text{Pb}/^{238}\text{U}$ age calculated from the four dates obtained from a coherent, concordant younger population of single-crystal analyses is 116.04 ± 0.15 Ma (2σ , MSWD = 0.23, N = 4), and is interpreted as the age of emplacement of Dike D006 (**Figure 3.10**).

3.4.4. Overprinting relationships and timing

Our interpretation of the geophysical potential field data (**Figure 3.3**) indicates that in some areas, NE-SW to ENE-WSW trending normal faults (e.g., the Bass Fault) are offset, and therefore postdated, by NNW-SSE trending faults and by NNE-SSW faults (e.g., north of Cape Paterson and Cape Liptrap). Crosscutting relationships in outcrop also record similar relative timing: NE-SW to ENE-WSW trending normal faults at the Caves are offset by NNW-SSE and NNE-SSW trending strike-slip faults (**Figure 3.6**). The acute angle between the NNW-SSE and NNE-SSW fault sets is approximately 40° , with the azimuth of the acute bisector (i.e., the inferred maximum shortening direction) being $\sim 345\text{--}350^\circ$ (see **Table 3.3** for a summary of the NNW-SSE and N-S to NNE-SSW trending fractures). The longest NNE-SSW trending faults show a sinistral component of horizontal offset, while the longest NNW-SSE faults exhibit dextral horizontal offset. The same crosscutting relationships and offsets between NNW-SSE and N-S strike-slip faults were also observed at Kilcunda (**Figure 3.6**), approximately 27 km NW of the Caves. The N-S trending faults at Kilcunda are interpreted to be part of the same fault set as the NNE-SSW trending faults at the Caves, as they have similar orientations and both exhibit sinistral horizontal offset. While there is no clear crosscutting relationship between the NNW-SSE and NNE-SSW fault sets, the acute angle between them and their kinematics suggest that they are most likely coeval conjugate pairs formed during a phase of NNW-SSE-oriented ($\sim 345\text{--}350^\circ$) shortening. This is further supported by the occurrence of a NNW-SSE ($334\text{--}344^\circ$) trending subvertical joint set at Harmers Haven North and Harmers Haven South (**Figure 3.7**), which could have formed coevally with the conjugate strike-slip faults, consistent with NNW-SSE directed maximum horizontal stress. By combining these basin-scale and outcrop-scale observations, we infer that NE-SW to ENE-WSW trending normal faults pre-date the NNW-SSE and N-S to NNE-SSW strike-slip fault sets and NNW-SSE joints.

Table 3.5 U-Pb isotopic data for zircons from Sample D006. Sample weights are calculated from crystal dimensions and are associated with as much as 50% uncertainty (estimated). Pb_c = Total common Pb including analytical blank (0.8 ± 0.3 pg per analysis). Blank composition is: $^{206}Pb/^{204}Pb = 18.55 \pm 0.63$, $^{207}Pb/^{204}Pb = 15.50 \pm 0.55$, $^{208}Pb/^{204}Pb = 38.07 \pm 1.56$ (all 2σ), and a $^{206}Pb/^{204}Pb - ^{207}Pb/^{204}Pb$ correlation of 0.9. Th/U is calculated from radiogenic $^{208}Pb/^{206}Pb$ and age. Measured isotopic ratios are corrected for tracer contribution and mass fractionation (0.02 ± 0.06 %/amu). ρ = error correlation coefficient of radiogenic $^{207}Pb/^{235}U$ vs. $^{206}Pb/^{238}U$. All uncertainties are given at 2σ . Ratios involving ^{206}Pb are corrected for initial disequilibrium in $^{230}Th/^{238}U$ using $Th/U = 4$ in the crystallization environment.

Sample	wt. (μg)	U (ppm)	Pb_c (pg)	mol% Pb^*	$\frac{Th}{U}$	$\frac{^{206}Pb}{^{204}Pb}$	$\frac{^{207}Pb}{^{206}Pb}$	\pm (%)	$\frac{^{207}Pb}{^{235}U}$	\pm (%)	$\frac{^{206}Pb}{^{238}U}$	\pm (%)	ρ	$^{206}Pb/^{238}U$ Age (Ma)	\pm (Ma)	$^{207}Pb/^{206}Pb$ Age (Ma)	\pm (Ma)
Sample D006: 1 zircon crystal per fraction																	
1	0.6	581	0.2	97	0.75	1518	0.0482	1.79	0.1206	1.91	0.018155	0.17	0.71	115.99	0.2	108	42.2
2	0.5	655	1	90	0.59	384	0.0486	3.9	0.1216	4.15	0.01817	0.26	0.94	116.08	0.31	126	91.9
3	0.3	93	0.4	91	0.81	87	0.0486	15.7	0.1217	16.76	0.018173	1	0.99	116.1	1.16	127	370.9
4	0.9	773	0.9	92	0.56	879	0.0485	1.78	0.1216	1.91	0.018178	0.26	0.54	116.13	0.3	124	42
5	0.4	95	0.3	97	0.25	435	0.0541	1.11	0.4352	1.19	0.058382	0.12	0.72	365.78	0.42	374	24.9
6	1.1	253	0.8	93	0.21	1284	0.0539	0.8	0.4345	0.87	0.058445	0.11	0.64	366.16	0.4	368	18.1

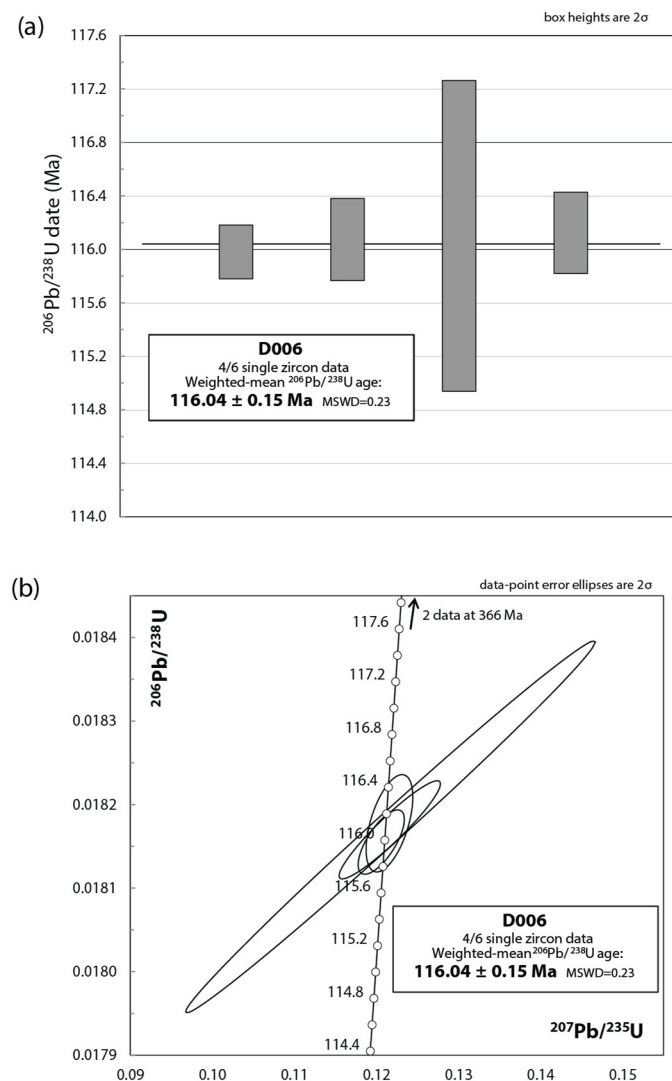


Figure 3.10 Results of U-Pb ID-TIMS analysis of four zircon crystals from Dike D006 (Harmers Haven; see **Figure 3.5** and **Figure 3.7d** for location). The weighted mean $^{206}\text{Pb}/^{238}\text{U}$ age calculated from a coherent, concordant population of single-crystal analyses is 116.04 ± 0.15 Ma (2σ , MSWD = 0.23, N = 4). This is interpreted to be the age of emplacement for Dike D006.

Soft sediment deformation observed in Strzelecki Group rocks provides further insight into the timing of outcrop-scale faulting. At Flat Rocks, a breccia injectite was emplaced into a NNW-SSE striking fault (FR-01 in **Table 3.4**; **Figure 3.9a**). The contact between the breccia and the surrounding rock is mineralized by calcite, with subhorizontal slickenlines on the vein surface facing the breccia. The breccia comprises sub-angular clasts of fine-grained sandstone in a matrix of massive, coarse-grained sandstone with calcite cement. A similar breccia occurs within a NE-SW trending normal fault (KC-01) at Kilcunda (**Figure 3.6**). The massive, coarse-grained matrix of the breccia injectite may have originated from an underlying, unconsolidated layer that was mobilized under increased overburden pressure. Fine-grained sandstone clasts in

the breccia exhibit similar grain sizes to the injectite host rock, suggesting that parts of the host rock were incorporated into the injectite as it was forced upwards.

The occurrence of this soft-sediment deformation breccia fill inside both a NE-SW trending normal fault and a NNW-SSE strike-slip fault suggests that subsurface sediment mobilization could have been synchronous with or postdate NNW-SSE faulting. It also indicates that NNW-SSE and earlier faulting took place early in the basin's history, shortly after initial basin opening, as some syn-rift sediment layers had not been completely consolidated.

Further timing constraints are provided by dolerite dikes that intrude the Lower Strzelecki Group in the study area. Dike traces across the study area generally trend NNW-SSE to NW-SE in map view and have wide spacing on the order of hundreds of meters. Because of the similar general orientation of the dike traces, it is assumed that dike intrusion events across the study area were all part of the same Cretaceous magmatic event.

NNW-SSE trending dikes crop out at Harmers Haven South (see **Figure 3.5** for location). Three different dike geometries and relationships with fractures were observed in map view (**Figure 3.7a–c**):

1. The dike is parallel to, and in some cases exploits, a NNW-SSE trending joint set that is pervasive across the Harmers Haven South locality (**Figure 3.7b**).
2. The dike is emplaced along two strike-slip faults of different generations (one fault offsets the other), with no evidence of offset in the dike itself (**Figure 3.7a**).
3. The main dike body is parallel to a 100 m-scale fault zone, with smaller dike apophyses branching out of it (**Figure 3.7c**).

All three forms of dike emplacement provide strong evidence that dike intrusion exploited and therefore postdates NW-SE to NNW-SSE trending faults and joints. The outcropping dikes at Harmers Haven North are also parallel to the pervasive NNW-SSE trending joint set (**Figure 3.7d**). The TIMS age for Dike D006, located at the western end of the outcrop is 116.4 ± 0.15 Ma. This gives us an Early Cretaceous upper age limit for the formation of the pervasive NNW-SSE trending joint set within our study area.

A subvertical dike (D004) exposed in a cliff face at the Caves exploits a subvertical NNW-SSE striking dextral strike-slip fault (TC-05, **Figure 3.8**; see **Figure 3.5** and **Figure 3.6** for location). A coal bed has been incorporated into the fault and smeared along the fault surface. Parts of the coal smear are present on both the NE and SW margins of the dike, indicating that dike emplacement postdates initial movement along the fault.

3.5. Discussion

3.5.1. Sequence of deformation from outcrop data

While fracture tracing on 2D (map-view) datasets aided with establishing overprinting relationships between fractures, particularly faults, field observations helped to further constrain their relative timing. Outcrop and hand sample-scale kinematic indicators were essential for separating syn-rift faults from those that are likely to be post-rift structures.

We have presented evidence for the formation of NE-SW to ENE-WSW striking normal faults, which show significant outcrop-scale displacement, during Early Cretaceous extension. These structures are truncated by NNW-SSE and N-S to NNE-SSW trending strike-slip conjugate faults (**Figure 3.6**), consistent with formation under a NNW-SSE maximum horizontal compressive stress and ENE-WSW minimum compressive stress regime. In turn, NNW-SSE faults were exploited by mafic dikes (**Figure 3.6** and **Figure 3.7**), providing an Early Cretaceous age limit for NNW-SSE and N-S to NNE-SSW strike-slip faulting.

Evidence for reactivation along NNW-SSE and N-S to NNE-SSW trending faults within the Cretaceous Strzelecki Group include multiple sets of shallowly plunging slickenlines (that are oblique to each other) on a single fault-fill vein surface (**Figure 3.9**). While the exact timing of each slip event could not be determined, the overall kinematics of these fault sets suggest that a NNW-SSE directed maximum horizontal compressive stress regime is likely to have caused strike-slip reactivation along optimally oriented NNW-SSE and N-S to NNE-SSW faults. This fits well with previous interpretations of several periods of post-rift, NNW-SSE directed shortening throughout the Cenozoic (Müller et al., 2012; Power et al., 2003; Willcox et al., 1992).

Based on cross-cutting and overprinting relationships observed in the field, the sequence of Cretaceous outcrop-scale deformation in the onshore study area (summarized in **Figure 3.11**) is as follows: 1) Early Cretaceous normal faulting under a local NW-SE or NNW-SSE directed extension; 2) NNW-SSE jointing and coeval NNW-SSE and N-S to NNE-SSW trending strike-slip faulting under a NNW-SSE oriented maximum horizontal compressive stress and ENE-WSW oriented minimum horizontal compressive stress regime, associated with uplift and inversion; 3) intrusion of mafic dikes at ca. 116 Ma, which could have closely followed NNW-SSE jointing and NNW-SSE and N-S to NNE-SSW faulting; and 4) Late Cretaceous – Cenozoic reactivation of strike-slip faults during periods of NNW-SSE oriented compression (Müller et al., 2012). Faults related to Late Cretaceous extension, which would have been coeval with offshore E-W to WNW-ESE trending faults, were not observed in the onshore study area.

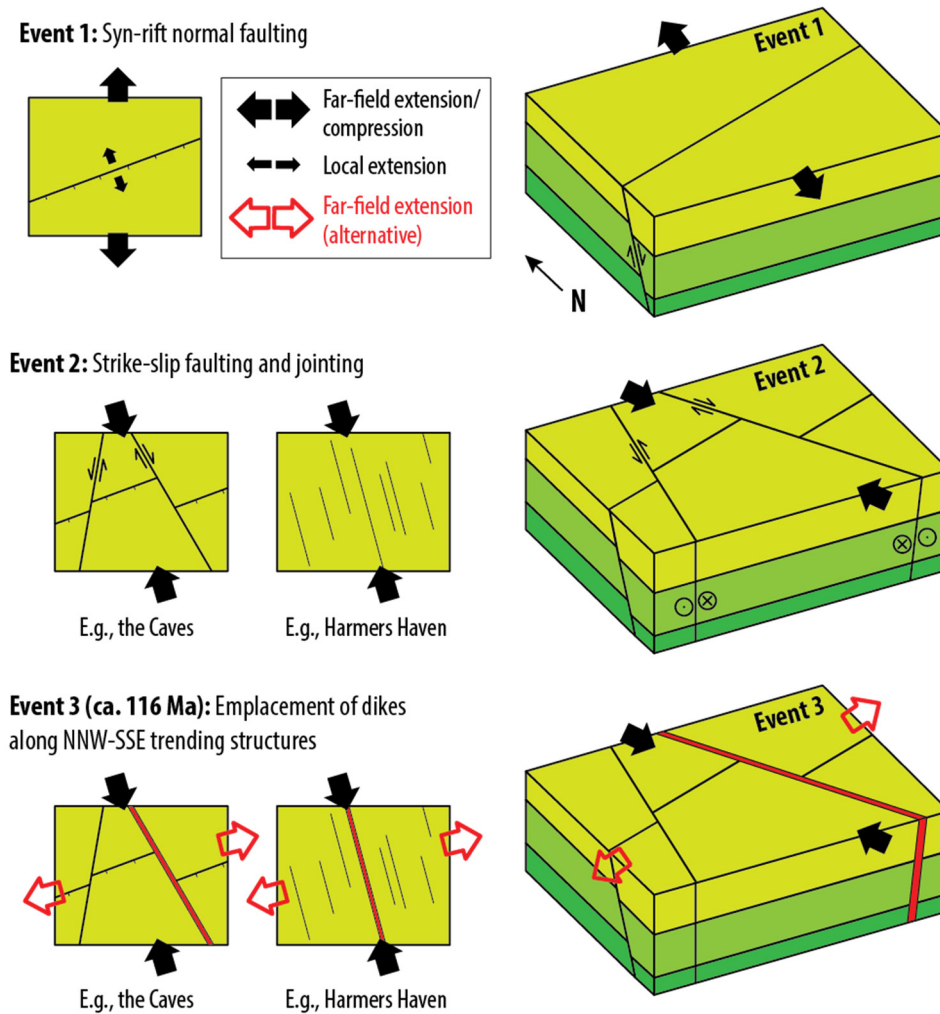


Figure 3.11 Schematic illustration of the sequence of Early Cretaceous outcrop-scale deformation in the onshore Gippsland Basin study area, based on field observations (refer to text for details on overprinting relationships). Red arrows indicate the inferred paleo-extension direction if Early Cretaceous magmatism were linked with ENE-WSW extension along the East Gondwana margin and the opening of the Tasman Sea, as opposed to NNW-SSE directed shortening. Events 2 and 3 could have been coeval.

3.5.2. Early Cretaceous magmatism in the Gippsland Basin

Published literature has documented pulses of Late Cretaceous to Cenozoic magmatism in the Gippsland Basin and other eastern basins of the ASM (Meeuws et al., 2016). Here we present the first published single zircon U-Pb ID-TIMS age for a magmatic intrusion in the eastern basins of the ASM. This result reveals that magmatic activity in the Gippsland Basin can be traced as far back as the Early Cretaceous to ca. 116 Ma (**Figure 3.10**). The dated Sample D006, obtained from a NNW-SSE trending dike at Harmers Haven North (**Figure 3.7d**), is up to 20 Myr older than intrusion ages derived from AFTA (Duddy and Green, 1992) on the baked contact of a NW-SE trending dike (D004) at the Caves, approximately 9 km to the east (**Figure 3.6** and **Figure 3.8**).

The discrepancy between the results of high-precision TIMS dating and AFTA invites us to re-evaluate the reliability of magma emplacement ages derived from AFTA, as they are sensitive to the thermal history, including burial and uplift, of the sample. A summary of the use of AFTA for reconstructing the thermal history of Australia's southeastern basins can be found in Dumitru *et al.* (1991) and Duddy & Green (1992). The published ages of dike emplacement (99.9 ± 5.3 Ma and 96.3 ± 4.2 Ma) were inferred from the thermal history of the host rock. They were derived from fission tracks in apatite grains from the baked contact at the Caves, which could have recorded a period of rapid cooling following dike emplacement, as suggested by Duddy & Green (1992). However, they could have also been influenced by subsequent events. For example, strong alteration of this dike raises the possibility that hydrothermal fluids may have passed through the faults at this locality, including the fault in which the dike had been emplaced. Such exposure to elevated temperatures may have affected the annealing of the apatite fission tracks and resulted in a younger age for the dike. It is unlikely that the dikes at Harmers Haven North and the Caves are associated with two separate magmatic events that are 20 Myr apart. All of the mapped dolerite dikes along the coast between Kilcunda and Inverloch (see **Figure 3.3** for location) exhibit a consistent NW-SE to NNW-SSE orientation. We therefore conclude that the dikes at Harmers Haven and the Caves (D006 and D004, respectively) are part of the same magmatic event and that AFTA on samples collected from baked contacts produces less reliable results (with errors up to 6.4 Ma; Duddy & Green 1992) than ID-TIMS U-Pb geochronology.

Early Cretaceous magmatism at ca. 116 Ma in the onshore Gippsland Basin may be related to Early Cretaceous volcanism in the eastern margin of Australia, such as the Whitsunday Volcanic Province, where two pulses of magmatism are recorded at ca. 118–113 Ma and ca. 110–105 Ma (Bryan and Ernst, 2008). The ca. 116 Ma age is also only slightly older than the age of the Mt. Dromedary Complex (ca. 100 Ma; Williams *et al.* 1982), approximately 150 km north of the Gippsland Basin. The timing of all of these magmatic events coincides with the change in tectonic regime along the East Gondwana margin from collisional to extensional at ca. 105–100 Ma (Bache *et al.*, 2014; Matthews *et al.*, 2012). Reconstructions by Bryan *et al.* (1997) and Bryan and Ernst (2008) suggest that a N-S trending rift system formed along the East Gondwana margin in the Early Cretaceous, extending from north Queensland to Zealandia (before it separated from Gondwana; Bache *et al.* 2014) and is linked to magmatism in the Whitsunday Province and the Mt. Dromedary Complex. The NNW-SSE trend and the newly obtained age of the mafic dikes in the onshore Gippsland Basin suggest that these intrusions could be a precursor to incipient rifting along the East Gondwana margin. The silicic composition of the Whitsunday Province does not rule out possibility that it is linked to mafic magmatism further south, as mafic magma (i.e., mantle input) plays a significant role in driving

silicic magmatic systems (Swallow *et al.* 2018 and references therein). It is likely that other NNW-SSE trending intrusions in the Gippsland Basin, particularly those that crop out between Kilcunda and Inverloch (**Figure 3.3**), were part of the same Early Cretaceous magmatic event but have not been recognized as such.

The ca. 116 Ma magmatic event is too young to be associated with initial rifting of the Gippsland Basin (ca. 142-146 Ma; Norvick & Smith 2001). The NNW-SSE orientation of the dikes would have required either NNW-SSE shortening or ENE-WSW extension, neither of which are compatible with the inferred, broadly N-S paleo-extension associated with rifting between Australia and Antarctica. The timing relationship between the proposed episode of Early Cretaceous, non-rift related magmatism and previously interpreted mid-Cretaceous cooling, uplift, and inversion in the Gippsland Basin (Duddy and Green, 1992; Dumitru *et al.*, 1991; Foster and Gleadow, 1992; Willcox *et al.*, 1992) remains speculative. If the latter are associated with a NNW-SSE oriented maximum horizontal compression (under which NNW-SSE trending joints and the associated strike-slip faults formed), then our interpretation of the overprinting relationships suggest that NNW-SSE compression and therefore cooling, uplift, and inversion must pre-date Early Cretaceous magmatism.

3.5.3. The role of basement faults in syn-rift faulting

The discussion on extensional models for the Gippsland Basin is complicated by the variability of syn-rift fault orientations across the basin, especially when we assume that trends of rift-related faults are perpendicular to the regional extension direction. The high obliquity between fault sets onshore and offshore (NE-SW to ENE-WSW and E-W to WNW-ESE, respectively) has led to the proposal of a multi-stage extension model, with a rotation of the regional extension direction that is associated with the Late Cretaceous commencement of Tasman seafloor spreading (Power *et al.*, 2003). However, it remains unclear how the far-field effects of Tasman seafloor spreading could have been superimposed on the opening of the Bass Strait and whether this interaction would have induced mid-Cretaceous uplift and inversion in the Gippsland Basin, followed by a rotation of the extension vector and Stage 2 rifting. Furthermore, a rotation of the extension vectors from NW-SE to NNE-SSW throughout the Cretaceous does not agree with previous interpretations of N-S to NNE-SSW directed lithospheric extension and overall rifting in the Bass Strait (Finlayson *et al.*, 1996; Hill *et al.*, 1994; K. C. Hill *et al.*, 1995).

The NE-SW to ENE-WSW orientation of observed rift-related normal faults is difficult to reconcile with Early Cretaceous N-S to NNE-SSW extension (Etheridge *et al.*, 1985; Miller *et al.*, 2002) without invoking basement influence on syn-rift faulting. Numerical fault growth models by Deng *et al.* (2017) show that, as older basement faults reactivate, they extend into

the overlying sedimentary units. Such reactivated faults influence the orientation of newly formed faults in the surrounding rocks. This arises due to stress perturbations adjacent to larger reactivated faults, which causes a local re-orientation of the stress field (Maerten et al., 2002). Simultaneously, new faults that are orthogonal to the extension direction can also form (Whipp et al., 2014) and eventually link with the oblique, reactivated faults with increasing strain (Deng et al., 2017).

Two scenarios for how inheritance of basement faults might have influenced syn-rift fault orientation are: reactivation of basement structures or local re-orientation of extension direction due to the presence of basement faults (**Figure 3.12**). In the first scenario, reactivation of NNE-SSW trending basement faults locally re-oriented the stress field and extension direction, which led to the formation of NE-SW syn-rift faults. Field observations at fault TC-01 (**Figure 3.6** and **Figure 3.8**), where there is a component of oblique slip parallel to the direction of regional paleo-extension, support the model of the reactivation of basement faults (**Figure 3.12a**) (Corti et al., 2007; Henza et al., 2011). The formation of NE-SW oriented faults under N-S to NNE-SSW regional extension would have required a local counter-clockwise rotation of the extension direction that approaches 90° to the NNE-SSW trending basement structures. However, the fact that the resulting NE-SW fault strike is acute to the trend of the basement structures is different to examples from the North Sea (offshore northern Norway) and East Greenland, where basement reactivation resulted in rift fault strikes that are parallel to the strike of basement structures (Phillips et al., 2016; Rotevatn et al., 2018). Furthermore, the NE-SW syn-rift faults should have a component of strike-slip movement (**Figure 3.12a**) if influenced by basement reactivation. The observation that displacement is mainly dip-slip, and the absence of kinematic indicators on other NE-SW syn-rift faults, means that we cannot exclude the possibility that these faults have predominantly extensional kinematics. This supports the second scenario of inheritance (**Figure 3.12b**), where the direction of extension is re-oriented near basement faults (i.e., weak zones), and the slip vectors remain mostly parallel to the fault dip direction (Morley, 2010; Philippon et al., 2015). Reactivation is not the only mechanism for basement inheritance, and future investigations should focus on how basement faults, fabrics, and other heterogeneities might induce local rotation of the extension direction without being reactivated.

E-W trending Late Cretaceous faults, which more accurately reflect the inferred N-S or NNE-SSW paleo-extension direction, would have been less pronounced in the onshore Gippsland Basin because of the influence of the NNE-SSW trending basement faults, similar to observations of greater strain localisation along reactivated faults with increasing strain in the Horda Platform, North Sea (Whipp et al., 2014). Rifting is more optimally oriented offshore, which implies that NNE-SSW trending basement structures are not present or less influential

offshore (**Figure 3.12c**). In our model, multiple rifting episodes that involve rotation of the regional extension direction are not required to explain non-parallel fault sets. Instead, pre-existing basement structures add geometric complexity to fault arrays in the cover rocks during rifting. This highlights the inadequacy of estimating paleo-extension vectors from fault orientation alone.

3.6. Conclusions

We have demonstrated the advantages of using a multi-scale dataset, comprising potential field geophysics, UAV-derived orthophotos, direct outcrop observations, and high-precision U-Pb geochronology, to map fractures in the sedimentary cover and basement of a rift basin and to link basin-scale structures with associated outcrop-scale deformation. This approach (i) facilitated the interpretation of relative timing between faulting, jointing, and intrusive events and (ii) guided interpretations of extension and shortening directions when insufficient data was available for fault slip analysis.

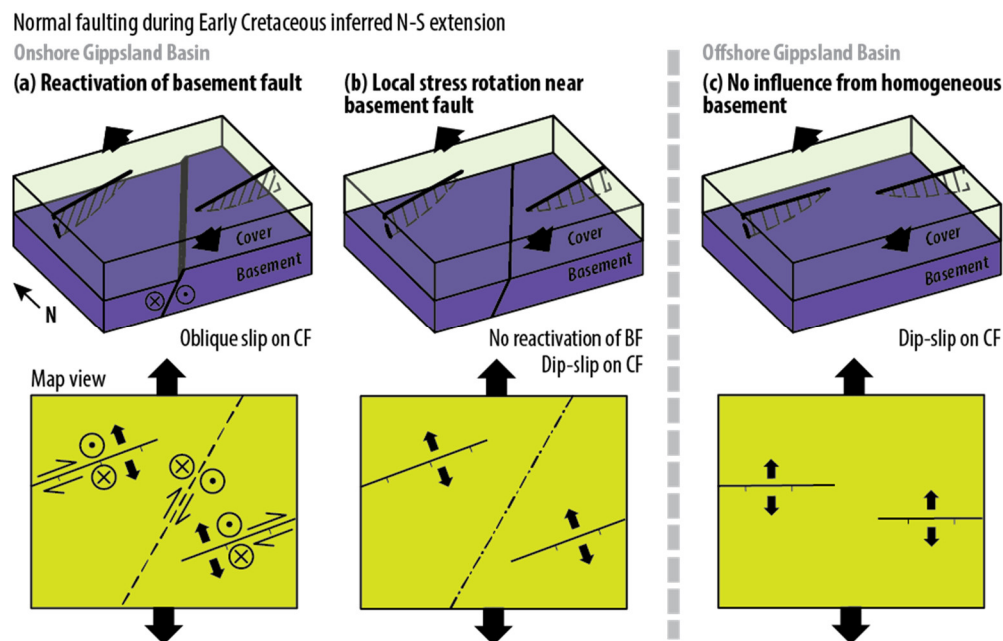


Figure 3.12 Schematic illustration of the influence of a pre-existing basement fault on faulting in the cover during subsequent extension. In (a) the strike-slip component of basement fault reactivation influences the kinematics of the new cover faults, resulting in oblique slip. In (b) locally misoriented faults form due to the topographic expression of the basement fault at the basement-cover interface or because the basement fault creeps slightly, rotating the stress field locally. (a) and (b) are possible scenarios for the onshore Gippsland Basin, where the cover is underlain by basement rocks with a NNE-SSW structural trend. These structures may be less influential or absent offshore, so that new cover faults are orthogonal to the inferred far-field extension direction (c). BF = basement fault; CF = cover fault.

We established the sequence of faulting and reactivation for the western onshore Gippsland Basin. We argue that uplift/inversion, associated with a NNW-SSE directed shortening, occurred in the Early Cretaceous before ca. 116 Ma, earlier than previous interpretations of uplift/inversion at ca. 90–95 Ma. This was followed by magmatism, which was the far-field expression of the onset of rifting along the East Gondwana margin. The new Early Cretaceous age of a mafic dike in the onshore Gippsland Basin challenges previous interpretations that magmatism in the Gippsland Basin did not occur until the Late Cretaceous.

NE-SW to ENE-WSW striking Early Cretaceous rift-related faults onshore are oblique to the expected E-W to WNW-ESE orientation predicted by the inferred regional N-S or NNE-SSW paleo-extension direction. The presence of NNE-SSW trending basement faults could have resulted in a local re-orientation of the far-field stress, exerting a strong influence on local extension vectors in the western onshore part of the basin during rifting and a lesser influence offshore (where faults trend E-W to WNW-ESE). Our results suggest that it is not necessary to invoke two stages of extension during rifting, separated by a rotation in the regional extension direction, to explain non-parallel fault sets. Lateral changes in structural style along rifts can therefore be attributed to mechanical heterogeneities in the basement, including weak zones such as pre-existing faults.

While many studies infer basement inheritance from subsurface data (e.g., seismic reflection data), this study adds to the wider understanding of inheritance by combining geophysical potential field and outcrop data. The findings presented here have implications for interpreting the influence of basement faults on basin development along the ASM and for paleotectonic studies of rift basins worldwide. We highlight the complications that arise when estimating regional extension vectors based on fault orientation alone, specifically in areas where basement structures interact with the far-field tectonic stress. In such areas, pre-existing structures add geometric complexity to fault arrays during rifting.

Acknowledgements

We thank Atle Rotevatn for editorial assistance, reviewers Thomas B. Phillips, Thomas B. Kristensen, and Simon Holford for their constructive feedback, and Roberto Weinberg for invaluable discussions in the field. The Department of Land, Water and Planning (DELWP) is thanked for providing the near-shore bathymetry dataset, and Geoscience Australia is thanked for curating the potential field data and making it freely available. Fieldwork was partly funded by an AAPG Grants-in-Aid Award to AS, who is also supported by a Monash University Faculty of Science Dean's International Postgraduate Research Scholarship.

Chapter 4

Who's your daddy? The scale-dependent influence of structural inheritance on fracture patterns

A. Samsu¹, A. R. Cruden¹, S. Micklethwaite¹, L. Grose¹, S. A. Vollgger¹

¹School of Earth, Atmosphere and Environment, Monash University
Clayton, VIC 3800, Australia

Abstract

Faults and fractures have been shown to exhibit geometric invariance across a range of scales, but the impact of structural inheritance on this pattern is poorly understood. Here we show how fracture orientations in sedimentary rocks vary at different scales when influenced by pre-rift structures in folded and faulted Neoproterozoic to Paleozoic basement rocks. We use high-resolution unmanned aerial vehicle (UAV) orthophotos to map basement folds and faults and thousands of fractures (i.e., joints and faults) in the cover rocks of the Gippsland Basin, southeast Australia. We compare these outcrop-scale observations with basin-scale faults (>1 km long) previously interpreted from potential field geophysics data. Length-coloured rose diagrams of fracture traces are used to visualize and compare the trends in fracture orientations. Early Cretaceous syn-rift normal faults exhibit the same ENE-WSW trend at both basin and outcrop scale. Pervasive outcrop-scale NNW-SSE joints record a subsequent regional shortening event, but this is only expressed at the basin scale as reverse reactivated ENE-WSW striking faults. Thus, NNE-SSW trending fabrics and/or faults in the underlying basement exert significant control on the orientation of basin-scale fractures in the cover but appear to have limited influence on outcrop-scale fracture orientations. Our observations show that fracture systems influenced by structural inheritance are not scale-invariant. In basins influenced by structural inheritance, a proper understanding of the structural architecture can only be achieved by analysing data that span multiple scales. Further, outcrop-scale fractures reflect the far-field paleostress more faithfully than basin-scale fractures, unless larger faults are present to locally perturb the far-field stress.

4.1. Introduction

The formation of fractures in a rift basin is primarily controlled by far-field stresses resulting from active tectonic processes. However, pre-existing mechanical heterogeneities in pre-rift “basement” rocks can interact with the far-field stress during the evolution of the rift basin, influencing the formation of fractures in the sedimentary “cover” rocks (“structural inheritance”). For example, multiple studies on rift systems (e.g., Morley et al., 1990; Corti et al., 2007) demonstrate that local stress perturbations in the vicinity of pre-existing structures can significantly alter stress trajectories, affecting the orientation and geometry of new fractures (Bourne and Willemse, 2001; de Joussineau et al., 2003; Maerten et al., 2002; Morley, 2010). Pre-existing faults or shear zones in the basement of a basin can be “inherited” by the overlying sedimentary cover through fault reactivation (Kirkpatrick et al., 2013; Phillips et al., 2016), which results in parallelism or “geometric similarity” between a reactivated basement structure and a newly formed cover fault (Holdsworth et al., 1997). Structural inheritance can also be recognized when the trend of cover fractures appear to change across areas that overlie different

basement domains even when the fractures do not directly link into the basement structures (Samsu et al., 2019; Wilson et al., 2010). This second mechanism of inheritance is a poorly understood phenomenon that nevertheless can have a significant impact on fracture orientations and connectivity.

While it is widely accepted that structural inheritance can impact the orientation of entire rifts as well as smaller-scale faults within rift basins (e.g., Corti et al., 2007; Henza et al., 2011; Reeve et al., 2015), few studies examine the influence of inheritance on the formation of fractures in one study area at multiple scales. In a study of the northeast Brazilian margin, Kirkpatrick et al. (2013) found that the orientation of regional rift faults are parallel to sub-vertical, crustal-scale shear zones in the basement – which could be attributed to reactivation of the basement shear zones during rifting (Phillips et al., 2016) – while syn-rift outcrop-scale faults are oblique to the shear zones and the pervasive basement fabric. Their findings suggest that the influence of pre-existing basement structures is scale-dependent. However, it is rarely the case that structures in basement rocks can be compared with the overlying cover rocks at the same scale. The interpretation of faults in cover rocks is usually conducted on seismic reflection data (e.g., Peace et al., 2017; Phillips et al., 2016; Reeve et al., 2015), while basement structures at the margins of rift basins are observed in outcrops (e.g., Kirkpatrick et al., 2013).

Our study uses the Cretaceous western onshore Gippsland Basin (southeast Australia; **Figure 4.1**) as a natural laboratory to investigate how pre-existing discrete faults and a pervasive fabric in the basement may have influenced fracture orientations in the overlying cover rocks. The onshore Gippsland Basin provides a unique opportunity to study the various scales at which inheritance operates. Firstly, the two known levels of basement underneath the basin – a Paleozoic and a Neoproterozoic-Cambrian basement – allow us to study multiple orders of inherited structures. Secondly, onshore exposure of basement and cover rocks along the coast allow us to directly compare structures in basement and cover rocks at the same scale.

We used high-resolution unmanned aerial vehicle (UAV) orthophotos of outcrops to map pre-existing structures in the basement and thousands of fractures in the cover rocks. Maps of fracture traces (including faults and joints) and orientation statistics of fracture data were used to separate regional fracture trends from local trends. In this paper, we compare existing interpretations of basin-scale (>1 km scale) faults with the outcrop-scale fracture data. Using field observations, we present possible hypotheses of how discrete discontinuities or pervasive mechanical anisotropies in the basement, such as bedding, fold axial plane foliations, faults, and rheological boundaries, affect deformation in the cover rocks during the syn-rift and post-rift stages of basin development. Our findings show that the orientations of fractures that have been influenced by pre-existing basement structures vary between scales of observation.

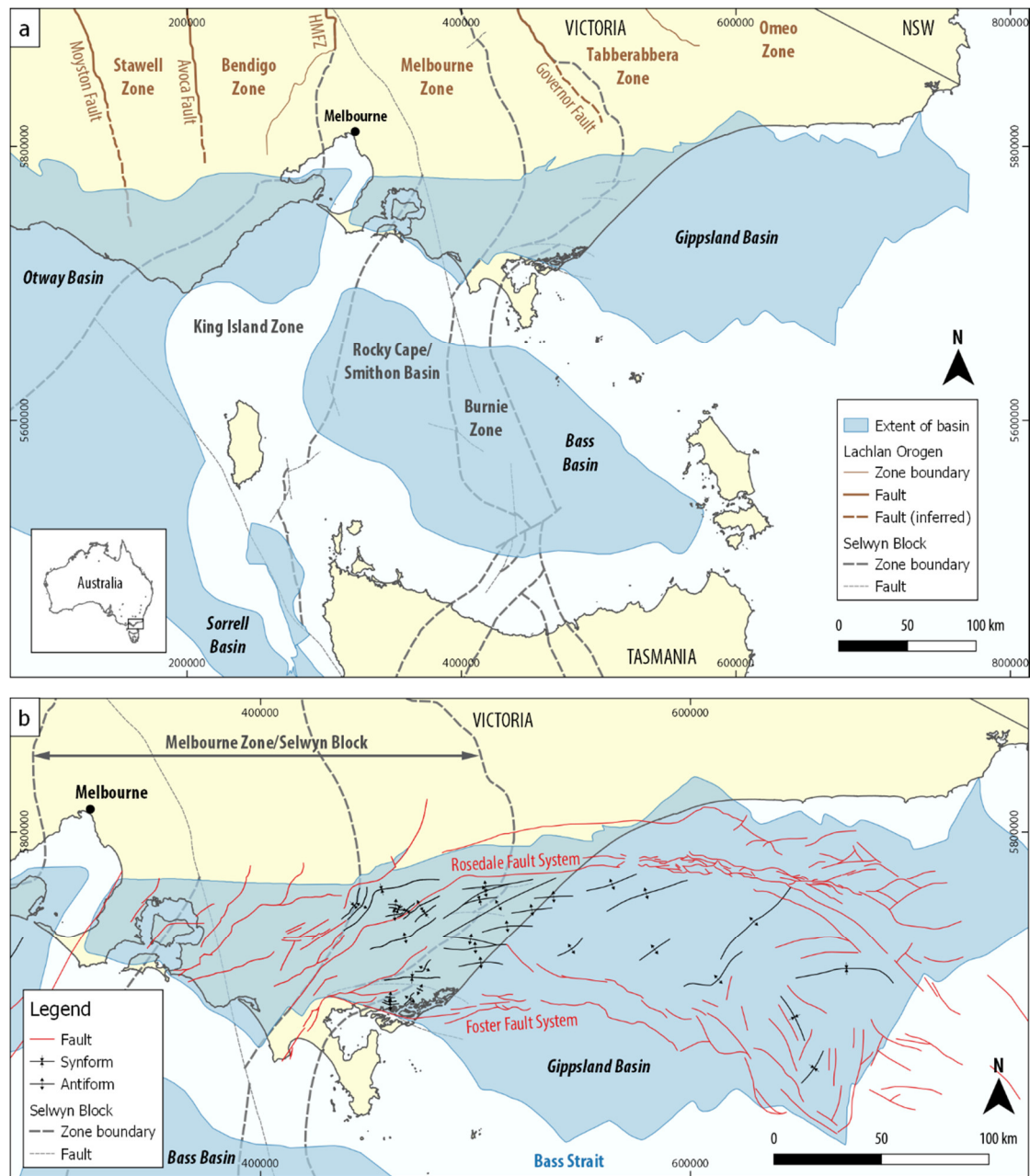


Figure 4.1 Location and major structures of the Cretaceous Gippsland Basin and the nearby Otway Basin and Bass Basin (shaded in blue). (a) Grey lines indicate major structures and boundaries of the underlying Neoproterozoic–Cambrian Selwyn Block (continuous lines are zone boundaries; dashed lines are faults), modified after Moore et al. (2016). Areas that are underlain by the Selwyn Block are shaded in grey. Brown lines represent the boundaries of tectonic zones of the Lachlan Orogen. HMFZ = Heathcote–Mt. William Fault Zone. (b) Faults and folds in the Gippsland Basin, modified after Constantine (2001) and Power et al. (2001). From west to east, structural trends change from NE–SW and ENE–WSW (western onshore Gippsland Basin), to E–W and NW–SE (eastern onshore and offshore Gippsland Basin); this transition coincides spatially with the eastern margin of the Selwyn Block. The coordinate reference system is GDA94 / MGA zone 55.

4.2. Geological setting

The Gippsland Basin is part of the Australian Southern Margin rift system, which formed during Jurassic–Cretaceous rifting between Australia and Antarctica (Miller et al., 2002 and references therein). Overall, the basin is characterized by three main sets of rift-related faults. NE-SW and ENE-WSW trending reverse-reactivated normal faults are dominant in the western onshore part of the basin. The eastern onshore part of the basin is populated by roughly E-W trending faults, and the offshore part of the basin contains WNW-ESE to NW-SE trending normal faults (Willcox et al., 1992).

Rifting in the Gippsland Basin began in the Early Cretaceous (**Figure 4.2**), first forming syn-depositional normal faults in the onshore Gippsland Basin that trend NE-SW to E-W (Willcox et al., 1992) (**Figure 4.1b**). Rifting was interrupted by a period of uplift and inversion at the end of the Early Cretaceous (Duddy and Green, 1992; Dumitru et al., 1991; Foster and Gleadow, 1992; Samsu et al., 2019; Willcox et al., 1992). This event was associated with NNW-SSE oriented compression, which formed NE-SW and ENE-WSW trending reverse faults and anticlines along reactivated rift-related normal faults in the onshore part of the basin (Norvick and Smith, 2001).

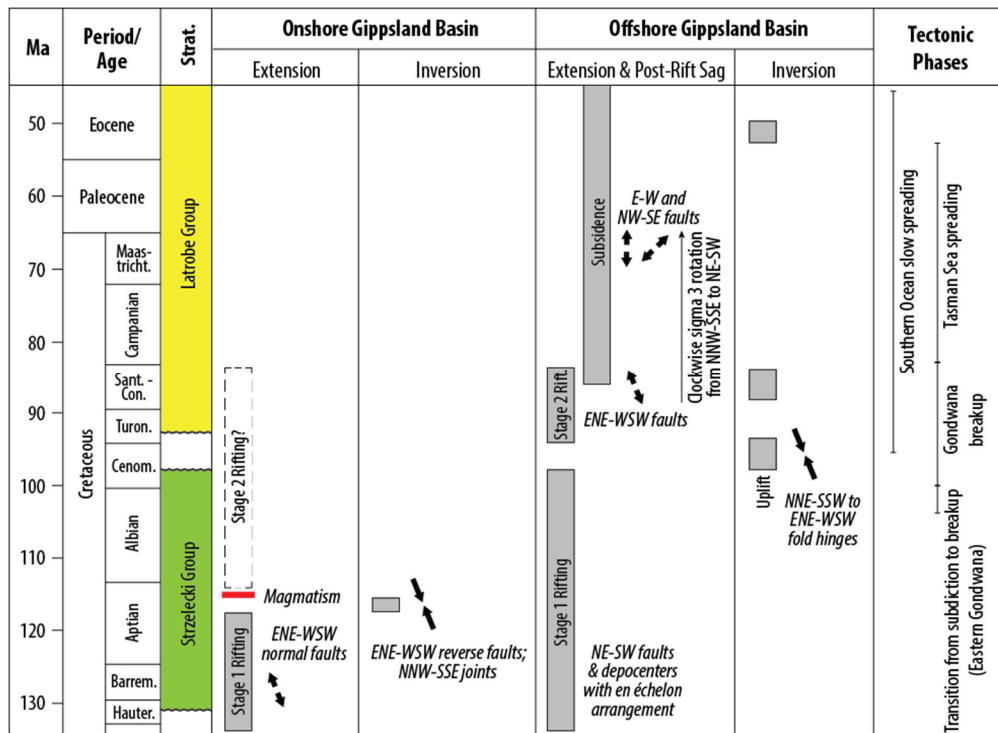


Figure 4.2 Summary of the deformation history in the Gippsland Basin and associated tectonic events. Deformation events in the offshore Gippsland Basin are derived from seismic reflection studies (Power et al., 2003). Cretaceous deformation in the onshore Gippsland Basin is derived from field studies and regional potential field geophysics (Samsu et al., 2019).

Rifting then resumed and continued into the Late Cretaceous, during which time E-W to NW-SE trending rift-related faults (e.g., the Rosedale and Foster fault systems; **Figure 4.1b**) formed in the eastern onshore and offshore Gippsland Basin (Power et al., 2003). The post-rift Cenozoic history records additional tectonic episodes associated with compression and a NNW-SSE oriented maximum horizontal stress. The stress state has not changed significantly since this time, as the present-day in-situ stress is characterized by a NW-SE oriented ($130 \pm 20^\circ$) maximum horizontal stress (Hillis and Reynolds, 2000).

This paper discusses the interaction between the two basement units underneath the Gippsland Basin – the folded and faulted Paleozoic basement and a deeper Neoproterozoic–Cambrian basement (separated by a Late Cambrian unconformity; Cayley et al., 2002) – and the syn-rift Lower Cretaceous Strzelecki Group cover rocks that unconformably overlie the basement. The following sections provide a brief overview of the geology and structural trends within these three units.

4.2.1. Cretaceous cover rocks

Rocks of the Lower Cretaceous Strzelecki Group are exposed in cliffs and wave-cut platforms along the coastline near San Remo and in the Cape Paterson area (**Figure 4.3**). These outcrops comprise alternating layers of mud-dominated and sand-dominated siliciclastic rocks with conglomeritic or organic matter-rich interbeds, which were deposited in a fluvial setting (Constantine, 2001). Dip angles of bedding are low, varying between 6° and 26° (Aghaei et al., 2017). High-angle changes in the strike of bedding occur across faults, some of which extend seawards beyond the wavecut platforms, where they can be interpreted from bathymetry data (Samsu et al., 2019). NW-SE to NNW-SSE trending dolerite dikes of Cretaceous age (Constantine, 2001; Duddy and Green, 1992; Samsu et al., 2019) crosscut the Strzelecki Group.

4.2.2. The Paleozoic basement

The western onshore part of the Gippsland Basin is underlain by Paleozoic rocks of the Melbourne Zone of the Lachlan Orogen, while the eastern onshore and offshore parts lie above the Tabberabbera Zone (VandenBerg et al., 2000) (**Figure 4.1a**). The Tabberabbera Zone comprises Cambrian–Ordovician turbidites that underwent low-grade metamorphism in the Late Ordovician to Early Silurian. The onshore Tabberabbera Zone rocks are characterized by NW-SE to E-W trending, upright to inclined, angular to chevron folds (Gray et al., 1998). The main Gippsland Basin rift trend above this basement is also NW-SE to E-W (**Figure 4.1b**).

The Melbourne Zone is bound to the west by the west-dipping Heathcote and Mount William faults, which separate it from the Bendigo Zone, and to the east by the east-dipping Governor Fault, separating it from the Tabberabbera Zone (VandenBerg et al., 2000). It is characterized

by Lower Silurian to Middle Devonian turbidites of the Murrindindi Supergroup, which were folded and underwent lower greenschist facies metamorphism during the Middle Devonian Tabberabberan Orogeny (VandenBerg et al., 2000). This metamorphism resulted in locally developed axial planar cleavage.

Rift-related faults in the Gippsland Basin overlying the Melbourne Zone basement trend NE-SW and ENE-WSW (**Figure 4.1b**). Major faults and fold axial traces in the Melbourne Zone basement trend predominantly NNW-SSE as a result of folding and thrusting associated with E-W shortening (VandenBerg et al., 2000). An exception to this structural trend is the northern part of the Melbourne Zone, where E-W trending faults and fold axial traces may indicate an episode of N-S shortening that postdates the E-W shortening (VandenBerg et al., 2000). In southern Victoria, a large portion of the Melbourne Zone is mostly covered by Cretaceous to recent sediments of the Gippsland Basin, so that the basement has not been mapped in the same detail as in the north. However, a NNE-SSW structural trend can be observed in Ordovician rocks that crop out on the Mornington Peninsula and Devonian rocks that are exposed at Cape Liptrap (Cayley et al., 2002; Keetley et al., 2001; Vollgger and Cruden, 2016) (**Figure 4.3**).

Exposed Paleozoic faults trend NNE-SSW (Cayley et al., 2002; Gray et al., 1999), such as the Waratah Fault, Bell Point Fault, and Selwyn Fault (**Figure 4.1**). The Waratah Fault, which is exposed along the southeastern side of Cape Liptrap, has been reactivated multiple times, up until the Holocene (Gardner et al., 2009). The seismically active Selwyn Fault follows the western margin of the Mornington Peninsula (**Figure 4.3**) (Cayley et al., 2002; Willcox et al., 1992). Because of the high contrast in the magnetic characteristics of the rocks on either side of the Selwyn Fault, and the length of the fault, it is interpreted that this structure links down into older faults in the Neoproterozoic–Cambrian basement that were active during the Cambrian Tyennan Orogeny (Cayley et al., 2002). The spacing between these deep crustal faults is relatively wide – for example, the Waratah Fault and Selwyn Fault are ~100 km apart.

4.2.3. The Neoproterozoic–Cambrian basement

The Paleozoic Melbourne Zone unconformably overlies the Neoproterozoic–Cambrian Selwyn Block (Cayley et al., 2002; McLean et al., 2010) (**Figure 4.1**). Folds in the Melbourne Zone, which formed during the Tabberabberan Orogeny, have longer wavelengths and lower amplitudes than those in the adjacent zones, to the west and east, respectively. Therefore, it has been inferred that the underlying Selwyn Block is more rigid than the surrounding lower crust and that it shielded the Melbourne Zone from extensive deformation (VandenBerg et al., 2000).

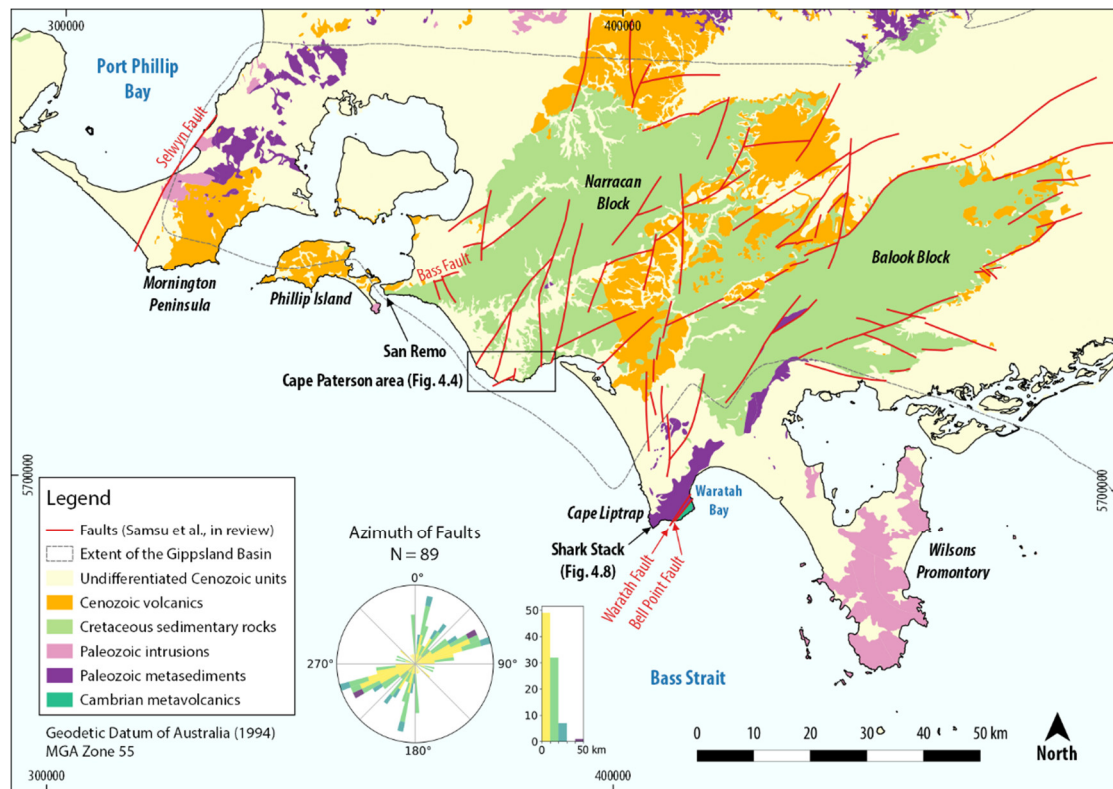


Figure 4.3 Map of basin-scale (>1 km-scale) faults interpreted from magnetic and gravity data (modified after Samsu et al., 2019). The rose diagram of fault traces was created using the GeoTrace plugin (Thiele et al., 2017) in QGIS and is coloured by fault length. Colours on the rose diagram correlate with fault length bins shown on the length histogram.

The Selwyn Block comprises metasedimentary and metavolcanic rocks of Neoproterozoic-Cambrian age that were accreted onto the Lachlan Orogen between 460 Ma and 370 Ma and previously deformed during the Late Cambrian Delamerian Orogeny (Cayley, 2011). The Cambrian minimum age for regional deformation is defined by an unconformity above Selwyn Block rocks, which crop out at several locations, including at Cape Liptrap (Cayley et al., 2002; VandenBerg et al., 2006). The Selwyn Block comprises several lithological and structural units, as indicated by N-S to NNE-SSW trending magnetic anomalies. The northern part of the block underlying the Melbourne Zone is subdivided into three zones: the westernmost King Island Zone, the central Rocky Cape Zone/Smithton Basin, and the eastern Burnie Zone. All of these zones have different lithologies with different magnetic characteristics, as described in detail in Moore et al. (2016). In south-central Victoria, the boundary between the King Island Zone and the Rocky Cape Zone/Smithton Basin is a steeply SW-dipping, NW-trending unnamed fault that displaces Devonian rocks against Cambrian rocks (Moore et al., 2016), which has been interpreted as a Cambrian fault that underwent reactivation during the Tabberabberan Orogeny (ca. 380 Ma) (Gray and Willman, 1991). The eastern boundary of the Selwyn Block and internal fabrics trend NE-SW (**Figure 4.1**).

4.3. Methods

A multi-scale structural mapping approach was employed across the western onshore Gippsland Basin study area in order to identify correlations between structures in basement and cover rocks. In this study, “fractures” include shear fractures and joints, all of which form when rocks fail in a brittle manner. The term “fault” is used to describe a zone comprising linked segments of shear fractures when the individual shear fractures cannot be recognized at the scale of observation. “Fracture zone” is used for areas of intensely fractured rock, which in wavecut platforms have typically been eroded. The term “joint” is used to describe a fracture that exhibits no offset along its length at the scale of observation. Fractures are considered systematic when they are parallel or sub-parallel or are regularly distributed, hence a fracture set consists of parallel to sub-parallel systematic fractures. Irregularly oriented fractures that demonstrate no obvious spatial relationship to one another are considered to be non-systematic.

Structures in basement rocks at the Shark Stack locality (Cape Liptrap; see **Figure 4.3** for location) were interpreted from field observations, with the help of orthophotos generated from aerial photographs collected from an unmanned aerial vehicle (UAV) (Vollgger and Cruden, 2019). Previous mapping of basin-scale (>1 km-scale) faults using gravity and magnetic data (Samsu et al., 2019), help to constrain general structural trends and distinguish between pre-rift and syn-rift structures in the basement. Fractures in cover rocks in the Cape Paterson area (see **Figure 4.3** for location) were interpreted semi-automatically from UAV orthophotos, which facilitated rapid collection of data on thousands of fractures over a wide area at high spatial resolution. Here we introduce the workflow used for collecting fracture data and for evaluating trends in the orientation of fracture traces.

4.3.1. Semi-automated fracture tracing

UAV-derived orthophotos of outcrops enabled the collection of fracture data at five outcrop localities (**Figure 4.4** and **Figure 4.5**) over a total area of ~ 0.934 km². These orthophotos are suitable for evaluation of fracture variability and clustering across a wide area using the areal sampling method (as defined by Watkins et al., 2015). As the individual mapped areas were relatively large (up to 0.330 km²), the likelihood for sampling bias at each map locality – which can be problematic when fracture patterns change with position (Rohrbaugh et al., 2002) – could be reduced. For a summary of the UAV photogrammetry workflow and the parameters chosen for the UAV surveys, see Table A1 in Appendix 2 (cf. Dering et al., 2019).

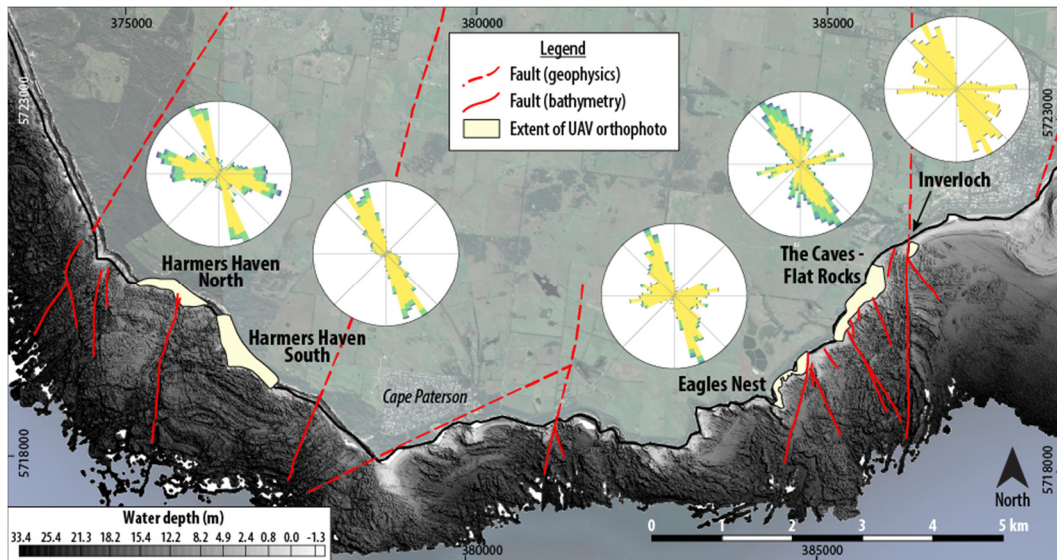


Figure 4.4 Map of the UAV photogrammetry survey areas, where outcrop-scale fractures in the Lower Cretaceous Strzelecki Group were traced, overlain on a greyscale image of near-shore bathymetry (modified after Samsu et al., 2019). The frequency of the orientations of fracture traces from each area is visualized as length-coloured rose diagrams. Colours correspond to fracture length, subdivided into 10 m bins (see **Figure 4.5** for colour ramp of length bins). See **Figure 4.3** for location of map.

4.3.2. Fracture orientation analysis using length-coloured rose diagrams

Circular histograms, or rose diagrams, are common statistical plots for analysing the orientation distribution of fractures within a study area (e.g., Marchegiani et al., 2006; Munro and Blenkinsop, 2012; Lavenu et al., 2013; Healy et al., 2016). Unweighted rose diagrams are calculated without discrimination between fractures of different lengths. Weighted rose diagrams are typically calculated by weighting the influence of a fracture's orientation by the fracture length. An alternative to binned rose diagrams are Gaussian smoothed rose diagrams (e.g., Robin and Jowett, 1986), which are useful for accentuating trends in orientation data. While these existing variations of rose diagram types help to identify fracture orientation trends, none of them show the length of the fractures that make up each trend in a rose diagram.

In this study, we are interested in the contribution of fractures of different lengths to fracture orientation trends within each outcrop area. Our approach is concerned with whether fractures of different lengths develop different orientations preferentially, therefore testing for scale-dependence. Fracture traces that are relatively long are often straight, continuous joints that have not been offset by subsequent shear fractures. Alternatively, they can represent larger faults, where individual shear fracture segments cannot be recognized at the scale of observation, either due to the close spacing between segment tips or weathering along the fracture. Shorter fracture traces mostly represent joints, shear fractures, or non-systematic fractures.

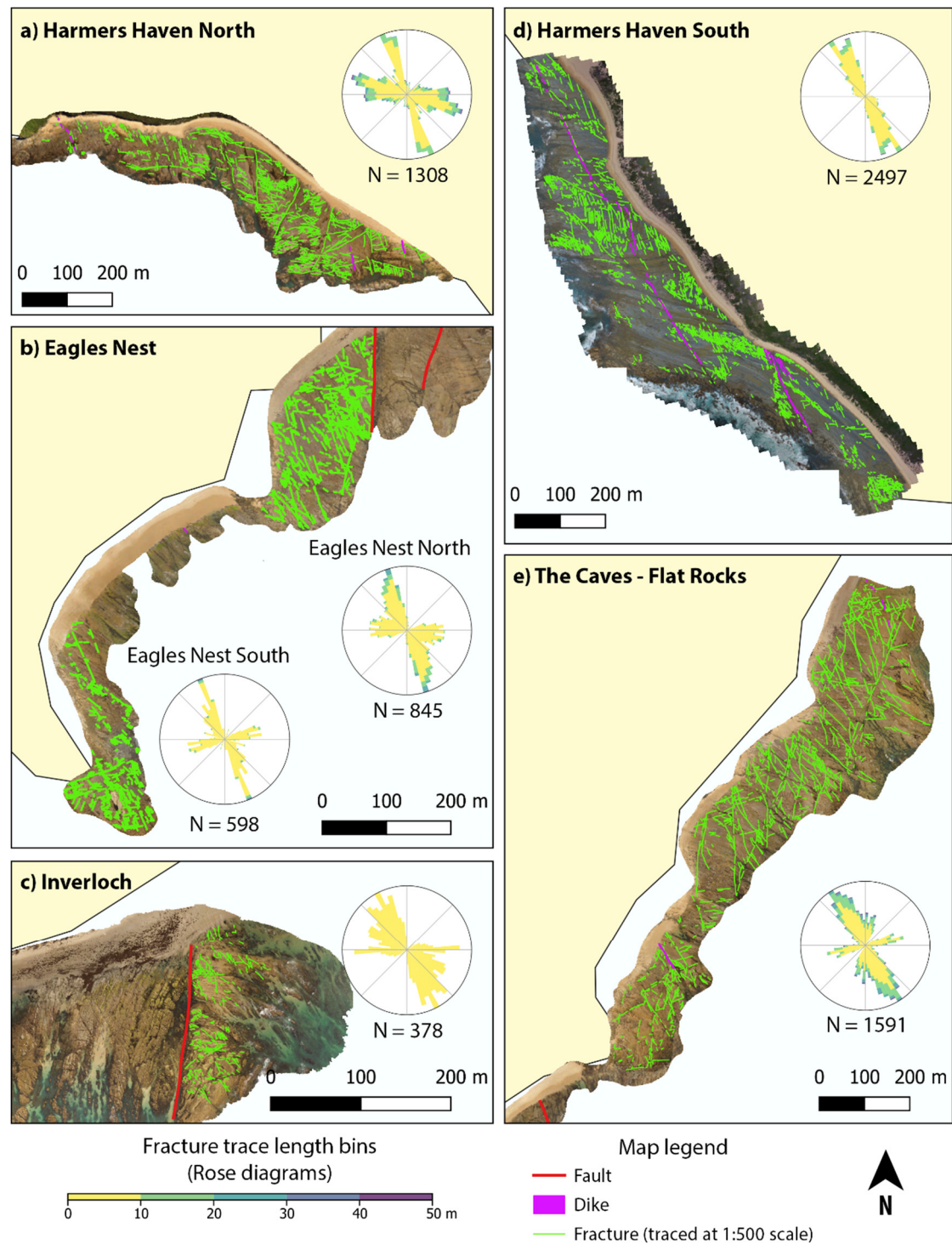


Figure 4.5 Fracture trace maps and rose diagrams, representing fractures <50 m in length, for the five studied outcrops (see **Figure 4.4** for locations). Fracture traces (interpreted at a scale of 1:500) are overlain on UAV orthophotos. Colours on the rose diagram correspond to fracture length, subdivided into 10 m bins.

Here we present a new technique for characterizing the trends in a fracture population, where the distribution of fracture lengths are plotted on an unweighted rose diagram to produce

“length-coloured rose diagrams.” These rose diagrams allow for a more comprehensive analysis of the fracture network, showing whether each peak orientation is associated with relatively “short” or “long” fracture traces. The petals of the rose diagram are subdivided into coloured segments that represent the percentage contribution of fractures within each length bin. This method has been implemented in the GeoTrace plugin for QGIS (QGIS Development Team, 2019; Thiele et al., 2017). Fracture orientations were compared between the five different outcrop localities (**Figure 4.4** and **Figure 4.5**). For each locality, all of the fractures that were traced at a scale (or ‘zoom’) of 1:500 (**Figure 4.6**) were treated as one population, resulting in one rose diagram per locality.

4.3.3. Fracture orientation analysis using gridded rose diagrams

A second analysis was performed to assess the heterogeneity of fracture patterns within individual outcrop localities, as there is usually significant variation in fracture density or orientations even within a small area. For the Harmers Haven North locality (see **Figure 4.4** for location), fractures were traced manually at a scale of 1:500. Grid tiles with 100 m by 100 m dimensions were overlain onto the fracture trace map, and a length-weighted binned rose diagram (with 10°-wide bins) was generated for the fracture trace segments in each grid tile, resulting in one rose diagram per grid tile (**Figure 4.7**). Grid tiles that contained less than 30 fracture trace segments were excluded from the analysis. This technique is implemented in the Line Direction Histogram plugin (Tveite, 2015) for QGIS. This method allowed us to test the consistency of fracture orientations throughout an outcrop. It also assisted in determining whether clustering or anomalous fracture patterns in a given locality are associated with changes in lithology, structural style, or other factors.

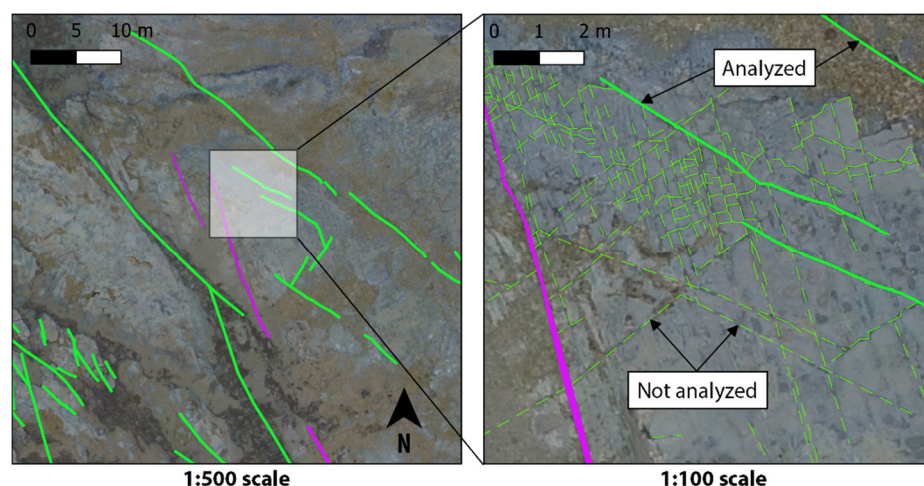


Figure 4.6 Fracture traces (green) interpreted from UAV orthophotos at 1:500 and 1:100 zoom levels. Fractures that can be seen at the 1:500 scale (thick, continuous lines) were included in the analyses of fracture orientations, so that we only compare fractures between outcrops that are observable at the same scale. Purple traces represent mafic dikes.

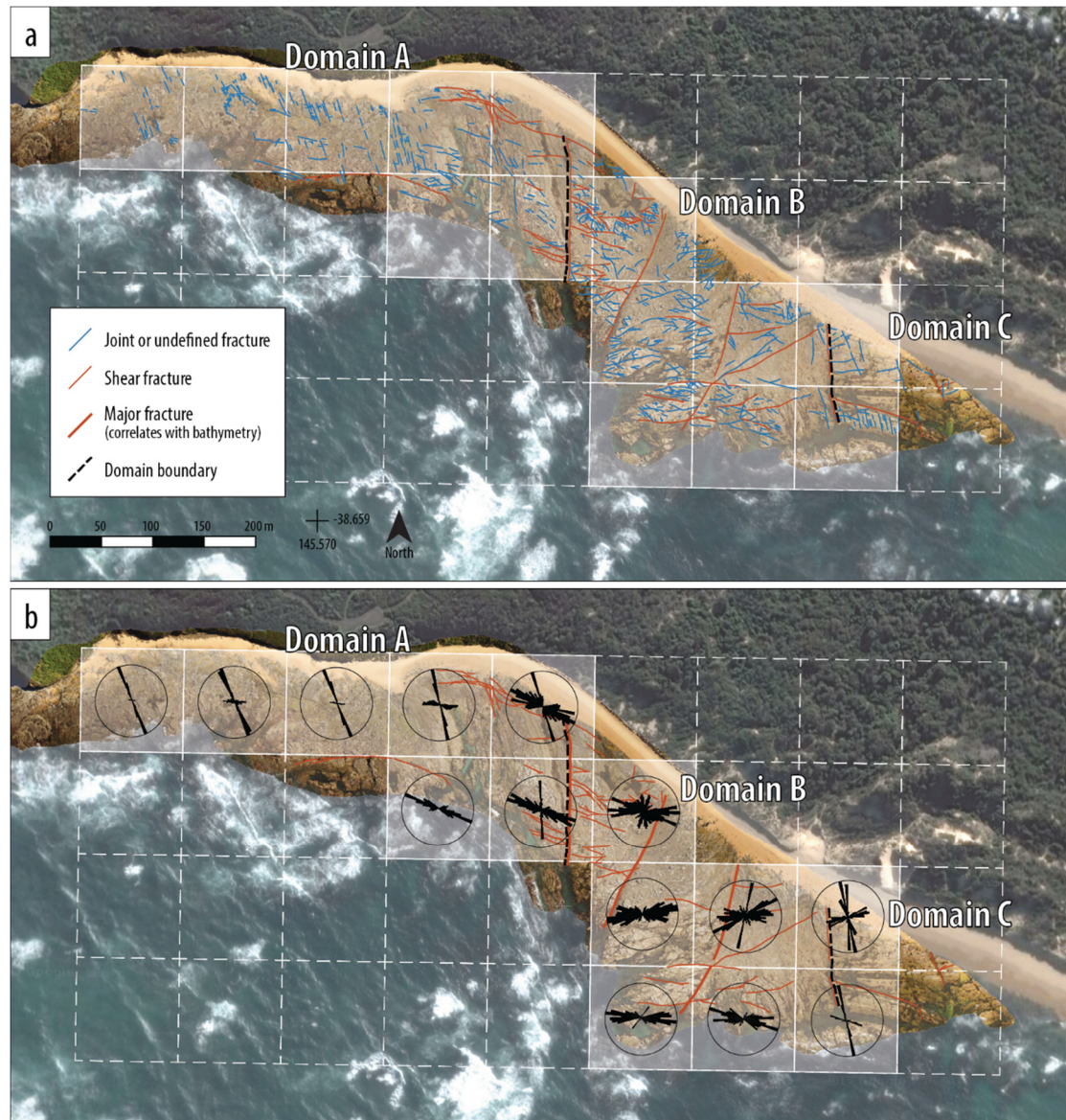


Figure 4.7 (a) Fracture trace map of the Harmers Haven North locality. The basemap is a high-resolution (3 cm/pixel) UAV orthophoto. A grid made up of 100 m x 100 m tiles is overlain on the orthophoto. (b) Length-weighted rose diagrams of fracture trace orientations calculated for each tile using the Line Direction Histogram plugin (Tveite, 2015) in QGIS. The background is a satellite image (source: Google Earth, 38.657362° and 145.572051°, May 14, 2016, accessed July 30, 2017).

4.4. Results

4.4.1. Structural characteristics of basement rocks (Cape Liptrap)

The Shark Stack outcrop is located near the southwestern tip of Cape Liptrap (**Figure 4.8**). Here, tightly folded turbidites of the Devonian Liptrap Formation are exposed on wavecut platforms and steep, SSW-facing cliffs (**Figure 4.9**). The rocks comprise steeply dipping, alternating beds of sandstone and mudstone, and they exhibit a first-order NNE-SSW structural

trend in map view (**Figure 4.8c**). The sequence of ductile and brittle deformation inferred for the Shark Stack locality is summarized in **Table 4.1**, interpreted using observations acquired from both field and UAV-based mapping of structures.

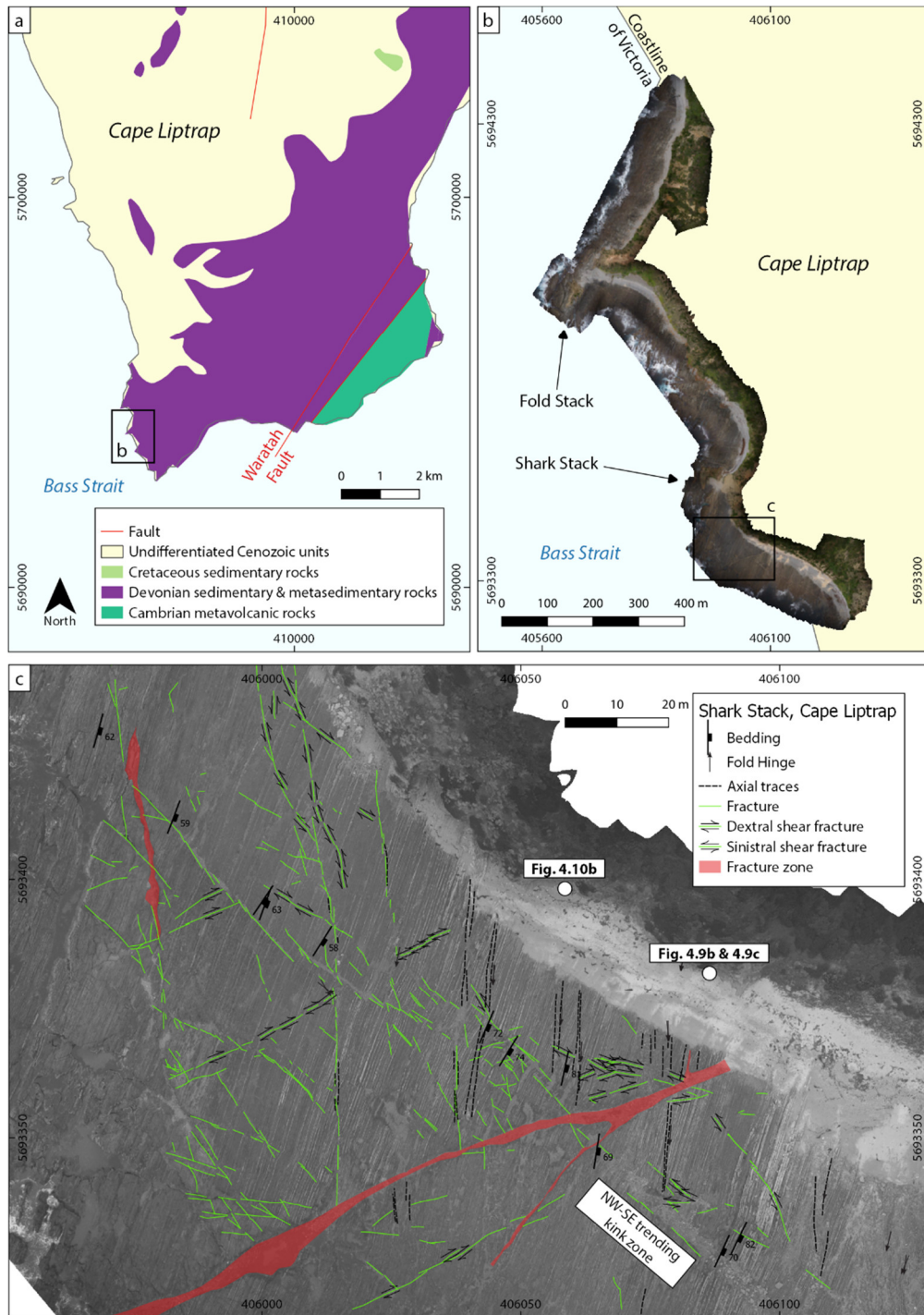


Figure 4.8 (a) Location of Shark Stack study area at the southwestern end of Cape Liptrap (see **Figure 4.3** for location), where a UAV orthophoto (b; 2 cm/pixel) was used as a basemap for structural mapping in the field. Structures at the Fold Stack locality have been described in detail in Vollgger and Cruden (2016). (c) Map of fractures, axial traces of folds, and structural measurements at Shark Stack. All of the fractures that are visible at a 1:500 scale are shown.

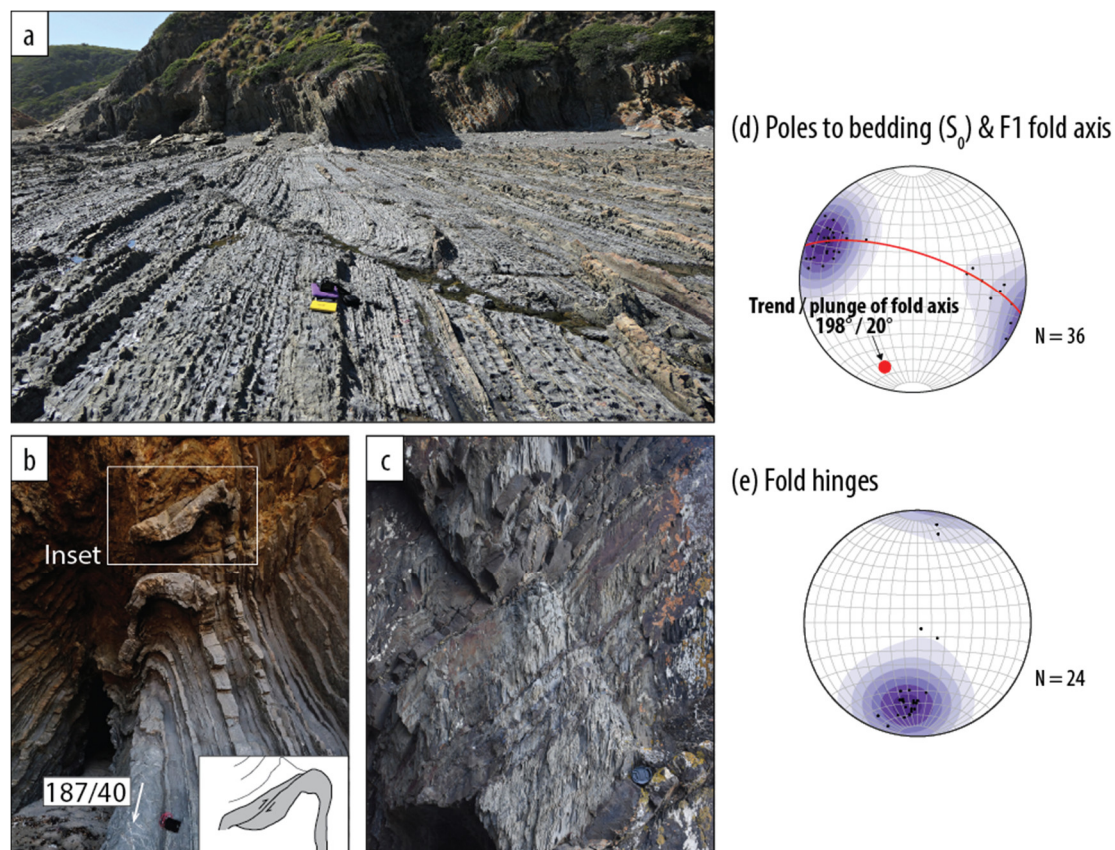


Figure 4.9 Structures at Shark Stack, Cape Liptrap: (a) Photograph of steeply dipping, alternating beds of sandstone and mudstone cropping out on a horizontal wavecut platform and along vertical cliff faces. These rocks form the Devonian basement underlying the onshore Gippsland Basin. (b) Photograph of disharmonic second-order F2 folds exposed in a cliff face. The inset shows a fold accommodation fault offsetting a sandstone bed in a reverse sense near the fold hinge. The arrow indicates the measured orientation of the hinge line. (c) Photograph of axial planar cleavage and parasitic folds on the limb of an F1 fold. All photographs were taken facing NNE. (d) Plot of poles to bedding measurements and the axis of a first-order F1 fold calculated from bedding measurements. The calculated fold axis is consistent with the orientation of the measured axial planar cleavage, which is orthogonal to the fold axis. (e) Plot of measured fold hinges; shallowly plunging fold hinges are F2 fold hinges associated with a D2 contractional event. All measurements are plotted on equal area lower hemisphere stereonet.

The strike of bedding in the fold limbs is predominantly NNE-SSW, with beds dipping steeply to sub-vertically towards the ESE and WNW (**Figure 4.9d**). The fold axis calculated from bedding measurements (from across the entire outcrop) trends 198° and plunges 20° , which represents the fold axis of the first-generation F1 folds at this locality. This fold axis is consistent with the F1 fold axis reported for the southern part of Fold Stack (201/11; Vollgger and Cruden, 2016). A steeply ESE-dipping to sub-vertical, axial planar cleavage is recorded in the mudstone units at the eastern end of the Shark Stack outcrop (**Figure 4.9e**), suggesting that local shortening was WNW-ESE. We interpret the F1 folds in the area to be related to ~E-W

shortening associated with the Devonian Tabberabberan Orogeny (385 – 380 Ma; VandenBerg et al., 2000). Reverse faults with a low strike angle to bedding offset sandstone beds, while associated strain is accommodated by ductile deformation of the mudstone layers.

The Shark Stack outcrop contains N-S trending zones of intensely folded beds (**Figure 4.10**). In map view, these structures appear to be either reverse kink bands or disharmonic folds (**Figure 4.10a**), though in side view (along subvertical cliffs) they appear exclusively as disharmonic folds (**Figure 4.10b**). Kink band formation in some zones has progressed to chevron folding. Similar “kink-folds” have been observed in shale-rich outcrops at the southernmost tip of Cape Liptrap, ~800 m southeast of Shark Stack. Axial traces of folds within these zones, mapped on the UAV orthophoto, trend predominantly N-S (**Figure 4.10a**), oblique to the first-order F1 fold axis. Fold hinges plunge mostly to the south (**Figure 4.9f**), consistent with axial traces mapped on the 2D dataset. We attribute these second-order F2 folds to a separate D2 folding event associated with NNE-SSW compression, sub-parallel to the strike of bedding. This interpretation is based on analogue experiments and field examples of kink bands in anisotropic media, which suggest that reverse kink bands result from local shortening parallel to the anisotropy (e.g., Cobbold et al., 1971; Stubbley, 1989). It is also supported by the results of mechanical experiments on pearlitic steel (Kapp et al., 2016) (**Figure 4.10c**). Pearlitic steel contains lamellar anisotropies, like the turbidites at Shark Stack, but at the micro and nano-scale. Kapp et al. (2016) show that kink bands form when loading is parallel to the orientation of the lamellae, and strain is initially accommodated (after 5% total strain) by local buckling of the harder cementite phases, which are analogous to the more competent sandstone units in our field example. Progressive deformation results in further localized bending of the layers and eventually the formation of fold accommodation faults near the fold hinges, which offset the sandstone beds in a reverse sense (**Figure 4.9b**).

Table 4.1 Summary of the sequence of ductile and brittle deformation at Shark Stack. The orientation of the trace of the structure on aerial imagery, the sense of movement along the horizontal, and the inferred orientation of the maximum horizontal principle stress (σ_H) are included.

Event	Structures	Trace Azimuth	Sense of Movement	Regime	σ_H Orientation
D1	F1 folds	NNE-SSW 3 - 37°		Contraction	WNW-ESE
D2	F2 folds	N-S 355 - 15°	Dextral	Contraction	NNE-SSW
D3	Fractures	ENE-WSW 50 - 75°	Dextral	Extension	ENE-WSW
D4	F4 kinks	NW-SE 310 - 320°	Dextral	Contraction	NNW-SSE
D4	Fractures	NNW-SSE 315 - 360°	Sinistral	Contraction	NNW-SSE

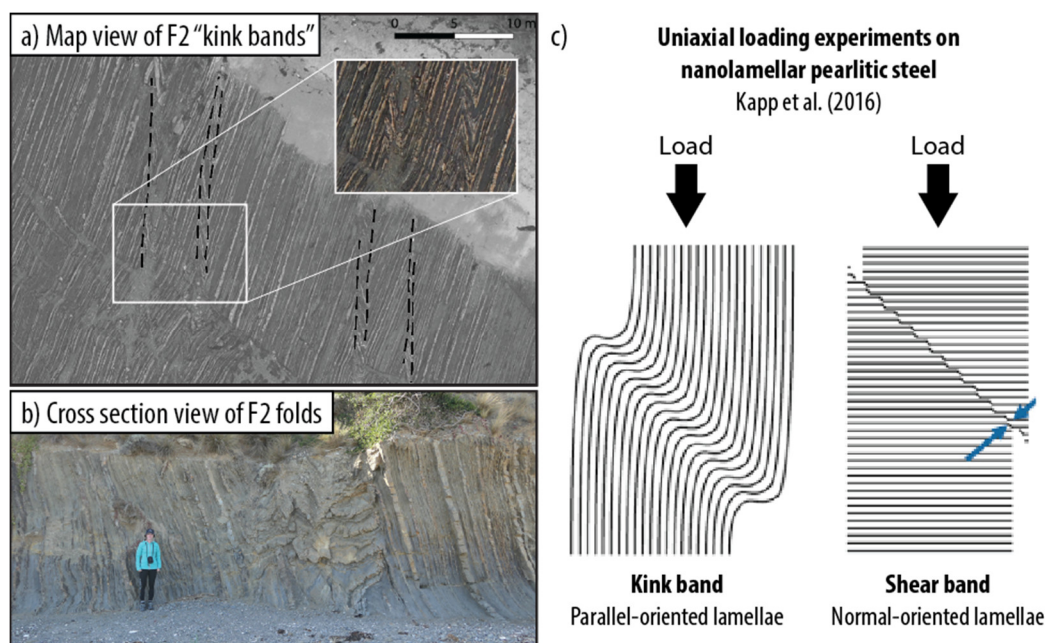


Figure 4.10 N-S trending zones of kinking in the wavecut platform (a) and cliff (b). Axial traces of folds are marked by the dashed lines. Kink bands at Shark Stack are analogous to kink bands in nanolamellar pearlitic steel (c) (Kapp et al., 2016).

Our interpretation of these broadly N-S trending tightly folded zones disagrees with the previous interpretation that the N-S trending fracture set at Fold Stack formed as tensile fractures as a result of N-S shortening (Vollgger and Cruden, 2016). Based on observations at Shark Stack, it is more likely that the N-S trending fractures at Fold Stack are shear fractures that formed at an acute angle to NNE-SSW directed compression during late stages of kink band development. However, field evidence for both N-S to NNE-SSW compression – including E-W trending folds, north-dipping reverse faults, and steeply dipping, E-W striking axial planar cleavage – at a later stage of the Tabberabberan Orogeny (following E-W compression) has also been found in the northern part of the Melbourne Zone (Gray and Mortimer, 1996; Wilson et al., 2017).

ENE-WSW trending dextral shear fractures and a larger fracture zone of the same orientation (**Figure 4.8c**) is attributed to a D3 brittle deformation event. Like the ENE-WSW trending fracture set at Fold Stack (Vollgger and Cruden, 2016), this set is parallel to Early Cretaceous rift-related normal faults within the Lower Cretaceous Strzelecki Group (Samsu et al., 2019). They are the only structures at Shark Stack that can be associated with Early Cretaceous Gippsland Basin rifting, although parallelism with Early Cretaceous rift-related faults is not a definitive age constraint.

A D4 deformation event is associated with a NW-SE trending kink band zone that extends across the middle and along the length of the entire Shark Stack outcrop, overprinting F2 kink

bands (**Figure 4.8c** and **Figure 4.10**). In this <3.3 m wide zone, the local sense of shear is dextral, and the kinks offset the sandstone and mudstone layers laterally by <1 m. Smaller, less developed kink bands of the same orientation are also present. A NNW-SSE trending set of sinistral shear fractures occurs in the northwest section of the outcrop (**Figure 4.8c**). The acute bisector between the F4 kink bands and the NNW-SSE fractures is $\sim 30^\circ$. Based on the orientation and kinematics of the F4 kink bands and the NNW-SSE trending fracture set, we interpret them as conjugate structures that formed during a phase of NNW-SSE directed D4 shortening.

The relative timing of D3 fractures and D4 kinks is ambiguous – the large ENE-WSW trending fracture zone potentially offsets NW-SE trending kink bands in the orthophoto (**Figure 4.8c**), but the amount of weathering in this part of the outcrop makes it difficult to confirm this. As the two sets are orthogonal to each other and both exhibit a dextral sense of movement, they cannot have formed coevally.

Most of the NW-SE trending structures at Shark Stack that were mapped using the UAV orthophoto are short F4 kink bands (<10 m in length) (**Figure 4.11**). Longer fractures (>10 m) are associated with NNW-SSE and ENE-WSW trending fracture sets. These fractures are relatively young D3 and D4 structures compared to pre-rift D1 and D2 structures and show high lateral continuity because they have not been overprinted by younger structures.

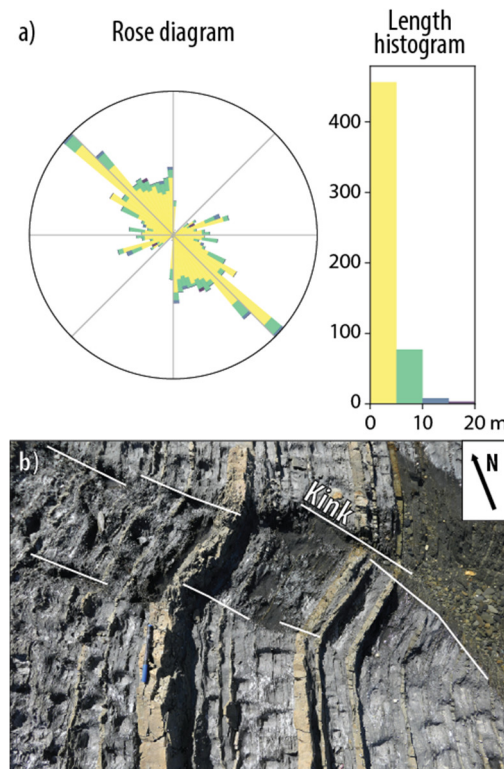


Figure 4.11 (a) Length-coloured rose diagram of outcrop-scale fractures at Shark Stack. (b) The NW-SE trending peak represents a large population of kinks that make up the NW-SE trending F3 kink bands.

The length-coloured rose diagram allows us to assign fractures of different length ranges to certain orientation trends. NW-SE kinks are <10 m in length, most of them being shorter than 5 m. Fractures that are longer than 10 m trend NNW-SSE and ENE-WSW.

4.4.2. The orientation of fractures in cover rocks (Cape Paterson area)

Fracture orientation trends in the Strzelecki Group cover rocks in the Cape Paterson area (see **Figure 4.3** for location) are presented as rose diagrams (**Figure 4.4** and **Figure 4.5**) and summarized in **Table 4.2**. Here we describe fracture orientations at five outcrop localities – Harmers Haven North, Harmers Haven South, Eagles Nest, the Caves – Flat Rocks, and Inverloch – and use peaks in the data to classify fracture traces into fracture sets. We also use overprinting relationships between fracture traces in the UAV orthophotos and field observations to identify the type of fractures that make up each fracture set.

The predominant trend at Harmers Haven North is NNW-SSE (335–350°) (**Figure 4.5a**). This fracture set comprises linear, systematic joints that are parallel to – and are potentially exploited by – NNW-SSE trending mafic dikes. We observe two other peaks in the data for this locality: WNW-ESE (280–295°) and E-W (80–100°), which correspond to shear fractures. These two sets are more prevalent in the central part of the outcrop, while the NNW-SSE trending set is more dominant in the western and eastern parts of the outcrop. Seven of the longer (>30 m) fracture traces at this locality are N-S to NNE-SSW trending faults across which the strike of bedding changes significantly. Despite their prominence in the fracture trace maps, these fractures are underrepresented in the non-length-weighted, length-coloured rose diagram (**Figure 4.5a**). A more detailed discussion of the spatial variability of fracture trends at Harmers Haven North (**Figure 4.7**) is presented below.

At Harmers Haven South, one wide peak in the rose diagram is present, trending NNW-SSE (325–345°) (**Figure 4.5d**). The NNW-SSE fracture set consists mostly of joints, some of which are exploited by NNW-SSE trending mafic dikes at the northern end of the outcrop. Faults trend NW-SE and some of them are also exploited by NW-SE trending mafic dikes.

The Eagles Nest locality was split into a southern and northern area (**Figure 4.5b**). The rose diagram of fracture traces in both areas combined show a dominant NNW-SSE (325–345°) peak. The second most dominant trend is represented by a wide peak, trending ENE-WSW (65–80°) and E-W (80–95°). In the southern area, NNW-SSE and ENE-WSW trending systematic fracture sets, which are mutually crosscutting, are present near the Eagles Nest pinnacle. The ENE-WSW trending normal fault slightly north of the pinnacle is associated with Early Cretaceous rifting. A NE-SW trending fracture set is confined to a small area west of the pinnacle. In the northern area, a large N-S trending fracture zone bounds the Eagles Nest

locality to the east. The N-S trending fault truncates an ENE-WSW trending fault and the NNW-SSE fracture set to the west. The ENE-WSW trending fault is accompanied by clusters of steeply-dipping deformation bands that are parallel to the main slip surface, similar to normal rift-related faults in the Caves – Flat Rocks area (Samsu et al., 2019). The significant rotation of sedimentary beds across this fault and the syn-sedimentary nature of ENE-WSW trending normal faults in the area (Samsu et al., 2019) suggests that the N-S fault postdates ENE-WSW normal faulting.

At the Caves – Flat Rocks, the main peak in the rose diagram corresponds to NNW-SSE (320–345°) trending shear fractures (**Figure 4.5e**). The second-most dominant peak is associated with ENE-WSW (65–85°) trending fractures, some of which are normal faults associated with Early Cretaceous rifting. ENE-WSW trending faults at the Caves exhibit up to 5 m dip-slip displacement and exhibit a dense network of subvertical deformation bands characteristic of Early Cretaceous normal faults in the Cape Paterson area (Samsu et al., 2019; also see Section 3.4.2). A third, less dominant NNE-SSW (10–20°) trend is made up of shear fractures. ENE-WSW trending faults are offset by NNW-SSE and NNE-SSW trending shear fractures, which may explain why this fracture set has the highest percentage of shorter (<10 m) fractures relative to their frequency. Kinematic indicators (i.e., slickenlines, dip-slip displacement) along ENE-WSW trending fractures allow us to discount the possibility that they are joints that abut against and therefore postdate NNW-SSE and NNE-SSW trending shear fractures.

Table 4.2 Fracture trends in Lower Cretaceous Strzelecki Group outcrops based on length-coloured rose diagrams (**Figure 4.5**). $N_{L \leq 50m}$ = total number of fracture traces at each locality with a length ≤ 50 m; N_{Trend} = number of fracture traces belonging to the corresponding trend.

Locality	$N_{L \leq 50m}$	Trend Azimuth		N_{Trend}
Harmers Haven North	1308	NNW-SSE	335 - 350°	267
		WNW-ESE	280 - 295°	246
		E-W	80 - 100°	259
Harmers Haven South	2497	NNW-SSE	325 - 345°	1055
Eagles Nest	1443	NNW-SSE	325 - 345°	404
		ENE-WSW	65 - 80°	180
		E-W	80 - 95°	188
The Caves - Flat Rocks	1591	NNW-SSE	320 - 345°	522
		ENE-WSW	65 - 85°	239
		NNE-SSW	10 - 20°	126
Inverloch	378	NW-SE to NNW-SSE	315 - 345°	141
		E-W	85 - 90°	27
		WNW-ESE to NW-SE	290 - 315°	86

The Inverloch locality is populated by fractures that are shorter than 20 m (**Figure 4.5c**). One sharp E-W trending peak (85–95°) and another sub-population of WNW-ESE to NNW-SSE (290–345°) trending fractures are represented in the rose diagram.

A common occurrence among the five described localities is the presence of a NNW-SSE trending fracture set, which mostly consists of sub-vertical joints. This joint set is interpreted to be a pervasive, regional outcrop-scale joint set that reflects Early Cretaceous shortening (Samsu et al., 2019), which postdates Early Cretaceous syn-rift normal ENE-WSW faulting and predates the Aptian intrusion of NW-SE and NNW-SSE trending mafic dikes in the study area. The formation of this joint set could also be coeval with reverse reactivation of the optimally oriented, aforementioned ENE-WSW trending normal faults, which agrees with an interpretation by Power et al. (2003) of similarly orientated compressional structures in the offshore Gippsland Basin.

4.4.2.1. Variability of fracture orientations within the Harmers Haven North locality

The Harmers Haven North outcrop was subdivided into three domains based on the main fracture orientations (**Table 4.2**; **Figure 4.7**). The western section of the outcrop (Domain A) exhibits a dominant NNW-SSE trending fracture set. Field observations confirm that this set is made up of joints, similar to the NNW-SSE trending fracture set at Harmers Haven South. Domain A also contains a single NNW-SSE trending dike that is parallel with the main joint set. A less prominent E-W trending fracture set is present in Domain A. The middle section of the outcrop (Domain B) does not exhibit a dominant fracture set. It contains a dense network of non-systematic shear fractures. Three of the NNE-SSW trending shear fractures in Domain B (represented by thick red lines in **Figure 4.7**) correspond to km-scale faults interpreted from near-shore bathymetry (**Figure 4.4**). The eastern section of the outcrop (Domain C) exhibits the same NNW-SSE joint set as observed in Domain A, although fractures of other orientations are also present.

4.4.2.2. Curved fractures at the Eagles Nest locality

The most dominant fracture set at Eagles Nest is the NNW-SSE trending set of up to 50 m long fractures (**Figure 4.12**). NNW-SSE trending fractures in the northern area curve eastwards into the N-S trending fracture zone. There is no evidence of shear along these NNW-SSE trending fractures, so they can be interpreted as joints, like the NNW-SSE trending joints at Harmers Haven North and Harmers Haven South (**Table 4.2**). The curved NNW-SSE joints at Eagles Nest are comparable with joints that “veer” from linearity (Cruikshank and Aydin, 1995) as they propagate into a changing stress field, which may result from stress perturbations near pre-existing structures. Photoelastic experiments on analogue materials (e.g., de Joussineau et al., 2003) demonstrate the deviation of stress trajectories near pre-existing defects (analogous to

faults in rocks) under a biaxial compressive load. Welch et al. (2014) discuss the development of local stress anomalies near tips, bends and splays in larger faults. At Eagles Nest, veering of the NNW-SSE joints would have resulted from the divergence of local maximum principal stress trajectories from the regional compression, which was due to local stress perturbations around the large N-S trending fracture zone.

4.4.3. Basin-scale fracture trends

The length-coloured rose diagram of regional fault traces shows that large, regional faults exhibit a range of trends between N-S and ENE-WSW (**Figure 4.3**). The interpretation of the timing of these faults and their orientations are outlined in Samsu et al. (2019). ENE-WSW trending faults are Early Cretaceous rift related faults that were reactivated during Early Cretaceous NNW-SSE directed compression, which was also responsible for NNW-SSE jointing at Harmers Haven and Eagles Nest. N-S to NNE-SSW trending faults crop out along the coast between Harmers Haven and Inverloch and appear as up to ~20 m wide fracture zones in near-shore bathymetry data (**Figure 4.4**). Similarities in their orientation and kinematics with pre-rift basement faults, such as the Waratah Fault and Selwyn Fault (Gardner et al., 2009; Gray et al., 1999; Samsu et al., 2019), suggest that they could have formed in association with reactivation of NNE-SSW trending basement fractures. For the purpose of this paper, we simply highlight that the orientation of regional faults in the onshore Gippsland Basin study area are different to the orientation of outcrop-scale fractures in both the basement and the cover rocks.

4.5. Discussion

4.5.1. The influence of multiple levels of basement on rift-related faults

The western onshore Gippsland Basin study area is underlain by two orders of basement, which likely had an impact on basin formation: the Paleozoic Melbourne Zone of the Lachlan Orogen and the Neoproterozoic – Cambrian Selwyn Block (**Figure 4.1**). Both levels of basement were subjected to multiple shortening events prior to Early Cretaceous rifting and opening of the Gippsland Basin, resulting in a first-order NNE-SSW structural trend (Cayley et al., 2002; Gray et al., 1999; McLean et al., 2010; Moore et al., 2016) that is oblique to subsequent Cretaceous rift-related structures.

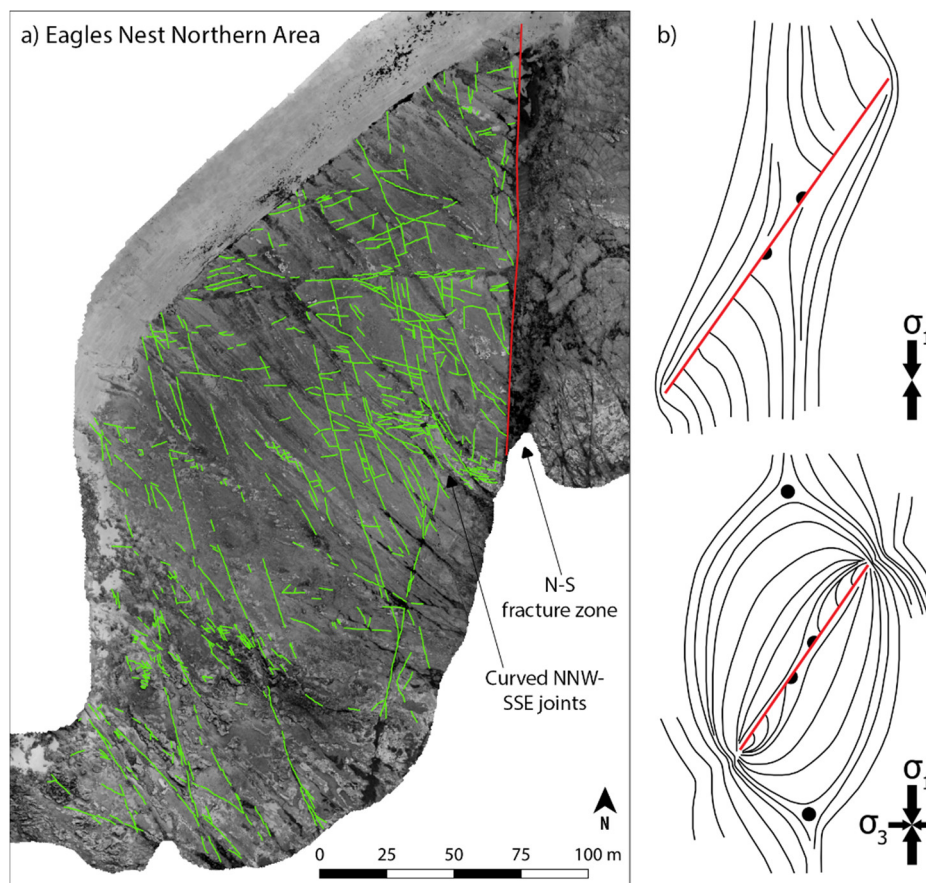


Figure 4.12 (a) Fracture traces at the northern part of the Eagles Nest locality, overlain on a high-resolution (3.2 cm/pixel) UAV orthophoto (See **Figure 4.4** for location). Veering of NNW-SSE trending joints in the vicinity of the large N-S trending fault is observed, which may be caused by perturbed stress trajectories around the larger fault. A similar phenomenon has been observed in photoelastic experiments of biaxial loading on analogue materials (b; modified from de Jossineau et al., 2003).

NNE-SSW trending faults in the Melbourne Zone formed as a result of roughly E-W shortening during the Devonian Tabberabberan Orogeny. Some of these faults, such as the Waratah and Selwyn faults, extend into the underlying Selwyn Block basement, so it has been suggested that reactivation of Selwyn Block faults exerted some control on Devonian deformation in the Melbourne Zone basement (Cayley et al., 2011) (A in **Figure 4.13a**).

Based on field observations of NNE-SSW trending D1 structures at Shark Stack and Fold Stack (Cape Liptrap; **Figure 4.9**), we infer that the Melbourne Zone underneath our study area exhibits a penetrative NNE-SSW trending anisotropy. The mechanical anisotropy created by alternating mudstone and sandstone units has the potential to locally perturb the far-field stress. Alternatively, relatively weak mudstone layers between competent sandstone layers may be prone to re-shearing when the crust is subject to later extension or compression. This anisotropy should have exerted a greater influence on regional faulting patterns in the cover compared to less pervasive, more localized fractures (B in **Figure 4.13a**).

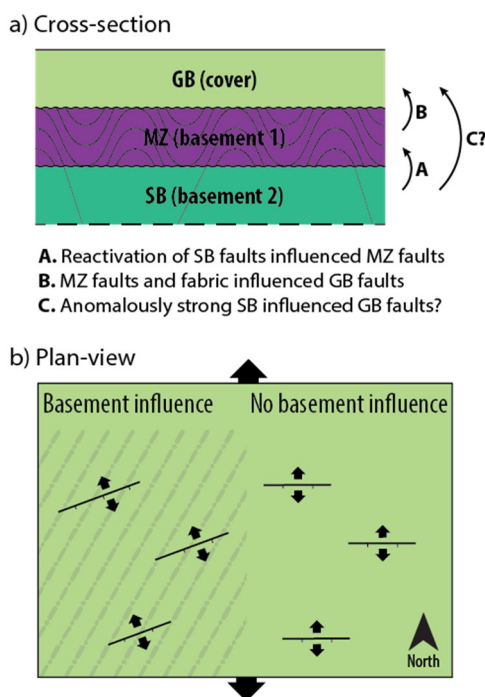


Figure 4.13 (a) Schematic cross section demonstrating the influence of different basement units on overlying units. Devonian faulting in the Melbourne Zone could have been controlled by the reactivation of pre-existing Cambrian faults in the Selwyn Block (A). The complex array of Early Cretaceous normal faults could have resulted from local stress re-orientation above Devonian faults and penetrative fabrics in the Melbourne Zone (B). It remains unclear how the relatively high strength of the Selwyn Block, juxtaposed against the weaker surrounding lower crust, could have affected Early Cretaceous rifting (C). GB = Gippsland Basin; MZ = Melbourne Zone; SB = Selwyn Block. (b) Schematic map-view illustration of normal fault orientations: They are oblique to the regional extension direction above an anisotropic basement, but they are orthogonal to regional extension where the basement is less influential.

The western onshore Gippsland Basin is populated by NE-SW and ENE-WSW trending syn-rift faults in the Early Cretaceous Strzelecki Group (Samsu et al., 2019; **Figure 4.3**). These faults formed oblique to the inferred N-S to NNE-SSW extension associated with the Early Cretaceous rifting of the Otway and Gippsland basins (Chantraprasert et al., 2001; Etheridge et al., 1985; Hill et al., 1994; K. C. Hill et al., 1995; Krassay et al., 2004; Miller et al., 2002; Norvick et al., 2001; Willcox et al., 1992). We infer the reason for this obliquity is the influence of the underlying anisotropic, heterogeneous basement (**Figure 4.13b**). The transition from NE-SW and ENE-WSW trending faults in the western onshore part of the basin to E-W and NW-SE trending faults in the eastern onshore and offshore parts (underlain by Ordovician – Silurian rocks of the Tabberabbera Zone) coincides with the postulated eastern margin of the Selwyn Block (and the overlying Melbourne Zone; Cayley et al., 2002) (**Figure 4.1**). The lower crustal Selwyn Block is inferred to be more rigid than the surrounding lower crust (Cayley et al., 2002; Teasdale et al., 2004), so that the Selwyn Block boundary separates an anomalously strong

lower crustal block from a ‘normal’ lower crustal block. However, it remains speculative whether the relatively high strength of the Selwyn Block, juxtaposed against weaker lower crust, would have resulted in the kinematics required to form ‘misoriented’ rift faults above the Selwyn Block (C in **Figure 4.13a**).

The variation in rift fault orientations could have resulted from rotated extension vectors above the Melbourne Zone/Selwyn Block basement during Early Cretaceous rifting, but this basement influence does not have to lead to the formation of cover fractures that are parallel to basement structures, which is the case with basement reactivation. Our observations are comparable with the results of field studies from northwestern Scotland (Wilson et al., 2010) and the East African rift system (Morley, 2010), where fracture orientations vary between areas that have different basement domains. Changes in fracture orientations are attributed to local re-orientation of the far-field, regional stress field above pre-existing basement fabrics that are oblique to the main rift trend (Morley, 2010), and direct reactivation of basement structures is not required for the basement to influence faulting in the cover in this way (Wilson et al., 2010).

4.5.2. Comparing outcrop-scale basement and cover structures

In general, outcrop-scale cover fractures in our study area have trends that are different to outcrop-scale basement fractures, with the exception of the ENE-WSW trending fracture set (**Figure 4.3** and **Figure 4.4**). D1 and D2 events recorded in basement rocks at Shark Stack – associated with WNW-ESE compression followed by NNE-SSW compression – are interpreted to have occurred prior to rifting, before the cover sediments were deposited (**Table 4.1**). These events led to the NNE-SSW trending strike of bedding and N-S trending axial traces of folds/kinks, respectively (**Figure 4.8c**). The D3 extensional event is represented by the ENE-WSW trending fracture set, which matches the ENE-WSW trending rift-related fractures in the cover (compare **Table 4.1** and **Table 4.2**). The D4 event, which is associated with a conjugate set of NW-SE trending kinks and NNW-SSE trending fractures, may reflect a NNW-SSE shortening event. NW-SE and NNW-SSE trending D4 fractures in the highly anisotropic basement rock may have resulted from the same NNW-SSE directed shortening which formed NNW-SSE trending joints in the relatively undeformed cover. The results of our comparison of basement and cover fractures shows that the same tectonic event can be reflected by differently oriented fracture trends in rose diagrams, perhaps due to differences in the mechanical anisotropy of the basement and cover rocks.

4.5.3 Comparing regional-scale faults with outcrop-scale fractures

Multi-scale mapping of fracture traces allowed us to compare the orientations of basin-scale (>1 km-scale) fractures with outcrop-scale (meters to tens of meters-scale) fractures. Rose diagrams of fracture traces at both scales show that the trends of outcrop-scale fractures that

formed due to shortening are different from the trends of basin-scale fractures (**Figure 4.14b**). Syn-rift normal faults, however, exhibit the same ENE-WSW trend at both basin scale and outcrop scale (**Figure 4.14a**). The latter observation could possibly be explained by the absence of additional fractures in our study area that are related to post-rift extensional events.

One persistent trend in the outcrop-scale fracture data is the NNW-SSE peak. This trend highlights the abundance and pervasiveness of a NNW-SSE trending subvertical joint set in the Strzelecki Group cover rocks across the entire study area. Samsu et al. (2019) have discussed the formation of this joint set under NNW-SSE directed maximum horizontal stress, coeval with a conjugate set of NNW-SSE and N-S to NNE-SSW trending strike-slip faults, which may coincide with Early Cretaceous (Aptian) basin uplift and the reverse reactivation of ENE-WSW rift faults (Holdgate et al., 2003; Power et al., 2003).

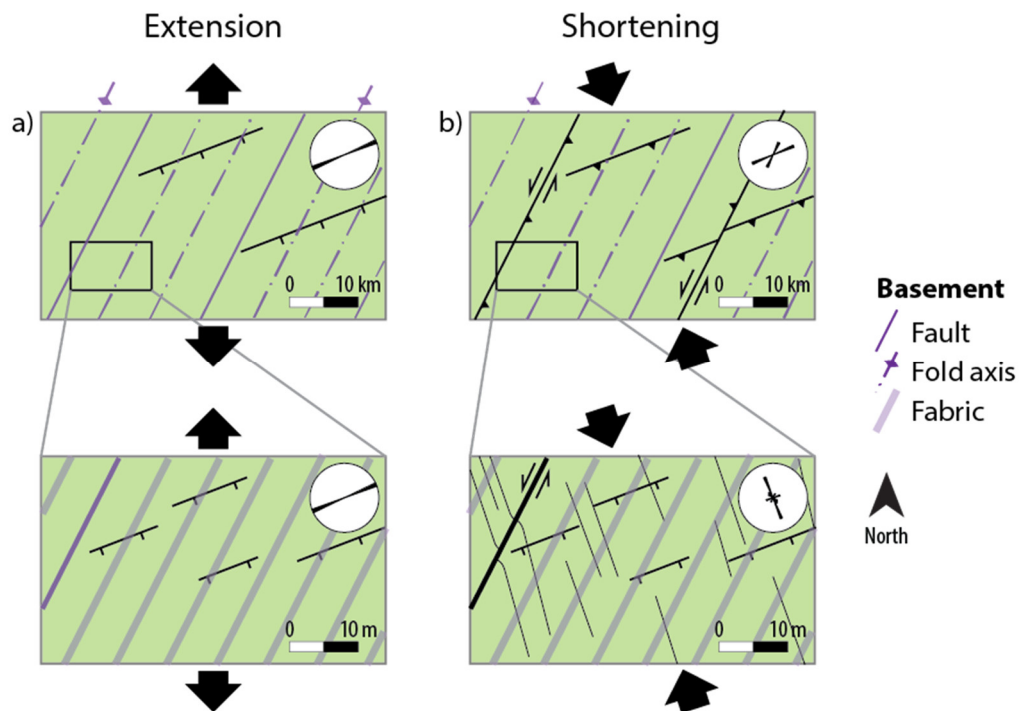


Figure 4.14 Plan-view schematic illustration of fracture traces in the cover – associated with Early Cretaceous extension (a) followed by shortening (b) – and their trends. The purple lines represent structures in the underlying Melbourne Zone basement. Extension-related fractures show the same ENE-WSW trend at basin scale (>1 km) and outcrop scale (meters-scale). During subsequent shortening, pre-existing basement structures and rift-related ENE-WW trending fractures are reactivated, so that new fractures are localized above or near reactivated structures at the basin scale. At outcrop scale, new sub-vertical joints formed parallel to the direction of shortening, though some joints veer towards larger, pre-existing faults.

The NNW-SSE trend is absent in the rose diagram for the basin-scale fracture traces (**Figure 4.3**). One explanation for this is that Early Cretaceous NNW-SSE directed shortening was accommodated, at a large scale, by reverse reactivation of ENE-WSW trending >1 km-long normal faults (**Figure 4.14b**), the formation of pop-up structures, and uplift of sub-basin blocks such as the Mornington High, the Strzelecki Ranges (Narracan Block), and the Hoddle Ranges (Balook Block) (**Figure 4.3**). NNW-SSE shortening could have also reactivated optimally oriented NNE-SSW trending basement faults in a strike-slip sense, which would explain the NNE-SSW fracture trend in the rose diagram for basin-scale faults (**Figure 4.14b**). At outcrop scale, NNW-SSE trending joints behave differently near large faults that either pre-date or are coeval with joint formation. At Eagles Nest, the joints veer into perpendicularity with a large N-S trending fracture zone that may have locally perturbed far-field stress trajectories. This joint set is absent adjacent to NNE-SSW trending faults at Harmers Haven North.

In fracture mechanics, the mode of fracturing is a function of the magnitude of the differential stresses (i.e., the diameter of the Mohr circle) and the effective confining pressure (i.e., the confining or lithostatic pressure minus the pore fluid pressure). Joints form under small differential stresses and low effective confining pressure, which are conditions of high pore fluid pressure. The orientation of small differential stresses may not be affected by distant or much deeper mechanical heterogeneities in underlying units, which can otherwise influence larger faults. Assuming that the NNW-SSE trending subvertical joint set reflects regional NNW-SSE directed compression in the Aptian, our results imply that outcrop-scale joints faithfully reflect the far-field regional stress during episodes of shortening, away from larger pre-existing faults. Basin-scale (>1 km-scale) faults, on the other hand, were forced to localize above optimally oriented reactivated faults, mimicking their orientation.

4.6 Conclusions

Pre-existing basement structures exert significant control on the orientation and distribution of fractures in the sedimentary cover rocks of a rift basin. However, this basement influence manifests itself differently at different scales. Inheritance does not always result in cover fractures that are parallel to basement structures, which is the case with basement reactivation. The mechanism for regional-scale inheritance in the western onshore Gippsland Basin is different to that of reactivation, where newly formed fractures in cover rocks are expected to be parallel to the reactivated basement structure. Instead, both basin-scale and outcrop-scale syn-rift faults in the western onshore Gippsland Basin are oblique to the basement trends as well as their expected orientation based on the known far field extension direction, suggesting that stresses above the basement structures were rotated such that faults in the cover rocks became misaligned to both their expected orientation and the basement anisotropy. This finding

should motivate us to explore and model the mechanisms of structural inheritance, other than reactivation, through additional field-based studies as well as analogue and numerical experiments.

When attempting to understand the influence of structural inheritance on deformation in a rift basin, it is important to consider not just the basement that directly underlies the sedimentary cover, but older, deeper basement units as well. When multiple levels of basement are present, it is challenging to distinguish the relative contributions of pre-existing structures from each basement unit. In the western onshore Gippsland Basin study area, widely-spaced faults in the deeper Neoproterozoic – Cambrian Selwyn Block basement were reactivated during Devonian deformation of the shallower Melbourne Zone basement. Because these faults appear to have been reactivated again during subsequent, post-rift deformation of the cover rocks, it is evident the Selwyn Block basement faults influence structural geometry over multiple tectonic events, albeit at a large scale. The pervasive anisotropy of the Melbourne Zone may have exerted a greater control than the Selwyn Block faults on more closely-spaced fractures (e.g., Cretaceous rift-related normal faults). It is therefore important to map structures in all of the basement units, at multiple scales, to explore the possibility of different wavelengths of basement influence.

Our findings demonstrate that structural inheritance leads to fracture patterns that are not scale-invariant. Pervasive outcrop-scale NNW-SSE joints are faithful recorders of a major regional shortening event, which is expressed at basin scale in reverse reactivated ENE-WSW optimally oriented faults. In basins that have been influenced by structural inheritance, a proper understanding of the structural architecture can only be achieved by analysing data that span multiple scales. This insight is relevant when we try to understand and predict the distribution and orientation of fractures, at regional, basin, and reservoir-scale, in order to model fluid transport in the crust. Our study also highlights the importance of mapping fractures in outcrop, which are analogous to naturally fractured reservoirs.

Acknowledgements

We thank Sam Thiele, Megan Withers, and Jonas Köpping for their assistance with data collection and stimulating discussions in the field. Fieldwork was partly funded by an AAPG Grants-in-Aid Award awarded to AS, who is supported by a Monash University Faculty of Science Dean's International Postgraduate Research Scholarship.

Data availability

The basemap used for structural mapping at Shark Stack (Cape Liptrap) is available at low resolution (10 cm/pixel) from <https://doi.org/10.26180/5c653193efa25> (Vollgger and Cruden, 2019). The datasets used for fracture mapping at Harmers Haven North, Harmers Haven South, Eagles Nest, the Caves–Flat Rocks, and Inverloch are included in Appendix 1.

Chapter 5

Inheritance without reactivation: Insights from crustal-scale analogue experiments

A. Samsu¹, A. R. Cruden¹, N. E. Molnar¹, R. F. Weinberg¹

¹School of Earth, Atmosphere and Environment, Monash University
Clayton, VIC 3800, Australia

Abstract

In contrast to basement fault reactivation, the influence of pre-existing basement weaknesses on non-parallel faults in cover rocks during rifting is not well-understood. This subtle form of structural inheritance can have a significant impact on the architecture of fault networks in rift basins that overlie multiple basement domains with different geomechanical properties and anisotropies. Here we use multi-layer, brittle-ductile, crustal-scale analogue experiments to study the influence of lower crustal anisotropies on fault patterns in the overlying upper crust during a single phase of orthogonal rifting. The experiments were designed to test if lower crustal anisotropies, oriented 45° to the extension direction, can lead to the formation of rift faults that are oblique to both the imposed extension direction and the lower crustal anisotropies themselves. This work builds on previous field-based studies of the onshore Gippsland Basin (southeast Australia), where basin-scale (>1 km long) NE-SW to ENE-WSW trending faults, which formed during Early Cretaceous N-S or NNE-SSW rifting, are prevalent above two levels of anisotropic basement with NNE-SSW to NE-SW structural trends. Our experiments show that a pervasive, vertically layered, narrowly spaced basement anisotropy in the lower crust is required to create basin-internal “extension-oblique” rift faults in the upper crust. The obliquity of these faults expresses the local re-orientation of strain within the anisotropic lower crust, which arises when strike-slip shear strains along the interfaces of mechanically contrasting materials are superposed on the imposed orthogonal extension, creating a transtensional regime. Our findings highlight a form of basement-cover interaction that does not involve basement reactivation.

5.1. Introduction

Rifts form in pre-deformed crust that is characterized by pervasive fabric anisotropies (i.e., foliation) and discrete zones of previous shearing and faulting. The influence of pre-rift structures on new rifts has been observed around the world, from reactivation of shear zones in the NE Brazilian margin (Kirkpatrick et al., 2013), northern Scotland (Phillips et al., 2016), the East African Rift System (Daly et al., 1989; Heilman et al., 2019), and the Australian Southern Margin (Gibson et al., 2013) to the “deflection” of rifts as they avoid rheologically stronger crustal regions, such as cratons, and propagate along mobile belts (e.g., Corti et al., 2007; Daly et al., 1989; Tommasi and Vauchez, 2001; Wilson, 1966). System-scale studies on the East African Rift System highlight the influence of pre-rift lithospheric structures and rheological variations on the along-axis orientation of entire rifts (Brune et al., 2017; Corti et al., 2007). However, the relationships between pre-existing crustal weaknesses and the architecture of individual basins and fault systems have received less attention.

Using aerial imagery and field observations, Wilson et al. (2010) and Samsu et al. (2019) demonstrated variations in the main orientations of brittle structures across areas that overlie different basement domains. Such a relationship potentially reflects a subtle influence from pre-existing basement structures, but not one that is caused by basement reactivation, which normally results in new extensional structures that are parallel with the basement foliation, shear zones, or faults (Heilman et al., 2019; Holdsworth et al., 1997; Kirkpatrick et al., 2013; Phillips et al., 2016). Stress re-orientation near pre-existing structures offers some explanation for dip-slip kinematics along faults that are oblique to the extension direction (Morley, 2010; Philippon et al., 2015), which we refer to here as “extension-oblique” faults.

Extension-oblique faults are common features of oblique rifts, where strain is accommodated by extension perpendicular to the rift trend and shear parallel to the rift trend (Withjack and Jamison, 1986). Analogue experiments of oblique rifting have shown that the orientation and kinematics of faults is controlled by the angle of obliquity between the rift trend and the relative displacement direction between the two moving plates (Agostini et al., 2009; Corti, 2008; Withjack and Jamison, 1986). These experiments address the kinematic boundary conditions that are required to create extension-oblique rifts but not the role of crustal fabrics in their formation.

In this study, we focus on an outstanding question: What intrinsic mechanical characteristics do pre-existing basement structures need to have in order to cause the formation of extension-oblique faults that are also oblique to the pre-existing structures themselves? We use crustal-scale analogue models to demonstrate that strain re-orientation above pre-existing anisotropies in the lower crust enables the formation of extension-oblique faults without direct reactivation of pre-existing weaknesses and their propagation into upper crustal cover rocks. The orientation of the resulting extension-oblique faults is controlled by the mechanical properties (e.g., strength) and geometry (i.e., the spacing and width of “weak zones” that create the anisotropy) of the lower crust. Our models were designed to replicate syn-rift normal faulting in the western onshore Gippsland Basin, southeast Australia, where extension-oblique faults are prevalent in an area that is underlain by two levels of anisotropic basement (Samsu et al., in prep.): Paleozoic metasediments of the Melbourne Zone and an inferred underlying, anomalously strong Neoproterozoic–Cambrian crustal block known as the “Selwyn Block” (Cayley et al., 2002) (Figure 5.1).

5.2. Crustal-scale inheritance in Australia

The Neoproterozoic–Cambrian Selwyn Block was accreted onto the eastern margin of Gondwana in the Late Cambrian Delamerian Orogeny (Cayley, 2011; Cayley et al., 2002). In its current position, the Selwyn Block underlies part of the Jurassic–Cretaceous Australian

Southern Margin (ASM) rift system, extending from the southeast Australian mainland underneath the Bass Strait and into Tasmania (Cayley et al., 2002; Moore et al., 2016) (**Figure 5.1b**). The presence of this heterogeneous, relatively strong, lower-crustal block may have impacted the evolution and architecture of the overlying ASM basins at multiple scales. At the system scale, the western margin of the Selwyn Block coincides with a deflection of the west-to-east propagating ASM rift system towards the south, bypassing the Bass Strait and instead continuing along the western margin of Tasmania (**Figure 5.1a**).

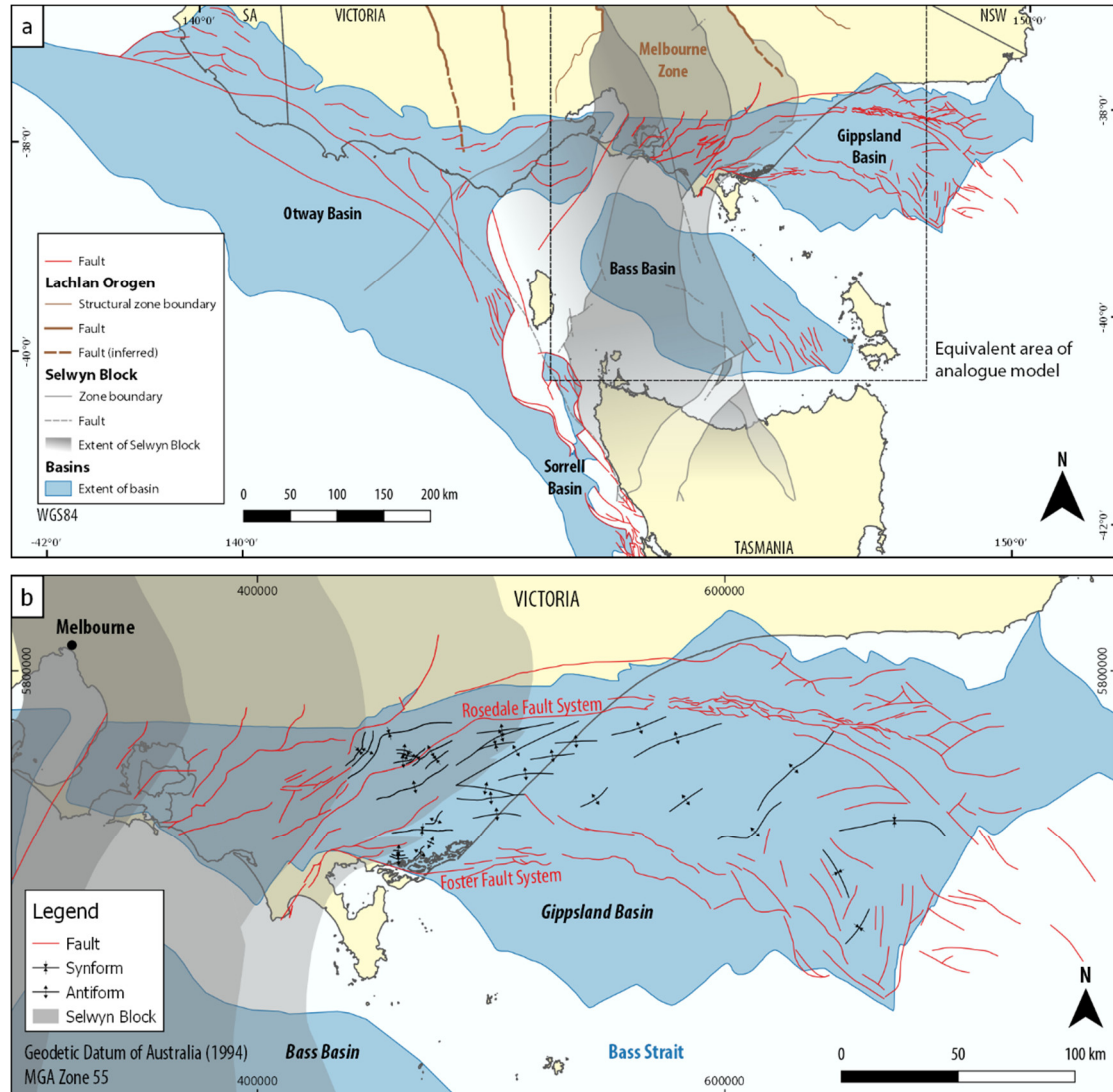


Figure 5.1 Map of the eastern basins of the Australian Southern Margin rift system, including the Otway, Sorrell, Gippsland, and Bass basins (modified from Samsu et al., 2019). The eastern part of the Otway Basin and the western part of the Gippsland Basin is underlain by the Paleozoic Melbourne Zone (Lachlan Fold Belt) basement and the Neoproterozoic – Cambrian Selwyn Block basement (Cayley et al., 2002; McLean et al., 2010)

At the basin scale, the influence of the Selwyn Block is evident in the eastern Otway Basin and western Gippsland Basin, where NE-SW to ENE-WSW trending Early Cretaceous faults are present above the Selwyn Block (Constantine, 2001; Moore et al., 2000; Norvick and Smith, 2001; Samsu et al., 2019; Willcox et al., 1992). This fault set is oblique to the inferred N-S or NNE-SSW direction of regional extension (e.g., Etheridge et al., 1985; Miller et al., 2002; Willcox and Stagg, 1990) and E-W trending orthogonal rift faults that typify areas beyond the inferred boundaries of the Selwyn Block.

Samsu et al. (2019, in prep.) used field observations from the western onshore Gippsland Basin to determine that NE-SW to ENE-WSW syn-rift faults are also at acute angles to the NNE-SSW Paleozoic basement fabric and the NE-SW structural grain of the Selwyn Block (Moore et al., 2016) and that the highly anisotropic basement may have contributed to the formation of these oblique rift faults. Others have attributed the obliquity of the NE-SW to ENE-WSW faults to transtension arising from NNW-SSE directed oblique extension in the Early Cretaceous (Power et al., 2003, 2001).

5.3. Experimental methods

Analogue modelling is a powerful tool for simulating crustal deformation in a controlled environment and testing hypotheses on its driving mechanisms, using simplified models that are scaled to a practical size (Cruden et al., 2006; Ranalli, 2001). In this study, the simplified analogue models were designed to approximately simulate an area of the onshore Gippsland Basin that straddles the postulated NE-SW trending eastern boundary of the Selwyn Block (**Figure 5.1**). These isostatically supported, crustal-scale, brittle-ductile multilayer experiments were extended in one direction at a constant rate to simulate orthogonal rifting with an upscaled divergence rate of ~ 2 mm/yr (**Figure 5.2**).

5.3.1. Boundary and initial conditions

All experiments were conducted on a brittle-ductile model lithospheric plate, with initial dimensions of $44\text{ cm} \times 40\text{ cm} \times 7\text{ cm}$, floating isostatically on a fluid model asthenosphere contained within a $65\text{ cm} \times 65\text{ cm} \times 20\text{ cm}$ acrylic tank (**Figure 5.2**). The simplified model lithosphere consists of a brittle upper crust, a ductile lower crust, and a ductile lithospheric mantle. The prototype layer thicknesses were estimated from forward modelling of geophysical potential field data (Moore et al., 2016) and seismological models (Gray et al., 1998; Kennett et al., 2013).

One side of the model was attached to a moving wall pulled by a linear actuator, imposing an orthogonal extensional boundary condition that simulates extension similar to that of broadly N-S rifting between Australia and Antarctica in the Early Cretaceous (Miller et al., 2002).

Orthogonal extension boundary conditions ensure that the formation of any faults that are oblique to the extension direction are caused by strength anisotropies in the model crust as opposed to imposed kinematic boundary conditions. We also did not place a linear “weak zone” seed in the middle of the model, because our intention was not to force a rift (e.g., Brune et al., 2017; Molnar et al., 2017; Zwaan and Schreurs, 2017). The experiments test the influence of increasing the degree of anisotropy of the strong lower crust on fault orientations in the cover. All other parameters in the models remained constant. Four experiments were carried out, and their initial lower crustal geometries are illustrated in **Figure 5.3**.

5.3.2. Scaling and materials

Model parameters (e.g., length, mass, and time) and the mechanical properties of the chosen analogue materials were scaled down so that deformation of the model lithosphere occurred within a convenient time period while still behaving consistently with nature (i.e., the prototype) (Ramberg, 1967). The scaling properties used in the experiments are summarised in **Table 5.1**.

A length scaling factor $L^* = L_m/L_p = 1 \times 10^{-6}$ was adopted (subscripts m and p refer to the model and natural prototype, respectively), so that 1 cm in the model represents 10 km in nature. The 44 cm \times 40 cm model surface area therefore corresponds to 440 km \times 400 km area in nature (**Figure 5.1**). The scaling factor for density ρ^* was set to 3.63×10^{-1} . The experiments were run under normal gravitational acceleration, so that the scaling factor for acceleration due to gravity $g^* = 1$, and therefore the scaling factor for stress $\sigma^* = \rho^* \times L^* = 3.63 \times 10^{-7}$. Granular materials were used to model the strong, brittle upper crust, while the weaker lower crust and lithospheric mantle were represented by viscous materials, resulting in Christmas tree-like strength profiles (**Figure 5.3**).

A granular mixture with a bulk density $\rho_b = \rho_m \approx 960 \text{ kg/m}^3$ was prepared to approximate a scaled natural density of $\rho_p = 2650 \text{ kg/m}^3$ for the upper crust. We used a mixture of dried quartz sand ($\rho_b = 1,580 \text{ kg/m}^3$) and hollow ceramic Enviropheres® BLF and BL150 ($\rho_b \approx 390 \text{ kg/m}^3$) with mass percentages of $\sim 77.9\%$, 21.2% , and 1.9% , respectively, similarly to Molnar et al. (2017). An internal friction angle $\phi < 38^\circ$ and cohesion value $c \sim 9 \text{ Pa}$ was assumed (Molnar et al., 2017). The quartz sand is characterized by a homogeneous grain size distribution, with $\sim 73\%$ of the grains falling in the 150–300 μm range.

We used polydimethylsiloxane (PDMS) and PDMS mixtures to model the ductile lower crust. PDMS is an optically clear, high viscosity, high molecular weight silicone polymer frequently used in analogue modelling (Cruden et al., 2006; Molnar et al., 2018, 2017; Pysklywec and Cruden, 2004). It has a density $\rho_m \approx 980 \text{ kg/m}^3$, which scales to a natural lower crust density $\rho_p \approx 2700 \text{ kg/m}^3$. Our PDMS (Wacker Elastomer NA) approximates a Newtonian fluid with a

viscosity $\eta \approx 4 \times 10^4$ Pa s. The PDMS mixtures have a slightly non-Newtonian rheology defined by the power law:

$$\sigma^n = a\dot{\epsilon}$$

where σ is stress, n is the power law exponent of the material, a is a material constant, and $\dot{\epsilon}$ is the strain rate.

The lower crust layer is divided into two triangular domains separated by a vertical interface 45° to the extension direction (**Figure 5.3**), consistent with the orientation of the NE-SW boundary and structural trend of the Selwyn Block in the corresponding area in nature (**Figure 5.1**). One triangular domain of “strong” lower crust (SLC) approximates the Selwyn Block. The SLC material is a mixture of PDMS, modelling clay (white Colorific Plasticine[®]), and 3M[®] K1 hollow glass microspheres (e.g., Cruden et al., 2006; Molnar et al., 2017; Riller et al., 2012). Combining the PDMS with modelling clay increases its effective viscosity and density, while adding glass microspheres reduces its density but increases its effective viscosity. The relative amounts of the three ingredients were adjusted until a density $\rho = 985$ kg/m³ and an effective viscosity of $\sim 5.7 \times 10^5$ Pa s (at our experimental strain rate of 1.0×10^{-4} s⁻¹) were achieved, scaling to a natural density of $\rho = 985$ kg/m³ and natural effective viscosity of 2.9×10^{22} Pa s, with 61.0 vol% PDMS, 16.9 vol% white Plasticine[®], and 22.1 vol% microspheres. The rheological properties of the PDMS mixture were measured using an Anton Paar Physica MCR-301 parallel plate rheometer. The experimental strain rate was estimated by dividing the velocity of the linear actuator (i.e., the rate at which the model was extended) by the total model thickness of 7 cm (Benes and Davy, 1996).

The SLC material is one order of magnitude more viscous than the neighbouring “normal” lower crustal (NLC) triangular domain, which consists of pure PDMS ($\sim 4.0 \times 10^4$ Pa s). Anisotropies within the SLC are reproduced by incorporating linear weak zones using a PDMS mixture consisting of 80.9 vol% PDMS, 9.0 vol% white Plasticine[®], and 10.1 vol% microspheres. This material has an effective viscosity of $\sim 7.3 \times 10^4$ Pa s, hence only slightly more viscous than the NLC material. In the reference experiment (Exp LE-01), the SLC material was substituted by the weak zone material to show that a slight contrast in viscosity has no effect on strain localisation or rotation (Section 5.4.1).

The model lithospheric mantle is a mixture of PDMS, modelling clay (black Colorific Plasticine[®]), and 3M[®] K1 hollow glass microspheres (bulk density $\rho = 1,067$ kg/m³). We used a mixture of 55.8 vol% PDMS, 29.7 vol% black Plasticine[®], and 14.6 vol% microspheres to achieve a density $\rho_m = 985$ kg/m³ and effective viscosity of 5.9×10^5 Pa s, corresponding with an upscaled density $\rho_p = 2940$ kg/m³ and viscosity of 3.0×10^{22} Pa s.

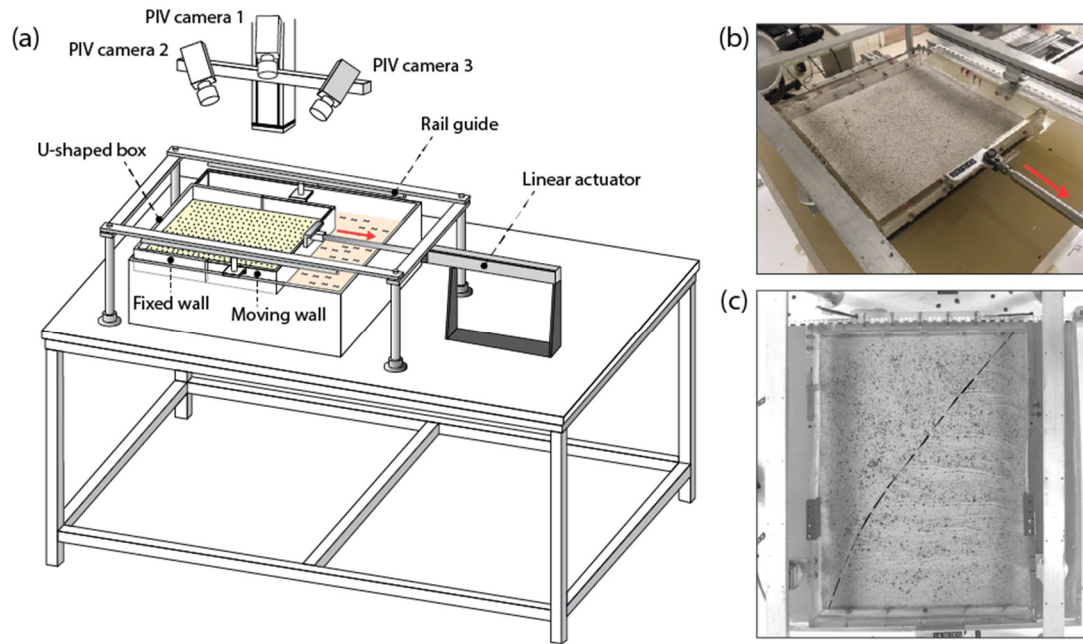


Figure 5.2 Experimental setup for orthogonal extension. In (a) and (b), the red arrow indicates the direction of extension. (c) Top view photograph of the model surface (Exp LE-05) at the end of the experiment. The dashed line indicates the final geometry of the lower crustal SLC-NLC boundary.

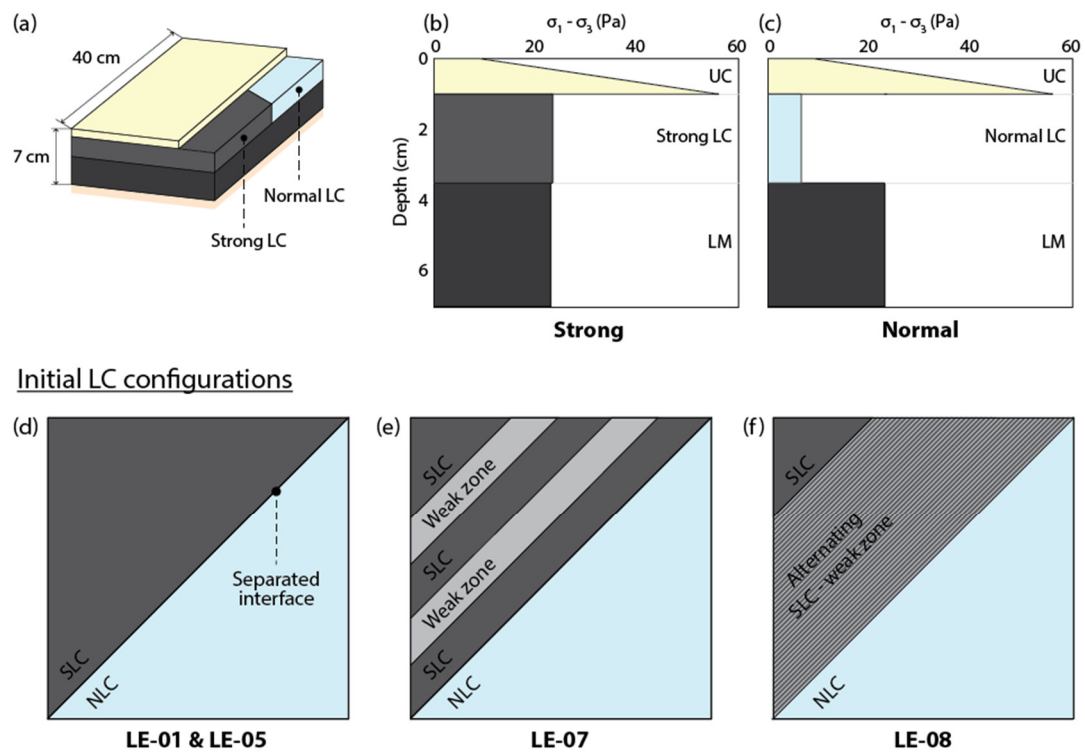


Figure 5.3 Structure (a) and strength profiles (b-c) of the multi-layer model lithosphere.

Table 5.1 Model scaling parameters and material properties. ESPH = Envirospheres; PDMS = polydimethylsiloxane; WPL = white Plasticine; BPL = black Plasticine; K1 = hollow ceramic microspheres; NS = Natrosol.

		Thickness		Density		Viscosity		
		Model	Nature	Model	Nature	Model	Nature	
		(mm)	(km)	(kg/m ³)	(kg/m ³)	(Pa s)	(Pa s)	Material
Normal crust								
Upper crust	Brittle	10	10	962	2650	-	-	Sand+ESPH
Normal lower crust (NLC)	Ductile	25	25	980	2700	4.0×10^4	2.0×10^{21}	PDMS
Strong crust								
Upper crust	Brittle	10	10	962	2650	-	-	Sand+ESPH
Strong lower crust (SLC)	Ductile	25	25	985	2715	5.7×10^5	2.9×10^{22}	PDMS+WPL+K1
Weak zone	Ductile	25	25	985	2715	7.3×10^4	3.6×10^{21}	PDMS+WPL+K1
Lithospheric mantle	Ductile	35	35	1067	2940	5.9×10^5	3.0×10^{22}	PDMS+BPL+K1
Asthenosphere	Fluid	-	-	1125	3100	380	1.9×10^{19}	NaCl-NS
Scaling factors: model/nature	$L^* = 1 \times 10^{-6}$			$\rho^* = 3.63 \times 10^{-1}$		$\eta^* = 2.0 \times 10^{-17}$		
Time scaling factor	$t^* = \eta^*/(\rho^* \cdot g^* \cdot L^*)$			$t^* = 5.5 \times 10^{-11}$		1 h in model ~ 2.1 Ma in nature		
Velocity scaling factor	$v^* = l^*/t^*$			$v^* = 1.8 \times 10^4$		41 mm/h in model ~ 20 mm/yr in nature		
Gravity scaling factor	$g^* = g_m/g_p$			$g^* = 1$				
Stress scaling factor	$\sigma^* = \rho^* \cdot L^*$			$\sigma^* = 3.63 \times 10^{-7}$				

The model asthenosphere is a mixture of Natrosol[®] 250 HH, NaCl (sodium chloride), formaldehyde, and deionized water (Boutelier et al., 2016; Molnar et al., 2017). Natrosol[®] hydroxyethylcellulose is a water-soluble polymer that can be used to modify the viscosity of an aqueous solution without significantly affecting its density (Boutelier et al., 2016). Natrosol[®] acts as a Newtonian fluid under shear rates typically employed in experimental tectonics (Boutelier et al., 2016). The model asthenosphere mixture has a viscosity $\mu_m = 380$ Pa s, scaling to a prototype viscosity $\mu_p = 1.9 \times 10^{19}$ Pa s, which is comparable with natural viscosity estimates for the asthenosphere (Artyushkov, 1983; Ranalli, 1995). The mixture has a density $\rho_m = 1,125$ kg/m³ (Molnar et al., 2017), equivalent to a natural density $\rho_p \approx 3,100$ kg/m³ (e.g., Pysklywec and Cruden, 2004).

5.3.3. Construction of the model layers

The ductile lower crust and lithospheric mantle were constructed to fit within a pair of U-shaped walls (Figure 5.2). These ductile layers were molded into rigid frames on top of a flat surface (Figure 5.4). They were placed within the frames ~72 h before the start of the experiment to allow enough time for the material to fill up the frames, settle, and expel trapped air bubbles. Because the lower crust layer comprised two strength domains, the two ductile lower crust domains (the SLC and NLC) were molded separately in two rigid frames (Figure 5.4a). When the mixtures had settled, the two pieces were put together to form the final rectangular-shaped lower crust layer. Beforehand, a 80:20 wt% paraffin oil and petrolatum jelly mixture (Duarte et al., 2014) was smeared onto the SLC-NLC interface to keep the two materials separate (Figure 5.3d). However, this had a negligible effect on strain localisation during the experiments, as the

mixture may have reacted chemically with Plasticine (Duarte et al., 2014) and lost its lubricating effect.

During preparation of the SLC domain of the lower crust layer for Exp LE-07, which had 5.4 cm-wide weak zones, the areas that were to be filled with the weaker material were cut with a knife and removed from the already moulded SLC. The cut interfaces were kept vertical by placing thin, rigid plastic sheets where the cuts were made. The “gaps” were then filled with the weak zone material. The plastic sheets were then removed once the weak zone material had settled. Preparation of the SLC domain of Exp LE-08, where narrowly spaced, ~2 mm-wide weak zones within the SLC were separated by ~2 mm-wide SLC material, required different steps (**Figure 5.4**). A pasta maker was used to uniformly flatten SLC and weak zone materials to a thickness of ~2 mm. For the assembly of the “strong” domain, the flattened layers were cut into strips and placed vertically in an alternating manner within the rigid frame. All linear weak zones incorporated into the model lower crustal layer were at a 45° angle relative to the extension-perpendicular walls. The rheological boundary between the SLC and NLC also has the same 45° orientation and crosses the centre of the model in map view (**Figure 5.4e**).

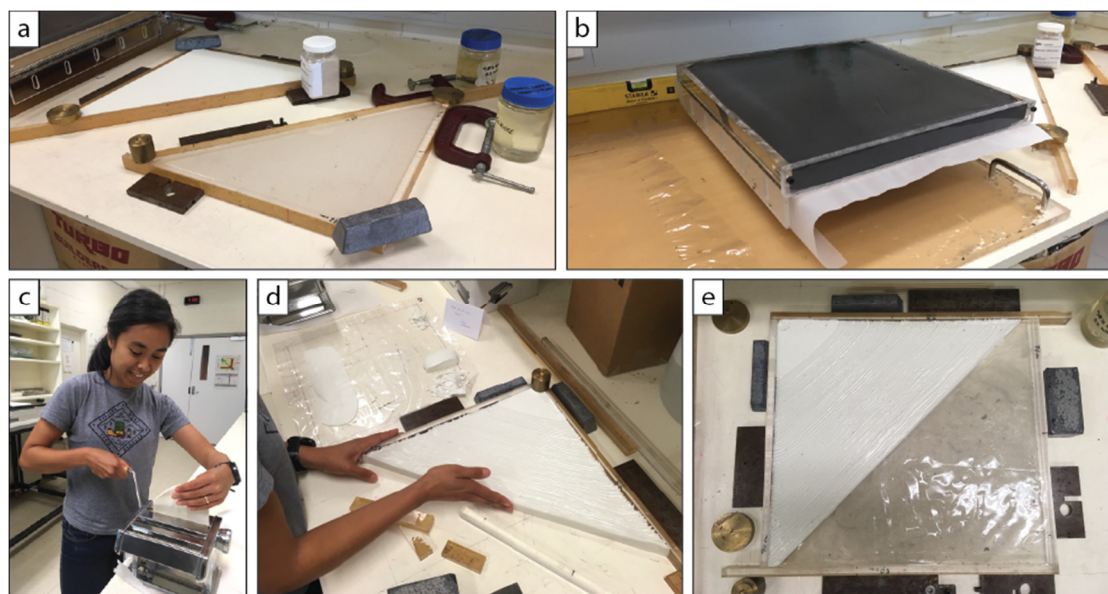


Figure 5.4 Preparation of the ductile lower crust and lithospheric mantle layers. (a) The SLC and NLC material were placed in separate rigid frames on top of a flat workbench; the two parts were united to form the lower crust once the mixtures have settled. (b) The lithospheric mantle material was placed into a rectangular rigid frame and attached to horizontal grips. Flattening of this layer was facilitated with a rolling pin. (c–e) Assembly of the lower crust layer for Exp LE-08. A pasta maker was used to uniformly flatten SLC and weak zone materials to a thickness < 2 mm (c). For the assembly of the “strong” domain, they were cut into strips and placed vertically in an alternating manner within the rigid frame (d), after which this domain was attached to the “normal” domain (e). Photos (c–e) courtesy of J. Samsu.

Specially designed 4 cm-wide horizontal grips were attached to the lithospheric mantle layer (**Figure 5.4b**); the grips were later fastened to the sides of the U-shaped walls that are perpendicular to the extension direction. The lithospheric mantle (along with the horizontal grips) and lower crust were placed in the tank and allowed to settle over a period of ~24 h, allowing sufficient time for the model to achieve isostatic equilibrium and for air bubbles to dissipate. The 80:20 wt% paraffin oil and petrolatum jelly mixture was used as a lubricant between the lateral boundaries of the model and the U-shaped walls to minimize boundary effects caused by friction.

Shortly before the start of the experiment, the model upper crust layer was deposited on top of the model lower crust by slow sifting the prepared granular mixture from a height of ~10 cm. The surface of the upper crust layer was not flattened or scraped off in order to avoid alterations in the mechanical properties of the layer (e.g., localized compaction). Fine coffee powder was sifted onto the surface of the model to serve as passive markers during deformation monitoring (see Section 5.3.4). Once all layers of the model lithosphere were in place, the horizontal grips were fastened to the extension-perpendicular sides of the U-shaped walls.

5.3.4. Deformation monitoring and analysis

Deformation in the upper crust layer was monitored during the experiment by stereoscopic particle imaging velocimetry (PIV) (Adam et al., 2005), so that the resulting strain distribution and fault orientations could be characterized over time. The PIV system comprises three high-speed cameras that provide a spatial resolution ≥ 1 mm and a temporal resolution ≥ 0.1 s (Molnar et al., 2017). Successive images were recorded at 15 s intervals during each experimental run. Surface strain and topographic data was derived following the workflow of Molnar et al. (2017). The incremental displacement field was computed using stereo cross correlation, forming the basis for deriving the strain tensor components,

$$E_{ij} = \frac{\partial V_i}{\partial_j} \text{ with } i \in \{x, y, z\} \text{ and } j \in \{x, y, z\}$$

where E_{ij} describes the gradient in the vector component i along the j axis (Adam et al., 2005), and V is the velocity vector. The scalar fields were used to derive incremental normal and shear strain as well as the height of the model surface, or digital elevation model (DEM). The cumulative strain was calculated as the sum of incremental strain and used to produce a grid of finite strain ellipses. The maximum normal strain on the surface was derived from the larger eigenvalue of the 2D strain matrix

$$\begin{vmatrix} E_{xx} & E_{xy} \\ E_{yx} & E_{yy} \end{vmatrix}$$

and the relationship

$$E_{surf} = \frac{(E_{xx} + E_{yy})}{2} + \sqrt{\frac{(E_{xx} + E_{yy})^2}{4} + \frac{(E_{xy} + E_{yx})^2}{4}}$$

A local coordinate system was chosen such that the z -direction is aligned with the surface normal. E_{xx} and E_{xy} are partial derivatives of the velocity components $\partial V_x/\partial x$ and $\partial V_x/\partial y$, and E_{yx} and E_{yy} are partial derivatives of the velocity components $\partial V_y/\partial x$ and $\partial V_y/\partial y$. Strain maps, complemented with topographic DEMs and top-view photographs of the model surface (illuminated with oblique lighting) enabled us to track the nucleation, growth, and distribution of faults at different stages of the experiments. At the end of each experiment, the granular upper crustal material was removed with a vacuum cleaner and the top surface of the lower crustal material was photographed, which show the final geometries of the lower crustal rheological boundaries.

5.4. Results

We present the results of four experiments: one reference experiment (Exp LE-01; **Figure 5.5**), where the lower crust is made up of two mixtures of similar rheology, and three other experiments (Exp LE-05, LE-07, and LE-08; **Figure 5.6**, **Figure 5.7**, and **Figure 5.8**; also see Appendix 3), where the arrangement of weak zones within the SLC domain is varied to represent different wavelengths of basement anisotropy (**Figure 5.3**). When viewing the models in map view, the upper side of the image is referred to as “north”, and the model is being extended towards the “south”. In describing the fault patterns, the upper crust is divided into two domains: the NW domain, underlain by the SLC (with or without weak zones), and the SE domain, which overlies the NLC (**Figure 5.6**). Faults near the western and eastern boundaries of the models curve towards parallelism with the model edges. This boundary effect results from friction between the model’s lateral boundaries and the confining U-shaped walls. It affects a small area outside the region of interest.

5.4.1. Reference experiment: quasi-homogeneous lower crust (Exp LE-01)

In the reference experiment LE-01, we tested the influence of two homogeneous lower crustal domains of slightly different viscosities on upper crustal fault patterns during orthogonal extension. The SLC mixture has the same composition as the weak zone in Exp LE-07 (refer to **Table 5.1** for properties of weak zone). The upper crust across the entire model area is characterized by an E-W trending horst and graben system (**Figure 5.5b**). Based on the topographic DEM (i.e., surface height of the model), randomly distributed E-W trending normal faults had begun to nucleate by ~ 0.3 h (3% extension). As extension progressed, the faults

propagated both westwards and eastwards. They reached their final length at ~ 2 h (21% extension), after which strain was accommodated by widening of graben structures. The orientation of the faults was not influenced by the presence of the oblique SLC-NLC interface. This suggests that the viscosity contrast between the SLC and NLC was negligible and that a higher viscosity contrast is required for the juxtaposition of two rheologically different lower crustal domains to influence the orientation of rift faults during orthogonal extension.

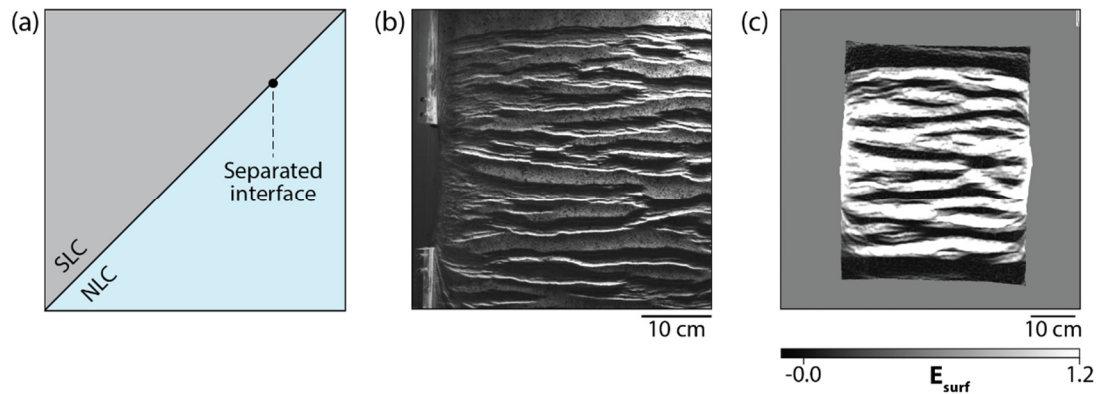


Figure 5.5 Initial lower crustal geometry (a) and results of reference experiment LE-01. (b) is a top-down photograph with oblique illumination, and (c) is the cumulative maximum normal strain on the surface at the end of the experiment. There is no difference in the fault pattern across the SLC-NLC boundary because of the negligible viscosity contrast between the SLC and NLC materials.

5.4.2. Strong vs. normal lower crust (Exp LE-05)

The lower crust in Exp LE-05 has the same initial geometry as the reference experiment, but the SLC material is one order of magnitude more viscous than the adjacent NLC. The effect of this strength contrast is apparent in the distinct styles of faulting above the two domains (**Figure 5.6a**). The SE domain is characterized by an E-W trending horst and graben system. Strain was localized along oppositely dipping faults which formed from an early stage (~ 0.8 h; 8% strain). The faults reached their final length at ~ 1.3 h (13% strain), when their lateral propagation was arrested at the model boundary and the diagonal SLC-NLC boundary. As extension progressed, the graben structures deepened as throw along the bounding faults increased. Once the boundary faults had propagated to the bottom of the brittle upper crust, strain was accommodated by widening of the graben.

In the NW domain, strain in the upper crust was more distributed, resulting in short, closely spaced faults. The faults initially formed in the south (~ 1.4 h; 15% strain) and then began nucleating in the north, near the model centre (~ 2.0 h; 21% strain) as extension progressed. By the end of the experiment, faults above the strong lower crust had not linked together via relay structures, so that their length remained shorter than the faults in the SE domain. Most of the

faults in the NW domain are E-W, but those within ~30 mm of the strong-normal lower crust boundary trend WNW-ESE, curving to approach perpendicularity to the boundary.

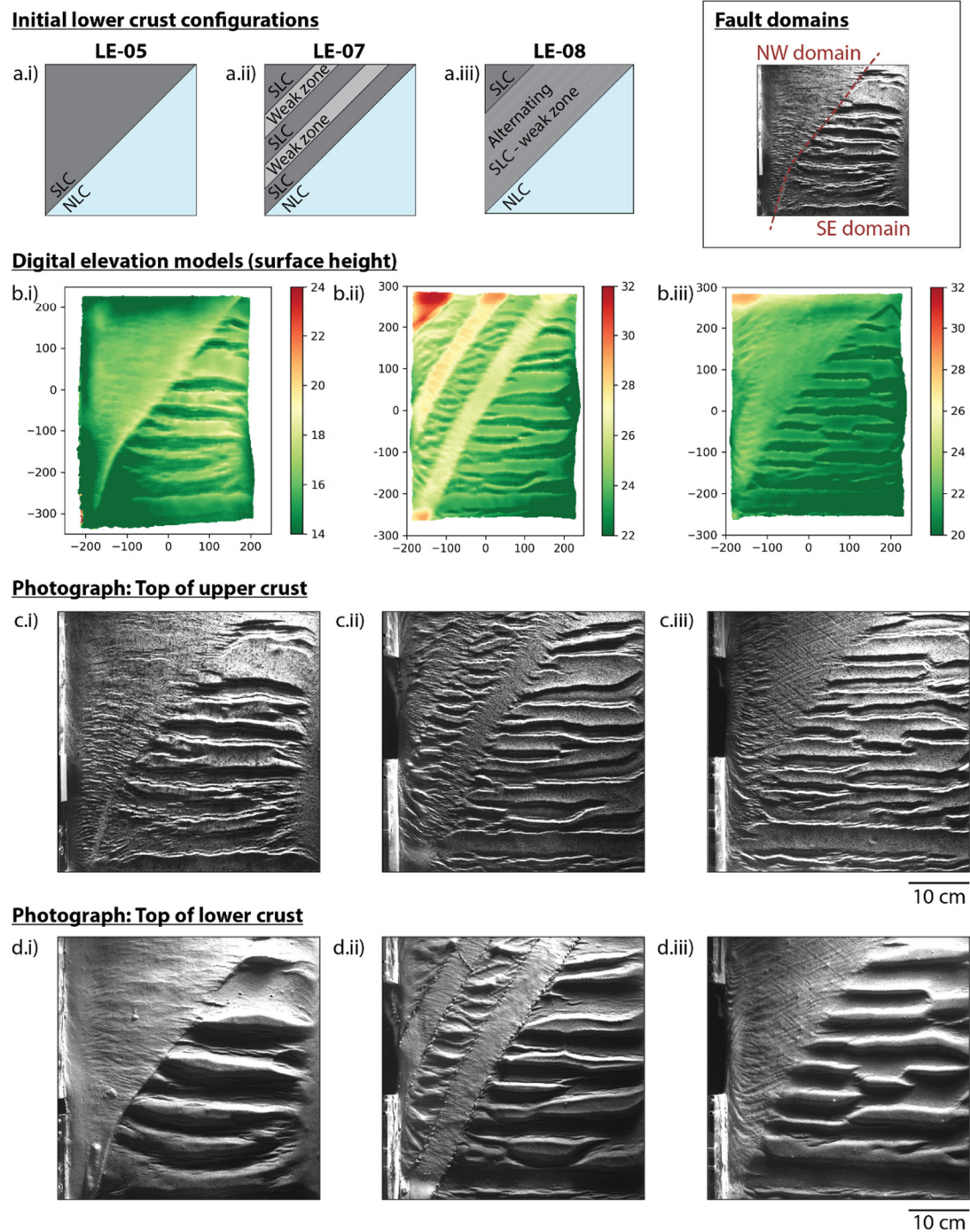


Figure 5.6 Results of orthogonal extension experiments at 4.5 h (47% strain) in map view, with no anisotropy (a.i), 5.4 cm-wide weak zones (a.ii), and ~2 mm-wide weak zones (a.iii) in the strong lower crustal block. The inset shows where the NW and SE domains are located when describing fault patterns. (b) Topographic DEM (in mm) from photogrammetric PIV data; (c) photograph of surface of upper crust; (d) photograph of surface of lower crust. SLC = strong lower crust; NLC = normal lower crust.

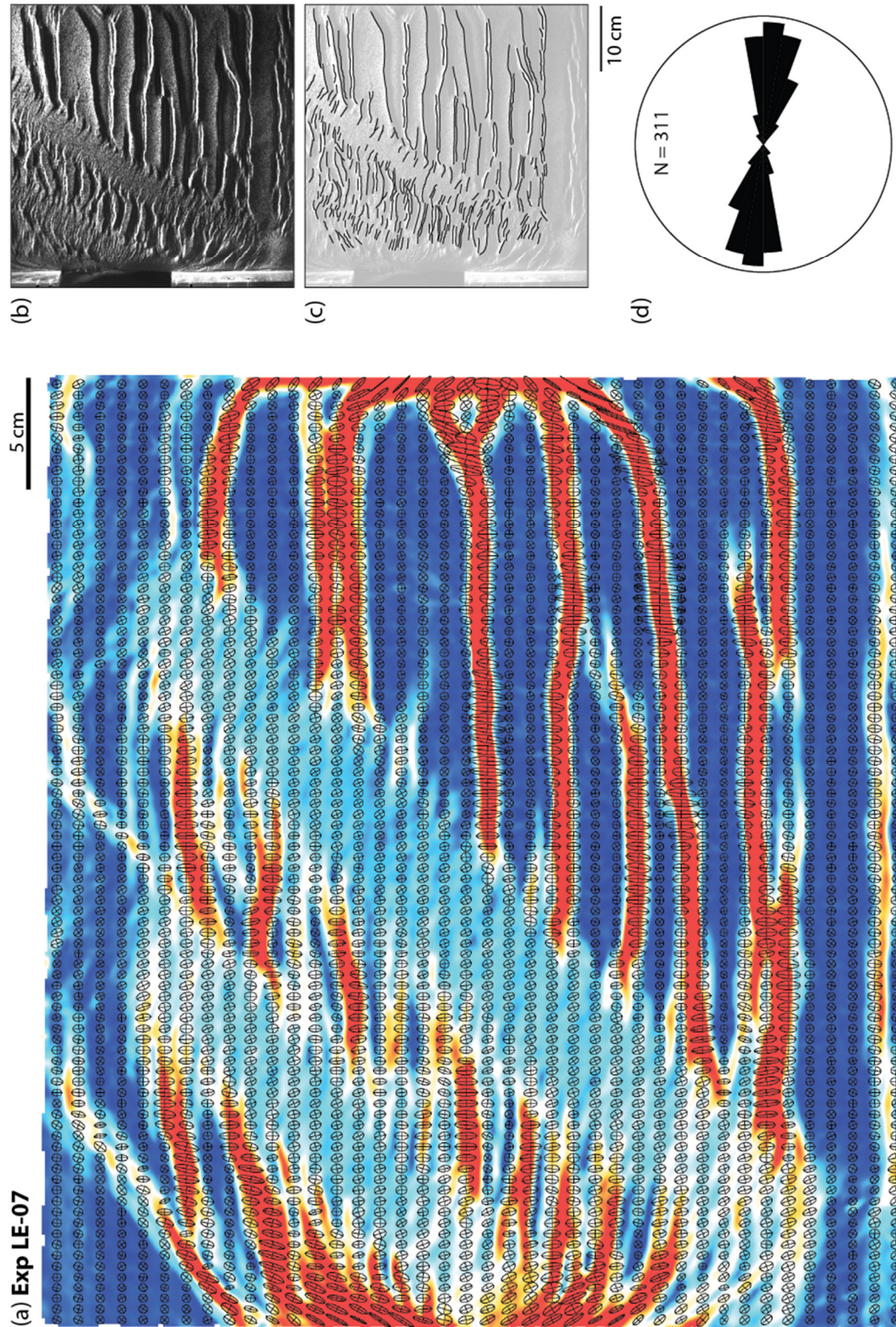


Figure 5.7 Results from Exp LE-07: (a) cumulative maximum normal strain on surface at the end of the experiment, overlain by 2D strain ellipses; (b) top-down photo of upper crust surface, (c) fault traces, and (d) rose diagram of fault traces.

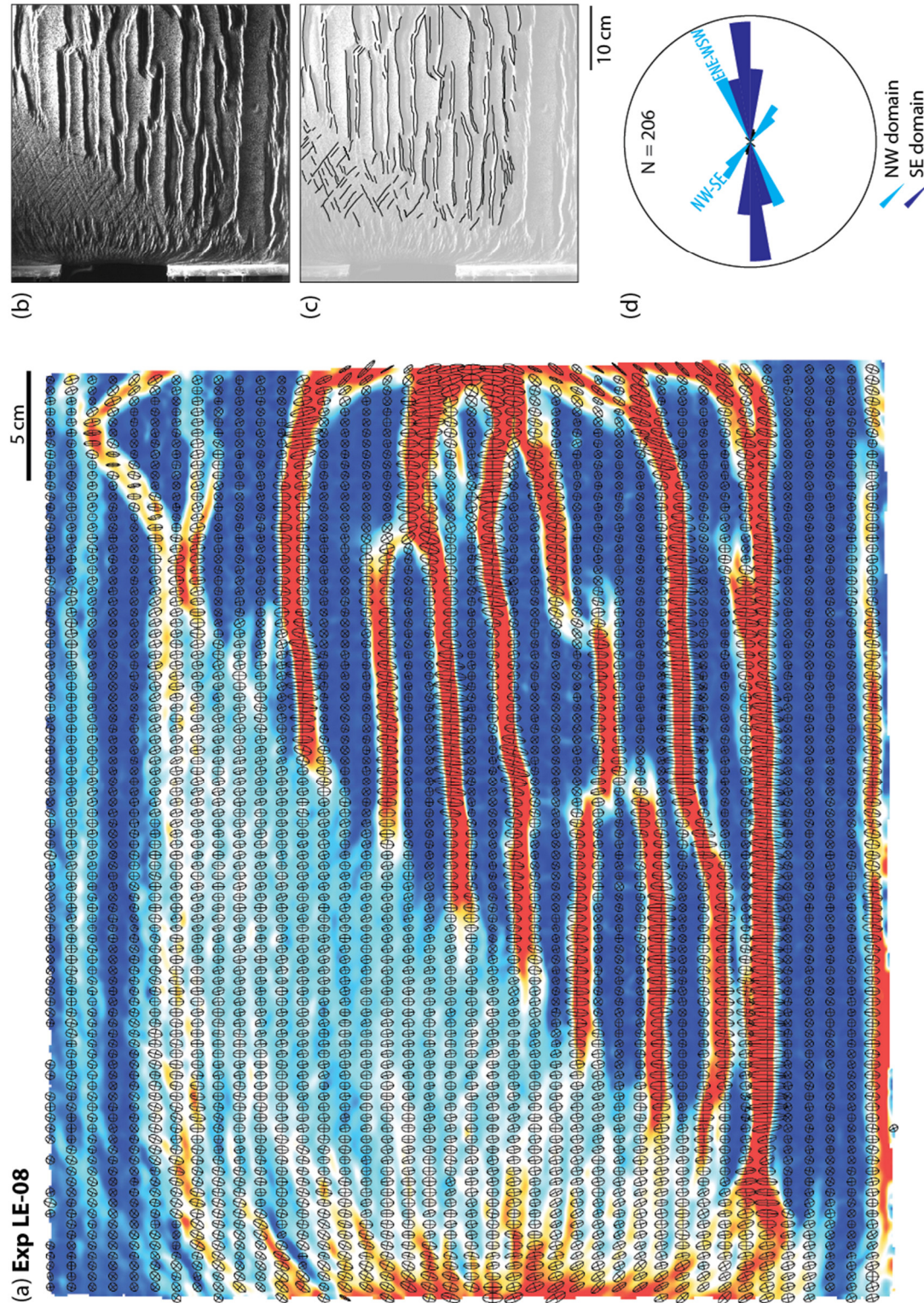


Figure 5.8 Results from Exp LE-08: (a) cumulative maximum normal strain on surface at the end of the experiment, overlain by 2D strain ellipses; (b) top-down photo of upper crust surface, (c) fault traces, and (d) rose diagram of fault traces.

5.4.3. Long-wavelength anisotropy in the strong lower crust (Exp LE-07)

The evolution and final pattern of faults in the SE domain in Exp LE-07 and LE-08 (Section 5.4.4) are very similar to the horst-and-graben style of faulting in the SE domain of Exp LE-05; hence they are not described here in more detail. In Exp LE-07, the fault pattern in the NW domain is influenced by the presence of two linear weak zones which are 5.4 cm wide and spaced 5.4 cm apart (**Figure 5.6b** and **Figure 5.7**). Faults above the weak zones form graben structures bound by oppositely dipping, E-W trending faults, comparable to the style of faulting in the SE domain. Their spacing appears to be an intermediate case between two end members of fault localisation (i.e., highest degree of localisation above the NLC and even distribution above the SLC). NW-SE trending faults above the SLC are evenly distributed and narrowly spaced.

In vertical view photographs of the model surface, E-W trending faults in the SE domain had begun forming by ~ 0.8 h (8% strain). E-W trending faults above the NW domain weak zones began forming at ~ 1.1 h (11% strain). Faults above the SLC began forming at ~ 2.0 h (21% strain), first nucleating at the boundaries of the weak zones and then propagating inwards, orthogonal to the lower crustal domain boundaries.

The formation of non-parallel faults in the NW domain (NW-SE faults above the SLC and E-W faults above the weak zones) was controlled by the widely spaced anisotropy in the underlying lower crust. This experiment demonstrates that strain partitioning occurred, which resulted from the presence of extension-oblique zones of highly contrasting strengths, simulated by large viscosity differences in the models. Finite strain ellipses at the end of this experiment exhibit an N-S maximum stretching direction in the SE domain and weak zones in the NW domain (consistent with the imposed N-S extension) and a NNW-SSE maximum stretching direction above the SLC in the NW domain (**Figure 5.7**).

5.4.4. Short-wavelength anisotropy in the strong lower crust (Exp LE-08)

In Exp LE-08, we implemented a higher degree of anisotropy than in Exp LE-07, with 2 mm-wide, alternating SLC and weak zones in the NW domain (**Figure 5.6c**). In the vertical view photographs of the model surface, E-W trending faults in the SE domain had begun to form by ~ 0.8 h (8% strain). Faults in the NW domain began forming at ~ 1.4 h (15% strain) near the model's western edge. Two sets of narrowly spaced, apparently conjugate (*sensu* Healy et al., 2014) or orthorhombic faults began forming at ~ 3.1 h (32% strain). These coeval NW-SE and ENE-WSW trending faults are oblique to the N-S extension direction and the NE-SW trending anisotropy and SLC-NLC boundary, and have a WNW-ESE (100°) oriented acute bisector (**Figure 5.8**). The obtuse bisector is NNE-SSW (010°), deviating slightly from the imposed N-S extension. The ENE-WSW trending faults are more pronounced than the WNW-ESE trending

set because they exhibit greater dip-slip displacement. Finite strain ellipses at the end of this experiment exhibit an N-S maximum stretching direction in the SE domain and a NNW-SSE maximum stretching direction in the NW domain (**Figure 5.8**).

Although the fault populations in the NW and SE domains exhibit different orientations, both patterns formed as products of the same imposed N-S directed net extension (**Figure 5.9**). Parallel, E-W trending faults in the SE domain represent extension-orthogonal normal faults that form in an Andersonian normal faulting regime (**Figure 5.6b**). In contrast, the orthorhombic fault pattern in the NW domain signifies a local change in the strain field due to the role of the pervasive anisotropy in the lower crust. Because these non-coaxial faults must accommodate the bulk N-S extension, we infer that these oblique fault sets must also have a strike-slip component (**Figure 5.6a**).

5.5. Discussion

In our experiments, upper crustal deformation was influenced by re-orientations of the stress and strain field across the SLC, as there are no weak units separating the upper crust and lower crust layers (cf. "attached stress regime" in Bell, 1996). As a result, faults in the brittle upper crust were localized above areas of necking and thinning in the ductile lower crust (compare **Figure 5.6c** and **Figure 5.6d**).

5.5.1. The influence of crustal strength on fault distribution

In Exp LE-05, the NW domain is populated by short, closely spaced faults, while the SE domain experienced a higher degree of strain localisation evidenced by widely spaced graben bound by long oppositely-dipping faults with large displacements (**Figure 5.6a**). Similarly, the spacing of faults in the NW domain above the weak zones of Exp LE-07 is greater than between faults above the SLC, but less than the spacing between faults in the SE domain (**Figure 5.6b**). These observations are consistent with numerical models of extensional systems (Sharples et al., 2015; Wijns et al., 2005) and analogue models of contractional tectonics (Riller et al., 2012; Schueller and Davy, 2008), which suggest that the strength ratio between the strong, brittle upper crust and the weaker, ductile lower crust controls the degree of strain localisation. In our experiments, this ratio is controlled by the viscosity of the lower crust material.

5.5.2. Rotation of strain axes above a strong, anisotropic lower crustal block

Despite having an orthogonal extension boundary condition, our experiments simulate transtension due to the presence of NE-SW trending anisotropies in the lower crust. The deformation observed in the brittle upper crust reflects underlying deformation in the lower crust, which is governed by ductile flow (Fossen and Tikoff, 1998). The obliquity of faults in

the NW domain of Exp LE-07 and LE-08 suggests that the model crust did not experience pure shear during extension. There is both a coaxial (pure shear) component from the N-S directed extension, which is an imposed boundary condition, and a strike-slip (simple shear) component of strain due to shearing along the NE-SW (45°) trending anisotropies in the lower crust (**Figure 5.10**). Therefore the model crust underwent bulk transtensional deformation with a sinistral strike-slip component.

Calculated finite strain ellipses at the end of Exp LE-08 (**Figure 5.8**) exhibit an N-S maximum stretching direction ϵ_{Hmax} in the SE domain. The NW domain is populated by strain ellipses with a NNW-SSE ϵ_{Hmax} , deviating slightly from N-S. We infer that the 2D horizontal strain ellipses result from a superposition of a coaxial strain component (the N-S imposed extension on the system) and a strike-slip component arising from dextral motion along the oblique, 45° pervasive anisotropy within the layered SLC and along the SLC-NLC interface (**Figure 5.11**). In the NW domain of Exp LE-08, each narrow SLC zone experienced internal sinistral shearing, resulting in an anti-clockwise rotation of the strain ellipse.

From the NNW-SSE trending ϵ_{Hmax} , we expected to observe ENE-WSW trending normal faults in the NW domain (**Figure 5.11a**). Instead, strain in this domain is accommodated by an orthorhombic fault system, where the ENE-WSW set is more dominant (**Figure 5.11b**). We infer that the ENE-WSW faults have a significant dip-slip offset and a minor strike-slip offset. To maintain strain compatibility (Fossen and Tikoff, 1998), a less dominant NW-SE fault set with a significant strike-slip component and a minor dip-slip component must form.

Exp LE-08 demonstrates that a lower crustal block, with a stronger average viscosity than the adjacent block and containing a vertically-layered, closely spaced, pervasive anisotropy, will behave as a single block. The geometric and mechanical properties of the block cause a rotation of the strain axes within the block.

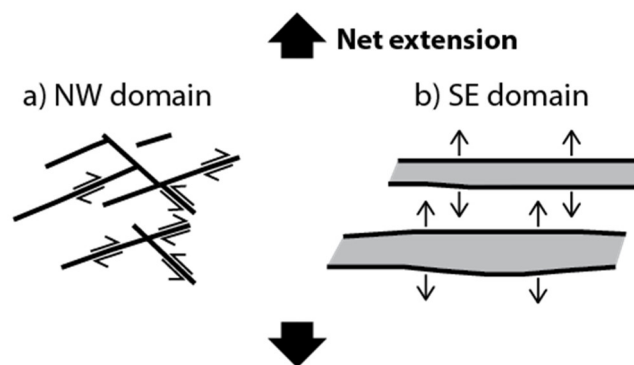


Figure 5.9 Schematic plan view illustration of the ways that the net N-S extension is accommodated in Exp LE-08: (a) an orthorhombic fault set, where the acute bisector trends WNW-ESE (100°); and (b) E-W trending faults which are orthogonal to the net extension direction.

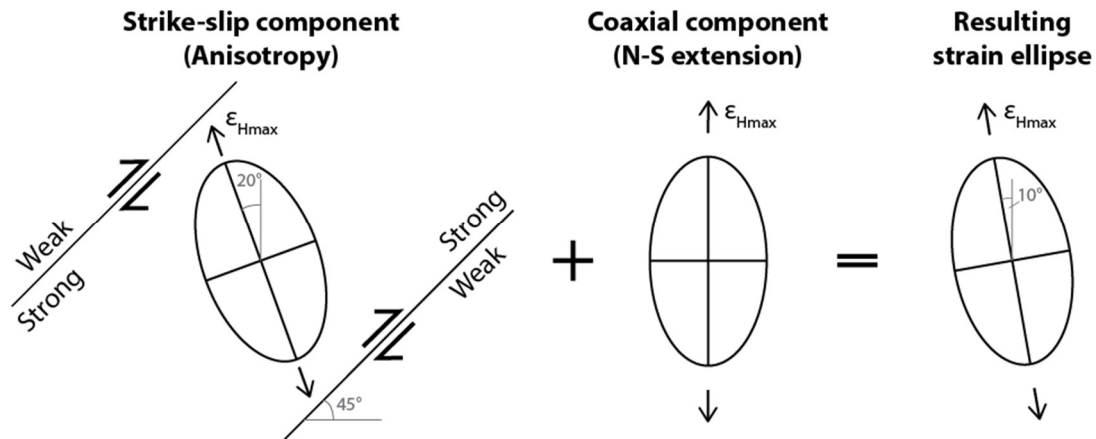


Figure 5.10 Schematic illustration of the components of strain in the highly anisotropic NW domain of Exp LE-08. Strike-slip kinematics at the interfaces between the strong and weak materials in the anisotropic lower crust result in internal sinistral shearing within the narrow SLC zones. These representative 2D strain ellipses are not to scale; the relative contributions of the strike-slip and coaxial component may be different in the experiment.

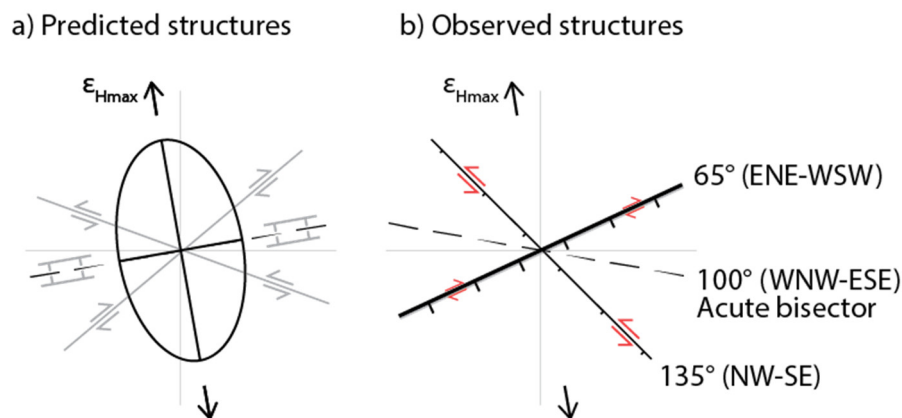


Figure 5.11 Schematic illustration of deformation and associated kinematics in the NW domain of Exp LE-08. (a) Representative finite strain ellipse (calculated from PIV data), with predicted normal fault and strike-slip fault orientations when the maximum horizontal stretching direction ϵ_{Hmax} is NNW-SSE. (b) The orientations of faults at the upper crust surface at the end of the experiment. ENE-WSW trending faults are wider than NW-SE faults, suggesting that they have accommodated a significant amount of dip-slip displacement (greater than strike-slip displacement).

5.5.3. The scale-dependent role of lower crustal anisotropies on fault patterns

In Exp LE-07, the presence of alternating 5.4 cm-wide SLC and linear weak zones in the NW domain resulted in strain partitioning. An N-S trending ϵ_{Hmax} is representative of the weak zones within the NW domain (**Figure 5.8**), which is characterized by E-W trending faults. The NNW-SSE trending ϵ_{Hmax} is confined to the SLC zones. In this experiment, E-W trending faults first

nucleated and propagated in the SE domain and in the weak zones of the NW domain until they reached the interface with the SLC zones; faults then propagated from the interfaces and into the centre SLC zones as NW-SE trending faults. We interpret that the SLC zones acted as transfer zones (cf. Zwaan and Schreurs, 2017), across which older faults in the SE domain and in the NW domain weak zones attempted to link (**Figure 5.12**). These NW-SE trending faults are likely to have sinistral strike-slip kinematics.

Exp LE-07 and LE-08 represent two end member scenarios where either: (a) strain is partitioned between zones of contrasting strength within an anisotropic lower crustal block (**Figure 5.12a**), or (b) the properties of zones of contrasting strength are “averaged” (**Figure 5.12b**). When the width of the alternating weak and strong zones is below a certain threshold, strain rotation occurs not just at the SLC-weak zone interfaces, but across the entire NW domain, as demonstrated by Exp LE-08. When the wavelength of the anisotropy is increased, alternating weak and strong zones within the SLC will tend to act as discrete lower crustal blocks with their own distinct mechanical properties, as opposed to being part of a pervasive fabric within a single block.

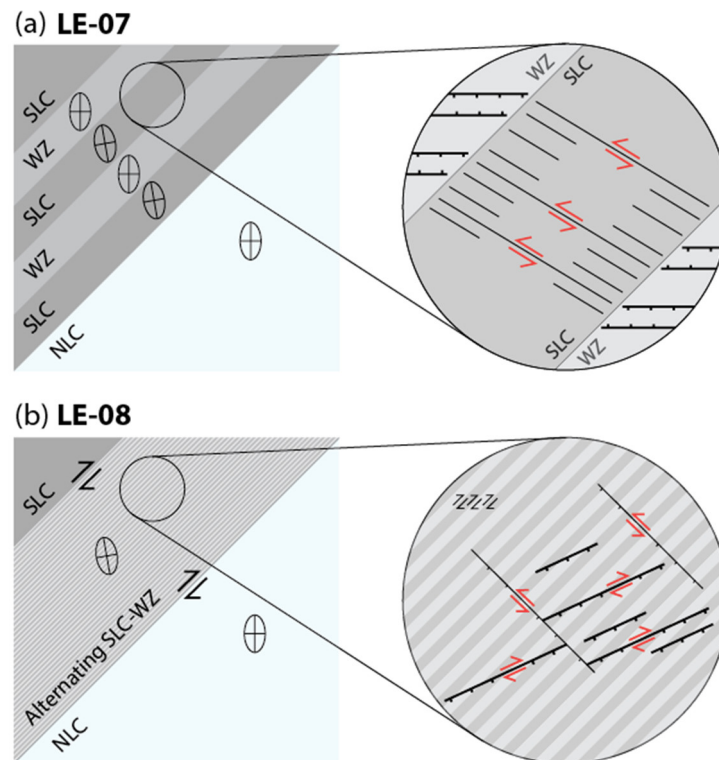


Figure 5.12 (a) Strain partitioning in the NW domain of Exp LE-07. The 2D strain ellipses are rotated anticlockwise in the SLC zones, but they remain consistent with the NLC in the weak zones. (b) Strike-slip movement along all strong-weak interfaces in the NW domain of Exp LE-08 results in an “averaging effect” of the anisotropic properties of the lower crust. Hence the strain ellipse is rotated anticlockwise across the entire NW domain. WZ = weak zone.

Anisotropies in the lower crustal block must be below a threshold wavelength, defined partly by the width and spacing of the linear weak zones, in order for the lower crust to behave as one block in which the strain field is rotated across the entire block. Although quantifying this threshold is beyond the scope of this study, its wavelength should correlate with the minimum fault displacement that can be resolved in our experiments. The threshold wavelength would also vary with the amount of strength contrast between the components of the anisotropic material. For example, strain partitioning may occur above a lower threshold wavelength when the viscosity of the SLC is more than eight times greater than the viscosity of the weak zone material (as in Exp LE-08).

5.5.4. Implications for natural rift basins and model limitations

Exp LE-08 replicated basin-scale (>1 km long) ENE-WSW trending normal faults in the onshore Gippsland Basin by introducing closely spaced anisotropies in the Paleozoic Melbourne Zone basement. However, the NW-SE trending faults and the orthorhombic fault pattern in our model do not match the interpreted fault pattern in the onshore Gippsland Basin, both at basin and outcrop scale. It is plausible that NW-SE faults could have formed during Early Cretaceous rifting, but as suggested by the analogue model, their lateral and dip-slip displacement may have been small relative to the displacement along ENE-WSW faults. Therefore, the contrast in the geophysical signature of the rocks on either side of the NW-SE faults may have been too subtle for these structures to have been resolved in geophysical potential field data. Moreover, NW-SE faults would not have been optimally orientated for reactivation during periods of NNW-SSE contraction during Late Cretaceous and Cenozoic inversion. In contrast, ENE-WSW faults experienced reverse reactivation, which created ENE-WSW trending pop-up structures that define the present-day topography.

While the interaction between NNE-SSW to NE-SW trending basement fabric and Early Cretaceous ENE-WSW faulting in the western part of the Gippsland Basin remains speculative, our experiments provide insight into the geometry of basement anisotropies that are required for the formation of extension-oblique structures during rifting, without requiring reactivation of basement faults as the mechanism for inheritance. Our experiments also demonstrate the influence of a transverse, anomalously strong, anisotropic crustal block on rift basin architecture, as opposed to the more widely explored role of crustal weaknesses (e.g., Autin et al., 2013; Bellahsen and Daniel, 2005; Corti, 2004; Faccenna et al., 1995; Henza et al., 2011, 2010).

Extension-oblique faults can form within rift basins, not just as basin-bounding faults, provided that oblique, pre-existing anisotropies are present in the pre-deformed crust. Oblique kinematics (Withjack and Jamison, 1986) are not required to create extension-oblique faults when the

basement is sufficiently anisotropic, and this anisotropy does not have to occur in the lithospheric mantle (cf. Agostini et al., 2009; Brune et al., 2017; Corti, 2008). Our models show that the local strain direction indicated by individual faults above a strongly anisotropic basement does not reflect the N-S orthogonal extension boundary condition, which is analogous to the regional extension direction in a natural rift setting. This finding demonstrates the risk in inferring regional extension directions from fault orientations and highlights the importance of understanding non-plane strains in rift evolution and passive margin formation (Brune et al., 2018; Dewey et al., 1998).

Our experimental results also indicate that reactivation of pre-existing lower crustal weak zones is not an inheritance mechanism that leads to extension-oblique faulting, as the resulting fault traces will not be parallel to the anisotropy in the lower crust (cf. Holdsworth et al., 1997; Phillips et al., 2016). Instead, the azimuths of the associated faults form acute angles with both the imposed N-S extension direction and the E-W trending extension-orthogonal faults above the NLC, where there is no influence from basement anisotropies.

5.6. Conclusions

The experimental results presented in this paper describe the control of crustal strength on fault spacing and the length scale-dependent relationship between lower crustal anisotropies and fault orientations in the upper crust during a single phase of rifting. The influence of strength anisotropies in the lower crust on fault variability in the upper crust is a function of: (i) scale (i.e., the width and spacing of anisotropies relative to the size of the modelled area), and (ii) the mechanical properties of the individual zones that make up the anisotropic material. We show that the basement of a rift basin needs to be sufficiently anisotropic for extension-oblique rift faults to form across a wide area, and not just adjacent to the boundaries between different basement domains. As a result of this mechanism, faults can form oblique to the trend of pre-existing basement anisotropies, demonstrating that basement inheritance does not always occur as a result of reactivation. It is therefore important to explore for evidence of inheritance other than parallelism between new rift faults and basement structures when determining whether inheritance has impacted the fault network architecture in rift basins.

Acknowledgements

AS is supported by a Monash University Faculty of Science Dean's International Postgraduate Research Scholarship.

Chapter 6

Discussion and conclusions

6.1. Thesis summary

The aim of this project was to better understand how pre-existing basement structures and anisotropies influence subsequent brittle deformation in rift basins. This project was broken down into two sub-aims, which focused on: (i) recognizing how structural inheritance operates at different scales and (ii) exploring other mechanisms of interaction between basement rocks and their overlying cover rocks, other than reactivation of pre-existing basement structures. These were achieved by multi-scale fracture mapping, analysis, and modelling of fractures in sedimentary cover rocks and their underlying basement in the onshore Gippsland Basin of southeast Australia.

Fractures were digitally mapped at a wide range of scales using regional potential field geophysics (magnetic and gravity data), near-shore bathymetry, and high-resolution aerial orthophotos derived from UAV photogrammetry. By integrating these digital datasets with field observations, fracture maps at basin (>1 km) to outcrop scale were produced, from which overprinting relationships between fracture sets were identified. The result is a synthesis of brittle deformation in the onshore Gippsland Basin (Chapter 3), from Early Cretaceous basin-forming rifting through to Early Cretaceous–Cenozoic uplift and contractional events. The complex array of Cretaceous rift-related faults in the Gippsland Basin is attributed to the reactivation of basin-scale Paleozoic – or potentially Cambrian – basement structures, which locally re-oriented extension vectors in the western onshore Gippsland Basin and are either absent or were less influential in the eastern onshore and offshore portions of the basin.

To investigate whether this style of inheritance operates similarly at both regional and outcrop scale (Chapter 4), the orientations of basin-scale to outcrop-scale fracture traces derived from regional geophysics were compared with those derived from outcrop orthophotographs. Outcrop-scale fractures in cover rocks were also compared with outcrop-scale basement structures. Results from this study show that structural inheritance is not scale-invariant; basin-scale fractures in the cover record a history of reactivation, while outcrop-scale fractures more faithfully record the far-field paleostress. However, reactivation may not be the only mechanism for basin-scale inheritance in the onshore Gippsland Basin. From direct field observations of basement rocks, it was found that basement foliation forms a pervasive mechanical anisotropy that can potentially re-orient the surrounding strain and stress field and therefore influence the orientation of rift-related faults. Chapter 4 hypothesises that this penetrative fabric may have been responsible for the formation of NE-SW to ENE-WSW trending Early Cretaceous rift-related faults, which have the incorrect orientation for the inferred regional extension direction and are oblique to NE-SW to NNE-SSW trending basement structures.

Analogue experiments were carried out to test whether a pervasive basement anisotropy could contribute to the formation of extensional faults that are oblique to the imposed extension direction and the underlying basement anisotropy (Chapter 5). The experimental results suggest that an anomalously strong, vertically layered, anisotropic basement block can induce a strain rotation that is either consistent across the entire basement block or compartmentalized into the individual weak and strong zones that make up the anisotropy. Whichever one of these effects prevails is controlled by the strength contrast and geometry (i.e., spacing and horizontal thickness) of the strong and weak layers that make up the anisotropy. The resulting “misoriented” faults are not parallel to the basement anisotropy, which signifies that structural inheritance occurred without basement fault reactivation.

6.2. Research implications and future research recommendations

This section addresses several discussion points that arose throughout the project but are outside the scope of the individual research chapters (Chapters 3, 4, and 5).

6.2.1. Terminology: reactivation vs. basement inheritance

Structural inheritance occurs when the properties of basement rocks are transferred onto younger, overlying units. As demonstrated in this thesis, reactivation of pre-existing basement structures (*sensu* Holdsworth et al., 1997) is not the only mechanism by which the basement and cover can interact. A second mechanism is invoked, where stresses in the basement, whether they align with the far-field tectonic stress or reflect a locally perturbed stress regime, are inherited by the unconformably overlying cover. This process can result in a more subtle form of inheritance, which is expressed by brittle structures in cover rocks that are misaligned relative to their expected orientation under a known tectonic paleostress regime but are also oblique to pre-existing basement fractures, shear zones, and fabrics.

Here I propose that we refer to the second basement-cover interaction as “basement inheritance”, although other terms such as “basement-induced stress rotation” or “basement stress transfer” may also be appropriate. Following the style of fault terminology, another possibility would be to refer to this subtle basement-cover interaction as “soft-linked inheritance”, while the term “hard-linked inheritance” can be applied to reactivation. However, this implies that either: a) reactivated basement structures are linked physically to new fractures, or b) new fractures nucleate at the reactivated structure, which Collanega et al.(2019) have argued against. Regardless of the new term that is chosen, the main message is that “basement inheritance” must be treated as a separate phenomenon to reactivation. It is important that this expression of inheritance receives more attention in future studies of rift basins, as the influence

of basement inheritance may be equally significant to reactivation for the architecture of fracture networks.

6.2.2. The mechanisms of basement inheritance

There are two situations in which basement properties can be inherited by unconformably overlying cover rocks. Firstly, the topographic expression at the basement-cover interface can determine locations of maximum or minimum horizontal stress, controlling strain localisation, the site of fracture nucleation, and direction of fracture propagation during a tectonic event. This differs from passive inheritance, where tectonic forces do not play a role, and an uneven basement topography may contribute to differential compaction in unconsolidated cover sediments.

Finite element models of thrust faulting have shown that basement topographic highs can concentrate stresses, produce stress shadows, and altering the local principal stress directions. This process depends on the geometry of the topographic feature and the contrast in the geomechanical properties of the basement and cover rocks, which controls the resistance to shear along the basement-cover interface (Schedl and Wiltschko, 1987). Simple numerical studies may provide interesting insight into the role of basement topographical features on basement-cover mechanical coupling, stress concentration, and strain localisation in an extensional system.

The second mechanism for basement inheritance is associated with re-orientation of the (tectonic) far field stress near pre-existing basement faults, shear zones, or other surfaces of weakness (see Section 1.3.2.2). Previous photoelastic and numerical experiments have demonstrated a perturbation of the stress field in response to a tectonic load around pre-existing fractures within an otherwise homogenous, elastic medium (de Joussineau et al., 2003; Maerten et al., 2016; Segall and Pollard, 1980; Welch et al., 2014) (see Section 1.3.3). In the future, numerical methods may also be useful for investigating the influence of slip along these pre-existing fractures on a second, overlying unit. The focus would be to determine how stresses are coupled between the two units, and if the stress regime of the lower unit would be transferred to the upper unit, controlling the likelihood of different modes and orientations of failure in the upper unit.

6.2.3. From 2D to 3D fracture datasets

A number of techniques are now available for collecting structural measurements from 3D digital outcrop models (e.g., McCaffrey et al., 2005; Seers and Hodgetts, 2016; Thiele et al., 2016; Trinks et al., 2005; Vollgger and Cruden, 2016). However, most of the continuous outcrop sections of cover rocks in the onshore Gippsland Basin study area are subhorizontal

wavecut platforms. The full potential of deriving 3D digital outcrop models from UAV photogrammetry could not be utilized, as fractures were rarely exposed in 3D. Regardless, this project demonstrated the advantages of combining outcrop-scale fracture data in basement and cover rocks at the same scale, suggesting that this workflow would be even more powerful when 3D outcrop fracture datasets are available. The most obvious limitation is the rarity of exposed contacts between basement and cover rocks.

6.2.4. Recommendations for future studies in the Gippsland Basin

In 2015, a 2D seismic survey was conducted within the onshore Gippsland Basin study area along four transects. This dataset had not been released to the public at the time of preparation of this thesis. In the future, this dataset will be valuable for further studies on structural inheritance in the Gippsland Basin, as the Paleozoic Melbourne Zone basement, the overlying Lower Cretaceous Strzelecki Group, and therefore the contact between the two units are imaged (Costelloe and Fomin, 2015). This dataset would provide additional constraints on the fault network architecture of the study area at a resolution range that lies between geophysical potential field data and outcrop data.

The relative high strength and rigid behaviour of the Selwyn Block during Cretaceous rifting in the Bass Strait may have impacted the development of the onshore fault networks in the Gippsland Basin. Cayley et al. (2011) have proposed that these Selwyn Block properties may have been inherited from the underlying Mesoproterozoic or Archean lithospheric mantle. Because of the important role of mantle-hosted structures in tectonic inheritance (see Section 1.3.1), another direction of research on the topic of tectonic inheritance could be focused on the relationship between deep mantle structures and Jurassic–Cretaceous rifting along the Australian Southern Margin. The Australian Lithospheric Architecture Magnetotelluric Program (AusLAMP) magnetotelluric data (Duang et al., 2016) would be a key component in this type of study.

6.2.5. Differentiating between oblique rift kinematics and inheritance

The studies outlined in this thesis were conducted under the premise that Jurassic–Cretaceous Australian Southern Margin continental rifting was driven by broadly N-S directed extension (Miller et al., 2002; Williams et al., 2011). Full-fit, palinspastic reconstructions of the Australian-Antarctic margin (Williams et al., 2011) provided a preferred model for the lithospheric stretching direction based on the location of the restored continent-ocean boundary and from matching geological structures across the conjugate Australian and Antarctic margins. However, additional constraints from structural geology could not be provided within the scope of this project, due to the sparseness of kinematic indicators on faults for fault slip inversion and estimation of the paleostress regime.

This uncertainty in the lithospheric stretching direction (and hence the direction of regional extension) poses a challenge in differentiating between the role of oblique extension and structural inheritance in shaping the fault network in a rift basin. Both oblique rifting and inheritance create a transtensional system (e.g., Brune et al., 2018), but their relative roles in influencing basin-scale rift fault orientations require further exploration. Zwaan and Schreurs (2017) used analogue experiments to show that rift obliquity exerts first-order control on rift linkage, and that reactivation plays a secondary role, but only when the orientation of the pre-existing weaknesses is favourable. These results from lithospheric-scale models provide interesting insights on the role of lithospheric weaknesses and extension direction on rift segmentation and transfer zones but not on rift basin-internal rift-related structures. Future experiments that compare oblique rifting of a homogeneous crust with orthogonal rifting with crustal-level, pervasive anisotropies can deliver key insights on the relative contributions of oblique rifting and inheritance to the formation of basin-scale, rift-oblique rift faults. Findings from such a study would be beneficial for geologists working on reconstructing the tectonic history of ancient rift basins from field observations and regional datasets.

6.3. Concluding remarks

Structural inheritance, along with relative plate movements, contribute to variations in the orientation and kinematics of brittle structures along rifts. This thesis includes several new insights that further our understanding of the influence of inheritance on basin to outcrop-scale fracture patterns:

- Distinguishing basement inheritance from reactivation: In an extensional system, reactivation of basement structures leads to strain localisation, but the more subtle basement inheritance controls the orientations of new basin-scale, rift-related faults through mechanical basement-cover coupling and a rotation of the strain and stress fields due to pervasive basement anisotropies.
- The scale dependency of inheritance: Where there is a strong basement influence, outcrop-scale fractures are not always parallel to basin-scale faults or fracture zones. In the case of the onshore Gippsland Basin, rift-related faults were influenced by both reactivation and basement inheritance. During subsequent contraction, basin-scale faults were optimally oriented for reverse reactivation, whereas outcrop-scale fractures more accurately reflect the far-field paleostress. It is important to document the mode and kinematics of fracturing for correlating fracture sets from the same deformation event across scales.

- Local strain is not a direct reflection of regional strain: Maximum 2D horizontal strain inferred from brittle structures is not necessarily aligned with the far-field extension vectors, as demonstrated by analogue experiments where the kinematic boundary conditions are known. Therefore, we cannot rely solely on fault orientations for inferring regional paleo-extension directions.

Continental rifts always form in pre-deformed crust, which means that structural inheritance is likely to influence the architecture of the rift and its associated basins to varying degrees. The scale-dependent nature of inheritance has broad implications for global plate modelling, regional tectonics, and predicting the fluid storage and transport capabilities of fracture systems. The potential impact of inheritance on rift basins globally serves as an incentive for geologists to map and characterize their underlying basement rocks.

References

- Abul Khair, H., Cooke, D., Hand, M., 2015. Paleo stress contribution to fault and natural fracture distribution in the Cooper Basin. *Journal of Structural Geology* 79, 31–41. doi:10.1016/j.jsg.2015.07.007
- Adam, J., Urai, J.L., Wieneke, B., Oncken, O., Pfeiffer, K., Kukowski, N., Lohrmann, J., Hoth, S., van der Zee, W., Schmatz, J., 2005. Shear localisation and strain distribution during tectonic faulting—new insights from granular-flow experiments and high-resolution optical image correlation techniques. *Journal of Structural Geology* 27, 283–301. doi:10.1016/j.jsg.2004.08.008
- Aghaei, H., Hall, M., Wagstaff, B., Tait, A., 2017. Stratigraphic reconstruction of the Strzelecki Group outcrops in west Gippsland: new data on the present-day thickness and amount of erosion. *Australian Journal of Earth Sciences* 64, 251–264. doi:10.1080/08120099.2016.1278033
- Agostini, A., Corti, G., Zeoli, A., Mulugeta, G., 2009. Evolution, pattern, and partitioning of deformation during oblique continental rifting: Inferences from lithospheric-scale centrifuge models. *Geochemistry, Geophysics, Geosystems* 10. doi:10.1029/2009GC002676
- Aitken, A.R.A., Betts, P.G., Weinberg, R.F., Gray, D., 2009. Constrained potential field modeling of the crustal architecture of the Musgrave Province in central Australia: Evidence for lithospheric strengthening due to crust-mantle boundary uplift. *Journal of Geophysical Research* 114, B12405. doi:10.1029/2008JB006194
- Andersen, O.B., Knudsen, P., Berry, P.A.M., 2010. The DNSC08GRA global marine gravity field from double retracked satellite altimetry. *Journal of Geodesy* 84, 191–199. doi:10.1007/s00190-009-0355-9
- Anderson, E.M., 1905. The dynamics of faulting. *Transactions of the Edinburgh Geological Society* 8, 387–402. doi:https://doi.org/10.1144/transed.17.3.217
- Angelier, J., 1990. Inversion of field data in fault tectonics to obtain the regional stress—III. A new rapid direct inversion method by analytical means. *Geophysical Journal International*

- 103, 363–376. doi:10.1111/j.1365-246X.1990.tb01777.x
- Artyushkov, E. V., 1983. *Geodynamics*. Elsevier, Amsterdam.
- Ashby, D.E., 2013. *Influences on Continental Margin Development: A Case Study from the Santos Basin, South-eastern Brazil*. Durham University. PhD Thesis.
- Autin, J., Bellahsen, N., Leroy, S., Husson, L., Beslier, M.O., D'Acremont, E., 2013. The role of structural inheritance in oblique rifting: Insights from analogue models and application to the Gulf of Aden. *Tectonophysics* 607, 51–64. doi:10.1016/j.tecto.2013.05.041
- Aydin, A., 2000. Fractures, faults, and hydrocarbon entrapment, migration and flow. *Marine and Petroleum Geology* 17, 797–814. doi:10.1016/S0264-8172(00)00020-9
- Bache, F., Mortimer, N., Sutherland, R., Collot, J., Rouillard, P., Stagpoole, V., Nicol, A., 2014. Seismic stratigraphic record of transition from Mesozoic subduction to continental breakup in the Zealandia sector of eastern Gondwana. *Gondwana Research* 26, 1060–1078. doi:10.1016/j.gr.2013.08.012
- Barton, C.A., Zoback, M.D., 1994. Stress perturbations associated with active faults penetrated by boreholes: Possible evidence for near-complete stress drop and a new technique for stress magnitude measurement. *Journal of Geophysical Research: Solid Earth* 99, 9373–9390. doi:10.1029/93JB03359
- Beacom, L.E., Holdsworth, R.E., McCaffrey, K.J.W., Anderson, T.B., 2001. A quantitative study of the influence of pre-existing compositional and fabric heterogeneities upon fracture-zone development during basement reactivation. *Geological Society, London, Special Publications* 186, 195–211. doi:10.1144/gsl.sp.2001.186.01.12
- Becker, A.A., 1992. *The Boundary Element Method in Engineering: A Complete Course*. McGraw-Hill.
- Bell, J.S., 1996. Petro geoscience 2. In situ stresses in sedimentary rocks (part 2): Applications of stress measurements. *Geoscience Canada*.
- Bellahsen, N., Daniel, J.M., 2005. Fault reactivation control on normal fault growth: An experimental study. *Journal of Structural Geology* 27, 769–780. doi:10.1016/j.jsg.2004.12.003
- Bellahsen, N., Fournier, M., D'Acremont, E., Leroy, S., Daniel, J.M., 2006. Fault reactivation and rift localization: Northeastern Gulf of Aden margin. *Tectonics* 25, TC1007. doi:10.1029/2004TC001626
- Bemis, S.P., Micklethwaite, S., Turner, D., James, M.R., Akciz, S., Thiele, S.T., Bangash, H.A.,

2014. Ground-based and UAV-Based photogrammetry: A multi-scale, high-resolution mapping tool for structural geology and paleoseismology. *Journal of Structural Geology* 69, 163–178. doi:10.1016/j.jsg.2014.10.007
- Benes, V., Davy, P., 1996. Modes of continental lithospheric extension: Experimental verification of strain localization processes. *Tectonophysics* 254, 69–87. doi:10.1016/0040-1951(95)00076-3
- Bergbauer, S., Pollard, D.D., 2004. A new conceptual fold-fracture model including prefolding joints, based on the Emigrant Gap anticline, Wyoming. *Geological Society of America Bulletin* 116, 294. doi:10.1130/B25225.1
- Bernecker, T., Partridge, A.D., 2001. Emperor and Golden Beach subgroups: the onset of Late Cretaceous sedimentation in the Gippsland Basin, SE Australia, in: Hill, K.C., Bernecker, T. (Eds.), *Eastern Australasian Basins Symposium*. pp. 391–402.
- Bernecker, T., Smith, M.A., Hill, K.A., Constantine, A.E., 2003. Oil and Gas, fuelling Victoria's economy, in: Birch, W.D. (Ed.), *Geology of Victoria*, GSA Special Publication 23. pp. 469–487.
- Bernecker, T., Woollands, M.A., Wong, D., Moore, D.H., Smith, M.A., 2001. Hydrocarbon prospectivity of the deepwater Gippsland Basin, Victoria, Australia. *Australian Petroleum Exploration Association Journal* 41, 79–101.
- Bertrand, L., Jusseaume, J., Géraud, Y., Diraison, M., Damy, P.-C., Navelot, V., Haffen, S., 2018. Structural heritage, reactivation and distribution of fault and fracture network in a rifting context: Case study of the western shoulder of the Upper Rhine Graben. *Journal of Structural Geology* 108, 243–255. doi:10.1016/j.jsg.2017.09.006
- Birch, G.F., 1987. *Igneous Rocks of the Gippsland Basin*.
- Bird, P.C., Cartwright, J.A., Davies, T.L., 2014. Basement reactivation in the development of rift basins: an example of reactivated Caledonide structures in the West Orkney Basin. *Journal of the Geological Society* 172, 77–85. doi:10.1144/jgs2013-098
- Bisdorn, K., Nick, H.M., Bertotti, G., 2017. An integrated workflow for stress and flow modelling using outcrop-derived discrete fracture networks. *Computers and Geosciences* 103, 21–35. doi:10.1016/j.cageo.2017.02.019
- Blaikie, T.N., Betts, P.G., Armit, R.J., Ailleres, L., 2017. The ca. 1740–1710 Ma Leichhardt Event: Inversion of a continental rift and revision of the tectonic evolution of the North Australian Craton. *Precambrian Research* 292, 75–92.

- doi:10.1016/j.precamres.2017.02.003
- Bourne, S.J., Willemse, E.J.M., 2001. Elastic stress control on the pattern of tensile fracturing around a small fault network at Nash Point, UK. *Journal of Structural Geology* 23, 1753–1770. doi:[https://doi.org/10.1016/S0191-8141\(01\)00027-X](https://doi.org/10.1016/S0191-8141(01)00027-X)
- Boutelier, D., Cruden, A., Saumur, B., 2016. Density and visco-elasticity of Natrosol 250 HH solutions: Determining their suitability for experimental tectonics. *Journal of Structural Geology* 86, 153–165. doi:10.1016/j.jsg.2016.03.001
- Brune, S., Corti, G., Ranalli, G., 2017. Controls of inherited lithospheric heterogeneity on rift linkage: Numerical and analogue models of interaction between the Kenyan and Ethiopian rifts across the Turkana depression. *Tectonics* 1–20. doi:10.1002/2017TC004739
- Brune, S., Popov, A.A., Sobolev, S. V., 2012. Modeling suggests that oblique extension facilitates rifting and continental break-up. *Journal of Geophysical Research: Solid Earth* 117, B08402. doi:10.1029/2011JB008860
- Brune, S., Williams, S.E., Müller, R.D., 2018. Oblique rifting: the rule, not the exception. *Solid Earth* 9, 1187–1206. doi:<https://doi.org/10.5194/se-9-1187-2018>
- Bryan, S.E., Constantine, A.E., Stephens, C.J., Ewart, A., Schön, R.W., Parianos, J., 1997. Early Cretaceous volcano-sedimentary successions along the eastern Australian continental margin: Implications for the break-up of eastern Gondwana. *Earth and Planetary Science Letters* 153, 85–102. doi:10.1016/S0012-821X(97)00124-6
- Bryan, S.E., Ernst, R.E., 2008. Revised definition of Large Igneous Provinces (LIPs). *Earth-Science Reviews* 86, 175–202. doi:10.1016/j.earscirev.2007.08.008
- Byerlee, J., 1978. Friction of rocks. *Pure and Applied Geophysics* 116, 615–626.
- Cartwright, J.A., Lonergan, L., 1996. Volumetric contraction during the compaction of mudrocks: A mechanism for the development of regional-scale polygonal fault systems. *Basin Research* 8, 183–193. doi:10.1046/j.1365-2117.1996.01536.x
- Cawood, P.A., 2005. Terra Australis Orogen: Rodinia breakup and development of the Pacific and Iapetus margins of Gondwana during the Neoproterozoic and Paleozoic. *Earth-Science Reviews* 69, 249–279. doi:10.1016/j.earscirev.2004.09.001
- Cayley, R.A., 2011. Exotic crustal block accretion to the eastern Gondwanaland margin in the Late Cambrian-Tasmania, the Selwyn Block, and implications for the Cambrian-Silurian evolution of the Ross, Delamerian, and Lachlan orogens. *Gondwana Research* 19, 628–649. doi:10.1016/j.gr.2010.11.013

- Cayley, R.A., Korsch, R.J., Moore, D.H., Costelloe, R.D., Nakamura, A., Willman, C.E., Rawling, T.J., Morand, V.J., Skladzien, P.B., O'Shea, P.J., 2011. Crustal architecture of central Victoria: Results from the 2006 deep crustal reflection seismic survey. *Australian Journal of Earth Sciences* 58, 113–156. doi:10.1080/08120099.2011.543151
- Cayley, R.A., Taylor, D.H., VandenBerg, A.H.M., Moore, D.H., 2002. Proterozoic - Early Palaeozoic rocks and the Tyennan Orogeny in central Victoria: The Selwyn Block and its tectonic implications. *Australian Journal of Earth Sciences* 49, 225–254. doi:10.1046/j.1440-0952.2002.00921.x
- Chang, H.K., Kowsmann, R.O., Figueiredo, A.M.F., Bender, A., 1992. Tectonics and stratigraphy of the East Brazil Rift system: an overview. *Tectonophysics* 213, 97–138. doi:10.1016/0040-1951(92)90253-3
- Chantraprasert, S., McClay, K.R., Elders, C., 2001. 3D Rift Fault Systems of the Western Otway Basin, SE Australia, in: Hill, K.C., Bernecker, T. (Eds.), *Eastern Australasian Basins Symposium*. pp. 435–446.
- Chattopadhyay, A., Chakra, M., 2013. Influence of pre-existing pervasive fabrics on fault patterns during orthogonal and oblique rifting: An experimental approach. *Marine and Petroleum Geology* 39, 74–91. doi:10.1016/j.marpetgeo.2012.09.009
- Cilona, A., Aydin, A., Likerman, J., Parker, B., Cherry, J., 2016. Structural and statistical characterization of joint and multi-scale faults in alternating sandstone and shale turbidite sequence at the Santa Susana Field Laboratory: Implications for their effects on groundwater flow and contaminant transport. *Journal of Structural Geology* 85, 95–114. doi:10.1016/j.jsg.2016.02.003
- Cobbold, P.R., Cosgrove, J.W., Summers, J.M., 1971. Development of internal structures in deformed anisotropic rocks. *Tectonophysics* 12, 23–53. doi:10.1016/0040-1951(71)90065-5
- Collanega, L., Jackson, C.A., Bell, R.E., Coleman, A.J., Lenhart, A., Breda, A., 2019. Normal fault growth influenced by basement fabrics: the importance of preferential nucleation from pre-existing structures. *Basin Research* in press. doi:10.1111/bre.12327
- Colwell, J.B., Willcox, J.B., 1993. Regional structure of the Gippsland Basin: Interpretation and mapping of a deep seismic data set.
- Coney, P.J., Edwards, A., Hine, R., Morrison, F., Windrim, D., 1990. The regional tectonics of the Tasman orogenic system, eastern Australia. *Journal of Structural Geology* 13, 519–543.

- Constantine, A., 2001. Sedimentology, Stratigraphy and Palaeoenvironment of the Upper Jurassic-Lower Cretaceous Non-Marine Strzelecki Group, Gippsland Basin, Southeastern Australia. Monash University. PhD Thesis.
- Cooke, M., Islam, F., McGill, G., 2011. Basement controls on the scale of giant polygons in Utopia Planitia, Mars. *Journal of Geophysical Research: Planets* 116, E09003. doi:10.1029/2011JE003812
- Corti, G., 2012. Evolution and characteristics of continental rifting: Analog modeling-inspired view and comparison with examples from the East African Rift System. *Tectonophysics* 522–523, 1–33. doi:10.1016/j.tecto.2011.06.010
- Corti, G., 2008. Control of rift obliquity on the evolution and segmentation of the main Ethiopian rift. *Nature Geoscience* 1, 258–262. doi:10.1038/ngeo160
- Corti, G., 2004. Centrifuge modelling of the influence of crustal fabrics on the development of transfer zones: Insights into the mechanics of continental rifting architecture. *Tectonophysics* 384, 191–208. doi:10.1016/j.tecto.2004.03.014
- Corti, G., van Wijk, J., Cloetingh, S., Morley, C.K., 2007. Tectonic inheritance and continental rift architecture: Numerical and analogue models of the East African Rift system. *Tectonics* 26, 1–13. doi:10.1029/2006TC002086
- Costelloe, R.D., Fomin, T., 2015. L206 South Gippsland Deep Crustal Seismic Survey, VIC 2015.
- Crouch, S.L., Starfield, A.M., 1983. *Boundary Element Method in Solid Mechanics: With Applications in Rock Mechanics and Geological Engineering*. Allen & Unwin, London.
- Cruden, A.R., Nasser, M.H.B., Pysklywec, R., 2006. Surface topography and internal strain variation in wide hot orogens from three-dimensional analogue and two-dimensional numerical vice models. *Geological Society Special Publications* 253, 79–104. doi:10.1144/GSL.SP.2006.253.01.04
- Cruikshank, K.M., Aydin, A., 1995. Unweaving the joints in Entrada Sandstone, Arches National Park, Utah, U.S.A. *Journal of Structural Geology* 17, 409–421. doi:10.1016/0191-8141(94)00061-4
- Daly, M.C., Chorowicz, J., Fairhead, J.D., 1989. Rift basin evolution in Africa: the influence of reactivated steep basement shear zones. *Geological Society, London, Special Publications* 44, 309–334. doi:10.1144/GSL.SP.1989.044.01.17
- de Joussineau, G., Petit, J.P., Gauthier, B.D.M., 2003. Photoelastic and numerical investigation

- of stress distributions around fault models under biaxial compressive loading conditions. *Tectonophysics* 363, 19–43. doi:10.1016/S0040-1951(02)00648-0
- De Paola, N., Holdsworth, R.E., McCaffrey, K.J.W., 2005. The influence of lithology and pre-existing structures on reservoir-scale faulting patterns in transtensional rift zones. *Journal of the Geological Society* 162, 471–480. doi:10.1144/0016-764904-043
- Dee, S.J., Yielding, G., Freeman, B., Healy, D., Kusznir, N.J., Grant, N., Ellis, P., 2007. Elastic dislocation modelling for prediction of small-scale fault and fracture network characteristics. *Fractured Reservoirs* 270, 139–155. doi:10.1144/Gsl.Sp.2007.270.01.10
- Delvaux, D., Moeys, R., Stapel, G., Petit, C., Levi, K., Miroshnichenko, A., Ruzhich, V., San'kov, V., 1997. Paleostress reconstructions and geodynamics of the Baikal region, Central Asia, Part 2. Cenozoic rifting. *Tectonophysics* 282, 1–38. doi:10.1016/S0040-1951(97)00210-2
- Deng, C., Gawthorpe, R.L., Finch, E., Fossen, H., 2017. Influence of a pre-existing basement weakness on normal fault growth during oblique extension: Insights from discrete element modeling. *Journal of Structural Geology*. doi:10.1016/j.jsg.2017.11.005
- Dentith, M., Mudge, S.T., 2014. *Geophysics for the Mineral Exploration Geoscientist*. Cambridge University Press.
- Dering, G.M., Micklethwaite, S., Thiele, S.T., Vollgger, S.A., Cruden, A.R., 2019. Review of drones, photogrammetry and emerging sensor technology for the study of dykes: Best practises and future potential. *Journal of Volcanology and Geothermal Research*. doi:10.1016/j.jvolgeores.2019.01.018
- Dewey, J., Holdsworth, R., Strachan, R., 1998. Transpression and transtension zones. Geological Society, London, Special Publications 135, 1–14.
- Duang, J., Taylor, D., Czarnota, K., Cayley, R., Chopping, R., 2016. AusLAMP MT over Victoria: New insight from 3D modelling highlights regions of anomalously conductive mantle and unexpected linear trends in the crust, in: ASEG-PESA 2016: Adelaide, Australia.
- Duarte, J.C., Schellart, W.P., Cruden, A.R., 2014. Rheology of petrolatum-paraffin oil mixtures: Applications to analogue modelling of geological processes. *Journal of Structural Geology* 63, 1–11. doi:10.1016/j.jsg.2014.02.004
- Duddy, I.R., Green, P.F., 1992. Tectonic development of the Gippsland Basin and environs:

- identification of key episodes using Apatite Fission Track Analysis (AFTA), in: Gippsland Basin Symposium 22-23 June 1992. Melbourne, pp. 111–120.
- Dumitru, T.A., Hill, K.C., Coyle, D.A., Duddy, I.R., Foster, D.A., Gleadow, A.J.W., Green, P.F., Kohn, B.P., Laslett, G.M., O’Sullivan, P.B., 1991. Fission track thermochronology: Application to continental rifting of south-eastern Australia. *The APEA Journal* 31, 131–142.
- Dunbar, J.A., Sawyer, D.S., 1989. How preexisting weaknesses control the style of continental breakup. *Journal of Geophysical Research* 94, 7278–7292. doi:10.1029/JB094iB06p07278
- Dyksterhuis, S., Müller, R.D., 2008. Cause and evolution of intraplate orogeny in Australia. *Geology* 36, 495–498. doi:10.1130/G24536A.1
- Eisenbeiß, H., 2009. UAV Photogrammetry. ETH Zürich. PhD Thesis. doi:ethz-b-000265761
- Ernst, R.E., Head, J.W., Parfitt, E., Grosfils, E., Wilson, L., 1995. Giant radiating dyke swarms on Earth and Venus. *Earth Science Reviews* 39, 1–58. doi:10.1016/0012-8252(95)00017-5
- Etheridge, M.A., Branson, J.C., Stuart-Smith, P.G., 1987. The Bass, Gippsland and Otway Basins, southeast Australia: A branched rift system formed by continental extension. *Sedimentary Basins and Basin-Forming Mechanisms* 12, 147–162.
- Etheridge, M.A., Branson, J.C., Stuart-Smith, P.G., 1985. Extensional basin-forming structures in Bass Strait and their importance for hydrocarbon exploration. *The APEA Journal* 25, 344–361.
- Faccenna, C., Nalpas, T., Brun, J.P., Davy, P., Bosi, V., 1995. The influence of pre-existing thrust faults on normal fault geometry in nature and in experiments. *Journal of Structural Geology* 17, 1139–1149. doi:10.1016/0191-8141(95)00008-2
- Fairhead, J.D., Binks, R.M., 1991. Differential opening of the Central and South Atlantic Oceans and the opening of the West African rift system. *Tectonophysics* 187, 191–203. doi:10.1016/0040-1951(91)90419-S
- Fazlikhani, H., Fossen, H., Gawthorpe, R.L., Faleide, J.I., Bell, R.E., 2017. Basement structure and its influence on the structural configuration of the northern North Sea rift. *Tectonics* 36, 1151–1177. doi:10.1002/2017TC004514
- Finlayson, D.M., Johnstone, D.W., Owen, A.J., Wake-Dyster, K.D., 1996. Deep seismic images and the tectonic framework of early rifting in the Otway Basin, Australian southern

- margin. *Tectonophysics* 264, 137–152. doi:10.1016/S0040-1951(96)00123-0
- Fossen, H., Tikoff, B., 1998. Extended models of transpression and transtension, and application to tectonic settings. *Geological Society, London, Special Publications* 135, 15–33. doi:10.1144/GSL.SP.1998.135.01.02
- Foster, D.A., Gleadow, A.J.W., 1992. Reactivated tectonic boundaries and implications for the reconstruction of southeastern Australia and northern Victoria Land, Antarctica. *Geology* 20, 267–270. doi:10.1130/0091-7613(1992)020<0267:RTBAIF>2.3.CO;2
- Foster, D.A., Gray, D.R., 2000. Evolution and Structure of the Lachlan Fold Belt (Orogen) of Eastern Australia. *Annual Review of Earth and Planetary Sciences* 28, 47–80. doi:0084–6597/00/0515–0047
- Gardner, T., Webb, J., Pezzia, C., Amborn, T., Tunnell, R., Flanagan, S., Merritts, D., Marshall, J., Fabel, D., Cupper, M.L., 2009. Episodic intraplate deformation of stable continental margins: evidence from Late Neogene and Quaternary marine terraces, Cape Liptrap, Southeastern Australia. *Quaternary Science Reviews* 28, 39–53. doi:10.1016/j.quascirev.2008.10.004
- Geoscience Australia, 2018a. Otway Basin [WWW Document]. URL <http://www.ga.gov.au/scientific-topics/energy/province-sedimentary-basin-geology/petroleum/offshore-southern-australia/otway> (accessed 8.8.18).
- Geoscience Australia, 2018b. Sorell Basin [WWW Document]. URL <http://www.ga.gov.au/scientific-topics/energy/province-sedimentary-basin-geology/petroleum/offshore-southern-australia/sorell> (accessed 8.8.18).
- Geoscience Australia, 2018c. Geophysical Archive Data Delivery System [WWW Document]. URL http://www.geoscience.gov.au/cgi-bin/mapserv?map=/nas/web/ops/prod/apps/mapserver/gadds/wms_map/gadds.map&mode=browse (accessed 3.12.18).
- Geoscience Australia, 2001. GSV West Gippsland VIMP Vic magnetic grid geodetic. doi:http://dx.doi.org/10.4225/25/5625A59767D4A
- Gibson, G.M., Totterdell, J.M., White, L.T., Mitchell, C.H., Stacey, A.R., Morse, M.P., Whitaker, A., 2013. Pre-existing basement structure and its influence on continental rifting and fracture zone development along Australia’s southern rifted margin. *Journal of the Geological Society* 170, 365–377. doi:10.1144/jgs2012-040
- Gillespie, P.A., Howard, C.B., Walsh, J.J., Watterson, J., 1993. Measurement and

- characterisation of spatial distributions of fractures. *Tectonophysics* 226, 113–141. doi:10.1016/0040-1951(93)90114-Y
- Gray, D.R., 1997. Tectonics of the southeastern Australian Lachlan Fold Belt: structural and thermal aspects. *Geological Society, London, Special Publications* 121, 149–177. doi:10.1144/GSL.SP.1997.121.01.07
- Gray, D.R., Foster, D.A., Gray, C., Cull, J., Gibson, G., 1998. Lithospheric Structure of the Southeast Australian Lachlan Orogen along the Victorian Global Geoscience Transect. *International Geology Review* 40, 1088–1117. doi:10.1080/00206819809465256
- Gray, D.R., Foster, D.A., Morand, V.J., Willman, C.E., Cayley, R.A., Spaggiari, C.V., Taylor, D.H., Gray, C.M., VandenBerg, A.H.M., Hendrickx, M.A., Wilson, C.J.L., 2003. Structure, metamorphism, geochronology and tectonics of Palaeozoic rocks, in: Birch, W.D. (Ed.), *Geology of Victoria*, GSA Special Publication 23. pp. 15–70.
- Gray, D.R., Janssen, C., Vapnik, Y., 1999. Deformation character and palaeo-fluid flow across a wrench fault within a Palaeozoic subduction-accretion system: Waratah Fault Zone, southeastern Australia. *Journal of Structural Geology* 21, 191–214. doi:10.1016/S0191-8141(98)00115-1
- Gray, D.R., Mortimer, L., 1996. Implications of overprinting deformations and fold interference patterns in the Melbourne Zone, Lachlan Fold Belt. *Australian Journal of Earth Sciences* 43, 103–114. doi:10.1080/08120099608728240
- Gray, D.R., Willman, C.E., 1991. Thrust-related strain gradients and thrusting mechanisms in a chevron-folded sequence, southeastern Australia. *Journal of Structural Geology* 13, 691–710. doi:10.1016/0191-8141(91)90031-D
- Gross, M.R., Fischer, M.P., Engelder, T., Greenfield, R.J., 1995. Factors controlling joint spacing in interbedded sedimentary rocks: integrating numerical models with field observations from the Monterey Formation, USA, in: Ameen, M.S. (Ed.), *Geological Society Special Publication*. pp. 215–233. doi:10.1144/GSL.SP.1995.092.01.12
- Hardebol, N.J., Bertotti, G., 2013. DigiFract: A software and data model implementation for flexible acquisition and processing of fracture data from outcrops. *Computers & Geosciences* 54, 326–336. doi:10.1016/j.cageo.2012.10.021
- Healy, D., Blenkinsop, T.G., Timms, N.E., Meredith, P.G., Mitchell, T.M., Cooke, M.L., 2014. Polymodal faulting: Time for a new angle on shear failure. *Journal of Structural Geology* 80, 57–71. doi:10.1016/j.jsg.2015.08.013

- Healy, D., Jones, R.R., Holdsworth, R.E., 2006. Three-dimensional brittle shear fracturing by tensile crack interaction. *Nature* 439, 64–67. doi:10.1038/nature04346
- Healy, D., Rizzo, R.E., Cornwell, D.G., Farrell, N.J.C., Watkins, H., Timms, N.E., Gomez-Rivas, E., Smith, M., 2016. FracPaQ: A MATLABTM toolbox for the quantification of fracture patterns. *Journal of Structural Geology* 95, 1–16. doi:10.1016/j.jsg.2016.12.003
- Healy, D., Yielding, G., Kuszniir, N., 2004. Fracture prediction for the 1980 El Asnam, Algeria earthquake via elastic dislocation modeling. *Tectonics* 23, 1–21. doi:10.1029/2003TC001575
- Heath, P.J., 2007. Analysis of potential field gradient tensor data: forward modelling, inversion and near-surface exploration. University of Adelaide. PhD Thesis.
- Heilman, E., Kolawole, F., Atekwana, E.A., Mayle, M., 2019. Controls of Basement Fabric on the Linkage of Rift Segments. *Tectonics*. doi:10.1029/2018TC005362
- Henza, A.A., Withjack, M.O., Schlische, R.W., 2011. How do the properties of a pre-existing normal-fault population influence fault development during a subsequent phase of extension? *Journal of Structural Geology* 33, 1312–1324. doi:10.1016/j.jsg.2011.06.010
- Henza, A.A., Withjack, M.O., Schlische, R.W., 2010. Normal-fault development during two phases of non-coaxial extension: An experimental study. *Journal of Structural Geology* 32, 1656–1667. doi:10.1016/j.jsg.2009.07.007
- Hill, K.A., Cooper, G.T., Richardson, M.J., Lavin, C.J., 1994. Structural framework of the Eastern Otway basin: inversion and interaction between two major structural provinces. *Exploration Geophysics*. doi:10.1071/EG994079
- Hill, K.A., Finlayson, D.M., Hill, K.C., Cooper, G.T., 1995. Mesozoic tectonics of the Otway Basin region: the legacy of Gondwana and the active Pacific margin — a review and ongoing research. *The APPEA Journal* 35, 467–493. doi:https://doi.org/10.1071/AJ94030
- Hill, K.C., Hill, K.A., Cooper, G.T., O’Sullivan, A.J., O’Sullivan, P.B., Richardson, M.J., 1995. Inversion around the Bass Basin, SE Australia. Geological Society, London, Special Publications 88, 525–547. doi:10.1144/GSL.SP.1995.088.01.27
- Hillis, R.R., Reynolds, S.D., 2000. The Australian Stress Map. *Journal of the Geological Society* 157, 915–921. doi:10.1144/jgs.157.5.915
- Holdgate, G.R., Gallagher, S.J., 2003. Tertiary, a period of transition to marine basin environments, in: Birch, W.D. (Ed.), *Geology of Victoria*, GSA Special Publication 23. pp. 289–335.

- Holdgate, G.R., McNicol, M.D., 1992. New directions - old ideas: hydrocarbon prospects of the Strzelecki Group onshore Gippsland Basin, in: Gippsland Basin Symposium 22-23 June 1992. Melbourne, pp. 121–132.
- Holdgate, G.R., Rodriguez, C., Johnstone, E.M., Wallace, M.W., Gallagher, S.J., 2003. The Gippsland Basin Top Latrobe Unconformity and its expression in other Southeast Australia basins. *The APPEA Journal* 43, 149–173.
- Holdgate, G.R., Wallace, M.W., Forbes, S., 2015. Pre-Cenozoic geology of the Latrobe Valley Area—onshore Gippsland Basin, S.E. Australia. *Australian Journal of Earth Sciences* 62, 695–716. doi:10.1080/08120099.2015.1085901
- Holdsworth, R.E., Butler, C.A., Roberts, A.M., 1997. The recognition of reactivation during continental deformation. *Journal of the Geological Society* 154, 73–78. doi:10.1144/gsjgs.154.1.0073
- Holdsworth, R.E., Stewart, M., Imber, J., Strachan, R.A., 2001. The structure and rheological evolution of reactivated continental fault zones: a review and case study. *Geological Society, London, Special Publications* 184, 115–137. doi:10.1144/GSL.SP.2001.184.01.07
- Homberg, C., Hu, J.C., Angelier, J., Bergerat, F., Lacombe, O., 1997. Characterization of stress perturbations near major fault zones: insights from 2-D distinct-element numerical modelling and field studies (Jura mountains). *Journal of Structural Geology* 19, 703–718. doi:10.1016/S0191-8141(96)00104-6
- Hubbert, M.K., 1937. Theory of scale models as applied to the study of geologic structures. *Geological Society of America Bulletin* 48, 1459–1520. doi:10.1130/GSAB-48-1459
- Jaeger, J.C., Cook, N.G.W., 1979. *Fundamentals of Rock Mechanics*. Chapman and Hall.
- Jaffey, A.H., Flynn, K.F., Glendenin, L.E., Bentley, W.C., Essling, A.M., 1971. Precision Measurement of Half-Lives and Specific Activities of ²³⁵U and ²³⁸U. *Physical Review C* 4, 1889–1906. doi:10.1103/PhysRevC.4.1889
- Kapp, M.W., Hohenwarter, A., Wurster, S., Yang, B., Pippan, R., 2016. Anisotropic deformation characteristics of an ultrafine- and nanolamellar pearlitic steel. *Acta Materialia* 106, 239–248. doi:10.1016/j.actamat.2015.12.037
- Kattenhorn, S.A., Aydin, A., Pollard, D.D., 2000. Joints at high angles to normal fault strike: an explanation using 3-D numerical models of fault-perturbed stress fields. *Journal of Structural Geology* 22, 1–23.

- Keetley, J.T., Hill, K.C., Nguyen, C., 2001. Mesoscopic fold and thrust structures at Cape Liptrap, Victoria, Australia; a PNG analogue?, in: Hill, K.C., Bernecker, T. (Eds.), *Eastern Australasian Basins Symposium*. pp. 25–28.
- Kennett, B.L.N., Fichtner, A., Fishwick, S., Yoshizawa, K., 2013. Australian seismological referencemodel (AuSREM): Mantle component. *Geophysical Journal International* 192, 871–887. doi:10.1093/gji/ggs065
- Kirkpatrick, J.D., Bezerra, F.H.R., Shipton, Z.K., Do Nascimento, A.F., Pytharouli, S.I., Lunn, R.J., Soden, A.M., 2013. Scale-dependent influence of pre-existing basement shear zones on rift faulting: a case study from NE Brazil. *Journal of the Geological Society* 170, 237–247. doi:10.1144/jgs2012-043
- Klitgord, K.D., Schouten, H., 1986. Plate kinematics of the central Atlantic, in: Vogt, P.R., Tucholke, B.E. (Eds.), *The Western North Atlantic Region*. Geological Society of America. doi:https://doi.org/10.1130/DNAG-GNA-M
- Krantz, R.W., 1988. Multiple fault sets and three-dimensional strain: Theory and application. *Journal of Structural Geology* 10, 225–237. doi:10.1016/0191-8141(88)90056-9
- Krassay, A.A., Cathro, D.L., Ryan, D.J., 2004. A regional tectonostratigraphic framework for the Otway Basin. *Eastern Australasian Basins Symposium II* 97–116.
- Lavenu, A.P.C., Lamarche, J., Gallois, A., Gauthier, B.D.M., 2013. Tectonic versus diagenetic origin of fractures in a naturally fractured carbonate reservoir analog (Nerthe anticline, southeastern France). *AAPG Bulletin* 97, 2207–2232. doi:10.1306/04041312225
- Lezzar, K.E., Tiercelin, J.-J., Le Turdu, C., Cohen, A.S., Reynolds, D.J., Le Gall, B., Scholz, C.A., 2002. Control of normal fault interaction on the distribution of major Neogene sedimentary depocenters, Lake Tanganyika, East African rift. *AAPG Bulletin* 86, 1027–1059.
- Lonergan, L., Cartwright, J., Jolly, R., 1998. The geometry of polygonal fault systems in Tertiary mudrocks of the North Sea. *Journal of Structural Geology* 20, 529–548. doi:10.1016/S0191-8141(97)00113-2
- Ludwig, K.R., 2012. *Isoplot/Ex*, v. 3.75. Berkeley Geochronology Center Special Publication 5.
- Ma, X., Wu, D., 1987. Cenozoic extensional tectonics in China. *Tectonophysics* 133, 243–255. doi:10.1016/0040-1951(87)90268-X
- Maerten, L., Gillespie, P., Pollard, D.D., 2002. Effects of local stress perturbation on secondary

- fault development. *Journal of Structural Geology* 24, 145–153. doi:10.1016/S0191-8141(01)00054-2
- Maerten, L., Maerten, F., Lejri, M., Gillespie, P., 2016. Geomechanical paleostress inversion using fracture data. *Journal of Structural Geology* 89, 197–213. doi:10.1016/j.jsg.2016.06.007
- Marchegiani, L., Van Dijk, J.P., Gillespie, P. a, Tondi, E., Cello, G., 2006. Scaling properties of the dimensional and spatial characteristics of fault and fracture systems in the Majella Mountain, central Italy. *Geological Society Special Publication* 261, 113–131. doi:10.1144/GSL.SP.2006.261.01.09
- Matthews, K.J., Seton, M., Müller, R.D., 2012. A global-scale plate reorganization event at 105–100 Ma. *Earth and Planetary Science Letters* 355–356, 283–298. doi:10.1016/j.epsl.2012.08.023
- Mattinson, J.M., 2005. Zircon U–Pb chemical abrasion (“CA-TIMS”) method: Combined annealing and multi-step partial dissolution analysis for improved precision and accuracy of zircon ages. *Chemical Geology* 220, 47–66. doi:https://doi.org/10.1016/j.chemgeo.2005.03.011
- McCaffrey, K.J.W., 1997. Controls on reactivation of a major fault zone: the Fair Head–Clew Bay line in Ireland. *Journal of the Geological Society* 154, 129–133. doi:10.1144/gsjgs.154.1.0129
- McCaffrey, K.J.W., Jones, R.R., Holdsworth, R.E., Wilson, R.W., Clegg, P., Imber, J., Holliman, N., Trinks, I., 2005. Unlocking the spatial dimension: digital technologies and the future of geoscience fieldwork. *Journal of the Geological Society* 162, 927–938. doi:10.1144/0016-764905-017
- McGinnis, R.N., Ferrill, D.A., Morris, A.P., Smart, K.J., Lehrmann, D., 2017. Mechanical stratigraphic controls on natural fracture spacing and penetration. *Journal of Structural Geology* 95, 160–170. doi:10.1016/j.jsg.2017.01.001
- McLean, M.A., Morand, V.J., Cayley, R.A., 2010. Gravity and magnetic modelling of crustal structure in central Victoria: what lies under the Melbourne Zone? *Australian Journal of Earth Sciences* 57, 153–173. doi:10.1080/08120090903416245
- McPhail, A., 2000. A Petrographic and Geochemical Study of Gippsland Basin Volcanics. University of Adelaide. PhD Thesis.
- Meeuws, F.J.E., Holford, S.P., Foden, J.D., Schofield, N., 2016. Distribution, chronology and

- causes of Cretaceous - Cenozoic magmatism along the magma-poor rifted southern Australian margin: Links between mantle melting and basin formation. *Marine and Petroleum Geology* 73, 271–298. doi:10.1016/j.marpetgeo.2016.03.003
- Michael, A.J., 1984. Determination of stress from slip data: faults and folds. *Journal of Geophysical Research* 89, 11517–11526. doi:10.1029/JB089iB13p11517
- Miller, J.M.L., Norvick, M.S., Wilson, C.J.L., 2002. Basement controls on rifting and the associated formation of ocean transform faults - Cretaceous continental extension of the southern margin of Australia. *Tectonophysics* 359, 131–155. doi:10.1016/S0040-1951(02)00508-5
- Mollard, J.D., 1962. Photo Analysis and Interpretation in Engineering-Geology Investigations: A Review, in: Fluhr, T., Legget, R.F. (Eds.), *Reviews in Engineering Geology*, Volume 1. Geological Society of America, New York, pp. 105–128.
- Molnar, N.E., Cruden, A.R., Betts, P.G., 2018. Unzipping continents and the birth of microcontinents. *Geology* 46, 451–454. doi:10.1130/G40021.1
- Molnar, N.E., Cruden, A.R., Betts, P.G., 2017. Interactions between propagating rotational rifts and linear rheological heterogeneities: Insights from three-dimensional laboratory experiments. *Tectonics* 36, 420–443. doi:10.1002/2016TC004447
- Moore, A.M.G., Stagg, H.M.J., Norvick, M.S., 2000. Deep-water Otway Basin: A new assessment of the tectonics and hydrocarbon prospectivity. *The APPEA Journal* 66–85.
- Moore, D.H., Betts, P.G., Hall, M., 2016. Constraining the VanDieland microcontinent at the edge of East Gondwana, Australia. *Tectonophysics* 687, 158–179. doi:10.1016/j.tecto.2016.09.009
- Moore, D.H., Betts, P.G., Hall, M., 2015. Fragmented Tasmania: the transition from Rodinia to Gondwana. *Australian Journal of Earth Sciences* 62, 1–35. doi:10.1080/08120099.2014.966757
- Moore, D.H., Wong, D., 2001. Down and out in Gippsland: using potential fields to look deeper and wider for new hydrocarbons. *Petroleum Exploration Society of Australia Special Publication* 1, 363–371.
- Morley, C.K., 2010. Stress re-orientation along zones of weak fabrics in rifts: An explanation for pure extension in “oblique” rift segments? *Earth and Planetary Science Letters* 297, 667–673. doi:10.1016/j.epsl.2010.07.022
- Morley, C.K., Nelson, R.A., Patton, T.L., Munn, S.G., 1990. Transfer zones in the East African

- rift system and their relevance to hydrocarbon exploration in rifts. *AAPG Bulletin* 74, 1234–1253. doi:10.1306/0C9B2475-1710-11D7-8645000102C1865D
- Muirhead, J.D., Kattenhorn, S.A., 2018. Activation of preexisting transverse structures in an evolving magmatic rift in East Africa. *Journal of Structural Geology* 106, 1–18. doi:10.1016/j.jsg.2017.11.004
- Müller, R.D., Dyksterhuis, S., Rey, P., 2012. Australian paleo-stress fields and tectonic reactivation over the past 100 Ma. *Australian Journal of Earth Sciences* 59, 13–28. doi:10.1080/08120099.2011.605801
- Müller, R.D., Seton, M., Zahirovic, S., Williams, S.E., Matthews, K.J., Wright, N.M., Shephard, G.E., Maloney, K.T., Barnett-Moore, N., Hosseinpour, M., Bower, D.J., Cannon, J., 2016. Ocean Basin Evolution and Global-Scale Plate Reorganization Events Since Pangea Breakup. *Annual Review of Earth and Planetary Sciences* 44, 107–138. doi:10.1146/annurev-earth-060115-012211
- Munro, M.A., Blenkinsop, T.G., 2012. MARD-A moving average rose diagram application for the geosciences. *Computers and Geosciences* 49, 112–120. doi:10.1016/j.cageo.2012.07.012
- Nakamura, A., 2016. Isostatic Residual Gravity Anomaly Grid of Onshore Australia 2016. doi:http://dx.doi.org/10.4225/25/589c606cbaf50
- Narr, W., Suppe, J., 1991. Joint spacing in sedimentary rocks. *Journal of Structural Geology* 13, 1037–1048. doi:10.1016/0191-8141(91)90055-N
- Nearmap, 2018. PhotoMaps by nearmap [WWW Document]. URL <http://maps.au.nearmap.com/?> (accessed 3.12.18).
- Nelson, R.A., 1985. *Geological Analysis of Naturally Fractured Reservoirs*. Gulf Publishing Company, Houston.
- Norvick, M.S., Smith, M.A., Power, M.R., 2001. The Plate Tectonic Evolution of Eastern Australasia Guided by the Stratigraphy of the Gippsland Basin, in: *Eastern Australasian Basins Symposium*. Hill, K.C. Bernecker, T., pp. 15–23.
- Norvick, M.S., Smith, M.S., 2001. Mapping the plate tectonic reconstruction of southern and southeastern Australia and implications for petroleum systems. *The APPEA Journal* 41, 15–35.
- O'Brien, G.W., Reeves, C.V., Milligan, P.R., Morse, M.P., Alexander, E.M., Willcox, J.B., Yunxuan, Z., Finlayson, D.M., Brodie, R.C., 1994. New ideas on the rifting history and

- structural architecture of the western Otway Basin: evidence from the integration of aeromagnetic, gravity and seismic data. *The APPEA Journal* 34, 529–554. doi:<https://doi.org/10.1071/AJ93042>
- O'Brien, G.W., Tingate, P.R., Goldie Divko, L.M., Miranda, J.A., Campi, M.J., Liu, K., 2013. Basin-scale fluid flow in the Gippsland Basin: implications for geological carbon storage. *Australian Journal of Earth Sciences* 60, 59–70. doi:10.1080/08120099.2013.755567
- O'Halloran, G.J., Johnstone, E.M., 2001. Late Cretaceous Rift Volcanics of the Gippsland Basin, SE Australia - New Insights from 3D Seismic, in: Hill, K.C., Bernecker, T. (Eds.), *Eastern Australasian Basins Symposium*. Melbourne, pp. 353–361.
- Okada, Y., 1992. Internal deformation due to shear and tensile faults in a half-space. *Bulletin - Seismological Society of America* 82, 1018–1040.
- Olsen, K.H., Scott Baldrige, W., Callender, J.F., 1987. Rio Grande rift: An overview. *Tectonophysics* 143, 119–139. doi:10.1016/0040-1951(87)90083-7
- Peace, A., Dempsey, E., Schiffer, C., Welford, J., McCaffrey, K., Imber, J., Phethean, J., 2018a. Evidence for Basement Reactivation during the Opening of the Labrador Sea from the Makkovik Province, Labrador, Canada: Insights from Field Data and Numerical Models. *Geosciences* 8, 308. doi:10.3390/geosciences8080308
- Peace, A., McCaffrey, K., Imber, J., van Hunen, J., Hobbs, R., Wilson, R., 2018b. The role of pre-existing structures during rifting, continental breakup and transform system development, offshore West Greenland. *Basin Research* 30, 373–394. doi:10.1111/bre.12257
- Peacock, D.C.P., Sanderson, D.J., 2018. Structural analyses and fracture network characterisation: Seven pillars of wisdom. *Earth-Science Reviews* 184, 13–28. doi:10.1016/j.earscirev.2018.06.006
- Pérez-Flores, P., Veloso, E., Cembrano, J., Sánchez-Alfaro, P., Lizama, M., Arancibia, G., 2017. Fracture network, fluid pathways and paleostress at the Tolhuaca geothermal field. *Journal of Structural Geology* 96, 134–148. doi:10.1016/j.jsg.2017.01.009
- Perincek, D., Cockshell, C.D., 1995. The Otway Basin: Early Cretaceous rifting to Neogene inversion. *The APPEA Journal* 35, 451–466.
- Perincek, D., Simons, B., Pettifer, G.R., 1994. The tectonic framework and associated play types of the western Otway Basin, Victoria, Australia. *The APPEA Journal* 34, 460–478. doi:<https://doi.org/10.1071/AJ93038>

- Philipp, S.L., Gudmundsson, A., Oelrich, A.R.I., 2007. How structural geology can contribute to make geothermal projects successful, in: *Proceedings European Geothermal Congress 2007*. Unterhaching, Germany, pp. 1–10.
- Philippon, M., Willingshofer, E., Sokoutis, D., Corti, G., Sani, F., Bonini, M., Cloetingh, S., 2015. Slip re-orientation in oblique rifts. *Geology* 43, 147–150. doi:10.1130/G36208.1
- Philit, S., Soliva, R., Labaume, P., Gout, C., Wibberley, C., 2015. Relations between shallow cataclastic faulting and cementation in porous sandstones: First insight from a groundwater environmental context. *Journal of Structural Geology* 81, 89–105. doi:10.1016/j.jsg.2015.10.001
- Phillips, T.B., Jackson, C.A.L., Bell, R.E., Duffy, O.B., Fossen, H., 2016. Reactivation of intrabasement structures during rifting: A case study from offshore southern Norway. *Journal of Structural Geology* 91, 54–73. doi:10.1016/j.jsg.2016.08.008
- Poirier, J.P., 1988. Considerations on the use of analogues in deformation studies. *Bulletin of the Geological Institutions of the University of Uppsala* 14, 49–54.
- Pollard, D.D., Segall, P., 1987. Theoretical Displacements and Stresses Near Fractures in Rock: With Applications To Faults, Joints, Veins, Dikes, and Solution Surfaces, in: Atkinson, B.K. (Ed.), *Fracture Mechanics of Rock*. Academic Press, London, pp. 277–349. doi:10.1016/b978-0-12-066266-1.50013-2
- Power, M.R., Hill, K.C., Hoffman, N., 2003. Structural inheritance, stress rotation, overprinting and compressional reactivation in the Gippsland Basin - Tuna 3D seismic dataset. *The APPEA Journal* 43, 197–221. doi:https://doi.org/10.1071/AJ02010
- Power, M.R., Hill, K.C., Hoffman, N., Bernecker, T., Norvick, M., 2001. The Structural and Tectonic Evolution of the Gippsland Basin: Results from 2D Section Balancing and 3D Structural Modelling, in: Hill, K.C., Bernecker, T. (Eds.), *Eastern Australasian Basins Symposium*. pp. 373–384.
- Price, R.C., Gray, C.M., Nicholls, I.A., Day, A., 1988. Cainozoic volcanic rocks, in: Douglas, J.G., Ferguson, J.A. (Eds.), *Geology of Victoria*. Geological Society of Victoria, Victorian Division, Melbourne, pp. 439–451.
- Pysklywec, R.N., Cruden, A.R., 2004. Coupled crust-mantle dynamics and intraplate tectonics: Two-dimensional numerical and three-dimensional analogue modeling. *Geochemistry, Geophysics, Geosystems* 5. doi:10.1029/2004GC000748
- QGIS Development Team, 2019. QGIS Geographic Information System. Open Source

- Geospatial Foundation Project.
- QGIS Development Team, 2018. QGIS Geographic Information System. Open Source Geospatial Foundation Project.
- Rahmanian, V.D., Moore, P.S., Mudge, W.J., Spring, D.E., 1990. Sequence stratigraphy and the habitat of hydrocarbons, Gippsland Basin, Australia. Geological Society, London, Special Publications 50, 525–544. doi:10.1144/GSL.SP.1990.050.01.32
- Ramberg, H., 1967. Gravity, Deformation and the Earth's Crust, as Studied by Centrifuged Models. Academic Press, London.
- Ranalli, G., 2001. Experimental tectonics: From Sir James Hall to the present. *Journal of Geodynamics* 32, 65–76. doi:10.1016/S0264-3707(01)00023-0
- Ranalli, G., 1995. Rheology of the Earth, 2nd ed. Chapman and Hall, London.
- Rawnsley, K.D., Rives, T., Petit, J.-P., 1992. Joint development in perturbed stress fields near faults. *Journal of Structural Geology* 14, 939–951. doi:https://doi.org/10.1016/0191-8141(92)90025-R
- Reeve, M.T., Bell, R.E., Duffy, O.B., Jackson, C.A.L., Sansom, E., 2015. The growth of non-colinear normal fault systems; What can we learn from 3D seismic reflection data? *Journal of Structural Geology* 70, 141–155. doi:10.1016/j.jsg.2014.11.007
- Riller, U., Clark, M.D., Daxberger, H., Doman, D., Lenauer, I., Plath, S., Santimano, T., 2017. Fault-slip inversions: Their importance in terms of strain, heterogeneity, and kinematics of brittle deformation. *Journal of Structural Geology* 101, B2–B6. doi:10.1016/j.jsg.2017.06.013
- Riller, U., Cruden, A.R., Boutelier, D., Schrank, C.E., 2012. The causes of sinuous crustal-scale deformation patterns in hot orogens: Evidence from scaled analogue experiments and the southern Central Andes. *Journal of Structural Geology* 37, 65–74. doi:10.1016/j.jsg.2012.02.002
- Ring, U., 1994. Urema graben 13, 313–326.
- Robin, P.Y.F., Jowett, E.C., 1986. Computerized density contouring and statistical evaluation of orientation data using counting circles and continuous weighting functions. *Tectonophysics* 121, 207–223. doi:10.1016/0040-1951(86)90044-2
- Rohrbaugh, M.B.J., Dunne, W.M., Mauldon, M., 2002. Estimating fracture trace intensity, density, and mean length using circular scan lines and windows. *AAPG Bulletin* 86, 2089–2104. doi:10.1306/61EEDE0E-173E-11D7-8645000102C1865D

- Rosendahl, B.R., 1987. Architecture of continental rifts with special reference to East Africa. *Annual Review of Earth and Planetary Sciences* 15, 445–503.
- Rotevatn, A., Kristensen, T.B., Ksienzyk, A.K., Wemmer, K., Henstra, G.A., Midtkandal, I., Grundvåg, S.A., Andresen, A., 2018. Structural inheritance and rapid rift-length establishment in a multiphase rift: the East Greenland rift system and its Caledonian orogenic ancestry. *Tectonics* 37, 1858–1875. doi:10.1029/2018TC005018
- Salazar-Mora, C.A., Huismans, R.S., Fossen, H., Egydio-Silva, M., 2018. The Wilson Cycle and Effects of Tectonic Structural Inheritance on Rifted Passive Margin Formation. *Tectonics* 37, 3085–3101. doi:10.1029/2018TC004962
- Salvini, R., Mastroiocco, G., Seddaiu, M., Rossi, D., Vanneschi, C., 2017. The use of an unmanned aerial vehicle for fracture mapping within a marble quarry (Carrara, Italy): photogrammetry and discrete fracture network modelling. *Geomatics, Natural Hazards and Risk* 8, 34–52. doi:10.1080/19475705.2016.1199053
- Samsu, A., Cruden, A.R., Hall, M., Micklethwaite, S., Denyszyn, S.W., 2019. The influence of basement faults on local extension directions: Insights from potential field geophysics and field observations. *Basin Research* 00, 1–26. doi:10.1111/bre.12344
- Sandiford, M., 2003. Neotectonics of southeastern Australia: linking the Quaternary faulting record with seismicity and in situ stress. *Geological Society of Australia Special Publication* 22, 101–113. doi:10.1130/0-8137-2372-8.107
- Sandiford, M., Wallace, M., Coblenz, D., 2004. Origin of the *in situ* stress field in south-eastern Australia. *Basin Research* 16, 325–338. doi:10.1111/j.1365-2117.2004.00235.x
- Sarafian, E., Evans, R.L., Abdelsalam, M.G., Atekwana, E., Elsenbeck, J., Jones, A.G., Chikambwe, E., 2018. Imaging Precambrian lithospheric structure in Zambia using electromagnetic methods. *Gondwana Research* 54, 38–49. doi:10.1016/j.gr.2017.09.007
- Schedl, A., Wiltschko, D. V., 1987. Possible effects of pre-existing basement topography on thrust fault ramping. *Journal of Structural Geology* 9, 1029–1037. doi:10.1016/0191-8141(87)90011-3
- Schimmel, M., Assumpção, M., VanDecar, J.C., 2003. Seismic velocity anomalies beneath SE Brazil from P and S wave travel time inversions. *Journal of Geophysical Research: Solid Earth* 108, 2191. doi:https://doi.org/10.1029/2001JB000187
- Schueller, S., Davy, P., 2008. Gravity influenced brittle-ductile deformation and growth faulting in the lithosphere during collision: Results from laboratory experiments. *Journal*

- of Geophysical Research: Solid Earth 113, 1–21. doi:10.1029/2007JB005560
- Seers, T.D., Hodgetts, D., 2016. Extraction of three-dimensional fracture trace maps from calibrated image sequences 12. doi:10.1130/GES01276.1
- Segall, P., Pollard, D.D., 1980. Mechanics of discontinuous faults. *Journal of Geophysical Research: Solid Earth* 85, 4337–4350. doi:10.1029/JB085iB08p04337
- Seymour, D.B., Calver, C.R., Green, G.R., 2007. The Geology and Mineral Deposits of Tasmania: a summary. *Tasmanian Geological Survey Bulletin* 72, 29.
- Sharples, W., Moresi, L.-N., Jadamec, M.A., Revote, J., 2015. Styles of rifting and fault spacing in numerical models of crustal extension. *Journal of Geophysical Research: Solid Earth* 120, 4379–4404. doi:10.1002/2014JB011813. Received
- Sibson, R.H., 2012. Reverse fault rupturing: competition between non-optimal and optimal fault orientations. *Geological Society, London, Special Publications* 367, 39–50. doi:10.1144/SP367.4
- Sibson, R.H., 1985. A note on fault reactivation. *Journal of Structural Geology* 7, 751–754. doi:10.1016/0191-8141(85)90150-6
- Smith, M.A., Bernecker, T., Liberman, N., Moore, D.H., Wong, D., 2000. Petroleum prospectivity of the deep-water gazettal areas V00-3 & V00-4, Southeastern Gippsland Basin, Victoria, Australia. *Victorian Initiative for Minerals and Petroleum Report* 65.
- Stearns, D.W., Friedman, M., 1969. Reservoirs in Fractured Rock 82–106.
- Strijker, G., Bertotti, G., Luthi, S.M., 2012. Multi-scale fracture network analysis from an outcrop analogue: A case study from the Cambro-Ordovician clastic succession in Petra, Jordan. *Marine and Petroleum Geology* 38, 104–116. doi:http://dx.doi.org/10.1016/j.marpetgeo.2012.07.003
- Stubley, M.P., 1989. Fault and kink-band relationships at Mystery Bay, Australia. *Tectonophysics* 158, 75–92. doi:10.1016/0040-1951(89)90317-X
- Swallow, E.J., Wilson, C.J.N., Charlier, B.L.A., Gamble, J.A., 2018. Mafic inputs into the rhyolitic magmatic system of the 2.08 Ma Huckleberry Ridge eruption, Yellowstone. *American Mineralogist* 103, 757–775. doi:10.2138/am-2018-6273
- Teasdale, J.P., Pryer, L., Romine, K., Stuart-Smith, P., Etheridge, M., Loutit, T., Buckingham, A., Shi, Z., Foss, C., Vizey, J., Henley, P., Petrovich, S., Guy-Villon, M., 2004. Australian Southern Margin SEEBASE™ Compilation, April 2004 [WWW Document]. URL <https://data.gov.au/dataset/9131aad8-7d83-4a2b-a678-542e2a1af68a> (accessed 6.26.18).

- Theunissen, K., Klerkx, J., Melnikov, A., Mruma, A., 1996. Mechanisms of inheritance of rift faulting in the western branch of the East African Rift, Tanzania. *Tectonics* 15, 776–790. doi:10.1029/95TC03685
- Thiele, S.T., Grose, L., Samsu, A., Micklethwaite, S., Vollgger, S.A., Cruden, A.R., 2017. Rapid, semi-automatic fracture and contact mapping for point clouds, images and geophysical data. *Solid Earth* 8, 1241–1253. doi:10.5194/se-8-1241-2017
- Thiele, S.T., Jessell, M.W., Lindsay, M., Ogarko, V., Wellmann, J.F., Pakyuz-Charrier, E., 2016. The topology of geology 1: Topological analysis. *Journal of Structural Geology* 91, 27–38. doi:10.1016/j.jsg.2016.08.009
- Thomas, W.A., 2006. Tectonic inheritance at a continental scale. *GSA Today* 16, 4–11.
- Tommasi, A., Vauchez, A., 2001. Continental rifting parallel to ancient collisional belts: an effect of the mechanical anisotropy of the lithospheric mantle. *Earth and Planetary Science Letters* 185, 199–210. doi:10.1016/S0012-821X(00)00350-2
- Tosolini, A.-M.P., McLoughlin, S., Drinnan, A.N., 1999. Stratigraphy and fluvial sedimentary facies of the Neocomian lower Strzelecki Group, Gippsland Basin, Victoria. *Australian Journal of Earth Sciences* 46, 951–970. doi:10.1046/j.1440-0952.1999.00757.x
- Totterdell, J., Blevin, J., Struckmeyer, H., Bradshaw, B., Colwell, J., Kennard, J., 2000. A new sequence framework for the Great Australian Bight: starting with a clean slate. *The APPEA Journal* 40, 95–118. doi:https://doi.org/10.1071/AJ99007
- Totterdell, J.M., Bradshaw, B.E., 2004. The structural framework and tectonic evolution of the Bight Basin. *Eastern Australasian Basins Symposium II* 41–61.
- Trinks, I., Clegg, P., McCaffrey, K., Jones, R., Hobbs, R., Holdsworth, B., Holliman, N., Imber, J., Waggott, S., Wilson, R., 2005. Mapping and analysing virtual outcrops. *Visual Geosciences* 10, 13–19. doi:10.1007/s10069-005-0026-9
- Tuckwell, G.W., Lonergan, L., Jolly, R.J.H., 2003. The control of stress history and flaw distribution on the evolution of polygonal fracture networks. *Journal of Structural Geology* 25, 1241–1250. doi:10.1016/S0191-8141(02)00165-7
- Tveite, H., 2015. The QGIS Line Direction Histogram Plugin [WWW Document]. URL <http://arken.nmbu.no/~havatv/gis/qgisplugins/LineDirectionHistogram/> (accessed 7.26.16).
- van Wijk, J.W., 2005. Role of weak zone orientation in continental lithosphere extension. *Geophysical Research Letters* 32, L02303. doi:10.1029/2004GL022192

- VanDecar, J.C., James, D.E., Assumpção, M., 1995. Seismic evidence for coherent flow of the crust and upper mantle below south America since the breakup of Gondwana. *Nature* 378, 25–31.
- VandenBerg, A.H.M., Cayley, R.A., Willman, C.E., Morand, V.J., Seymon, A.R., Osborne, C.R., Taylor, D.H., Haydon, S.J., McLean, M., Quinn, C., Jackson, P., Sandford, A.C., 2006. Walhalla–Woods Point–Tallangalook special map area geological report, Geological Survey of Victoria Report 127. GeoScience Victoria. Department of Primary Industries.
- VandenBerg, A.H.M., Willman, C.E., Maher, S., Simons, B.A., Cayley, R.A., Taylor, D.H., Morand, V.J., Moore, D.H., Radojkovic, A., 2000. The Tasman Fold Belt System in Victoria. Geological Survey of Victoria Special Publication 462.
- Vaucher, A., Barruol, G., Tommasi, A., 1997. Why do continents break-up parallel to ancient orogenic belts? *Terra Nova* 9, 62–66. doi:10.1111/j.1365-3121.1997.tb00003.x
- Veevers, J.J., Powell, C.M., Roots, S.R., 1991. Review of seafloor spreading around Australia. I. synthesis of the patterns of spreading. *Australian Journal of Earth Sciences* 38, 373–389. doi:10.1080/08120099108727979
- Victorian Department of State Development Business and Innovation, 2014. Victoria - Seamless Geology 2014 [WWW Document]. Bioregional Assessment Source Dataset. URL <https://data.bioregionalassessments.gov.au/datastore/dataset/2872d02e-66cb-42b6-9e5a-63abc8ad871b> (accessed 7.18.18).
- Vollgger, S., Cruden, A., 2019. Cape Liptrap orthomosaic. doi:<https://doi.org/10.26180/5c653193efa25>
- Vollgger, S.A., Cruden, A.R., 2016. Mapping folds and fractures in basement and cover rocks using UAV photogrammetry, Cape Liptrap and Cape Paterson, Victoria, Australia. *Journal of Structural Geology* 85, 168–187. doi:10.1016/j.jsg.2016.02.012
- Watkins, H., Bond, C.E., Cawood, A.J., Cooper, M.A., Warren, M.J., 2019. Fracture distribution on the Swift Reservoir Anticline, Montana : Implications for structural and lithological controls on fracture intensity. Geological Society, London, Special Publications 487.
- Watkins, H., Bond, C.E., Healy, D., Butler, R.W.H., 2015a. Appraisal of fracture sampling methods and a new workflow to characterise heterogeneous fracture networks at outcrop. *Journal of Structural Geology* 72, 67–82. doi:10.1016/j.jsg.2015.02.001

- Watkins, H., Butler, R.W.H., Bond, C.E., Healy, D., 2015b. Influence of structural position on fracture networks in the Torridon Group, Achnashellach fold and thrust belt, NW Scotland. *Journal of Structural Geology* 74, 64–80. doi:10.1016/j.jsg.2015.03.001
- Welch, M.J., Souque, C., Davies, R.K., Knipe, R.J., 2014. Using mechanical models to investigate the controls on fracture geometry and distribution in chalk. *Geological Society, London, Special Publications* 406, 281–309. doi:10.1144/sp406.5
- Whipp, P.S., Jackson, C.A.L., Gawthorpe, R.L., Dreyer, T., Quinn, D., 2014. Normal fault array evolution above a reactivated rift fabric; a subsurface example from the northern Horda Platform, Norwegian North Sea. *Basin Research* 26, 523–549. doi:10.1111/bre.12050
- Wijns, C., Weinberg, R., Gessner, K., Moresi, L., 2005. Mode of crustal extension determined by rheological layering. *Earth and Planetary Science Letters* 236, 120–134. doi:10.1016/j.epsl.2005.05.030
- Will, T.M., Frimmel, H.E., 2018. Where does a continent prefer to break up? Some lessons from the South Atlantic margins. *Gondwana Research* 53, 9–19. doi:10.1016/j.gr.2017.04.014
- Willcox, J.B., Colwell, J.B., Constantine, A.E., 1992. New ideas on Gippsland Basin regional tectonics, in: *Gippsland Basin Symposium 22-23 June 1992*. Melbourne, pp. 93–110.
- Willcox, J.B., Stagg, H.M.J., 1990. Australia's southern margin: a product of oblique extension. *Tectonophysics* 173, 269–281. doi:10.1016/0040-1951(90)90223-U
- Williams, I.S., Tetley, N.W., Compston, W., McDougall, I., 1982. A comparison of K-Ar and Rb-Sr ages of rapidly cooled igneous rocks: two points in the Palaeozoic time scale re-evaluated. *Journal of the Geological Society* 139, 557–568. doi:10.1144/gsjgs.139.5.0557
- Williams, S.E., Whittaker, J.M., Müller, R.D., 2011. Full-fit, palinspastic reconstruction of the conjugate Australian-Antarctic margins. *Tectonics* 30. doi:10.1029/2011TC002912
- Williamson, P.E., Swift, M.G., O'Brien, G.W., Falvey, D.A., 1990. Two-stage Early Cretaceous rifting of the Otway Basin margin of southeastern Australia: Implications for rifting of the Australian southern margin. *Geology* 18, 75–78. doi:10.1130/0091-7613(1990)018<0075:TSECRO>2.3.CO;2
- Willman, C.E., VandenBerg, A.H.M., Morand, V.J., 2002. Evolution of the Southeastern Lachlan Fold Belt in Victoria. *Australian Journal of Earth Sciences* 49, 271–289. doi:10.1046/j.1440-0952.2002.00914.x
- Wilson, C.J.L., Moore, D.H., Luzin, V., Salvemini, F., 2017. Costerfield antimony-gold

- deposit, southeast Australia: Coupling between brittle deformation and dissolution-precipitation reactions in the Melbourne Zone. *Ore Geology Reviews* 91, 741–764. doi:10.1016/j.oregeorev.2017.08.024
- Wilson, J.T., 1966. Did the Atlantic Close and then Re-open? *Nature* 211, 676–681.
- Wilson, R.W., Holdsworth, R.E., Wild, L.E., McCaffrey, K.J.W., England, R.W., Imber, J., Strachan, R.A., 2010. Basement-influenced rifting and basin development: a reappraisal of post-Caledonian faulting patterns from the North Coast Transfer Zone, Scotland. Geological Society, London, Special Publications 335, 795–826. doi:10.1144/SP335.32
- Withjack, M., Jamison, W.R., 1986. Deformation produced by oblique rifting. *Tectonophysics* 126, 99–124. doi:https://doi.org/10.1016/0040-1951(86)90222-2
- Zang, A., Stephansson, O., 2010. *Stress Field of the Earth's Crust*, 1st ed. Springer Netherlands. doi:10.1007/978-1-4020-8444-7
- Zeeb, C., Gomez-Rivas, E., Bons, P.D., Virgo, S., Blum, P., 2013. Fracture network evaluation program (FraNEP): A software for analyzing 2D fracture trace-line maps. *Computers & Geosciences* 60, 11–22. doi:10.1016/j.cageo.2013.04.027
- Zhang, Y.-Z., Dusseault, M.B., Yassir, N.A., 1994. Effects of rock anisotropy and heterogeneity on stress distributions at selected sites in North America. *Engineering Geology* 37, 181–197. doi:10.1016/0013-7952(94)90055-8
- Zwaan, F., Schreurs, G., 2017. How oblique extension and structural inheritance influence rift segment interaction: Insights from 4D analog models. *Interpretation* 5, SD119–SD138. doi:10.1190/INT-2016-0063.1
- Zwaan, F., Schreurs, G., Naliboff, J., Buiter, S.J.H., 2016. Insights into the effects of oblique extension on continental rift interaction from 3D analogue and numerical models. *Tectonophysics* 693, 239–260. doi:10.1016/j.tecto.2016.02.036

Appendix 1

This digital appendix contains:

- Gravity and magnetic grids used for basin-scale (>1 km-scale) fracture interpretation in Chapter 3
- Files related to UAV photogrammetry and 2D orthophotos used for outcrop-scale fracture interpretation in Chapters 3 and 4
- Vector shapefiles of interpreted fracture traces, Chapters 3 and 4
- QGIS project with links to the above datasets

The fileset can be downloaded via the following link:

<https://monash.figshare.com/s/cddf2fc067a0a9af4cd8>

Appendix 2

Acquisition of UAV orthophotos (Chapter 4)

We generated high-resolution orthophotos for the Harmers Haven North, Harmers Haven South, Eagles Nest, the Caves – Flat Rocks, and Inverloch localities using a UAV photogrammetry workflow outlined in Bemis et al. (2014) and Vollgger & Cruden (2016). The four survey areas are horizontal wave-cut platforms made up of the Lower Cretaceous Strzelecki Group, providing a 2D dataset that sufficed for digital fracture tracing. The parameters of the UAV surveys, which were carried out on four non-consecutive days, are summarized in Table A1. Despite varying light conditions between each survey, we were able to produce photogrammetric models of consistent quality by using the same image capture and processing workflow for each model.

Prior to capturing the aerial photographs, we placed randomly distributed ground control points (GCP) across the study area. The coordinates of the GCP were surveyed using either a handheld Garmin eTrex handheld GPS with an accuracy of ~3 m or a dual-frequency ProMark 500 RTK GPS with an accuracy of 1–5 cm and were later used for model georeferencing. For the Harmers Haven North and Eagles Nest survey areas, we did not use any GCP and instead used coordinates from the onboard GPS to reference the photogrammetric model.

We used a Zenmuse X3 (FC350) camera with a 20 mm fixed focal length lens, mounted on a DJI Inspire 1 multi-rotor UAV, to capture downward-looking (nadir) aerial photographs at two-second to six-second intervals. The UAV was flown at constant altitude above ground level (AGL) and a maximum speed of 4 m/s. The camera was set to aperture priority (f/2.8). Missions were flown along transects that were oriented roughly parallel to the length of the outcrop. Flights were configured with an 85% forward overlap and a 75% side overlap.

Selected images were imported into Agisoft Photoscan and processed into two-dimensional (2D) orthophotos using structure-from-motion (SfM) algorithms. The resulting orthophoto for each area covers 0.040 to 0.330 km² with ~2–3.5 cm/pixel resolution.

Table A1 Summary of UAV survey parameters for Harmers Haven North (HHN), Harmers Haven South (HHS), Eagles Nest (EN), the Caves – Flat Rocks (TC-FR), and Inverloch (INV) and properties of resulting orthophotos. The locations for outcrop access points are given in GDA94 / MGA zone 55 (EPSG:28355) coordinates. AGL = above ground level; GSD = ground sampling distance; GCP = ground control point.

Locality		HHN	HHS	EN	TC-FR	INV
Access point	Easting	375636	376471	384317	385183	386212
	Northing	5720519	5720025	5719176	5719940	5721244
Image capture	Date	20-10-2016	24-11-2015	23-09-2016	07-09-2016	07-09-2016
	Time	9:15 - 10:25	12:00 - 14:00	11:05 - 12:35	9:50 - 12:05	9:50 - 12:05
	Cloud cover	sunny	cloudy	partly cloudy	partly cloudy	partly cloudy
	Interval	2 - 4 s	4 - 6 s	2 s	2 - 4 s	2 - 4 s
	Altitude (AGL)	80 m	50 m	85 m	90 m	40 m
	Velocity	< 4 m/s	< 4 m/s	< 4 m/s	< 4 m/s	< 4 m/s
	Aperture	f/2.8	f/2.8	f/2.8	f/2.8	f/2.8
	Forward overlap	85%	85%	85%	85%	85%
	Side overlap	75%	75%	75%	75%	75%
	Ground resolution	2.94 cm/pixel	1.94 cm/pixel	3.18 cm/pixel	3.50 cm/pixel	3.25 cm/pixel
Processing	No. of images	427	704	637	605	115
	No. of GCPs	11	15	0	0	10
	GPS	Handheld GPS	DGPS RTK	Onboard GPS	Onboard GPS	Handheld GPS
Orthophoto	Coverage area	0.148 km ²	0.330 km ²	0.182 km ²	0.234 km ²	0.040 km ²

References

- Bemis, S.P., Micklethwaite, S., Turner, D., James, M.R., Akciz, S., Thiele, S.T., Bangash, H.A., 2014. Ground-based and UAV-Based photogrammetry: A multi-scale, high-resolution mapping tool for structural geology and paleoseismology. *Journal of Structural Geology* 69, 163–178. doi:10.1016/j.jsg.2014.10.007
- Vollgger, S.A., Cruden, A.R., 2016. Mapping folds and fractures in basement and cover rocks using UAV photogrammetry, Cape Liptrap and Cape Paterson, Victoria, Australia. *Journal of Structural Geology* 85, 168–187. doi:10.1016/j.jsg.2016.02.012

Appendix 3

Additional figure for Chapter 5: Cumulative maximum normal strain on surface calculated from PIV data of Exp LE-05, LE-07, and LE-08 at different stages of the experiments. Faults develop first in the SE domain above the NLC. Faults in the NW domain develop later and in a less localized fashion, except above the weak zones in Exp LE-07.

